Technical Aspects of Sacral Neuromodulation in Pelvic Intraoperative Neuromonitoring

AGH University of Science and Technology

Tomasz Wojciech Moszkowski

Supervisor: **Prof. dr hab. inż. Piotr Augustyniak**

Assisting supervisor: **Prof. Dr. -Ing. Klaus-Peter Hoffmann**

Department of Automatics and Biomedical Engineering
AGH – University of Science and Technology, Kraków, Poland

This dissertation is submitted for the degree of
Doctor of Engineering

Faculty of Electrical Engineering,
Automatics, Computer Science and
Biomedical Engineering

November 2017

Techniczne Aspekty Neuromodulacji Krzyżowej w Miednicznym Neuromonitoringu Śródoperacyjnym

AGH

Akademia Górniczo-Hutnicza
im. Stanisława Staszica w Krakowie

Tomasz Wojciech Moszkowski

Promotor: **Prof. dr hab. inż. Piotr Augustyniak**

Promotor pomocniczy: **Prof. Dr. -Ing. Klaus-Peter Hoffmann**

Katedra Automatyki i Inżynierii Biomedycznej
Akademia Górniczo-Hutnicza im. S. Staszica w Krakowie

Niniejsza rozprawa została złożona celem otrzymania stopnia
Doktora Inżyniera

Wydział Elektrotechniki, Automatyki,
Informatyki i Inżynierii
Biomedycznej

Listopad 2017

I dedicate this thesis to my loving mother, Marta Moszkowska, my father who is no longer here, Leszek Moszkowski, my always supportive brothers, Paweł and Jakub Moszkowscy, and their loving families …

Dedykuję tę rozprawę doktorską mojej kochającej mamie, Marcie Moszkowskiej, mojemu tacie, którego już tutaj nie ma, Leszkowi Moszkowskiemu, moim zawsze wspierającym braciom, Pawłowi i Jakubowi Moszkowskim, oraz ich kochającym rodzinom …

Declaration

I hereby declare that except where specific reference is made to the work of others, the contents of this dissertation are original and have not been submitted in whole or in part for consideration for any other degree or qualification in this, or any other university. This dissertation is my own work and contains nothing which is the outcome of work done in collaboration with others, except as specified in the text and Acknowledgements. This dissertation contains fewer than 65,000 words including appendices, bibliography, footnotes, tables and equations and has fewer than 150 figures.

Tomasz Wojciech Moszkowski
9. November 2017

Oświadczenie

Oświadczam, że zawartość niniejszej rozprawy doktorskiej, z pominięciem miejsc w tekście z konkretnym odniesieniem do pracy innych, jest oryginalna i nie została wcześniej złożona ani w części ani w całości w celu rozpatrzenia nadania jakiegokolwiek stopnia naukowego lub kwalifikacji na tej lub na jakiejkolwiek innej uczelni. Ta rozprawa jest moją samodzielną pracą i nie zawiera żadnych elementów, które są wynikiem pracy we współpracy z osobami trzecimi z wyjątkiem miejsc w tekście z wyraźnym zaznaczeniem tego faktu oraz poza rozdziałem "Podziękowania (Acknowledgements)". Niniejsza rozprawa zawiera mniej niż 65 000 słów włącznie z dodatkami, bibliografią, przypisami, tabelami i równaniami. Ponadto rozprawa zawiera mniej niż 150 ilustracji.

Tomasz Wojciech Moszkowski
9 Listopad 2017

Acknowledgements

To Thilo Krüger, Karin Somerlik-Fuchs, and Celine Wegner for their incessant support, technical and neurophysiological expertise, enthusiasm, and ever constructive criticism.

To Prof. Dr. med. Werner Kneist and PD. Dr. med. Daniel W. Kauff for their clinical support, surgical prowess, and invaluable medical expertise.

To Dr. med. Nicolas Wachter and Dr. Axel Heimann without whom the experimental study would not be possible.

To Prof. David Vodušek for the help with interpreting the electrophysiological data and providing insight into the neurophysiology of the somatic and autonomic nervous system.

To Prof. dr. inż. Piotr Augustyniak and Prof. Dr. Ing- Klaus-Peter Hoffmann for supervising me on my journey to obtaining a doctoral degree.

To the Federal Ministry of Education and Research (Bundesministerium für Bildung und Forschung, BMBF, Germany) for the financial support of the work described in this dissertation (autoPIN Project, grant no. 13GW0022C).

Thank you!

Abstract

INTRODUCTION: Surgery is the main treatment option for rectal cancer patients and poses the risk of postoperative anorectal and urogenital dysfunction due to iatrogenic nerve damage. Pelvic intraoperative neuromonitoring (pIONM) offers the surgeon a means to preserve the autonomic nervous system by monitoring the anorectal and urogenital function during total mesorectal excision (TME). **OBJECTIVES:** To investigate the feasibility and limitations of neuromonitoring of the pelvic autonomic nervous system using transcutaneous electrical nerve stimulation (TENS) using a multi-channel stimulation array as an alternative to the currently used direct nerve stimulation (DNS). Suitability for intraoperative nerve mapping and function monitoring formed the main criteria for the comparison. **METHODS:** Finite element modeling (FEM) of the electrical field resulting from DNS and TENS, the influence of the modeled electrical field on the activation of a model of the autonomic nervous system, and experimental investigation on five male porcine specimens were investigated to evaluate the suitability of TENS for intraoperative nerve mapping and function monitoring. **RESULTS:** The simulated electric field distribution within the lesser pelvis due to DNS and TENS caused activation of the autonomic nervous system for specific stimulation sites and electrode configurations. DNS exhibited higher selectivity in evoking action potentials in specific nerve fibers. Narrow stimulation amplitude ranges and a small number of effective electrode configurations limited the stimulation selectivity and sensitivity to nerve damage during TENS. Although suitable for the identification of nerve damage via DNS, the standard processed EMG of the internal anal sphincter (IAS) could not be used during TENS because of the presence of stimulation artifacts. Previously unobserved evoked potentials within the IAS activity due to DNS and TENS were discovered and their presence was associated with damage of the inferior hypogastric plexus. Possible influence of muscular relaxants on the recorded signals was identified. **CONCLUSION:** TENS proved to be impractical for intraoperative nerve mapping because of limited stimulation selectivity. The electrode configurations associated with identifying the nerve damage suggested the suitability of TENS for function monitoring. However, the specific stimulation conditions needed for achieving sensitivity to nerve damage resulted in a limited number of cases that had to be additionally validated by targeted nerve incision. **OUTLOOK:** Future research

should focus on improving the sensitivity of monitoring the nerve damage by improving the stimulation and signal acquisition methods. **SIGNIFICANCE:** Extracorporeal stimulation of the pelvic autonomic nerves might reduce the time needed for preoperative preparation, allow continuous monitoring of the neural function, and lead to better functional preservation following TME.

Streszczenie

WSTĘP: Zabieg chirurgiczny, który jest główną formą leczenia pacjentów z rakiem odbytnicy, nosi ze sobą ryzyko pooperacyjnych dysfunkcji odbytniczo-analnych i urogenitalnych w związku z jatrogennym uszkodzeniem nerwów. Śródoperacyjny neuromonitoring w chirurgii miednicy mniejszej (*ang.* pelvic intraoperative neurophysiological monitoring, pIONM) oferuje chirurgowi metodę ochrony autonomicznego układu nerwowego poprzez monitorowanie funkcji odbytniczo-analnych i urogenitalnych podczas zabiegu całkowitej resekcji mezorektum (*ang.* total mesorectal excision, TME). **CEL:** Celem niniejszej pracy jest zgłębienie zdatności i ograniczeń neuromonitoringu autonomicznego układu nerwowego w miednicy mniejszej przy wykorzystaniu przezskórnej elektrycznej stymulacji nerwowej (*ang.* transcutaneous electrical nerve stimulation, TENS) z wykorzystanej wielokanałowej macierzy elektrod stymulacyjnych jako alternatywy do obecnie stosowanej bezpośredniej stymulacji nerwów w polu operacyjnym (*ang.* direct nerve stimulation, DNS). Zdatność do śródoperacyjnej identyfikacji struktur nerwowych oraz obserwacji funkcjonalnej unerwienia stanowiły dwa główne kryteria porównawcze. **METODYKA:** Modelowanie za pomocą metody elementów skończonych (*ang.* finite element method, FEM) pola elektrycznego wywołanego przez TENS i DNS, wpływ modelowanego pola na pobudzenie modelu autonomicznego układu nerwowego oraz badania doświadczalne na pięciu prosięcych samcach zostały wykorzystane do oceny zdatności TENS w celu identyfikacji struktur nerwowych oraz monitorowania ich funkcji. **WYNIKI:** Zamodelowany rozkład pola elektrycznego w miednicy mniejszej na skutek DNS i TENS spowodował wzbudzenie autonomicznego układu nerwowego dla określonych miejsc stymulacji oraz konfiguracji elektrod. DNS wykazała wyższą selektywność w wywoływaniu potencjałów czynnościowych w określonych strukturach nerwowych. Podczas TENS, wąskie zakresy intensywności stymulacji oraz mała liczba efektywnych konfiguracji elektrod ograniczyły selektywność stymulacji i zdolność identyfikacji uszkodzenie nerwów. Pomimo praktyczności do identyfikacji uszkodzenia nerwów podczas DNS, standardowa metoda przetwarzania sygnału elektromiograficznego (EMG) wewnętrznego zwiaracza odbytu nie mogła być zastosowana w przypadku TENS z powodu obecności artefaktów stymulacji w sygnale. Odkryto dotychczas niezaobserwowane potencjały wywołane w aktywności EMG wewnętrznego zwieracza odbytu. Ich obecność

była skorelowana z wystąpieniem uszkodzenia struktury nerwowej dolnego splotu podbrzusznego. Zauważono możliwy wpływ środków zwiotczających umięśnienie szkieletowe na amplitudę potencjałów wywołanych. **PODSUMOWANIE:** TENS okazała się nieprakty-czna dla zastosowania w identyfikacji struktur nerwowych z powodu niskiej selektywności stymulacji. Konfiguracje elektrod stymulacyjnych, dla których zauważono związek z wystąpieniem uszkodzenia nerwów, zasugerowały zdatność TENS do monitorowania funkcji unerwienia autonomicznego. Jednakże mała liczba przypadków, w których udało się zidentyfikować uszkodzenie nerwów oraz fakt, że uszkodzenie to musiało być potwierdzone przez celowe przecięcie struktur nerwowych były wynikiem bardzo konkretnych warunków stymulacyjnych. **PERSPEKTYWY ROZWOJU:** Przyszłe badania powinny skupiać się na polepszeniu wrażliwości monitorowania uszkodzenia struktur nerwowych przez polepszenie metod stymulacji nerwowej oraz metod pozyskiwania sygnałów z wewnętrznego zwieracza odbytu. **ZNACZENIE:** Stymulacja autonomicznego układu nerwowego za pomocą źródeł umieszczonych poza polem operacyjnym może zredukować czas potrzebny do przedoperacyjnego przygotowania pacjenta, pozwolić na ciągłe monitorowanie funkcji unerwienia autonomicznego oraz polepszyć sprawność funkcjonalną po zabiegu całkowitego usunięcia mezorektum.

Contents

List of Figures

List of Tables

Nomenclature

Acronyms / Abbreviations

AEP Auditory evoked potentials

AP Action potential

EAS External anal sphincter

EEG Electroencephalography

EMG Electromyography

ENG Electroneurography

FEM Finite element method

HID Human interface device

IAS Internal anal sphincter

IHP Inferior hypogastric plexus

IONM Intraoperative neurophysiological monitoring

MEP Motor evoked potential

MRI Magnetic resonance imaging

NRRD Nearly raw raster data file format

pIONM Pelvic intraoperative neurophysiological monitoring

PSN Pelvic splanchnic nerve

SEP Somatosensory evoked potential

SHP Superior hypogastric plexus

STL Stereolithography file format

TENS Transcutaneous electrical nerve stimulation

TME Total mesorectal excision

Chapter 1

Introduction

The increased risk of rectal cancer in the aging society, it's early detection, and the focus to assure postoperative quality of life justify the scientific interest in pelvic intraoperative neurophysiological monitoring.

1.1 Rectal cancer in the aging society

Rectal cancer is one of the most common cancerous diseases plaguing the modern society [1]. In the United States of America, the colorectal cancer[1] is the third most common type of cancer observed in both women and men [2]. The American Cancer Society anticipates 95 520 cases of colon cancer and 39 910 cases of rectal cancer by the end of 2017. A total of 50 260 cases may prove fatal [3]. Internationally, 944 717 cases were identified in the year 2000. The highest rates of colorectal cancer were identified in the US, Canada, Japan, western Europe, New Zealand, Israel and Australia. Algeria and India formed the other side of the incidence spectrum. In 2011 in Poland alone, the incidence was 3461 men and 2247 women [4]. The rise of the incidence over the last century allegedly correlates with widespread industrialization.

95% of all colorectal cancers are the so called adenocarcinomas – a cancer of glandular origin which occurs in the epithelial tissue [5]. The ethiology of the disease remains largely unclear. However, several genetic mutations have been identified as possible causes: a mutation within the adenoma carcinoma pathway gene, which controls the growth of the mucosa of the large intestine, and hereditary nonpolyposis colorectal cancer pathway.

An entire spectrum of symptoms characterizes rectal cancer. 43% of patients report a change of bowel habits in the form of diarrhea, a change in stool consistence, a feeling of

[1] Colorectal cancer inflicts either the colon or the rectum

incomplete voiding, and tenesmus[2]. Thirteen out of 50 patients report occult bleeding, one in five reports abdominal pain and bloating, 9% experience general discomfort, and 5% report pelvic pain which may signify invasion of the nerve trunks. Inflammation of the peritoneum due to rectal perforation and jaundicing occurs in 3% due to possible metastases.

The treatment of rectal cancer is a multidisciplinary approach: it is often a combination of colorectal surgery, medication oncology, and radiation therapy. The surgery can involve transanal excision, transanal endoscopic microsurgery, endocavity radiotherapy, and minimally invasive sphincter sparing procedures (low anterior rectal resection, coloanal anastomosis, abdominal perineal resection). Additionally, adjuvant medical treatment is undertaken in the form of radiotherapy, intraoperative radiotherapy, chemotherapy, chemoradiation therapy, and radioembolization. In Poland in 2011, 32.51% of all cases were treated with a combination of chemoradiation and surgical therapy, 26.07% underwent surgery, 16.07% accounted for a combination of chemotherapy and surgery, 12.49% underwent radiation therapy and surgery, and 8% underwent any combination of radio- and chemotherapy. In total, surgery constitutes the main treatment option in 87.14% of all cases in Poland alone [4].

1.2 Risks in rectal cancer surgery

Rectal cancer surgery has been associated with disruption of urinary, anoneorectal, and sexual function. Dysfunctions of urinary bladder voiding occur in 26% to 39% of cases, fecal incontinence in between 39% and 47% of cases, sexual dysfunctions (problems with sexual arousal, ejaculation, lubrication, orgasm, and overall sexual satisfaction) in between 62% to 76% of cases [6, 7].

The ethiology of the urogenital and anorectal dysfunction resulting from rectal cancer has been found to be neurogenic. Direct damage to the autonomic nervous system within the lesser pelvis disrupts the function of the organs that control the urinary, anoneorectal and sexual function. During the excision of rectal cancer, direct proximity of the autonomic nerve tissue to the operative field exposes the nerves to high risk of damage due to mechanical cutting, electrical cauterization, strain, excessive heat, and bleeding. Research has shown that the damage inflicted to the pelvic splanchnic nerves, inferior hypogastric plexus, hypogastric nerves, and the pelvic nerve (see Figure 1.1) causes fecal incontinence, failure in bladder voiding and urinary retention, and disturbance of erection, lubrication and sexual arousal [7, 8, 9, 10, 11, 12]. Thus, motivated by the prospect of preserving postoperative function,

[2] A constant urge to pass stools

modern surgical techniques employ various methods to minimize the risk of autonomic nerve damage during rectal cancer surgery.

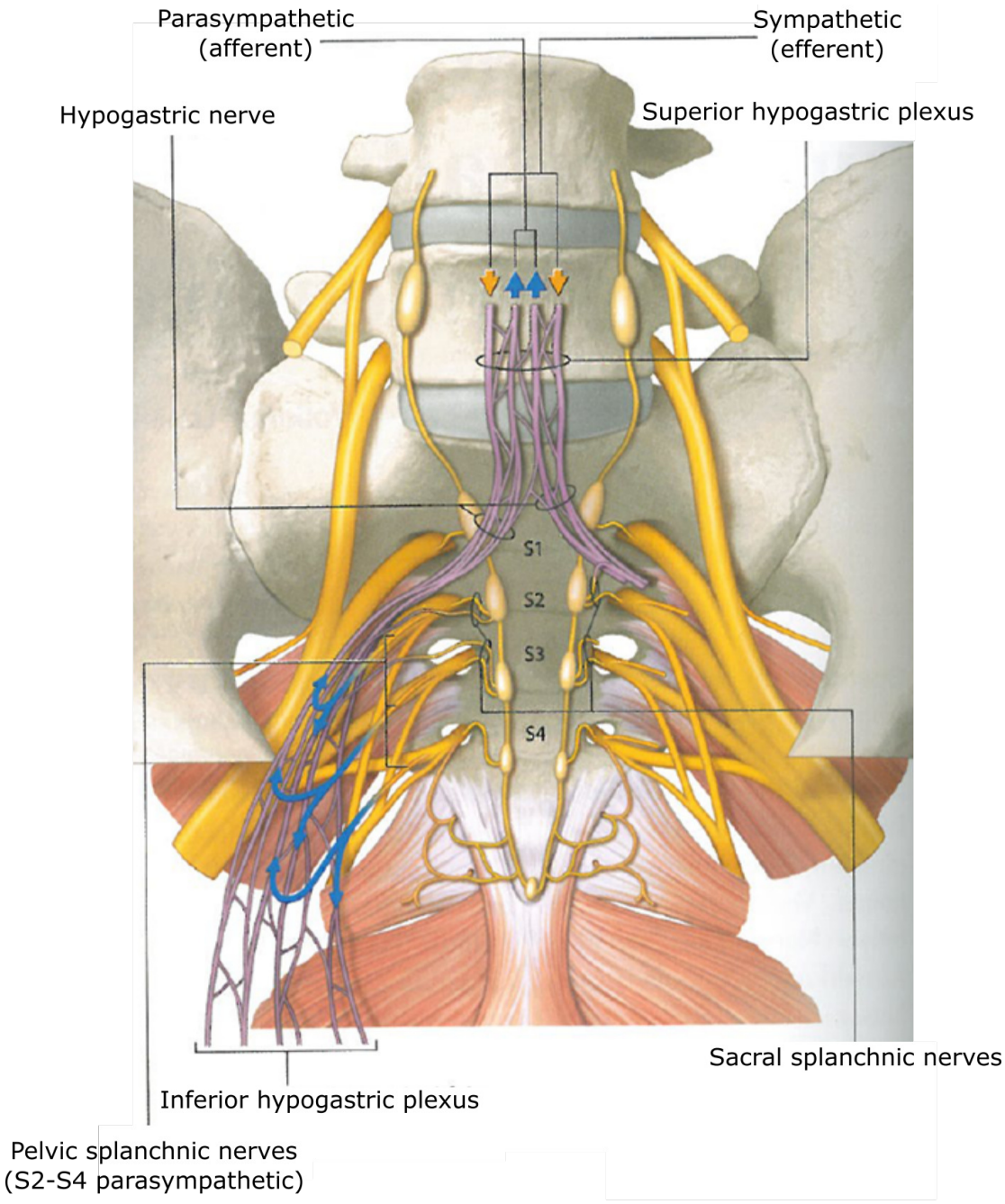

Figure 1.1 Parts of the pelvic autonomic nervous system are at high risk of injury during rectal surgery (image adapted from [13])

1.3 Nerve-sparing rectal cancer surgery

Moriya classified rectal surgical techniques based on the level of nerve preservation [14]:

- **Total preservation of the autonomic nervous system** whose goal is to maintain preoperative function. This technique is best applicable to patients with T2 tumor[3].
- **Resection of the sympathetic nervous system but complete preservation of pelvic nerves** which has been associated with preservation of micturition in both sexes and erectile function in males. This technique is best suited for patients with T3 tumor.
- **Partial preservation of pelvic nerves** which aims to partially preserve micturition. This technique is best suited for patients with node-positive[4] rectal cancer.
- **Extended lateral lymphadenectomy without nerve preservation** where no function preservation is possible.

A notable surgical technique that aims to completely preserve the urogenital and anorectal function is the so called total mesorectal excision (TME). TME is defined as a surgical procedure that targets tumors that lie in the middle and lower rectum [15]. Cancer excision is achieved through resection of a significant part of the rectum together with the so called mesorectum — fatty and connective tissue containing blood vessels that surrounds the rectum (see Figure 1.2). The TME technique consists of five distinct steps:

1. Laparotomy and exploration of the abdominal and pelvic cavities to intraoperatively identify and diagnose the cancerous tissue.
2. Mobilization of the left colon and the splenic flexure.
3. Mobilization of the rectum.
4. Resection of the rectal tumor, sigmoid colon, and mesorectum.
5. Reconstruction of the rectum.

This procedure aims to achieve functional preservation by retaining the structure of the autonomic nerves and the anal musculature that contributes to controlling fecal continence.

[3] Cancer staging according to the classification of malignant tumors system (TNM). The letter "T" indicates that the cancerous tissue forms a tumor; the following number indicates the tumor size - the higher the number, the bigger the tumor [15]

[4] Node-positive cancer refers to severe lymph node infiltration. This type of cancer has high risk of systemic metastases [15].

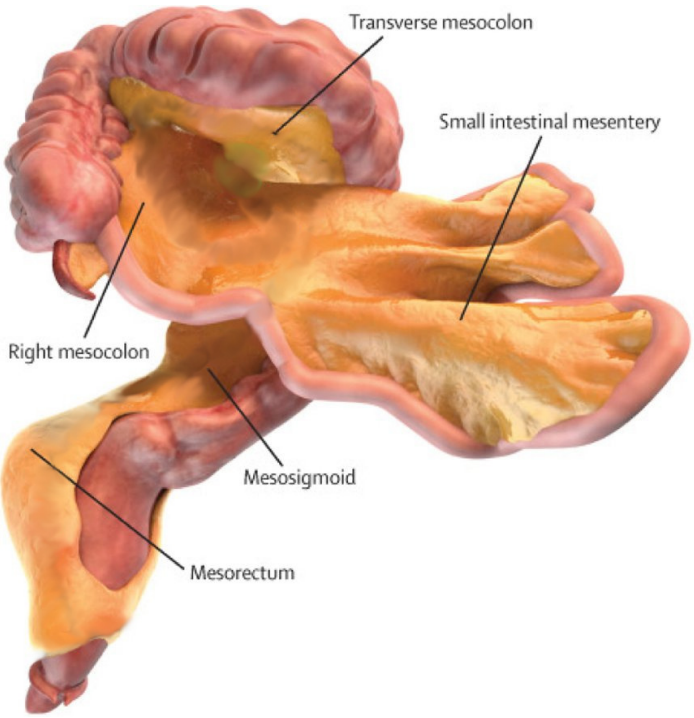

Figure 1.2 Depiction of the lower intestinal tract including the mesentery and mesorectum (image adapted from [16])

For better nerve preservation, Runkel et al. proposed a variation of TME that uses the autonomic nerve structures as anatomical landmarks within the pelvic floor to guide the path of incision [17]. Nerve preservation can be achieved by exposing and visualizing the nerve tissue within the operative field. This has become significantly easier with the use of laparoscopic techniques which offer optical magnification of the operative field, illumination, and angulation – the ability to reach angulated areas of the operative field with laparoscopic tools.

Although modern surgical techniques strongly focus on nerve preservation, a significant percentage of patients still experience postoperative functional impairment [18]. This is because the complex and highly variable neuroanatomy of the pelvic autonomic nervous system complicates intraoperative visualization of nerves despite the use of modern laparoscopic techniques [19]. Also, visual nerve preservation has recently been deemed an insufficient predictor of preserved nerve and postoperative function. Thus, successful nerve sparing requires further methodological improvement.

Chapter 2

State of the art

2.1 Intraoperative neuromonitoring

Functional impairment due to nerve damage during surgery motivates the need to monitor the nerve function using intraoperative neurophysiological monitoring (IONM) techniques. IONM focuses on patient safety, preserving nerve function, and optimizing the surgical outcome. Over the last 100 years, IONM has evolved from visually observing the facial muscles in 1898 during the surgery near the facial nerve to standardized adoption in many fields, including neurosurgery, spine surgery, orthopedic surgery, otolaryngology, and general surgery (see Table 2.1 on page 8). IONM helps to evaluate the nerve function with the use of electrophysiological techniques such as electromyography (EMG), motor evoked potentials (MEPs), and somatosensory evoked potentials (SEPs) (see Table 2.2 on page 9) [20].

The need to identify and monitor the nerve function driven by difficult visual identification of the autonomic nerve structures is even more pronounced in rectal cancer surgery and motivates the use of neurophysiological monitoring [22]. Within the scope of this dissertation, the neurophysiological monitoring techniques applied during rectal cancer surgery will be referred to as pelvic intraoperative neurophysiological monitoring (pIONM). Research has shown that intraoperative electrical stimulation of the inferior hypogastric plexus and pelvic splanchnic nerves could be used to predict postoperative urogenital and anorectal function [18, 23, 24]. Simultaneous monitoring of the activity of the internal anal sphincter and the urinary bladder exhibited the potential to increase the nerve identification rate due to conjoint action [25]. The method could predict functional nerve integrity, provide insight into the neuroanatomy of the pelvic floor and increase the intraoperative identification rates of the neural structures [26]. Kauff et al. have shown in a prospective study that the use of pIONM during surgery correlates with a significantly lower incidence of short-term and long-term urinary dysfunction than in a control group [27]. In minimally invasive laparoscopic total

Table 2.1 Scopes of application of intraoperative neurophysiological monitoring (source: [21])

Scope of application	Nerves/ structures	Postoperative dysfunctions
Thyroid surgery	Branches of vagal nerve	
	Recurrent laryngeal nerve	Dysphonia
		Dyspnea
		Dysphagia
	Superior laryngeal nerve	Voice alterations
Skull base, posterior fossa, and brainstem surgery	Spinal cord	Hypesthesia
		Hemiparesis
		Paraplegia
		Quadriplegia
		Coma
Skull base, posterior fossa, brainstem, and head-and-neck surgery	Cranial nerves CN I-XII	
	Olfactory nerve CN I	Reduced or absend smell sensation
	Optic nerve CN II	Visual loss
	Oculomotor nerves CN II, IV, VI	Syndrome of superior orbital fissure
		Eyelid ptosis
		Eyeball fixation
		Exophthalmus
		Pupil dilation
		Low vision limitation
		Diplopia
	Trigeminal nerve CN V	Trigeminal neuralgia
		Sensory disturbances in the face
		Jaw muscle paresis
		Activation of trigeminocardiac reflex → (transient) asystole
	Facial nerve CN VII	Paralysis of the mimetic musculature
	Acoustic nerve CN VIII	Hearing reduction or loss
	Glossopharyngeal nerve CN IX	Sensory disturbances of the palate
		Bitter taste will not be perceived
		Loss of gag reflex
	Vagal nerve CN X	Uvular deviation
		Aphonia
		Dysphagia
	Spinal accessory nerve CN XI	Shoulder drop
	Hypoglossal nerve CN XII	Tongue atrophy
Spine surgery	Brachial plexus	Paralysis of shoulder and arm muscles
		Pain
		Atrophia
	Lumbosacral plexus	Paralysis of lower limb muscles
		Inguinal pain
		Lower limb sensory disturbances
	Spinal cord	Hypesthesia
		Hemiparesis
		Paraplegia
		Quadriplegia
		Coma
	Conus medullaris	Conus syndrome
	Cauda equina	Cauda syndrome
Pelvic surgery	Pelvic autonomic nerves (superior hypogastric plexus, hypogastric nerve, inferior hypogastric plexus, splanchnic nerves, neurovascular bundles	Sexual dysfunction Bladder dysfunction Anorectal dysfunction

Table 2.2 Measurement modalities employed in intraoperative neurophysiological monitoring (source: [21])

Methods	Application
Manometry	Pelvic surgery
Intravesical pressure	
Intraurethral pressure	
Intracavernosal pressure	
Tumescence measurement	Pelvic surgery
Electrically evoked compound action potential (ECAP)	Neurosurgery
Electrocochleography	Neurosurgery
Electroencephalography (EEG)	Cerebrovascular surgery
Conventional EEG	Cardiovascular suergery
Processed EEG	Interventional neuroradiology
Electroneurography (ENG)	Peripheral nerve surgery
	Nerve root surgery
	Plexus surgery
Electromyography (EMG)	Thyroid surgery
Spontaneous EMG	Spine surgery
Triggered EMG	Pelvic surgery
	Parotis surgery
	Neurosurgery
	Peripheral nerve surgery
Evoked potentials (EP)	
Auditory evoked potentials (AEP)	Neurosurgery
Brainsem AEP (BEAP)	Cardiovascular surgery
Mid-latency AEP (MLAEP)	Interventional neuroradiology
Long-latency AEP (LLAEP)	
Descending neurogenic evoked potentials (DNEP)	Spine surgery
Percutaneous stimulation (PERC)	
Epidural stimulation (EPI-DNEP)	
Spinuous process stimulation (SP-DNEP)	
Motor evoked potentials (MEP)	Spine surgery
Transcranial electric MEP (TCeMEP)	Neurosurgery
Somatosensory evoked potentials (SSEP)	Peripheral nerve surgery
Cortical SSEP	Spine surgery
Spinal SSEP	Cerebrovascular surgery
Dermatomal SSEP	Interventional neuroradiology
Visual evoked potentials (VEP)	Orbital surgery
	Pituitary gland surgery
Intraoperative language monitoring	Neurosurgery

mesorectal excision, the long term effect of pIONM on postoperative anorectal and urogenital function is being currently investigated in a multi-centric randomized study on a total of 188 patients [28] with one year follow-up. The scope of application ranges from open, laparoscopic, trans-anal minimally invasive, to even robot-assisted surgery of rectal cancer [29, 30, 31].

2.2 Neuromonitoring as a part of rectal surgery

pIONM combines electrical stimulation of the autonomic nervous system exposed during rectal surgery with simultaneous monitoring of the autonomically innervated internal anal sphincter and the detrusor vesicae muscle (see Figure 2.1).

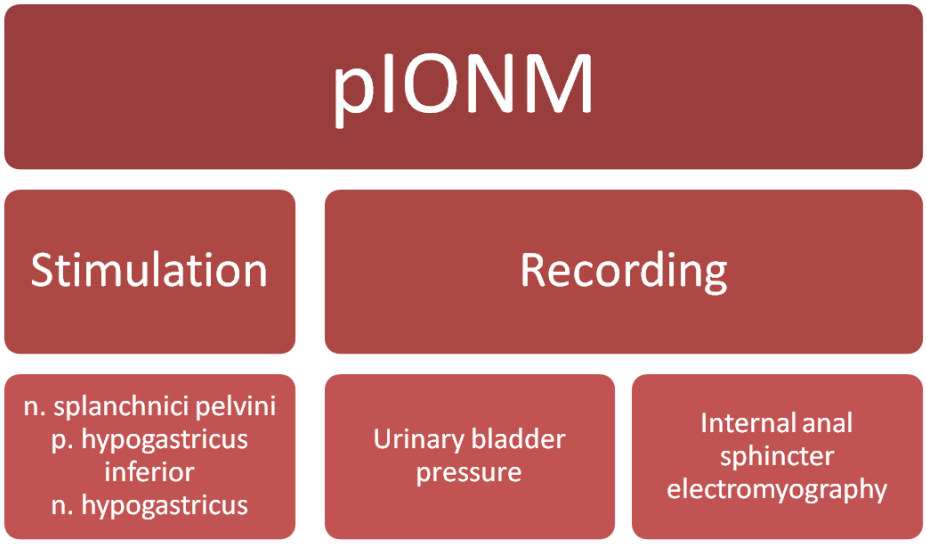

Figure 2.1 The state of the art of pelvic intraoperative neurophysiological monitoring

pIONM is performed during rectal cancer surgery upon exposing the autonomic nervous system. Depending on surgical indications, rectal cancer surgery employs techniques ranging from open surgery, laparoscopy, to robotic assistance [14, 32, 17, 33]. Below is an example of exposing the autonomous nerve structures during open total mesorectal excision.

1. Opening of the abdominal cavity.
2. Uncovering of the peritoneal fascia.
3. Exposing of the *superior hypogastric plexus* on the promontory.
4. Dissecting between the presacral and the mesorectal fascia.

5. Exposing of the *inferior hypogastric plexi* and the *pelvic splanchnic nerves*.

6. Dissecting the mesorectum laterally.

During rectal surgery, the surgeon uses a bipolar hand probe to stimulate the exposed tissues that may contain the nerve structures of interest (see Figure 2.2). The literature reports using monophasic cathodic pulses with an amplitude ranging from 3 to 12 mA, a pulse width of 200 µs, and a stimulation frequency of 30 Hz [18, 23].

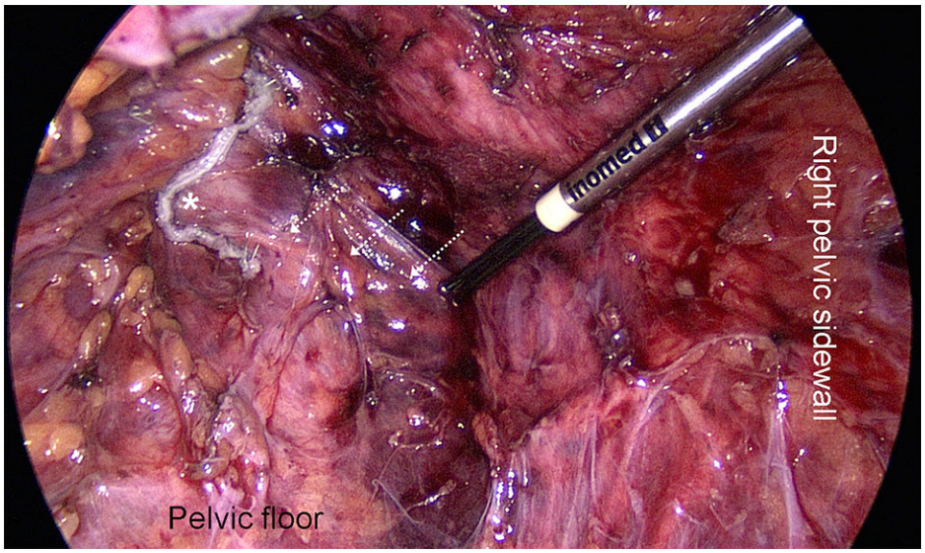

Figure 2.2 Stimulation of the pelvic sidewall using a bipolar probe to identify the autonomic nerve structures during total mesorectal excision (source: [34])

Changes within the urinary bladder pressure are monitored during surgery by cystomanometry using a dedicated transducer; changes in the activity of the smooth muscle tissue of the internal anal sphicter (IAS) are recorded using bipolar needle electrodes (see Figure 2.3). Additionally, the activity of the external anal sphincter – under voluntary control of the somatic nervous system – helps to intraoperatively assess the influence of insufficient muscle relaxation on the EMG signal of the IAS. The resulting recording is displayed as *free-running* EMG. Figure 2.4 shows an intraoperative measurement using the three modalities prior to and during stimulation of the autonomic pelvic nerves.

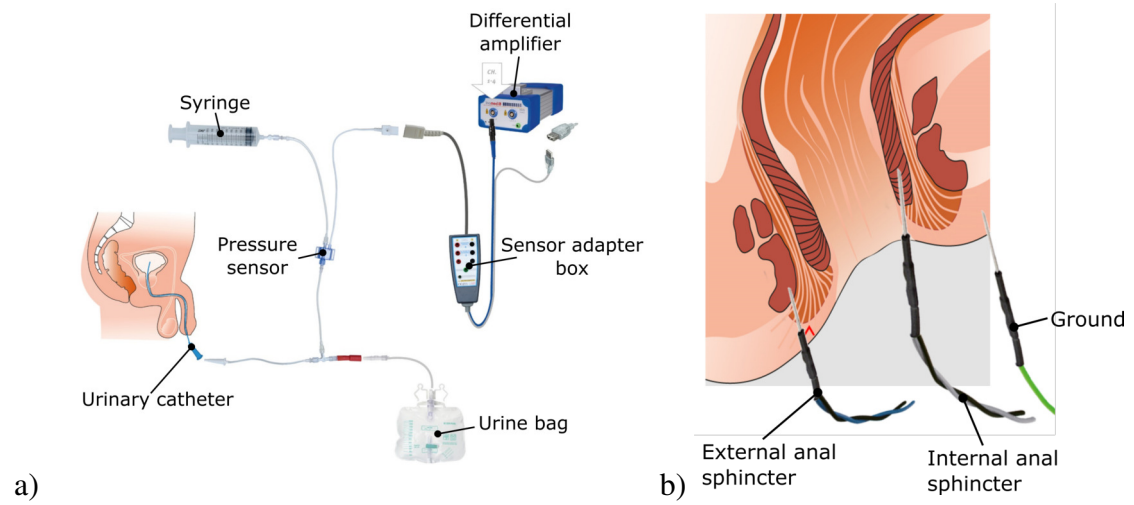

Figure 2.3 The setup for recording during pIONM: a) a catheter set for pressure measurement, b) a set of bipolar needle electrodes for insertion into the external and internal anal sphincters (source: materials obtained from inomed Medizintechnik GmbH, Emmendingen, Germany).

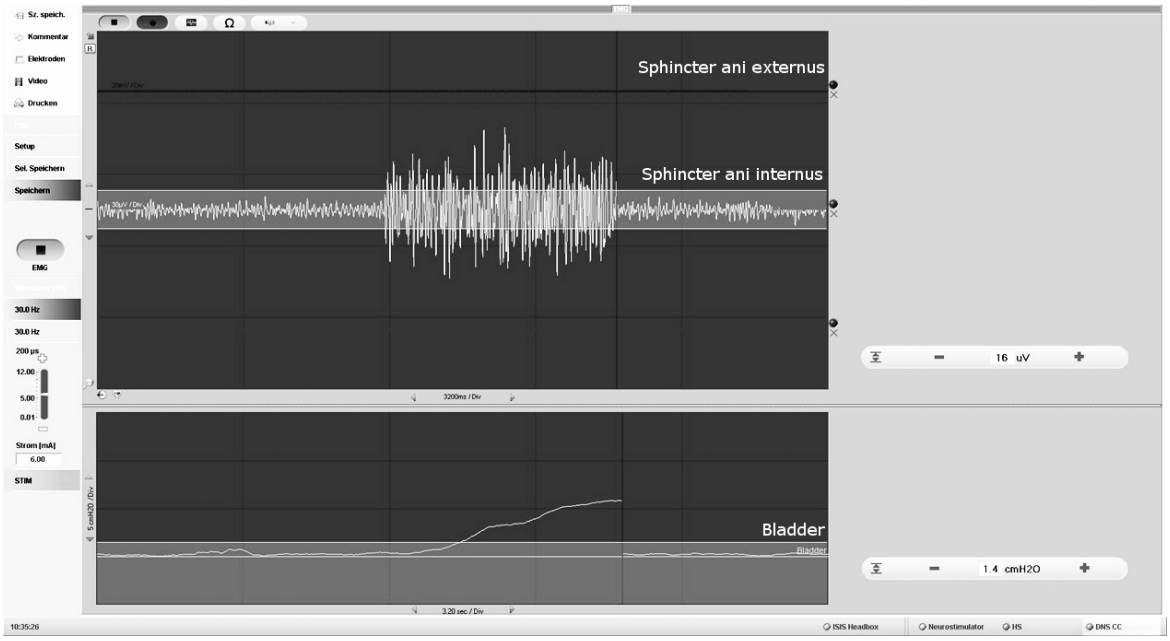

Figure 2.4 A screenshot from NeuroExplorer Software (v. 5.1.2, inomed Medizintechnik GmbH, Emmendingen, Germany) taken during intraoperative stimulation of the inferior hypogastric plexus (IHP) and simultaneous measurement of the electromyographic activity of the internal anal sphincter (IAS) and the urinary bladder pressure. The figure depicts a stimulation-induced amplitude increase within the EMG of the IAS (upper curve) and urinary bladder pressure (lower curve) (source: material obtained from inomed Medizintechnik GmbH, Emmendingen, Germany).

2.3 Practicability of pelvic intraoperative neurophysiological monitoring

The rectal surgeon inserts the stimulation probe into the operative field only upon exposing the autonomic nervous system, when the nerves are exposed to risk of injury. This intermittent electric stimulation necessitates prolonging the surgical procedure and may introduce time intervals during which unobserved nerve damage may occur [35].

Intermittent stimulation faced a similar challenge during monitoring of the recurrent laryngeal nerve in thyroid surgery. To be able to continuously observe the function of the nerves at risk, researchers have proposed several electrode designs to allow continuous stimulation of the vagus nerve [36, 37, 38, 39]. Continuous stimulation helped to identify real-time adverse changes of the evoked potential characteristics [40] and monitor the evolution of the recurrent laryngeal nerve injury [37].

However, the neuroanatomy of the fine nerve fibers and plexi of the pelvic autonomous nervous system required a customized approach. Kauff et al. used a tripolar surface electrode (see Figure 2.5) for direct in-situ placement to continuously stimulate the inferior hypogastric plexus and the pelvic splanchnic nerves during open low anterior rectal resection [41]. Although capable of successful stimulation of the autonomous nervous system, the electrode obstructed the operative field, often dislocated, and its design prohibited direct implementation in laparoscopic surgery. This necessitated developing a method of continuous stimulation outside of the operative field adapted especially for laparoscopic surgery of the rectal cancer. Up to this day, no method proved reliable for continuous stimulation during monitoring of autonomic pelvic nerves.

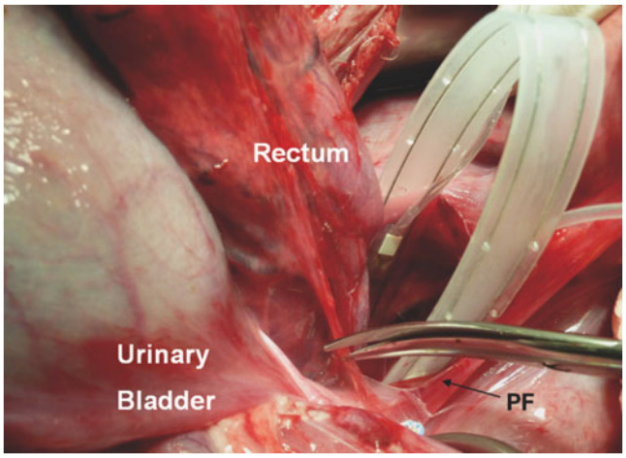

Figure 2.5 Tripolar electrode prototype for continuous *in-situ* stimulation of the inferior hypogastric plexus during pIONM (source: [41])

Chapter 3

Problem analysis

Implementing an alternative method of stimulation using surface electrodes placed on the lower back over the sacral spine could be a tool to cause neuromodulation[1] in the sacral nerve roots and the autonomous nervous system. Preliminary studies suggest that transcutaneous electrical nerve stimulation (TENS) may be effective in treating dysfunctions of the lower urinary tract [42]. Unfortunately, up to this date, its feasibility for neuromonitoring during rectal cancer surgery has not been confirmed.

3.1 Thesis statement

This work aims at exploring the feasibility of transcutaneous electric nerve stimulation (TENS) as a way of stimulation outside of the operative field in pelvic intraoperative neurophysiological monitoring (pIONM). The work will prove the following thesis:

Investigating the electrical and spatial parameters of electrical stimulation of the autonomous nervous system within the pelvic floor by a combination of numerical and in-vivo *modeling is an effective tool to assess the feasibility of transcutaneous electrical nerve stimulation for the purposes of pelvic intraoperative neurophysiological monitoring.*

3.2 Approach

The feasibility of using TENS as a way of stimulation outside of the operative field in pIONM will be assessed by investigating the influence of electrical field on neural excitability using numerical modeling and analysing the electrophysiology of the internal anal sphincter (IAS)

[1] Changing of the physiological pattern of neural control

under TENS of the autonomous nervous system stemming from the sacral nerve roots in an experimental study:

- The electrical field resulting from electrical stimulation will be obtained using finite element modeling (FEM). The reaction of a Hodgkin-Huxley membrane model to the electric field resulting from FEM will provide insight into the excitability of the autonomous nervous system within the pelvic floor.
- The stimulation conditions will be applied to an animal model during an experimental study which will investigate the electrophysiology of the internal anal sphincter in five swine specimens during TENS using a stimulation array.

The feasibility of TENS in pIONM will be assessed in reference to direct nerve stimulation (DNS). The assessment will be performed according to two criteria based on surgeons' expectations:

- The ability to perform **intraoperative nerve mapping**.
- The ability to assess the **nerve function** in different phases of surgery.

3.2.1 Intraoperative nerve mapping

Intraoperative nerve mapping uses electrical stimulation to identify the neuroanatomical landmarks within the pelvic floor. This helps the surgeon to locate the proper plane of dissection during total mesorectal excision and avoid the sheath containing the autonomic nerve fibers responsible for anorectal and urogenital functions.

The numerical modeling will be used to investigate whether TENS can evoke a neural response within the autonomic nervous system. Computed over the same anatomical geometry of the pelvic region, models of DNS and TENS will serve to investigate the the propagation of the electrical field within the modeled tissues. Differences in stimulation selectivity of both of the stimulation methods will be identified and assessed in terms of suitability for intraoperative nerve mapping.

In order to be practicable within the operating room (OR) for intraoperative nerve mapping, neurostimulation should not only produce a response from the autonomic nervous system but also result in an identifiable response within the innervated organs. The experimental study will be divided into two parts: 1) reproducing a stimulation-induced increase in the amplitude of the processed EMG of the IAS due to DNS of the autonomic nervous system and 2) an attempt to achieve comparable results during TENS using different configurations of surface electrodes of a stimulation array placed on the back above the sacral area. This

work will assess whether the standard method of signal processing used for the EMG of the IAS implemented during DNS will also be applicable to TENS. The assessment will help to investigate whether TENS can produce a similar IAS EMG response as the reference DNS method.

Complete immobility of the skeletal-muscle-rich pelvic floor during TME as well as reduction of muscular cross-talk between the internal and external anal sphincters necessitate the intraoperative use of muscular relaxants [43]. Because of the specificity of the smooth muscle tissue, using muscular relaxants does not influence the IAS activity induced by DNS. Lower stimulation selectivity of TENS may involve activating skeletal muscle tissue. The experimental study will validate if the signals evoked by TENS come from the autonomic outflow by exploring the influence of muscular relaxants on the IAS EMG. The numerical study will provide additional insight into the possible involvement of skeletal muscle tissue of the pelvic floor based on differences in current distribution. Because the reliability of the method depends on minimizing the influence of the signals resulting from activating the sacral somatic outflow – a possible source of interference within the recorded signals – the results of numerical modeling will help to assess the influence of TENS and DNS on evoking responses from the pudendal nerve.

3.2.2 Nerve function monitoring

Intraoperative nerve mapping helps the surgeon to create a mental model of the position of the autonomic nerves in the context of the operative field. By repeating the stimulation routine during each critical phase of the surgery, the surgeon can evaluate the autonomic nerve function and identify any changes in the reaction of the monitored smooth muscle tissue during total mesorectal excision.

In order to identify possible iatrogenic nerve damage, it is paramount that TENS be able to perform nerve function monitoring. The numerical study will simulate targeted nerve incision of the autonomic innervation. DNS simulations will help evaluate whether the targeted nerve incision successfully prohibited conducting action potential activity along the simulated autonomic nerve fibers. A comparison between the results before and after targeted nerve incision will help to assess whether the nerve damage can be identified based on the recording of action potentials on distal parts of simulated nerve fibers. Simulations before and after nerve incision using the stimulation array model will help to assess the extent to which nerve damage can be identified using TENS.

Analogously to nerve mapping, any kind of nerve damage needs to be identifiable by recording the stimulation-induced response of the autonomously innervated smooth muscle tissue of the IAS. The experimental study will assess the identifiability of nerve damage by

comparing the signal traits evoked by both the DNS and TENS during different phases of rectal resection, including targeted nerve incision. Differences in methodology between the two approaches will provide insight into the technical aspects of both stimulation modalities in assessing nerve damage.

3.3 Organisation of dissertation

The dissertation is organized as follows. Chapter 4 describes the methodology applied to the numerical and experimental study. Chapter 4.1 setup for investigating the autonomous nerve excitability resulting from simulations of the electric field within the pelvic floor during electric stimulation. Chapter 4.2 presents the technical setup, originally developed software for automated transcutaneous electrical nerve stimuation, preoperative preparation of specimens, and the study procedure for the *in-vivo* testing of the feasibility of TENS as an alternative to DNS. Chapters 5.1 (page 51) and 5.2 (page 68) present the distribution of the electric current resulting from DNS and TENS, stimulation selectivity, and the sensitivity to nerve damage, obtained from the numerical study. Chapter 5.3 (page 85) exposes the differences between the modeled DNS and TENS in terms of stimulation selectivity and sensitivity to nerve damage. Chapter 5.4 (page 95) contains the results from the experimental study focusing on the analysis of the activity of the internal anal sphincter under DNS of the inferior hypogastric plexus and under TENS. A thorough analysis of the processed and raw electromyogram of the IAS is presented. The feasibility of both stimulation methods for identifying targeted damage of the IHP based on experimental data is assessed. The association between the injection of muscle relaxants and EMG activity of the IAS under TENS is presented. Chapter 6.1 and 6.2 (page 112 and 118, respectively) discuss the suitability of TENS for intraoperative mapping and for nerve function monitoring. Limitations of the modeling and experimental studies are discussed in Chapter 6.3 (page 122). A summary of key findings, conclusions, research significance and outlook for future research are discussed in Chapter 7.2 (page 126). Appendices A to D contain supportive material for the chapters regarding the methodology and results.

Chapter 4

Materials and methods

This chapter concerns two major topics. Section 4.1 describes the measures to prepare an environment for the simulation of how the electric field resulting from stimulation influences modeled neuronal activity. Section 4.2 explains the preparation of the animal experiments with a brief description of adaptations made to a CE-marked system for intraoperative neuromonitoring and a description of the development of original software for automated stimulation.

4.1 Numerical model of stimulation-induced neural activity

This section describes the step-by-step approach to preparing the model for investigating the autonomous nerve excitability resulting from the electric field generated by DNS and TENS based on a FEM approach.

4.1.1 Anatomical model of the pelvic floor from segmented data from magnetic resonance imaging

A segmented tissue model database obtained from magnetic resonance imaging (MRI) served as a basis for the geometry of the pelvic floor [44]. For the purposes of this study, I selected the 34-year-old male model (Duke, DOI:10.13099/ViP-Duke-V2.0, see Table 4.1) which consisted of 22 tissue groups (see Table 4.2).

Table 4.1 Morphometric characteristics of the Duke model from the Virtual Population [44].

Property	Value
Model name	Duke
Gender	Male
Age	34 years
Height	1.77 m
Weight	72.4 kg
BMI	23.1 kg/m^2
No. of tissue groups	22

Table 4.2 Organs and tissue groups supplied in STL format files within the Duke model from the Virtual Population database. The asterisk (*) signifies the tissue groups within the pelvis.

Organ/ tissue group	Organ/ tissue group
Urinary bladder*	Liver
Skeletal bone*	Male reproductive system*
Cartilage*	Mandible
Cerebellum	Muscle tissue*
Cerebrospinal fluid*	Subcutaneous and visceral fat*
Grey matter of the cerebrum	Respiratory system
White matter of the cerebrum	Skull
Eyes	Spinal cord
Gastrointestinal tract*	Thalamus
Heart	Tongue
Kidneys	Brainstem

4.1.2 3D volumetric geometry of the pelvic floor with BioMesh3D

This section is an elaboration of my original work published in [45]. Within the supplied Duke model, each tissue group is represented by a triangular surface mesh and delivered in stereolithography (STL) format. The format describes each triangle as a set of three points in the Cartesian coordinate system. In order to analyze the electric field using FEM, the surface meshes representing the surfaces of the tissue groups had to be converted into volumetric models, where a set of tetrahedra represents the volume of each tissue group.

Autonomic nervous system

The original model lacked the autonomic nervous tissue controlling the function of the urinary bladder and the anal sphincter complex and was created separately using Blender™. A literature analysis of the pelvic innervation [46, 47] served as a basis for creating a 3D model of the nerve tissue: the superior hypogastric plexus, hypogastric nerves, inferior hypogastric plexus, pelvic splanchnic nerves (S2, S3, S4), pudendal nerves, as well as the branches innervating the urinary bladder and internal anal sphincter. Each nerve was modeled using a Beziér curve. A 3 mm diameter circle was extruded along each Beziér curve to model the nerve surface (see Figure 4.1). All autonomic nerve surfaces were subsequently exported into STL files as surface models (see Figure 4.2). Figure 4.3 shows the modeled autonomic nervous tissue in the context of the surrounding organs.

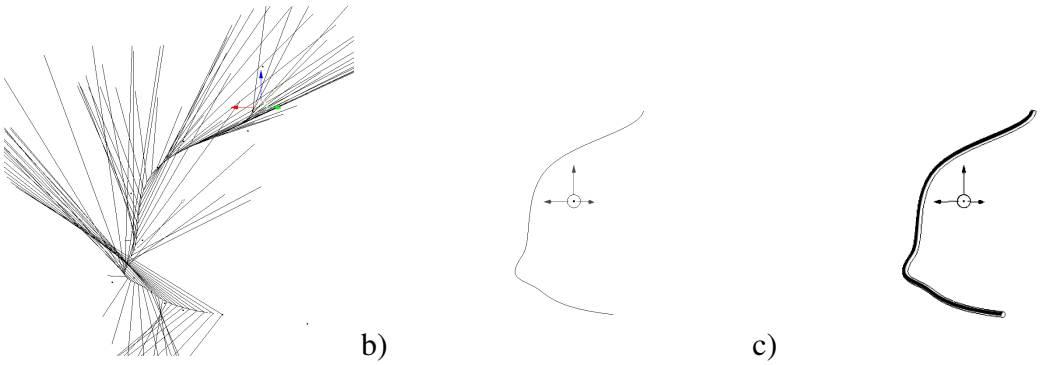

a) b) c)

Figure 4.1 Nerve definition using Beziér curves in Blender software: a) a set of end points defining a curve, b) the resulting Beziér curve, c) the resulting nerve after extruding a 3 mm diameter circle along the curve.

The entire tissue model was adapted to only contain the region relevant during total mesorectal excision: from the sigmoid colon to the height of male reproductive organs.

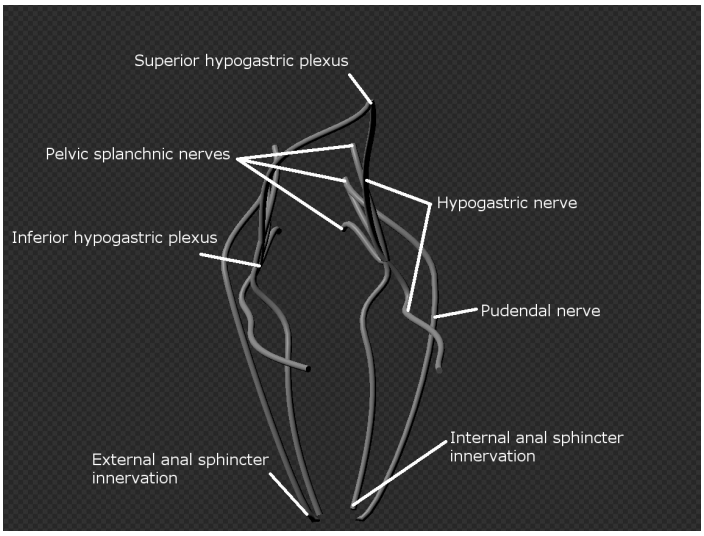

Figure 4.2 The 3D model of the autonomous the internal anal sphincter and the bladder was created using Beziér curves in Blender software. Additionally, the model contained the somatic innervation of the external anal sphincter.

Voxelization of the surface model

Because the finite element method can only be applied to a volumetric domain, the model containing only the surface information of each tissue group needed to be augmented with volumetric information. The BioMesh3D software (Center for Integrative Biomedical Computing, University of Utah, USA, version 1.0) allowed to generate the volumetric mesh.

The three-dimensional surface meshes were transformed into voxels (volumetric pixel). This enabled to represent the data in the form of three-dimensional matrices which were required as the input by the BioMesh3D software. The process of voxelization analyzed the input surface mesh using a ray-tracing algorithm and subdivided the entire volume into voxels, where each set of voxels belonged to a different tissue group. The ray-tracing was performed along the X, Y and Z axis using a Matlab® (Mathworks, Natick, MA, USA) algorithm by Adam H. Aitkenhead (The Christie NHS Foundation Trust). The resulting voxels had a cubic shape with a 1 mm edge.

The lacking skin layer was obtained using boundary dilation (with a diameter of 3 mm) of the outer boundary surface of the voxelized model. The result was saved in nearly raw raster data format (NRRD) containing matrices were each element represented a voxel assigned to a corresponding tissue group. Projections of the obtained matrices are summarized in Tables 4.3 and 4.4.

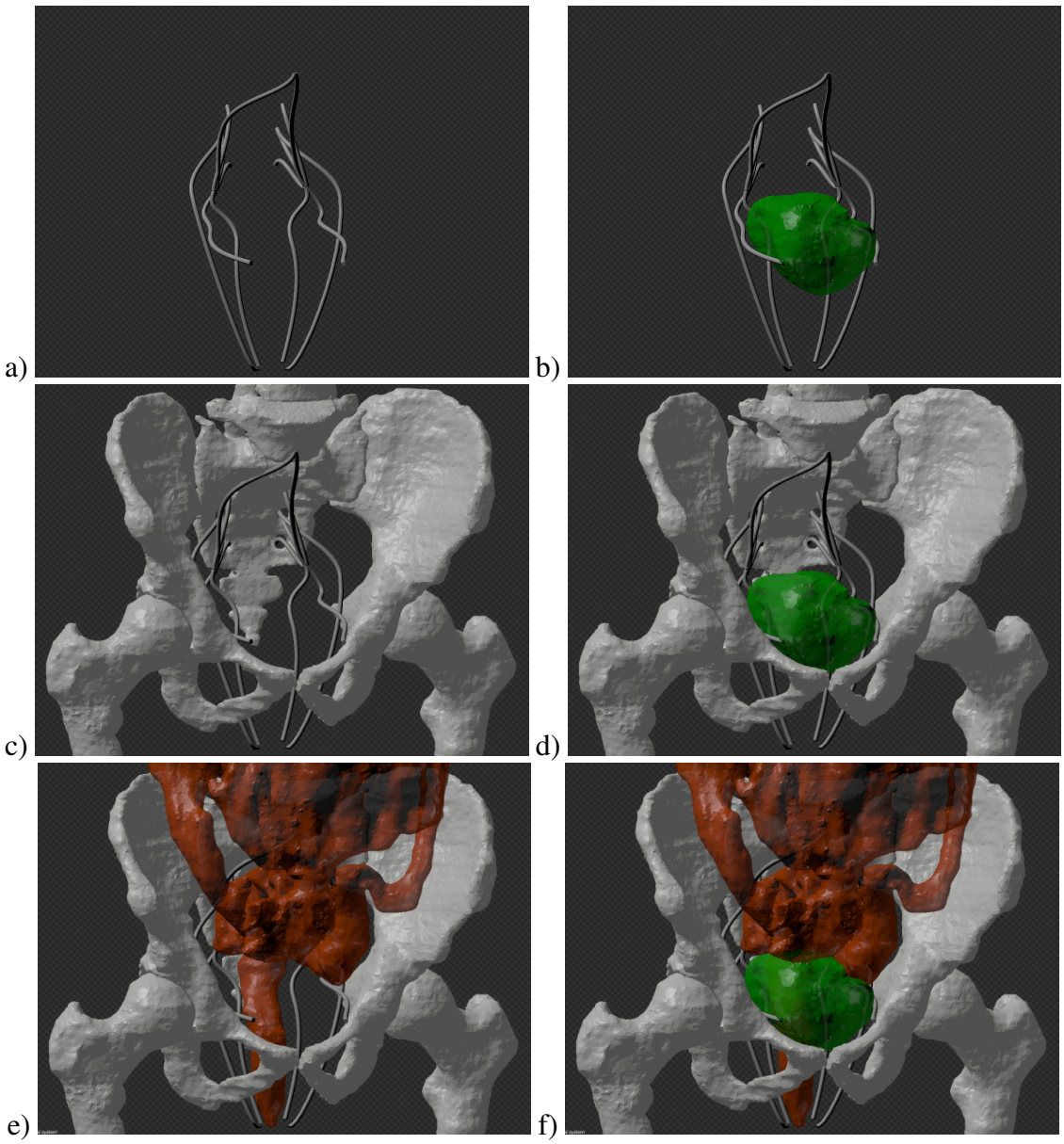

Figure 4.3 The nerve tissue in relation to other tissue structures: a) sole nerve tissue, b) with the bladder, c) with bone tissue, d) with bone tissue and the bladder, e) with the bone tissue, the small, and the large intestine, f) with the bone tissue, the bladder, the small, and the large intestine.

Table 4.3 Representation of the voxelized models of the bladder, bone tissue, cartilage, cerebro-spinal fluid, and fatty tissue in three orthogonal projections: axial, frontal, and sagittal. The pixel density represents the number of voxels: the darker the shade, the more voxels there are along the axis orthogonal to the given view.

	Axial view	Frontal view	Sagittal view
Bladder	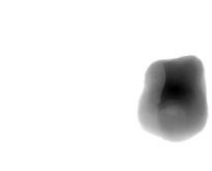		
Bone		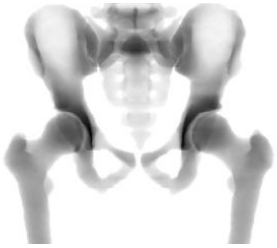	
Cartilage			
Cerebro-spinal fluid			
Fat	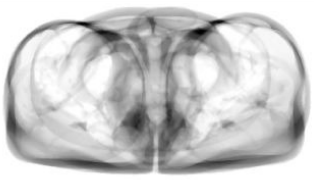	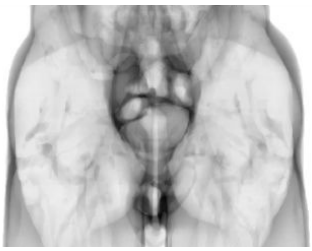	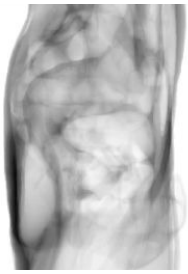

Table 4.4 Representation of the voxelized models of the gastro-intestinal tract, muscle and neural tissue, reproductive system, and skin in three orthogonal projections: axial, frontal, and sagittal. The pixel density represents the number of voxels: the darker the shade, the more voxels there are along the axis orthogonal to the given view.

	Axial view	Frontal view	Sagittal view
Gastro-intestinal			
Muscle	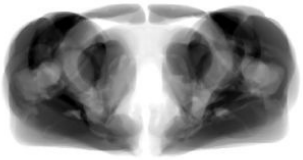	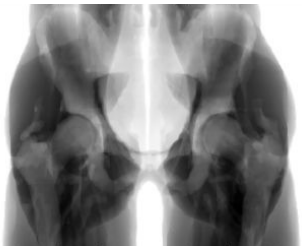	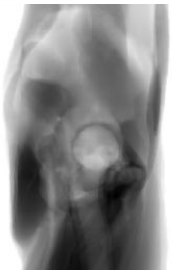
Neural			
Reproductive			
Skin	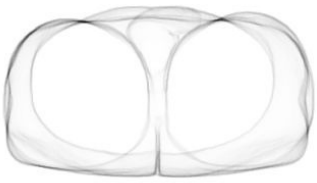		

Volumetric mesh

The NRRD data served as input for the BioMesh3D – an algorithm that creates volumetric meshes based on voxelized segmented data. The BioMesh3D algorithm isolated each tissue within the segmented data, extracted the tissue boundaries, calculated the medial axes of each tissue group, determined its sizing field, and generated seed points on junctions where the tissues met. In the first stage, the algorithm positioned the seed points at random. Relative distances between the seed points were derived from the sizing field. Using these distances, an energy metric was calculated and the seed points were iteratively repositioned in such a way as to minimize the energy between each point. This assured a high accuracy of a distribution of seed points to represent complex parts of the anatomical geometry. Based on these optimized seed points, a volumetric mesh was generated using the Delanauy algorithm implemented in TetGen software (Numerical Mathematics and Scientific Computing, Weierstrass Institute for Applied Analysis and Stochastics, Berlin, Germany, version 1.5.0). The complete documentation to BioMesh3D can be found in [48]. Also, please, refer to Figure 4.4 for a graphical explanation of the algorithm.

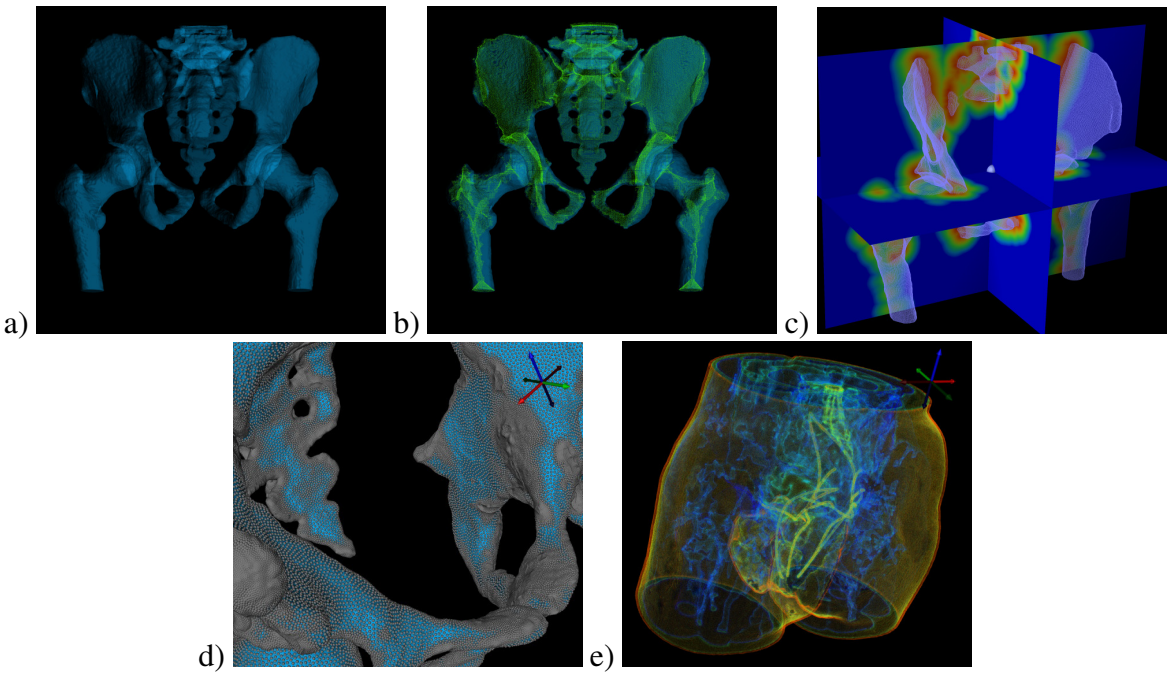

Figure 4.4 In order to generate a high-quality volumetric mesh, a) the BioMesh3D pipeline extracted the boundary of each tissue group, b) calculated medial axes of the boundaries, c) calculated the sizing field to each iso-surface of the material, and d) generated seed points along the surface to generate a volumetric mesh. The volumetric mesh was represented as a point cloud in (e), each color representing a different tissue group.

The resulting model is a volumetric mesh containing the following tissue groups and organs: nerve, subcutaneous and visceral fat, skin, bone, cartilage, gastro-intestinal, muscle, bladder, cerebrospinal fluid.

Two sets of stimulation electrodes for DNS and TENS, modeled using Blender (Blender Foundation, the Netherlands, version 2.77a), supplemented the resulting volumetric mesh. The electrodes set for TENS was comprised of three rectangular pads (6 cm×4 cm) with rounded corners and ten circular electrodes (⌀1 cm) forming a stimulation array (see Figure 4.5). In terms of geometry, the modeled electrodes corresponded to the electrodes used during animal experiments as described in Section 4.2. The electrode set for DNS consisted of ten bipolar electrodes as pairs of stainless steel balls (each ⌀2 mm and 3 mm inter-electrode distance). The geometry of the bipolar electrodes corresponded to the dimensions of the contacts of a laparoscopic hand probe used during pIONM (see Figure 4.6).

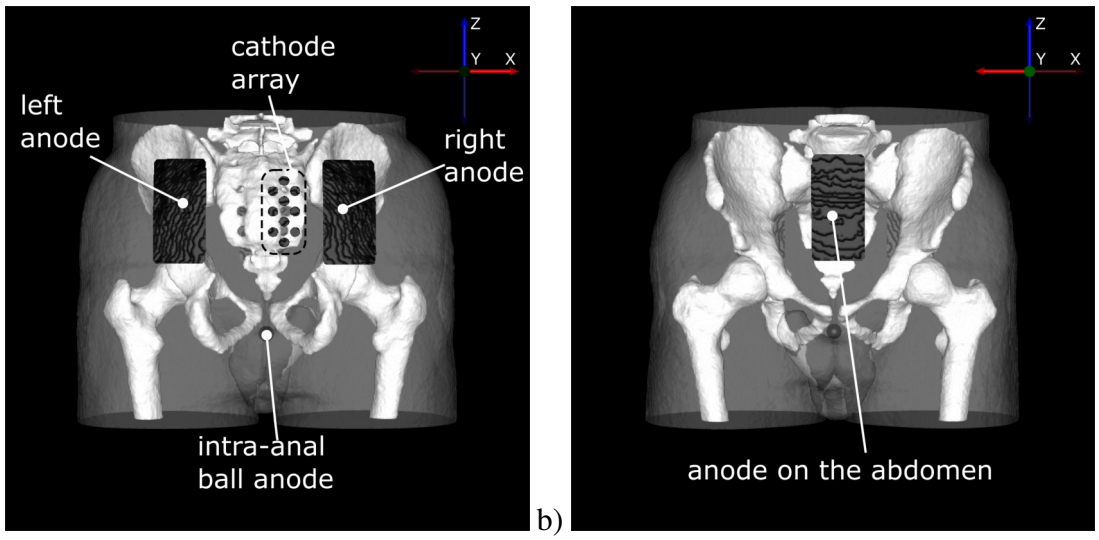

Figure 4.5 Views of the anatomical model and the modeled surface electrodes: a) posterior view, b) anterior view.

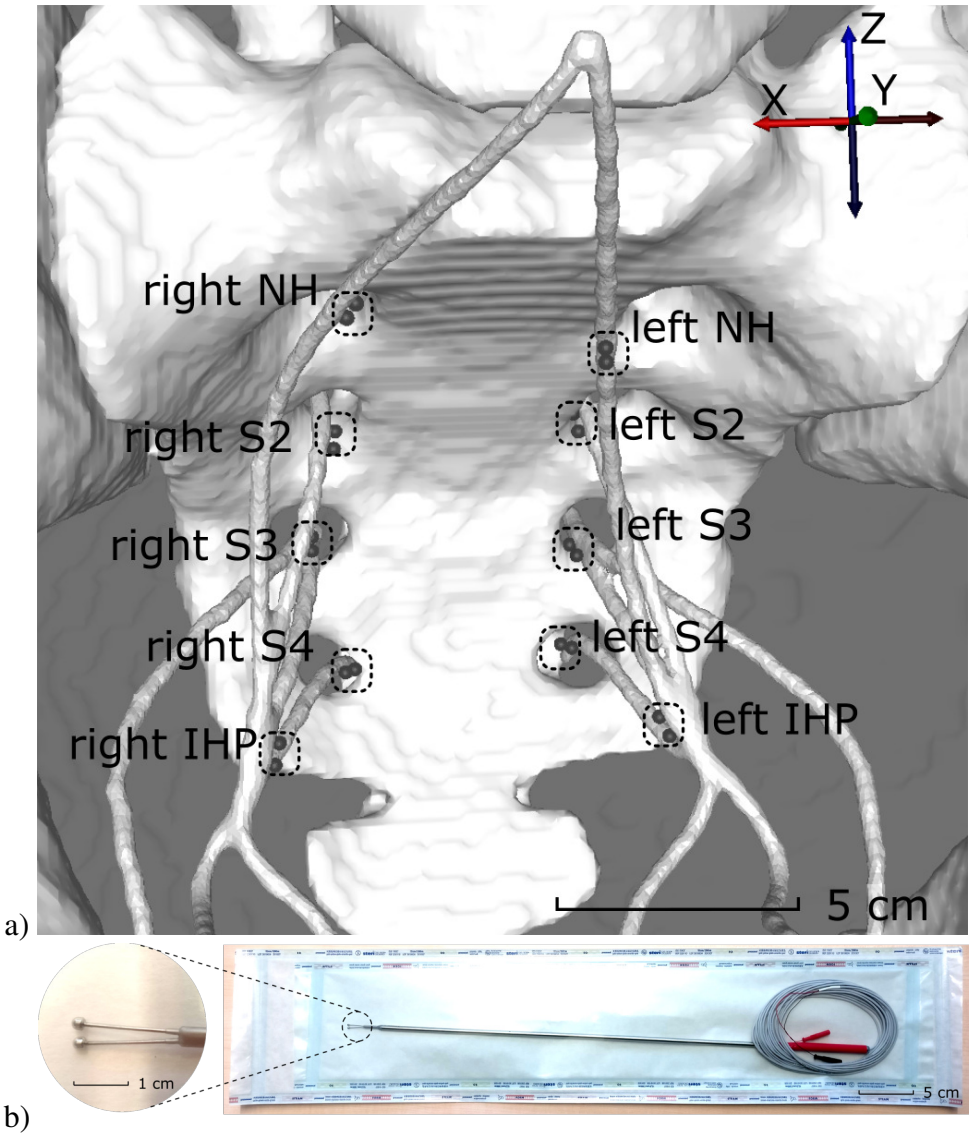

Figure 4.6 Ten stimulation sites with corresponding simulated electrode pairs (a). Each bipolar electrode consists of two stainless steel balls (⌀2 mm). Laparoscopic hand probe for *in-situ* stimulation (Art. no. 520336, inomed Medizintechnik GmbH, Germany) served as a reference in designing the model (b). Legend: NH - hypogastric nerve, S2-S4 - sacral roots, IHP - inferior hypogastric plexus.

4.1.3 Finite element modeling in SCIRun

The volumetric geometry described in section 4.1.2 served as input for the SCIRun Problem Solving Environment (Center for Integrative Biomedical Computing, University of Utah, USA, version 4.7) for modeling the electric field within the tissues. The software uses a pipeline described by Dannhauer et al. (refer to [48]) which solves the quasi-static approximation of the Maxwell's equation according to the model suggested in [49].

The model served to solve a forward problem in which the known conductivity of the volume conductor, boundary current and potential distributions served to find the internal electric current and potential distributions. The forward problem is defined by

$$\nabla \cdot (\sigma \nabla u) = 0, \quad (x \in \Omega), \tag{4.1}$$

where σ is a conductivity tensor field and u is the electric potential field defined on domain Ω describing the entire volume conductor. The conductivity tensor field is assumed to be homogenous and isotropic within a given tissue group. However, inhomogeneity is achieved through the use of different tissue conductivities (see Table 4.5).

Table 4.5 Conductivities assigned to the model tissue groups based on [50].

Tissue group	Conductivity (S/m)
Muscle	8.00×10^{-2}
Bone	2.51×10^{-1}
Gastrointestinal tract	5.11×10^{-1}
Subcutaneous and visceral fat	3.77×10^{-2}
Urinary bladder	1.75
Cartilage	1.61×10^{-1}
Cerebrospinal fluid	2.00
Male reproductive organs	2.51×10^{-1}
Skin	2.00×10^{-4}
Autonomic nervous tissue	1.71×10^{-2}

A Neumann boundary condition imparted to the model allowed no current flux through the outermost boundary of the model geometry excluding the boundaries belonging to stimulation electrodes. This is described by equation (4.2)

$$\sigma \frac{\partial u}{\partial n} = 0, \quad (x \in \partial\Omega \setminus \cup_{l=1}^{L} e_l) \tag{4.2}$$

where $\frac{\partial u}{\partial n}$ is the electric flux normal to the outermost boundary of the model geometry ($\partial\Omega$)

and e_l are parts of the domain that are coincident with the electrodes $1,2,...,L$.

Equation (4.3) describes a Dirichlet boundary condition which grounded the model at a desired node of the geometry

$$u(x,y,z)|_{\overline{\Omega_k}} = 0 \tag{4.3}$$

where $\overline{\Omega_k}$ is a part of the domain coincident to the node k.

Equations (4.4) and (4.5) define the boundary conditions governing the behavior of the stimulation electrodes

$$u + z_l \sigma \frac{\partial u}{\partial n} = U_l, \quad (on\ \partial\Omega_{e_l},\ l = 1,2,\ldots,L), \tag{4.4}$$

$$\int_{\partial\Omega_{e_l}} \sigma \frac{\partial u}{\partial n} dS = I_l, \quad (on\ \partial\Omega_{e_l},\ l = 1,2,\ldots,L), \tag{4.5}$$

where $\sigma\frac{\partial u}{\partial n}$ is the current density flux, U_l is the electric potential, and I_l is the total current flowing in or out of the electrode l. $\partial\Omega_l$ refers to the domain of the l^{th} electrode.

The SCIRun software used the Galerkin method to compute an approximate solution to the forward problem by assuming the form

$$\overline{u}(x,y,z) = \sum_{i=1}^{N} u_i \phi_i(x,y,z), \tag{4.6}$$

where $\overline{u}$ is the approximate electric potential field, ϕ_i is a set of basis functions, u_i is a set of unknown coefficients, i is a node index, N is the total number of nodes in the model. The method represents the forward problem described by equations (4.1) through (4.5) in matrix form

$$MU = I \longrightarrow U = M^{-1}I, \tag{4.7}$$

where M represents the boundary conditions and the model conductive properties, U is a set of unknown electric potentials, and I is the electric current. Matrices M, I and U are sorted

to describe the volume conductor and the electrode domain (indices n and e respectively)

$$M = \begin{pmatrix} A & -B \\ -B^T & C \end{pmatrix}, \tag{4.8}$$

$$I = \begin{pmatrix} i_n \\ i_e \end{pmatrix}, \tag{4.9}$$

$$U = \begin{pmatrix} u_n \\ u_e \end{pmatrix}. \tag{4.10}$$

Assuming (4.8), (4.9) and (4.10), the forward problem in (4.7) takes the form

$$\begin{pmatrix} A & -B \\ -B^T & C \end{pmatrix} \begin{pmatrix} u_n \\ u_e \end{pmatrix} = \begin{pmatrix} i_n \\ i_e \end{pmatrix} \tag{4.11}$$

with

$$A(i,j) = \int_D \sigma \nabla \phi_i \cdot \nabla \phi_j dD + \sum_{l=1}^{L} \frac{1}{z_l} \int_{e_l} \phi_i \phi_j dD_{e_l}, \tag{4.12}$$

$$B(i,j) = \frac{1}{z_l} \int_{D_{e_l}} \phi_i dD_{e_l}, \tag{4.13}$$

$$C(l,l) = \frac{1}{z_l} \int_{D_{e_l}} dD_{e_l}, \tag{4.14}$$

where D is the model domain, D_{e_l} is the domain of the l^{th} electrode, and z_l is the contact impedance of the l^{th} electrode. SCIRun uses minimal residual iteration process in computing approximate solution (4.6) as described in [51].

4.1.4 Simulation protocols in SCIRun

A programmed set of stimulation procedures helped to calculate the electric field within the model resulting from DNS and TENS. Table 4.6 describes the procedures and their corresponding stimulation sites. Each stimulation protocol – both during DNS and TENS – assumed that 1 mA cathodic current flew between the cathode and anode. Figure 4.7 summarizes the convergence criteria for each simulation.

Each simulation resulted in an approximation of electric potential field. Each electrical

Table 4.6 Protocols for the simulation of the electric field during direct and transcutaneous electric nerve stimulation. Legend: DNS – direct nerve stimulation, IHP – inferior hypogastric plexus, NH – hypogastric nerve, PSN – pelvic splanchnic nerve, TENS – transcutaneous electrical nerve stimulation.

Stimulation type	Scenario no.	Stimulation site
DNS	0	left S2 PSN
	1	right S2 PSN
	2	left S3 PSN
	3	right S3 PSN
	4	left S4 PSN
	5	right S4 PSN
	6	left NH (S2 level)
	7	right NH (S2 level)
	8	right IHP
	9	left IHP
TENS	0-9	Cathodes 1-10 vs. intra-anal anode
	10-19	Cathodes 1-10 vs. anode on the abdomen
	20-29	Cathodes 1-10 vs. anode left
	30-39	Cathodes 1-10 vs. anode right

Table 4.7 A summary of the convergence criteria for the minimal residual iterative method used in SCIRun (Center for Integrative Biomedical Computing, University of Utah, USA)

Criterium	Value
Iteration process	Minimal residual
Target error	1×10^{-7}
Maximum no. of iterations	3500
Preconditioning method	Jacobian

field yielded a current density field according to

$$\mathbf{J} = -\sigma \nabla \overline{u}, \tag{4.15}$$

where $\mathbf{J}$ is the current density vector field, σ is the conductivity field within the model, and $\overline{u}$ is the approximated solution of the electric potential field. Additionally, calculating streamlines served to visualize the current flow.

4.1.5 Myelinated fiber model with extracellular stimulus

The electric field resulting from the TENS and DNS simulation procedures acted as input for the neural fiber model. NEURON modeling software (Yale University, USA, [52], version 7.4) was used to simulate the propagation of action potentials along nerve fibers. The following steps constituted the schema to create a model of each nerve fiber:

1. Create one fiber to represent each modeled nerve.
2. Subdivide each fiber into myelinated segments and nodes of Ranvier.
3. Model each node of Ranvier using the Hodgkin-Huxley membrane model.
4. Model each myelin sheath as a passive membrane channel represented as a simple conductor.
5. Assign an extracellular mechanism to every segment.

The geometry of the Beziér curves from the 3D model described in section 4.1.2 was imported into the NEURON software. Each nerve fiber was represented by one neural axon subdivided into alternating myelin sheath segments and nodes of Ranvier. Table 4.8 summarizes the geometrical dimensions of the nerve fibers and Figure 4.9 is a graphical representation of the modeled autonomic nervous system. The electrical and spatial properties, including the number of compartments in the nodes of Ranvier and the myelinated parts of the axon, were selected according to [53]. Each node of Ranvier contained a single Hodgkin-Huxley model compartment (see Figure 4.7). The total current flowing from the extracellular space into the intracellular space is given by:

$$I = C_m \frac{dV_m}{dt} + g_K(V_m - V_K) + g_{Na}(V_m - V_{Na}) + g_l(V_m - V_l) \tag{4.16}$$

where $\frac{dV_m}{dt}$ is the time-dependent electrochemical gradient spanning across the lipid bilayer, g_K, g_{Na}, and g_l are the potassium channel, sodium channel, and leakage conductances, V_m is the membrane potential, V_K, V_{Na}, and V_l are the potassium, sodium, and leakage equilibrium potentials.

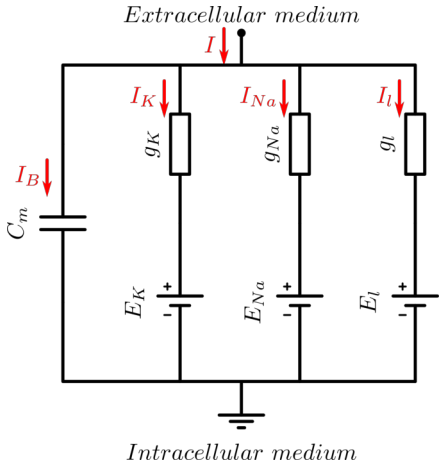

Figure 4.7 A single compartment of Hodgkin-Huxley model of action potential generation. Each compartment of the model represents electrophysiological behavior of neural cell membranes, where C_m is the capacitance of the lipid bilayer, g_K and g_{Na} are conductances representing voltage-gated potassium and sodium channels, respectively. The leakage conductance is represented by g_l. The voltage sources E_K, E_{Na}, and E_l represent the electrochemical gradients driving the flow of ions through the channels.

Each myelin sheath contained ten compartments consisting of resistive and capacitive elements (see Figure 4.8). Table 4.9 summarizes the electrical properties of the nodes of Ranvier and the myelin sheaths as presented in [53]. In order to allow using extracellular potential to stimulate the modeled nerve fibers, each compartment was augmented with an extracellular mechanism as described in [54].

Table 4.8 Geometrical characteristics of nerve fibers modeled in NEURON software (Yale University, USA) as described in [53].

Property	Value
Fiber diameter	10 µm
Ranvier node length	3.183 µm
No. of compartments in a single Ranvier node	1
Myelin sheath length	1 mm
No. of compartments in a single myelin sheat	10

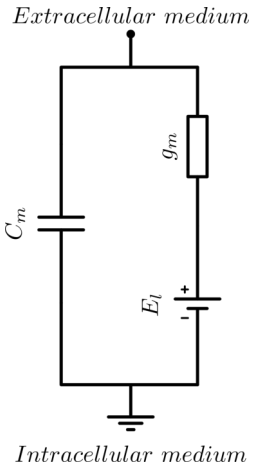

Figure 4.8 A single compartment of the modeled myelin sheath. Each compartment consists of a lipid bilayer capacitance C_m, a membrane conductance g_m, and a leakage reversal potential E_l.

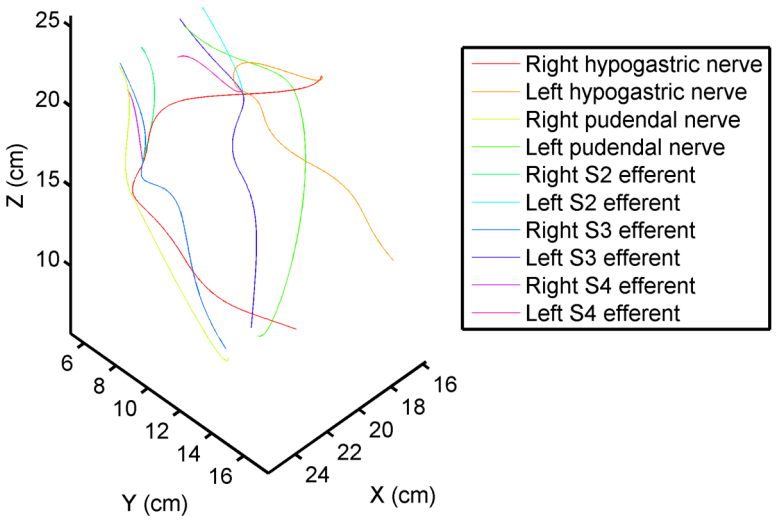

Figure 4.9 Three-dimensional depiction of the nerve fibers. Each nerve was modeled as a single axon.

Table 4.9 Electrical characteristics of the nerve fibers modeled in NEURON software (Yale University, USA) according to [53].

Property	Value
Sodium conductance	$1.2\,\mathrm{S/cm^2}$
Potassium conductance	$9 \times 10^{-2}\,\mathrm{S/cm^2}$
Leakage conductance	$2 \times 10^{-2}\,\mathrm{S/cm^2}$
Resting potential	$0\,\mathrm{V}$
Sodium equilibrium potential	$115\,\mathrm{mV}$
Potassium equilibrium potential	$-12\,\mathrm{mV}$
Leakage equilibrium potential	$-5 \times 10^{-2}\,\mathrm{mV}$
Axoplasmic resistance per unit axon length	$1.26 \times 10^{8}\,\Omega/\mathrm{cm}$
Myelin conductance per unit length	$5.6 \times 10^{-9}\,\mathrm{S/cm}$
Myelin capacitance per unit length	$1.87 \times 10^{-11}\,\mathrm{F/cm}$
Nodal capacitance per unit axon length	$3.14 \times 10^{-9}\,\mathrm{F/cm}$

4.1.6 Interface between the electric field model and the neural model

The extracellular mechanism assumes that the electric stimulus is distributed along the nerve fiber and takes the form of a potential distribution. The distribution takes a discrete form, where each sample of the external electric field serves as input for one compartment of the extracellular mechanism. In order to extract samples of the electric field from the finite element model (Section 4.1.3), the electric potential field was projected using linear interpolation onto each compartment of a given nerve fiber (as described in Section 4.1.5). Field projections were obtained for stimulation amplitude between 1 and 25 mA with 1 mA steps.

4.1.7 Simulation protocols in NEURON

The simulation of the evolution of the action potential was performed for electric fields resulting from FEM simulations of all stimulation scenarios: DNS and TENS. Two situations were simulated: 1) influence of the electric field on an intact nerve and 2) influence of the electric field on a damaged nerve. A 5 mm long nerve incision was inflicted onto the S3 efferent nerve fibers and the hypogastric nerves at the level of the inferior hypogastric plexus (see Figure 4.11a). The nerve damage was simulated through disconnecting the equivalent circuit model of the nerve fibers at the given sites. The resulting discretized electric field served as a basis for creating a time-dependent distribution of the electric field along each nerve fiber in the form of rectangular pulses.

The stimulation amplitude corresponded to the magnitude of the electric field at a given

location along each nerve fiber. Electric fields for stimulation amplitudes in the range between 1 mA and 25 mA and a constant pulse width of 200 µs served as model inputs. Each pulse was generated 1 ms after starting the simulation (see Figure 4.10). The time-dependent changes of the transmembrane potential were recorded during the entire simulation from the distal ends of each nerve fiber relative to the sacral region (see Figure 4.11b). Placing the virtual recording electrodes at the distal ends of the S3 pelvic splanchnic nerves and the pudendal nerves emulated the recording of the myoelectric activity of the internal and external anal sphincters.

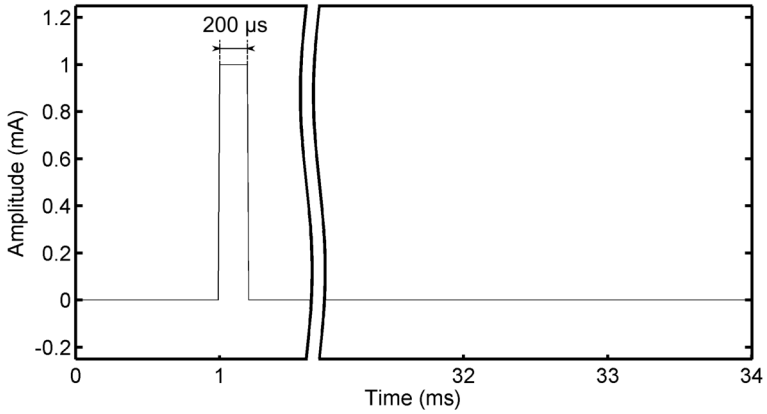

Figure 4.10 Simulated pulse stimulus at 1 mA amplitude and a pulse width of 200 µs. Each pulse was generated 1 ms after starting the simulation.

The solver properties summarized in Table 4.10 served for the simulation of the transmembrane potential along each nerve fiber. The stop time (33 ms) was chosen to simulate what happens within one stimulation period at 30 Hz pulse frequency taking into account the fact that each pulse occurs 1 ms after the starting time. This was done in order to illustrate the propagation of the electric field along the nerve fibers in the form of stimulation artifacts. The (33 ms) correspond to the standard stimulation frequency used during pelvic intraoperative neurophysiological monitoring [55].

Table 4.10 Properties of the solver used during simulation of the action potential [56].

Property	Value
Type	Backward Euler
Starting time	0 ms
Stop time	34 ms
Time step	25 µs

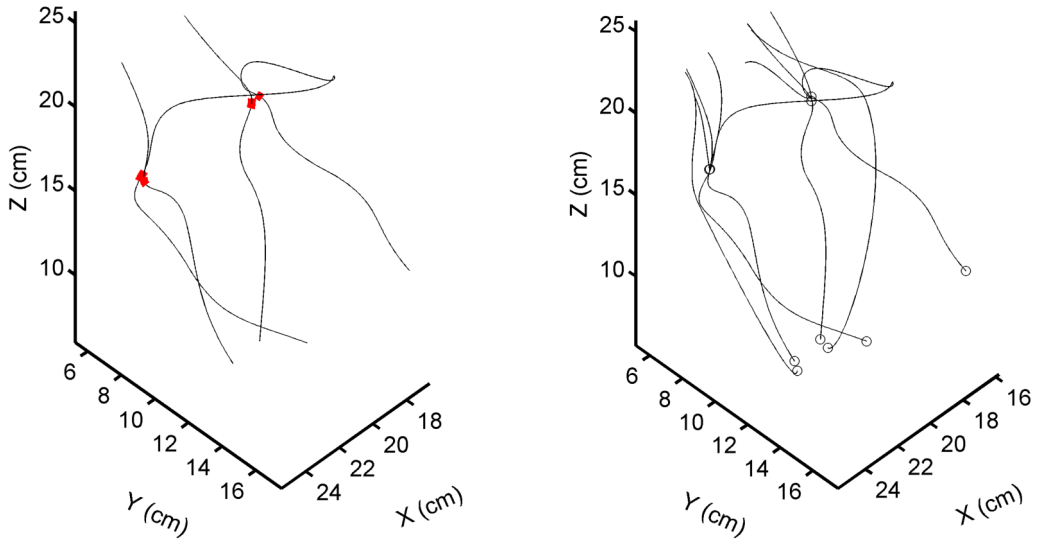

a) b)

Figure 4.11 Sites at which the nerve model was disconnected in order to simulate targeted nerve damage (a). The red part of the lines depicting the nerves symbolizes the disconnected part of the model. Sites used to record the trans-membrane potential from the distal ends of the simulated nerve fibers (depicted with a circle) (b).

4.2 Animal experiments

4.2.1 Setup for pelvic intraoperative neuromonitoring

For the purposes of this study, inomed Medizintechnik GmbH provided a portable system for IONM (ISIS Xpress). The system is a medical product allowing to perform IONM using various monitoring modalities (e.g. MEP, SSEP, triggered EMG, free-running EMG, AEP, VEP, and pIONM). The system is comprised of a central PC unit, a neurostimulator, and a signal amplifier (see Figure 4.12). The signal amplifier and the neurostimulator allow recording of physiological signals and stimulation of the neural tissue, respectively. Table 4.11 summarizes the main technical parameters of the system regarding signal acquisition and electrical stimulation.

4.2.2 Electric stimulation

Fraunhofer Institute for Biomedical Engineering (IBMT) manufactured an electrode array for transcutaneous stimulation of the sacral nerve roots. The array consisted of ten 1 cm stainless steel contacts. A 1.5 m-long color-coded cable was soldered onto each contact. Each cable end was supplied with a DIN 42 802 connector to ensure compatibility with the

Table 4.11 Specification of the modules comprising the ISIS Xpress system for intraoperative neuromonitoring.

Module	Specifications	
ISIS Amplifier	Sampling frequency:	20 kHz
	No. channels:	8 per module
	Resolution:	16 bit
	Range:	10 mV_{p-p}
	Pass band:	50 mHz to 3 kHz
ISIS Neurostimulator	No. stimulation channels:	up to 12
	Stimulation current:	up to 250 mA
	Voltage limitation:	410 V

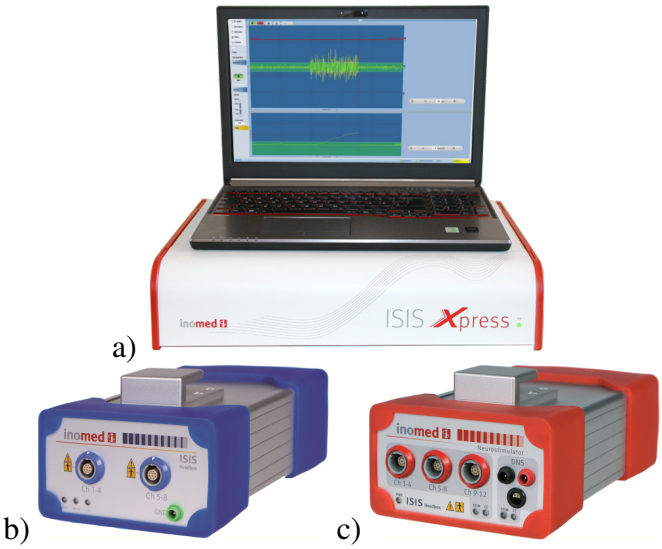

Figure 4.12 The portable ISIS Xpress system for pelvic intraoperative neurophysiological monitoring consists of a) a PC workstation, b) a biosignal amplifier, c) and a neurostimulator (Materials supplied by inomed Medizintechnik GmbH, Emmendingen).

medical-grade ISIS Xpress system. Additionally, each contact was covered with neoprene padding for easier electrode fixation and handling. Throughout the entire study, the electrode array was connected to cathodic inputs of two electrode adapter boxes (see Figure , Art. no. 540511, inomed Medizintechnik GmbH, Emmendingen, Germany) for channel inputs one to ten. The anodic input alternately connected to one of four anodes, three of which were made of 9 cm $\times$ 5 cm carbon electrode pads (Art. no. Z 0072, AAM GmbH, Triberg, Germany) and one $\oslash$2.5 cm stainless steel electrode for intra-anal application manufactured at Fraunhofer IBMT. For the purposes of this study, only the distal contact was used as an anode for electric stimulation. Additionally, the electrode was comprised of a set of contact pads for intra-anal signal acquisition. However, intra-anal signal acquisition is out of scope of this dissertation and the results showing the feasibility of intra-anal recording of the internal anal sphincter EMG have been published elsewhere [57]. The electrode adapter boxes were connected to inputs one to ten of the neurostimulator. Figure 4.13 shows the setup for electric stimulation.

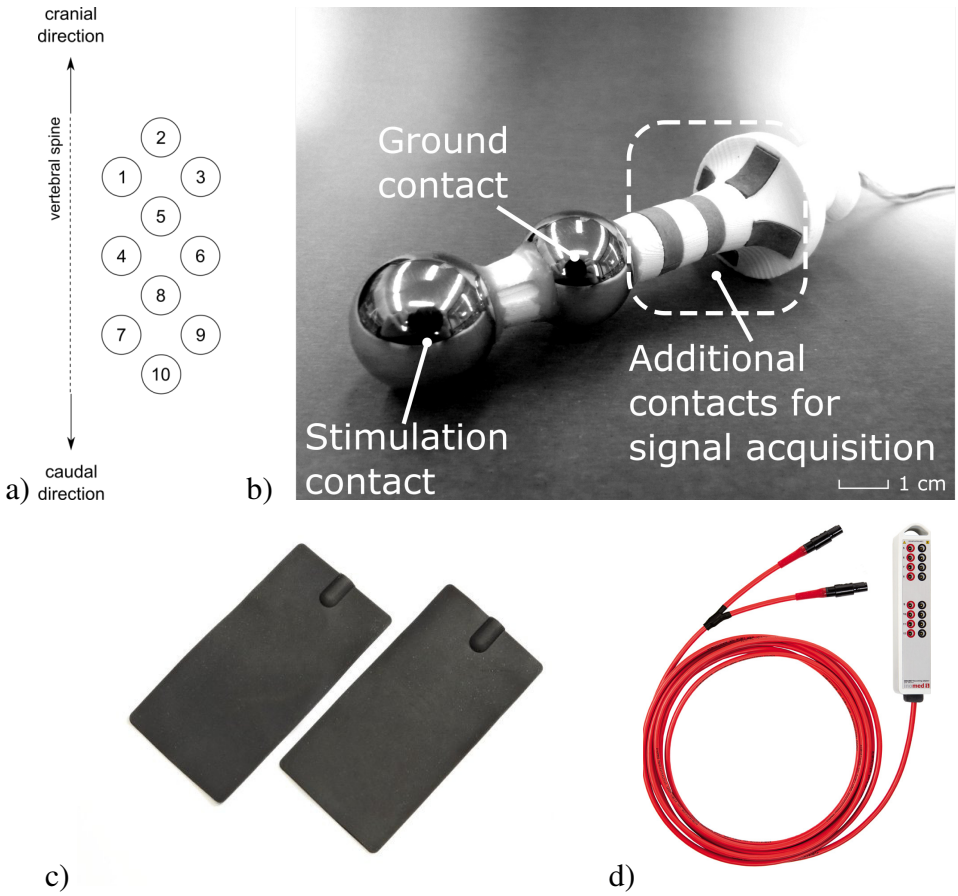

Figure 4.13 Setup for transcutaneous electrical nerve stimulation: a) a diagram of a ten-electrode stimulation array made of ⌀1 cm cathodic copper contacts, b) an intra-anal electrode (manufactured at Fraunhofer Institute for Biomedical Engineering, St. Ingbert, Germany), c) remaining three anodes were made of 9 cm × 5 cm carbon electrode pads (Art. no. Z 0072, AAM GmbH, Triberg, Germany), and d) a stimulation electrode adapter box (Art. no. 540511, inomed Medizintechnik GmbH, Emmendingen, Germany) . For the purposes of this study, only the distal contact of the intra-anal electrode was used as an anode for electric stimulation. Additionally, the electrode was comprised of a set of contact pads for intra-anal signal acquisition. However, intra-anal signal acquisition is out of scope of this dissertation and the results showing the feasibility of intra-anal recording of the internal anal sphincter EMG have been published elsewhere [57].

4.2.3 Signal acquisition

The EMG activity of the IAS and EAS was acquired using concentric bipolar needle electrodes (Art. no. 530666, inomed Medizintechnik GmbH, Emmendingen, Germany) placed inside surgically exposed IAS and EAS. Both needles used a common ground electrode inserted into the fatty tissue in the swine buttock. The contacts were connected into an electrode adapter box (Art. no. 520300, inomed Medizintechnik GmbH, Emmendingen, Germany), the box was connected into the channel inputs of the ISIS signal amplifier. Figure 4.14 depicts the setup for signal recording.

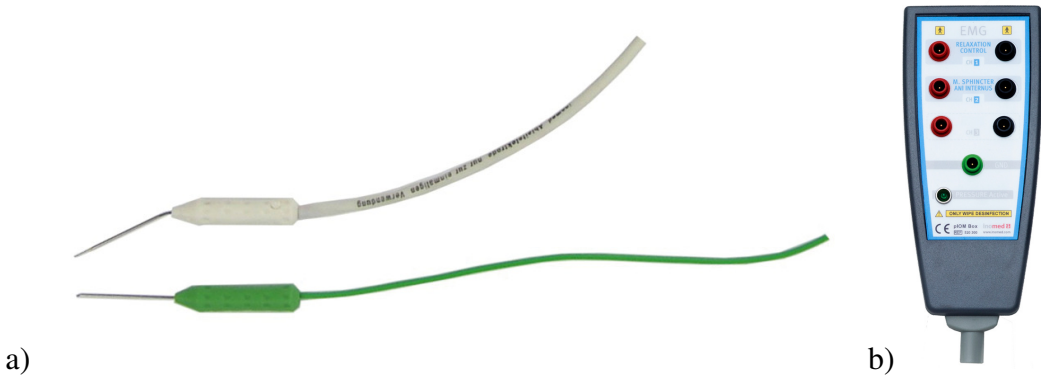

a) b)

Figure 4.14 Setup for recording of sphincter electromyographic activity. Two concentric bipolar needle electrodes (Art. no. 530666, inomed Medizintechnik GmbH, Emmendingen, Germany) were used for recording of the internal (IAS) and external anal sphincter (EAS) electromyography (a). One concentric needle was placed inside the surgically exposed IAS and one in the EAS. Common ground electrode (green) was used for both channels (Materials supplied by inomed Medizintechnik GmbH, Emmendingen, Germany). The electrodes were connected into the corresponding channels within an electrode adapter box (Art. no. 520300, inomed Medizintechnik GmbH, Emmendingen, Germany) (b). The box was connected into channel inputs of the signal amplifier.

4.2.4 Specimen preparation and study procedure

The animal study was performed on five male pig specimens, with a median weight of 29 kg (range 27-32), with the approval of a local ethics committee (approval code G 14-1-061). The preparation of the specimens was undertaken by highly qualified medical personnel as described in [58, 57, 59]. The pigs were anesthetized, intubated and placed in supine position. The skin on the lower back above the sacral area of each pig was shaved, abraded and massaged using Spectra 360 electrode gel (Parker, Fairfield, USA). Anatomical landmarks were used to place the stainless steel electrode array on the right side of the back directly

over the S2-S4 sacral region. The carbon electrodes were placed lateral left and right to the electrode array on the back as well as on the abdomen directly above the pubic area in each specimen. Additionally, the ball electrode was situated inside the anal canal. For an overview of the stimulation setup, refer to Section 4.2.2 on page 38.

The ground needle electrode was placed lateral right to the anal canal within the right buttock. Two bipolar needle electrodes were placed inside the surgically exposed IAS and EAS. The signals were acquired using the ISIS Amplifier and the setup described in Section 4.2.3 on page 42. Trigger information – representation of the time-dependent electric current flowing through the stimulation probe – was recorded in an additional channel of the amplifier.

Each specimen underwent nerve-sparing low anterior rectal resection with simultaneous exposition of the SHP, IHP, and the PSN. A non-depolarising neuromuscular blocker – vecuronium bromide – in a dosis adapted to each specimen's weight was injected into each specimen after the surgical procedure to prohibit any activity of skeletal muscle tissue. After the entire experiment, the specimens were sacrificed with an overdose of thiopental sodium (Trapanal®, Nycomed, Konstanz, Germany).

4.2.5 Direct nerve stimulation

DNS of the left and right IHP (see Figure 4.15) was performed intraoperatively by a highly qualified colorectal surgeon using a handheld probe (Art. no. 522610, inomed Medizintechnik GmbH, Emmendingen, Germany). After electrophysiological localization of the IHP in all specimens, the IHP was electrically stimulated in three phases:

1. After low anterior rectal resection.
2. After an incision to the IHP proximally to the stimulation site (i.e. between the stimulation site and the sacral branching of the plexus innervation).
3. After an incision to the IHP distally to the stimulation site (i.e. between the stimulation site and the nerve branching of the IAS).

The stimulation amplitude started at 1 mA and was increased as needed, until the stimulation-induced myographic activity of the IAS could be observed. Each stimulation train lasted at least 5 seconds and a simultaneous recording from the IAS and EAS needle electrodes was performed.

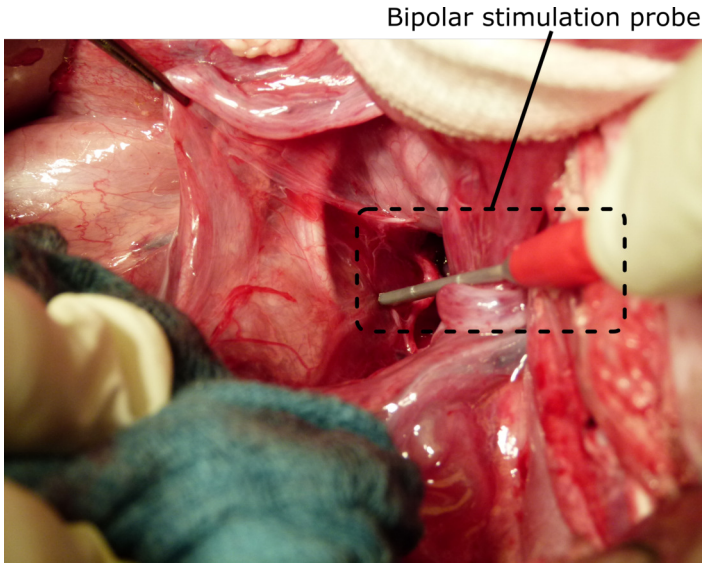

Figure 4.15 Stimulation of the right inferior hypogastric plexus in a pig specimen using a handheld bipolar probe. The procedure was performed at the University Medical Center Mainz, Department of General, Visceral and Transplantation Surgery by highly qualified medical personnel.

4.2.6 Transcutaneous electrical nerve stimulation

TENS using the electrodes described in Section 4.2.2 was performed in five phases:

Phase 1: After positioning each specimen in prone position.

Phase 2: After positioning each specimen in supine position.

Phase 3: After minimally invasive low anterior rectal resection.

Phase 4: Within 50 minutes after skeletal muscle relaxation.

Phase 5: After bilateral nerve incision.

Each stimulation procedure consisted of 40 stimulation trains (10 second duration, 10-second inter-train rest interval, 25 mA, 30 Hz stimulation frequency, and 200 µs pulse width). Each 10-second train corresponded to a different cathode-anode configuration. Each stimulation procedure was programmed using the software described in Section 4.2.7 on page 46 and performed in an automated manner.

For each phase, a recording of the IAS and EAS activity during stimulation was performed for all electrode configurations. After testing all ten cathodes of the stimulation array, the anode was changed (see Figure 4.16 for a depiction of the electrode configurations).

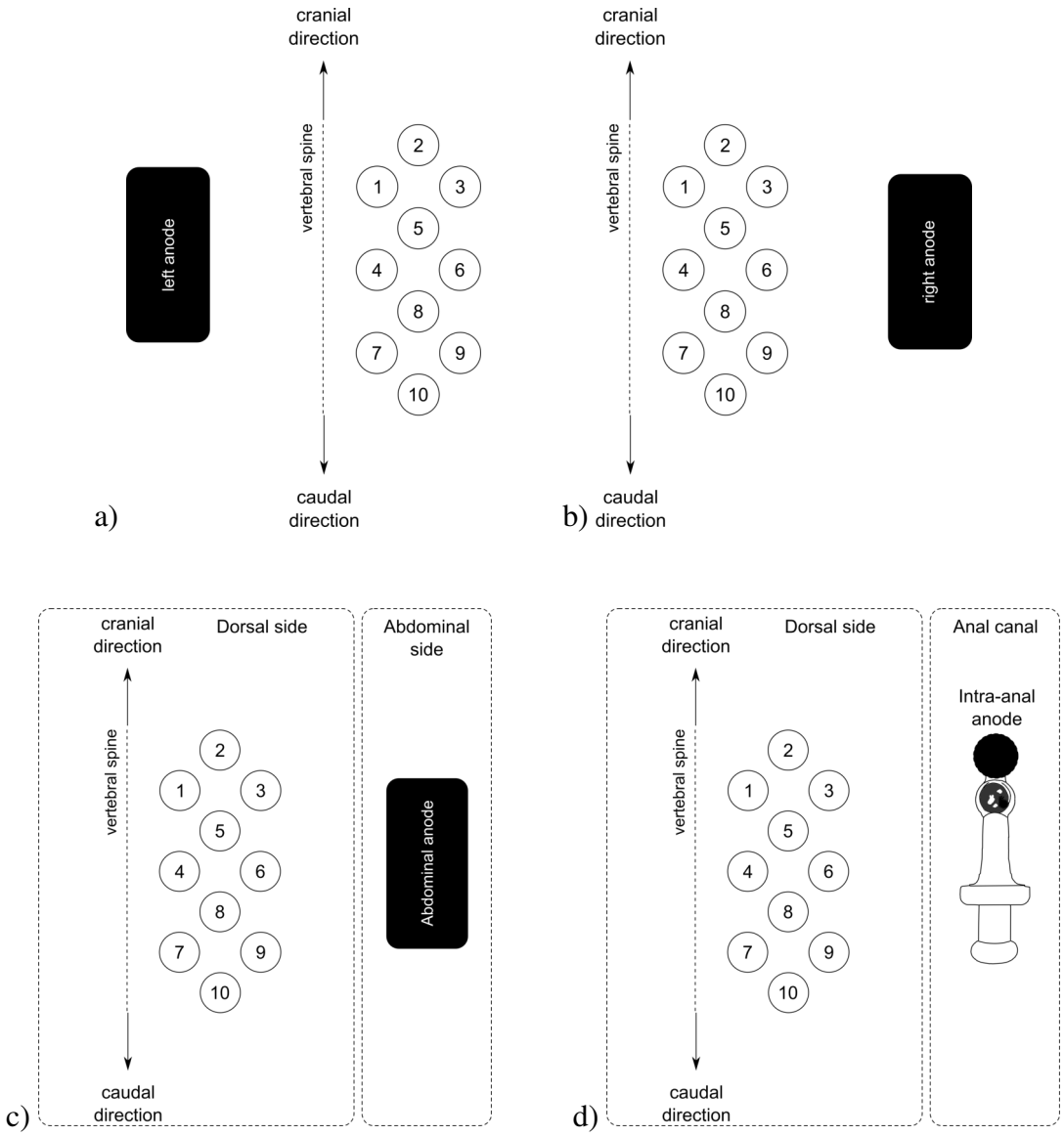

Figure 4.16 Electrode positions for transcutaneous electrical nerve stimulation. The stimulation array was placed on top of the right S2-S4 sacral region of each specimen and an anode was placed lateral left (a), lateral right (b), on the abdomen (c), and in the anal canal (d). The figure shows the channel distribution. The array consisted of ten 1 cm stainless steel electrodes and was supplied by Fraunhofer IBMT, St. Ingbert, Germany.

4.2.7 Software for automated stimulation

A piece of software developed using LabVIEW (National Instruments Corporation, Austin, TX, USA, version 2014) helped to automate the process of stimulation (see Section 4.2.6 on page 44) and perform repetitive stimulation procedures on the animal specimens. The software allowed to:

- Program automatic stimulation procedures including multiple stimulation trains occurring at defined time intervals.
- Variate the stimulation parameters: current amplitude (mA), pulse frequency (Hz), pulse width (µs), used output channel range (up to 12), pause duration (s), stimulation duration (s).
- Adjust the stimulation parameter ranges: minimal value, step size and maximal value.
- Set the polarity of stimulation (positive, negative, or biphasic).
- Display the progress of the stimulation procedure online.
- Document the stimulation procedures, the stimulation status, and the results of the impedance measurement in log files.

A state machine controlled by a software counter formed the backbone of the program. The software could sequentially switch between the machine states based on user input to control the phases of the automated stimulation (see Table 4.12). Appendix A on page 139 gives a comprehensive description of the LabVIEW source code of the developed software.

The software communicated with the ISIS Neurostimulator via a USB-Human interface device (HID) (supplied by inomed Medizintechnik GmbH). The communication was based on a set of functions which granted low-level control of the neural stimulator (see Figure 4.17). Each function used the USB-HID library to issue commands into the ISIS Neurostimulator.

The interface allowed the user to program the procedures for automatic stimulation by setting the parameter ranges of choice (Figure 4.18a) and also displayed the results of an impedance and current measurements in the form of a table of values (Figure 4.18b).

The feasibility of the developed software for proof of concept animal model application has been tested and published in [59].

Table 4.12 A state machine architecture forms the backbone of the software for non-invasive stimulation. This table lists the states forming the state machine (source: [59]).

State	Description	Diagram
Initialize	Initializes the communication with the ISIS Neurostimulator via a USB-Human interface device (HID)	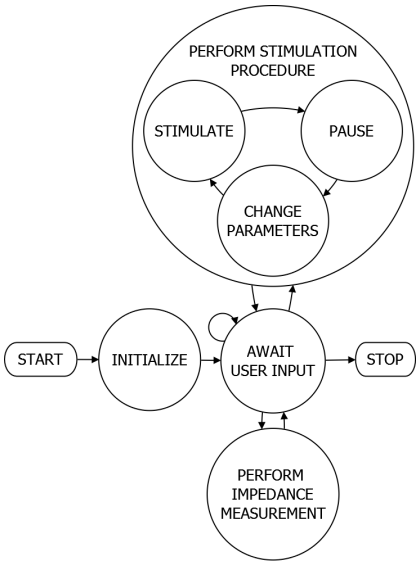
Await user input	Switches between the machine states according to the interaction between the user and the graphical user interface	
Perform stimulation procedure	Initializes the stimulator to start stimulation with a predefined set of stimulation parameters and loops through the given parameter ranges	
Perform impedance measurement	Initializes the stimulator to measure the impedance of the electrodes in the stimulation array	

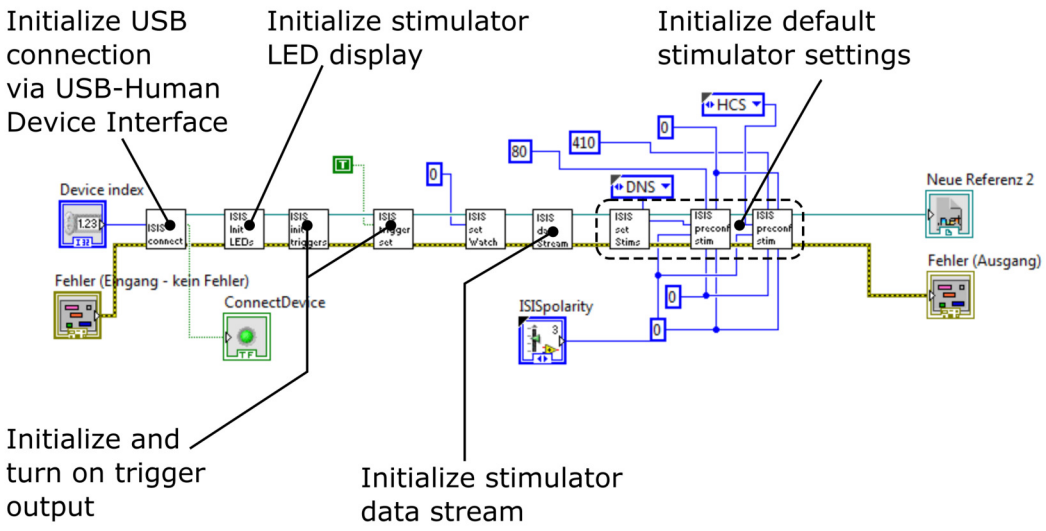

a)

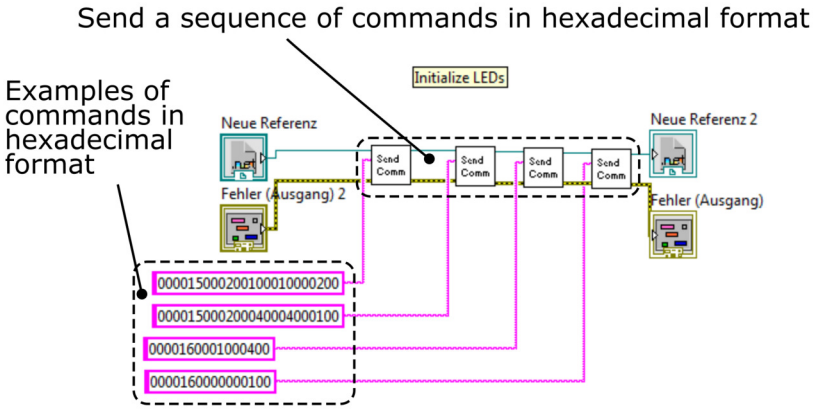

b)

Figure 4.17 Examples of low-level functions developed in LabVIEW (National Instruments Corporation, Austin, TX, USA, version 2014) controlling the neural stimulator: a) initialization of the stimulator LEDs, trigger channels, voltage limits and the stimulation polarity, b) initialization of the LED status lights.

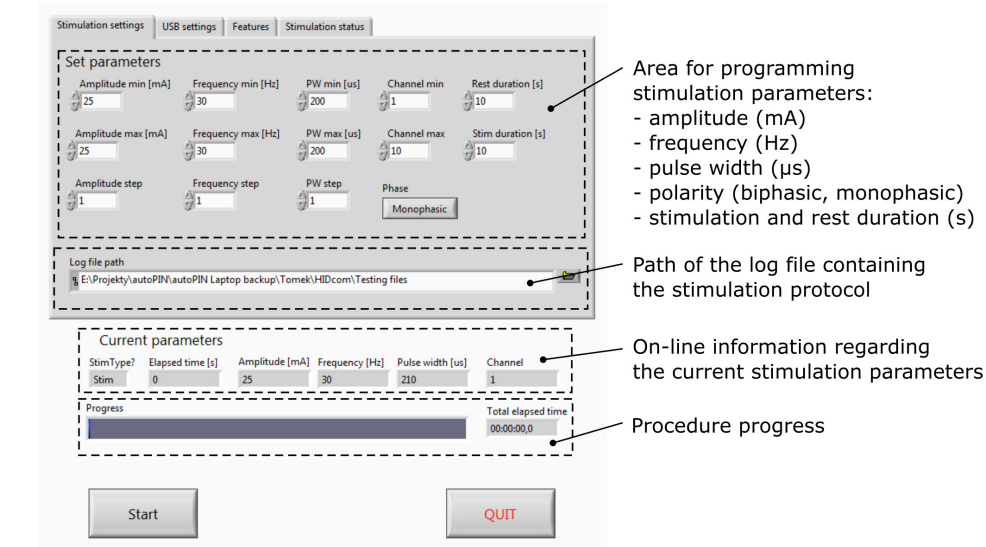

a)

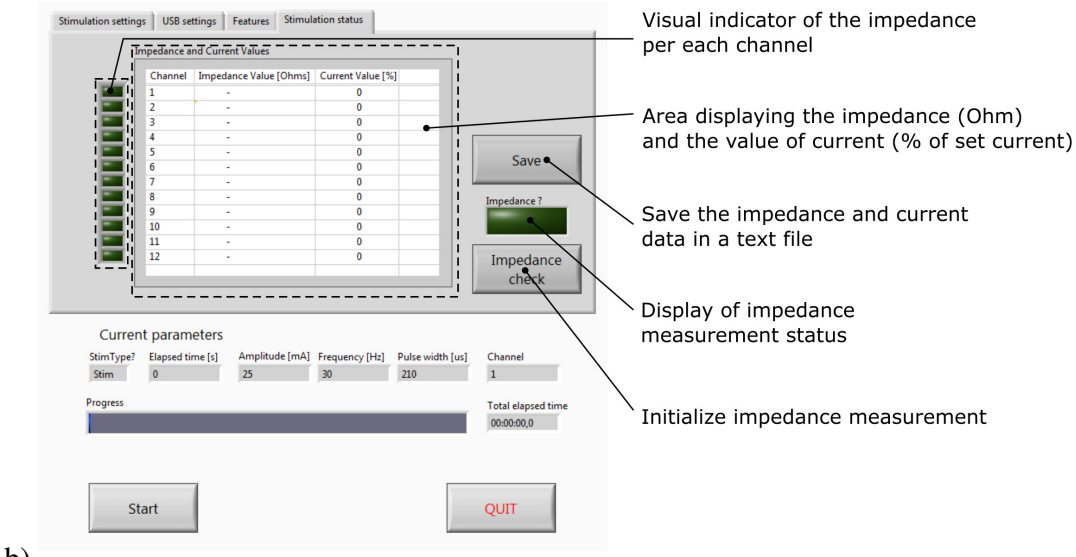

b)

Figure 4.18 Graphical user interface of the software for navigated stimulation: a) parameter input area and stimulation procedure progress, b) impedance and current measurement.

4.2.8 Software for signal acquisition and signal processing

The entire monitoring procedure was performed using NeuroExplorer software for IONM (inomed Medizintechnik GmbH, Emmendingen, Germany) which allowed to record the IAS activity as raw signals (within the technical specifications of the amplifier) and as processed EMG (band-pass filtered between 5 and 25 Hz to highlight the stimulation-induced modulation of the IAS activity that occurs predominantly within the spectrum between 5 and 20 Hz [55]).

Matlab software (MathWorks™, Natick, Massachusetts, USA, version 2009) was used for off-line signal processing. The trigger signal was used to synchronize the time intervals between stimulation pulses occurring at a frequency of 30 Hz (refer to Section 4.2.5). For the signals acquired during DNS, the 33 ms time windows were averaged over a period of ten seconds. The signals acquired during TENS were averaged over exactly ten seconds. Before averaging, the low-frequency offset component was subtracted from each 33 ms signal clip. This was done by subtracting an offset value from the signal in each clip. The last value in each signal clip was treated as the signal offset. The signals were subsequently displayed between -5 and 33 ms in order to visualize any stimulation artifacts occurring at 0 ms. Gaussian-based peak detection algorithm according to [60] was used to identify any deflections, their latencies, and amplitudes within the averaged signals. A script in Matlab allowed to apply this signal processing technique on all the data recorded from all the animal specimens in an automated manner.

4.2.9 Results interpretation and statistical analysis

The processed EMG of the IAS during DNS and TENS was analyzed qualitatively to identify amplitude increases signifying a successful neuromonitoring outcome [24] using the NeuroExplorer software (inomed Medizintechnik GmbH, Emmendingen, Germany). The raw signals of the averaged IAS EMG were analyzed qualitatively and quantitatively to investigate the presence of stimulation artifacts and other possible signal traits. Non-parametric Kruskall-Wallis statistical test was used for comparisons of multiple groups of signals acquired during TENS. For comparisons entailing two groups, the Mann-Whitney U-Test was used. The statistical and quantitative analysis of the signals were performed using Matlab (MathWorks™, Natick, Massachusetts, USA, version 2009).

Chapter 5

Results

5.1 Numerical simulation study of direct nerve stimulation

5.1.1 Electric field during direct nerve stimulation

Solving the quasi-static approximation of the forward problem defined by

$$\nabla \cdot (\sigma \nabla u) = 0, \quad (x \in \Omega) \tag{5.1}$$

under the boundary conditions simulating DNS yielded ten solutions for the electric potential field within the modeled geometry of the pelvis. Each solution corresponded to one of ten stimulation sites commonly used during DNS of the autonomous nervous system during colorectal surgery (see Table 5.1) and a stimulation amplitude of 1 mA.

From the electric potential fields obtained for each of the ten stimulation sites, the field gradient served to compute the current density distribution. Figures 5.1 and 5.2 visualize the current density magnitude projected onto the surface of the modeled autonomous nervous system. In each case, the highest current density is observable in the nearest vicinity of each pair of stimulation electrodes.

Lines of force were calculated for each solution by integrating the current density fields over a set of seed points in the vicinity of the stimulation electrodes. Figures 5.3 and 5.4 depict the lines of force with projected current density magnitude for each stimulation site. Each line of force depicted the trajectory that the electric current took inside the volume conductor in the vicinity of each electrode pair. For every stimulation site, the lines of force projected radially from one stimulation contact to the other while penetrating the surrounding tissues. This is the case not only for highly conductive tissues such as the neural tissue, but also for the poorly conductive bone tissue. The lines of force projected in all directions. This

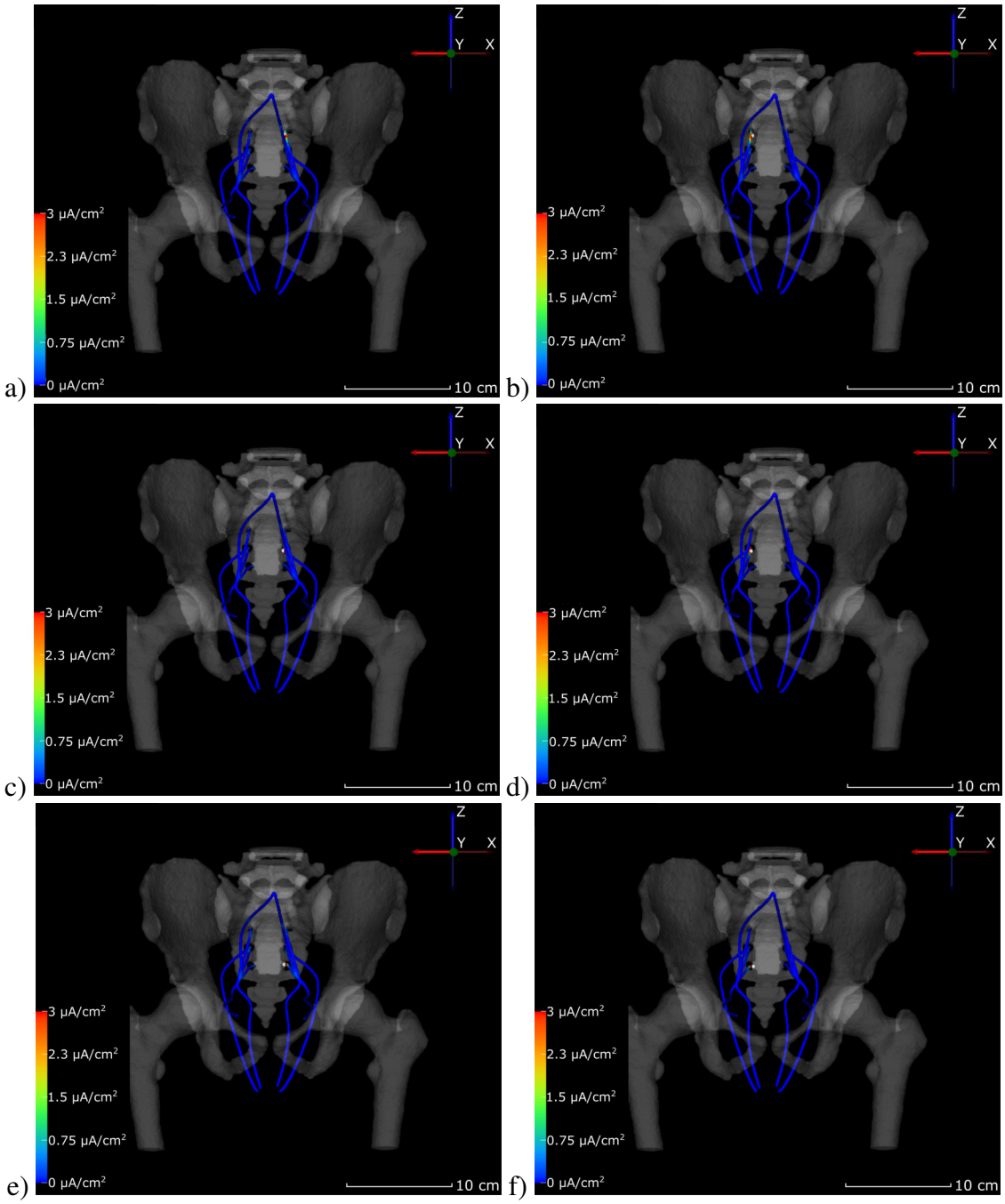

Figure 5.1 Current density projected onto the neural tissue during direct nerve stimulation at 1 mA. This figure depicts stimulation of six sacral nerve roots: a) right S2, b) left S2, c) right S3, d) right S3, e) left S4, and f) right S4.

Table 5.1 Protocol for the simulation of the electric field during direct nerve stimulation. Legend: PSN – pelvic splanchnic nerve, NH – hypogastric nerve, IHP – inferior hypogastric plexus

Scenario no.	Stimulation site
0	left S2 PSN
1	right S2 PSN
2	left S3 PSN
3	right S3 PSN
4	left S4 PSN
5	right S4 PSN
6	left NH (S2 level)
7	right NH (S2 level)
8	right IHP
9	left IHP

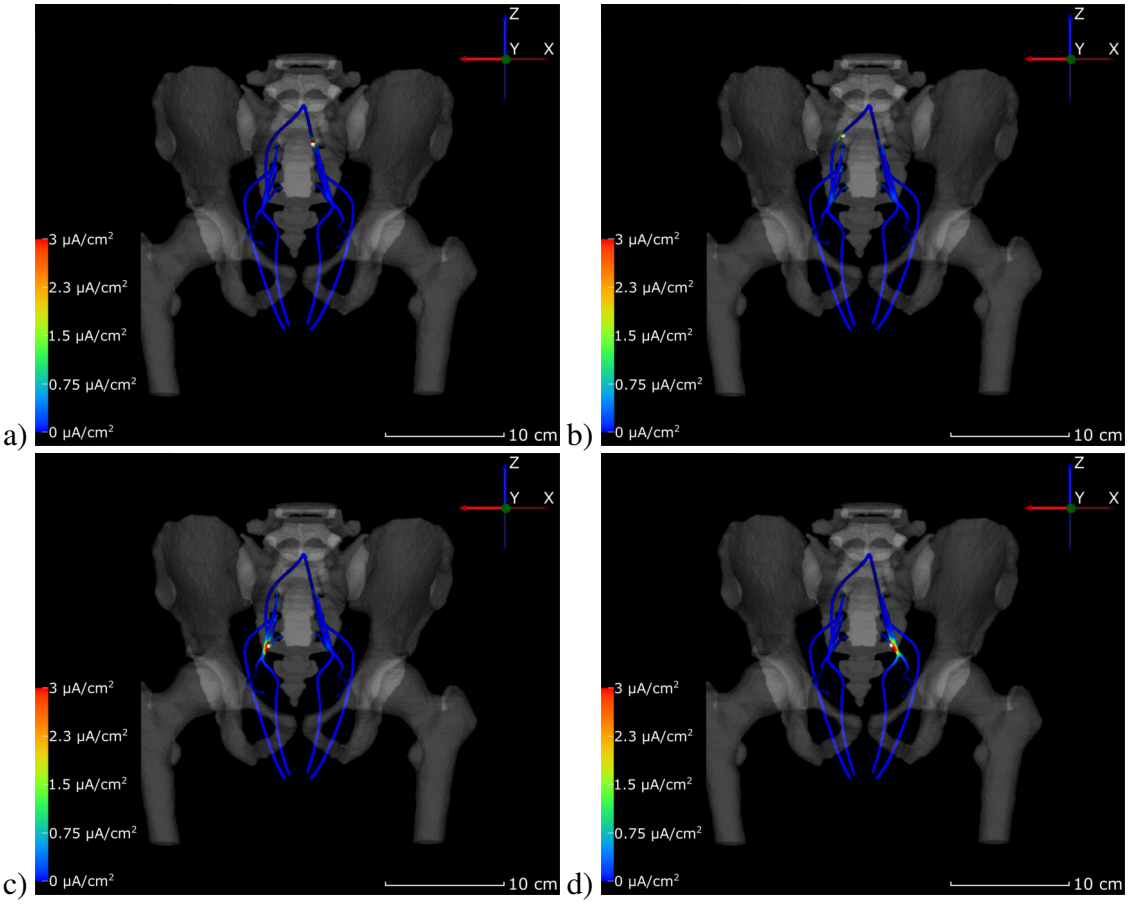

Figure 5.2 Current density projected onto the neural tissue during direct nerve stimulation at 1 mA. This figure depicts stimulation of the right (a) and left (b) hypogastric nerve, and right (c) and left (d) inferior hypogastric plexus.

result contradicts the result one would expect from *in-situ* stimulation when apposing the stimulation probe onto the wall containing neural structures. In the latter case the electric current should spread inside the tissues projecting radially away from the tissue wall. The interface between the tissue wall and the gas (air in the case of open surgery, CO_2 in the case of laparoscopic surgery) would form an impenetrable barrier for the electric current. However, the model geometry assumed that the electric contacts were immersed inside the conductive tissues. Thus, the lines of force projected in all directions to all the tissues surrounding the electrode contacts. The highest current density is observable in the direct vicinity of each stimulation contact.

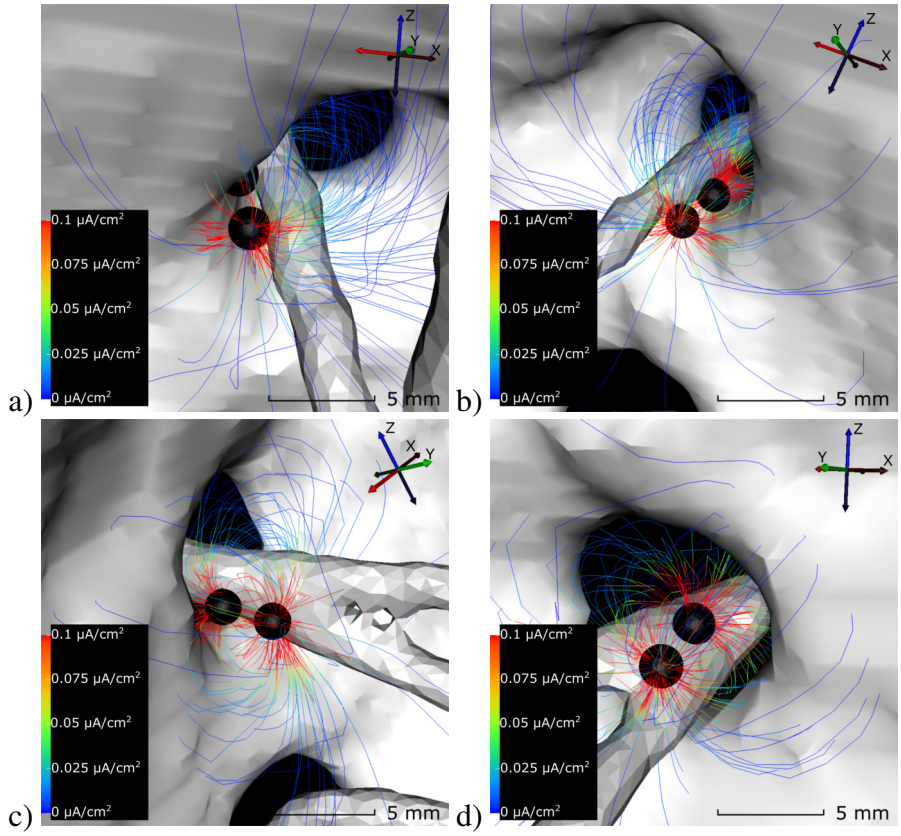

Figure 5.3 Current lines of force with projected current density during direct nerve stimulation at 1 mA. A model of bipolar stimulation electrode (⊘ 2 mm) was placed in the vicinity of the sacral foramina. Contact was maintained between the electrodes and the left S2 sacral nerve root (a), right S2 sacral nerve root (b), left S3 sacral nerve root (c), and right S3 sacral nerve root (d). Current density was projected onto the lines of force and represented as a color map.

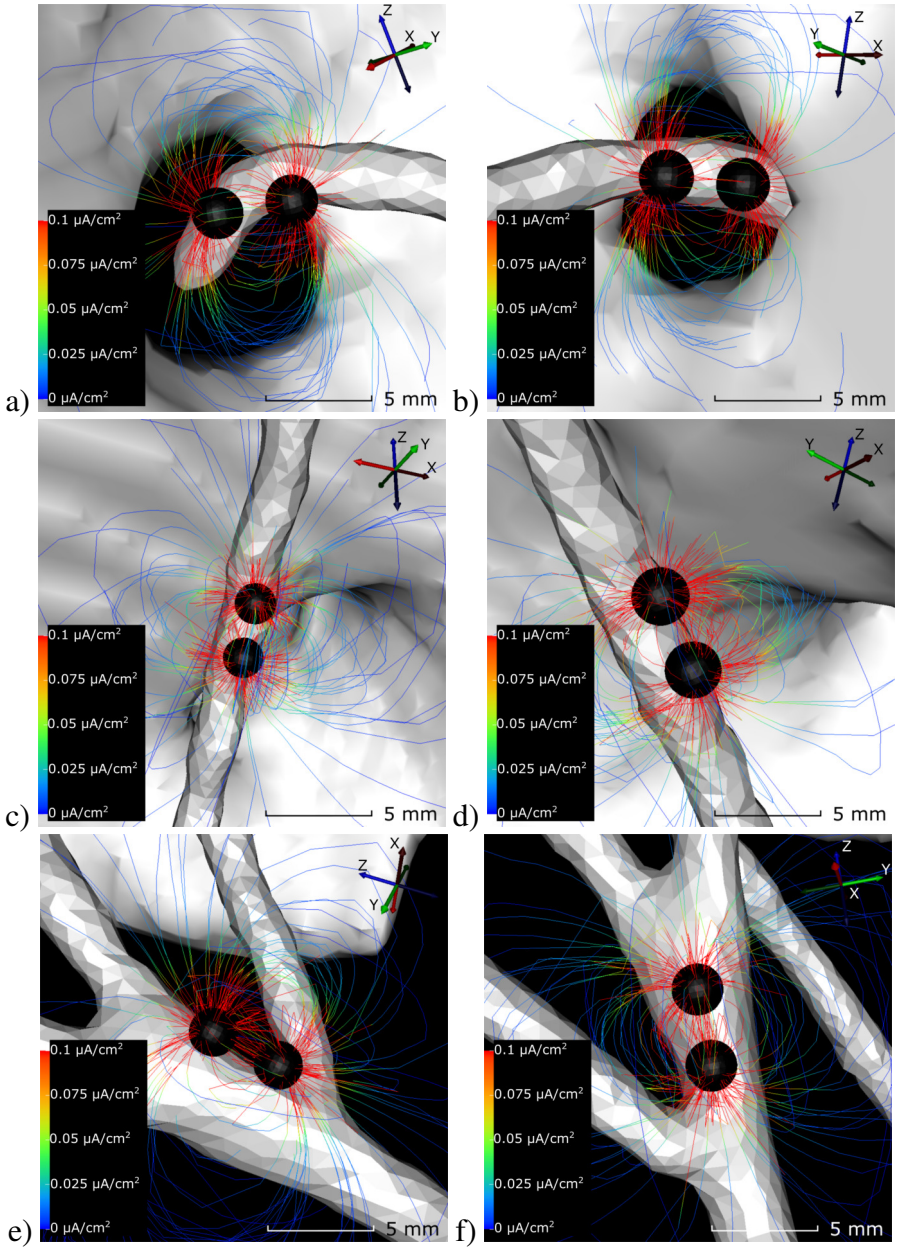

Figure 5.4 Current lines of force with projected current density during direct nerve stimulation at 1 mA. A model of bipolar stimulation electrode (⊘ 2 mm) was placed in the vicinity of the sacral foramina. Contact was maintained between the electrodes and the left S4 sacral nerve root (a), right S4 sacral nerve root (b), the middle part of the left (c) and right (d) hypogastric nerve, and the left (e) and right (f) inferior hypogastric plexus. Current density was projected onto the lines of force and represented as a color map.

5.1.2 Projection of electric field onto neural tissue

The electric potential field resulting from the simulation of DNS served to calculate the electric potential along each simulated nerve fiber of the membrane potential model. The electric potential field was projected onto coincident neural tissue (consisting of ten nerves, refer to 4.9 on page 35) using linear interpolation. The linear characteristics of the quasi-static solution allowed to calculate the electric potential field along each nerve fiber for a range of stimulation amplitudes (1 to 25 mA with 1 mA steps). Figure 5.5 shows an example of the potential field observed along the left IAS innervation originating from the S3 sacral nerve root during stimulation of the left S3 PSN. Each projected potential field exhibited a bipolar change of the electric potential in the vicinity of the stimulation electrodes. Appendix B.1 on page 149 contains a more comprehensive summary of the obtained electrical fields projected onto the neural tissue.

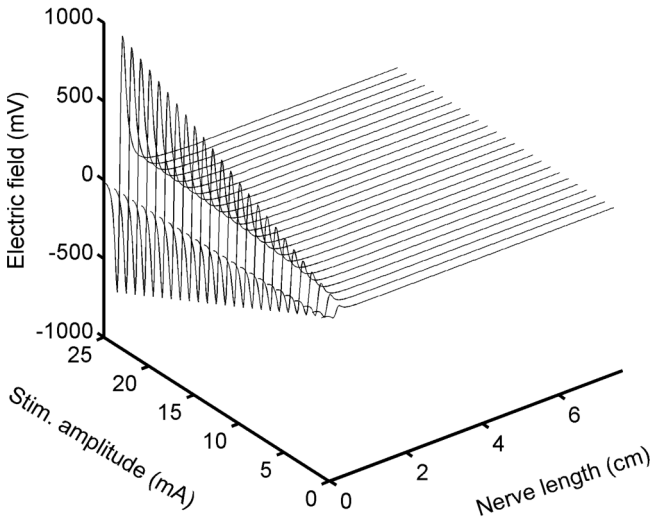

Figure 5.5 Electric field projected onto the left IAS innervation originating from the S3 sacral nerve root during direct stimulation of the left S3 pelvic splanchnic nerve. The field is depicted for stimulation amplitudes ranging from 1 to 25 mA with 1 mA steps. A bipolar change of the electric field can be observed within the first 0.5 cm of the nerve length, which corresponds to the site of nearest vicinity of the stimulation electrode contacts.

5.1.3 Simulated membrane potential before nerve incision

All field projections served as extracellular stimuli in simulation of the membrane potential of each modeled fiber of the autonomous nervous system. Based on input electrical field

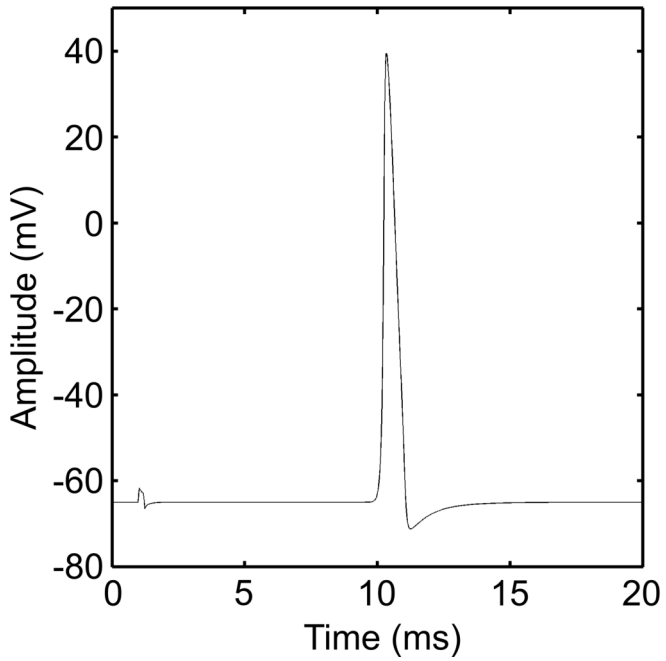

Figure 5.6 Membrane potential modeled in the distal part of the left IAS innervation originating from the S3 sacral nerve root during direct stimulation of the left S3 pelvic splanchnic nerve. This simulation is a result of 2 mA stimulation using a 200 µs pulse. The stimulation pulse occurred 1 ms after the beginning of the simulation, which is also to be seen as a biphasic stimulation artifact. A nerve action potential occurs approximately 10 ms after the beginning of the simulation.

resulting from each stimulation site, a time evolution of the membrane potential was obtained for every simulated nerve fiber at a range of stimulation amplitudes between 1 and 25 mA. This resulted in a total of 2500 simulations:

$$(25 \text{ stimulation amplitude levels}) \times (10 \text{ DNS stimulation sites}) \times (10 \text{ simulated nerves})$$

Membrane potentials were modeled at distal ends of all nerves as described in Table 5.2. Figure 5.6 shows an example of the membrane potential modeled at the distal end of the left IAS innervation originating from the S3 sacral nerve root during stimulation of the left S3 PSN. Appendix C.1 on page 157 contains a summary of all the membrane potentials modeled before nerve incision.

Figure 5.7 illustrates how stimulation at different sites affects all the modeled nervous tissue. Unilateral stimulation of the inferior hypogastric plexus resulted in an action potential recorded unilaterally from the distal parts of the S2, S4 PSNs, innervation of the internal anal sphincter, and the bladder innervation.

Table 5.2 Simulated recording and stimulation sites during direct nerve stimulation. Legend: PSN – pelvic splanchnic nerve, NH – hypogastric nerve, IHP – inferior hypogastric plexus.

Recording site	Stimulation site
left S2 PSN	left S2 PSN
right S2 PSN	right S2 PSN
left S3 IAS innervation	left S3 PSN
left pudendal nerve	left S3 PSN
right S3 IAS innervation	right S3 PSN
right pudendal nerve	right S3 PSN
left S4 PSN	left S4 PSN
right S4 PSN	right S4 PSN
left NH	left NH (S2 level)
right NH	right NH (S2 level)
right S2 PSN	right IHP
right S3 PSN	right IHP
right S4 PSN	right IHP
right NH	right IHP
left S2 PSN	left IHP
left S3 PSN	left IHP
left S4 PSN	left IHP
left NH	left IHP

Unilateral stimulation of in the hypogastric nerve at the level of S2 resulted in an action potential recorded unilaterally from the distal part of the bladder innervation.

At low stimulation amplitudes (between 1 and 14 mA for the right side and between 1 and 19 mA for the left side), stimulation of the S4 PSN produced an action potential recorded from the distal parts of the S4 PSN. Conversely, at higher stimulation amplitudes (above 15 mA for the right side and above 20 mA for the left side), the stimulation at the same site resulted additionally in an action potential recorded from the distal part of the IAS innervation.

Stimulation of the left S3 PSN produced an action potential recorded from the distal part of the left IAS innervation (recorded first at 2 mA stimulation amplitude) and the left pudendal nerve (recorded first at 4 mA stimulation amplitude).

Stimulation of the right S3 PSN produced an action potential recorded from the distal part of the right IAS innervation (recorded first at 4 mA stimulation amplitude) and the right pudendal nerve (recorded first at 3 mA stimulation amplitude). Additionally, at higher stimulation amplitudes, stimulation of the same site resulted in a reaction of the right S2 PSN (at 14 mA), the right S4 PSN (at 20 mA) and the left S2 PSN (at 23 mA).

Unilateral stimulation of the S2 PSN resulted in unilateral S2 PSN reaction.

5.1.4 Simulated membrane potential after nerve incision

The simulation of the membrane potential under DNS after nerve incision was performed on the bladder and IAS innervation. As described in section 4.1.7 on page 36, these nerves underwent an incision slightly distally from the level of the IHP. The field projections derived for these nerves from the FEM simulations served as extracellular stimuli. Based on the electrical field input resulting from all ten stimulation sites in the range between 1 and 25 mA, a time evolution of the membrane potential was obtained for these four nerve fibers. This resulted in a total of 1000 simulations:

$$(25 \text{ stimulation amplitude levels}) \times (10 \text{ DNS stimulation sites}) \times (4 \text{ simulated nerves})$$

Figure 5.8 shows an example of the membrane potential recorded at the distal end of the left IAS innervation originating from the S3 sacral nerve root during 2 mA stimulation of the left S3 PSN before and after the nerve incision. Table 5.3 contains a summary of the obtained membrane potentials before and after the nerve incision for the entire range of stimulation amplitudes in the four aforementioned nerves.

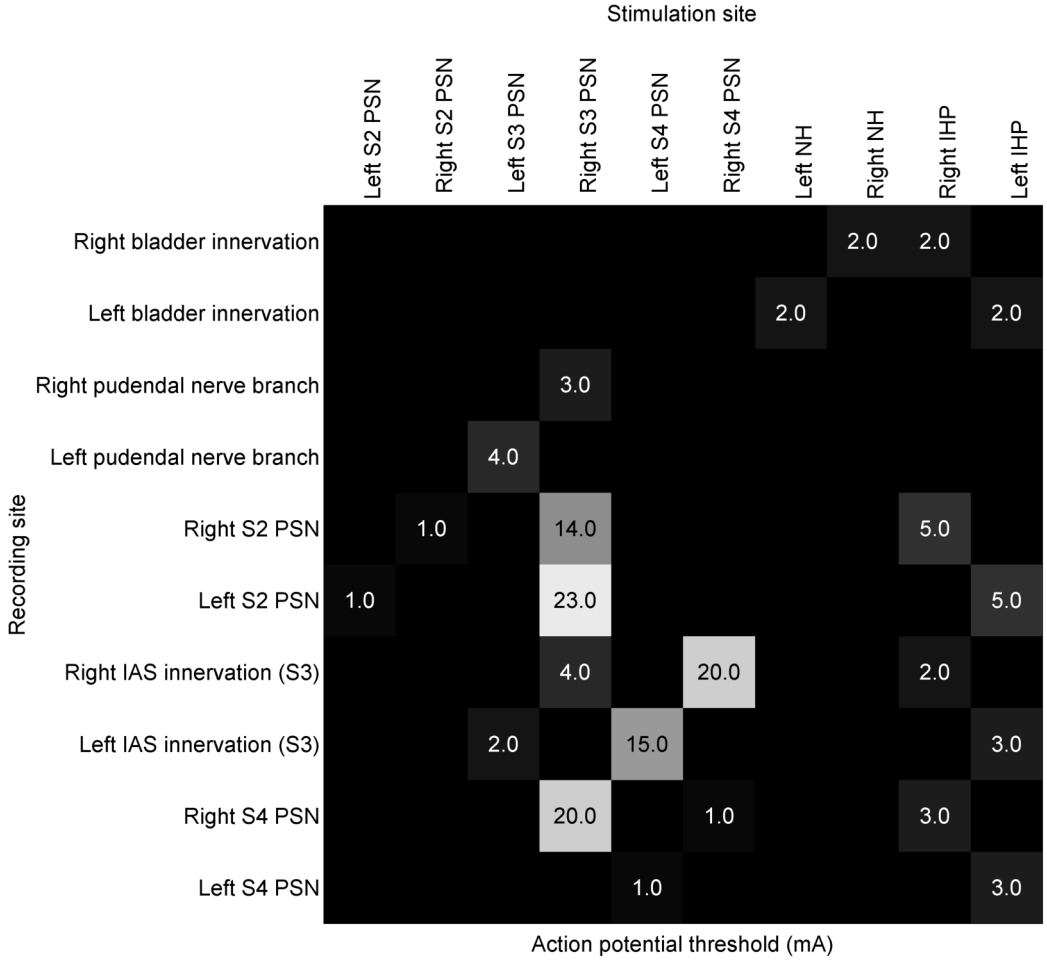

Figure 5.7 Stimulation amplitudes at which an action potential was first observed in distal parts of modeled nerves during simulated direct nerve stimulation before nerve incision. The simulated stimulation amplitudes ranged from 1 and 25 mA . The amplitudes have been color-coded in grayscale: the darker the shade, the lower the value. Pitch black without a value depicts a situation where no action potential was recorded from a given nerve due to stimulation at a given site. Legend: NH – hypogastric nerve, IHP – inferior hypogastric plexus, PSN – pelvic splanchnic nerve, IAS – internal anal sphincter.

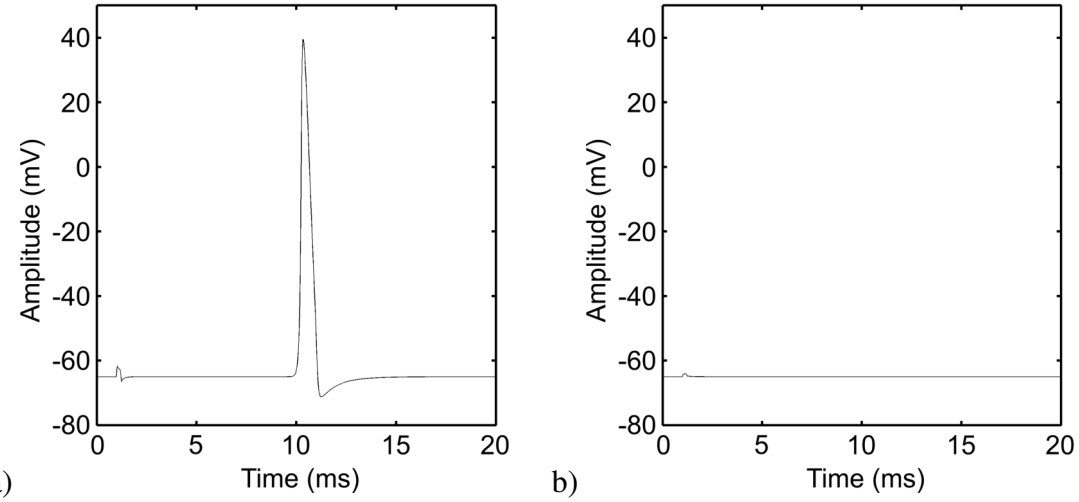

Figure 5.8 Membrane potential modeled in the distal part of the left IAS innervation originating from the S3 sacral nerve root during direct stimulation of the left S3 pelvic splanchnic nerve before (a) and after nerve incision (b). This simulation is a result of 2 mA stimulation using a 200 µs pulse. The stimulation pulse occurred 1 ms after the beginning of the simulation, which is also to be seen as a biphasic stimulation artifact. A nerve action potential occurs approximately 10 ms after the beginning of the simulation only before nerve incision.

Table 5.3 Membrane potential modeled in the distal ends of four simulated nerves before and after nerve incision during direct nerve stimulation. Legend: NH – hypogastric nerve, IHP – inferior hypogastric plexus, IAS – internal anal sphincter, PSN – pelvic splanchnic nerve.

Description	Before incision	After incision	Description	Before incision	After incision
Recording: left IAS innervation (S3) Stimulation: left S3 PSN	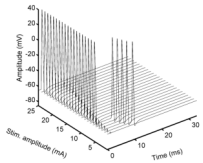	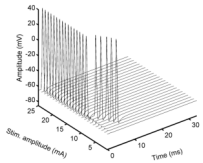	Recording: right IAS innervation (S3) Stimulation: right S3 PSN	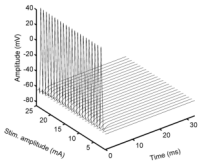	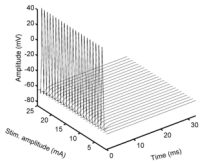
Recording: left bladder innervation Stimulation: left NH	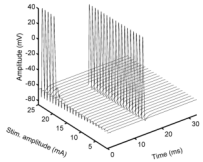	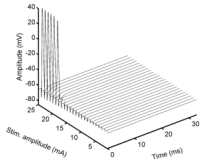	Recording: right bladder innervation Stimulation: right NH	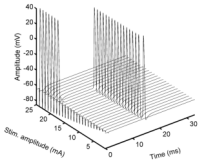	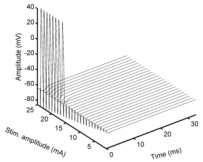
Recording: right IAS innervation Stimulation: left IHP	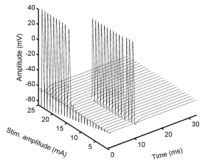	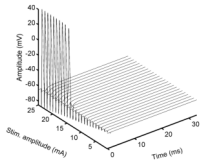	Recording: right bladder innervation Stimulation: right IHP	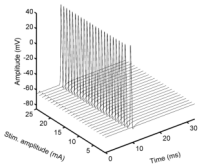	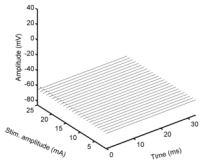
Recording: left IAS innervation Stimulation: left IHP	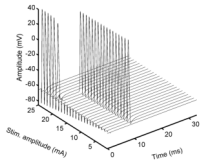	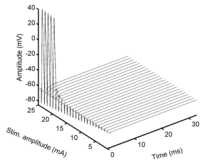	Recording: left bladder innervation Stimulation: right IHP	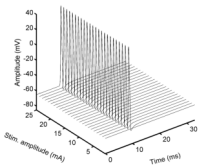	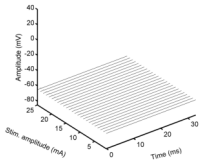

In order to develop an idea whether the nerve incision affected the occurrence of the membrane potential, it was important to identify any differences in the resulting membrane potential in the simulation before and after nerve incision. Figure 5.9 compares the threshold stimulation amplitudes before and after nerve incision at which an action potential was recorded at the distal end of the corresponding nerves. Figure 5.10 depicts stimulation amplitude ranges, derived from these results, in which a response could be recorded only before nerve incision. Three distinct, mutually exclusive cases could be identified within the dataset:

1. Nerve incision **completely prohibited** the conduction of the action potential along the nerve fiber, which resulted in a lack of recordable action potential at the distal end of the nerve regardless of the stimulation intensity.

2. Nerve incision prohibited the conduction of the action potential **only for a specific range of stimulation intensities.** After exceeding a threshold stimulation intensity, the action potentials reoccurred within the recording site.

3. Nerve incision **did not affect** the conduction of the action potential along a given nerve fiber.

Complete obstruction of the action potential occurred in the bladder innervation during the stimulation of the left and right hypogastric plexi. In these cases, an action potential could be recorded only before the nerve incision (already at 2 mA stimulation amplitude). The action potential did not reoccur after further increasing the stimulation intensity within the tested range from 1 to 25 mA.

Current intensity ranges, containing a minimal and maximal threshold stimulation intensity within the tested stimulation range, in which stimulation of the damaged nerve resulted in a lack of distally recordable action potential were observed in the IAS innervation when stimulating the inferior hypogastric plexi and the left S3 sacral nerve root and in the bladder innervation when stimulating the hypogastric nerves. After increasing the current intensity, the action potentials reoccurred within the recording sites. Figure 5.11 depicts the latencies of the action potentials recorded at distal parts of the four concerning nerves. In the cases where the nerve incision affected the nerve only for a range of stimulation amplitudes, the latency of the action potential at threshold stimulation amplitude differed before and after the nerve incision. Stimulation of the left and right hypogastric nerve resulted in action potentials recorded from the bladder innervation at 14.13 ms and 15.18 ms of latency before nerve incision. These action potentials were evoked already at 2 mA. After the nerve incision, these latencies were equal to 1.75 ms and 1.85 ms and could be evoked at a substantially

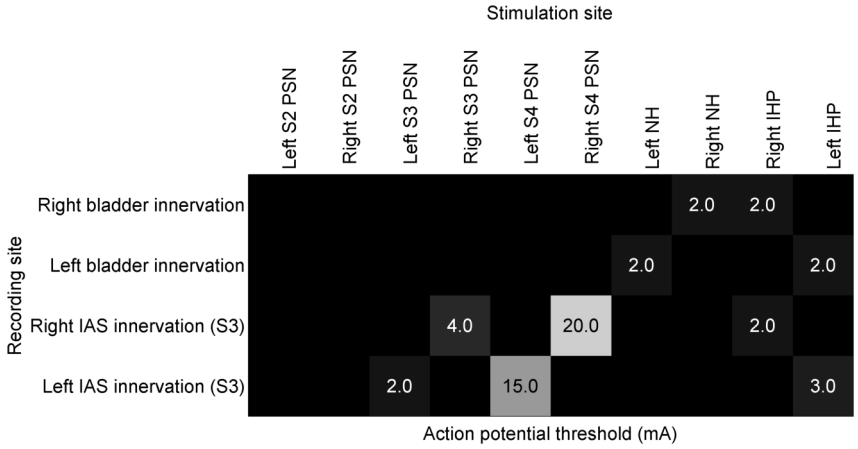

a)

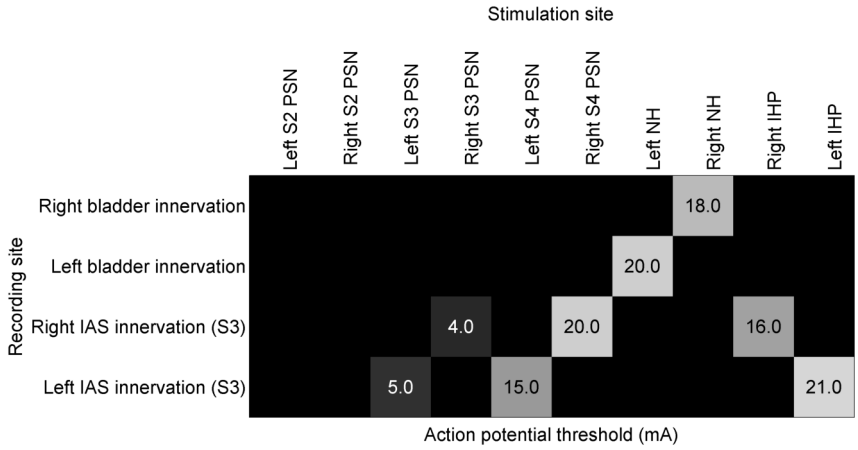

b)

Figure 5.9 Comparison of stimulation thresholds needed to evoke simulated neural activity during direct nerve stimulation before (a) and after nerve incision (b). Each value depicts the minimal stimulation amplitude in mA that resulted in evoking an action potential within the simulated model. The darker the shade of gray, the lower the stimulation threshold. Pitch black depicts situations where no action potential was evoked by stimulation in range between 1 and 25 mA. Legend: NH – hypogastric nerve, IHP – inferior hypogastric plexus, PSN – pelvic splanchnic nerve, IAS – internal anal sphincter.

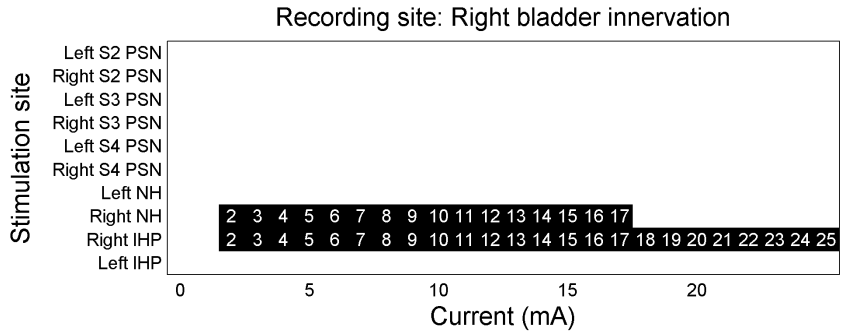

a)

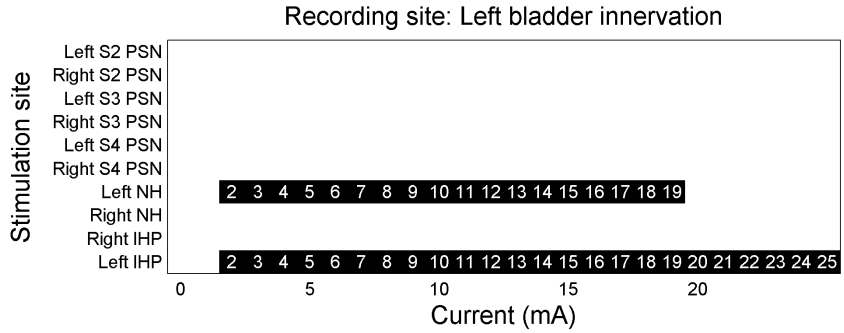

b)

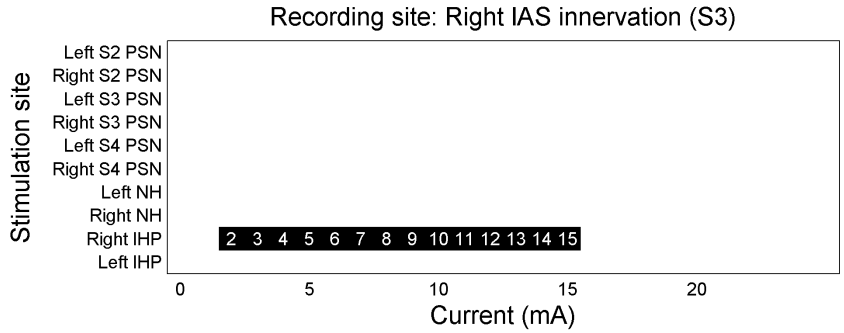

c)

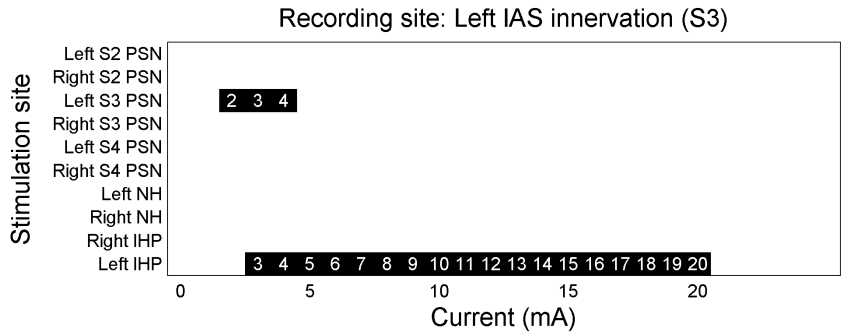

d)

Figure 5.10 Ranges of stimulation amplitudes for which the nerve incision effects in a lack of neural activity during direct nerve stimulation. Black boxes symbolize the stimulation amplitudes for which a nerve reaction resulted from stimulation only before the nerve incision. The stimulation amplitudes are additionally depicted within the black boxes as white text for more clarity. Legend: NH – hypogastric nerve, IHP – inferior hypogastric plexus, PSN – pelvic splanchnic nerve, IAS – internal anal sphincter.

higher stimulation amplitude: 20 mA and 18 mA for the left and right hypogastric nerve, respectively. A similar behavior could be observed during simulations of direct stimulation of the left and right IHP and recording the evoked potentials in the left and right IAS innervation. The latencies of the action potentials recorded prior to nerve incision were higher than following nerve incision: 9.85 ms and 10.50 ms evoked at 3 mA and 2 mA before the nerve incision and 1.53 ms and 1.65 ms evoked at 16 mA and 21 mA after the nerve incision.

Observing the IAS and bladder innervation during stimulation of both IHP and the hypogastric nerves, respectively, exposed the following pattern: 1) the stimulation intensity evoking an action potential was lower before nerve incision than after nerve incision, 2) stimulating the damaged nerve with the stimulation amplitude that evoked an action potential before the nerve incision did not yield a response after nerve incision, 3) further increase of stimulation amplitude eventually led to evoking an action potential also after the nerve incision, and 4) the latency of the action potentials evoked after nerve incision was significantly lower than before nerve incision. The lower latency implied that the action potentials, evoked at a higher stimulation amplitude, originated from a site distal to the stimulation site – thus "omitting" the site of nerve damage – and in the vicinity of the recording site.

Nerve incision did not affect the conduction of the action potential in the right IAS innervation during stimulation of the right S3 PSN. One could observe that 1) the latencies changed only slightly before and after the nerve incision and 2) these latencies were visibly lower than the ones obtained from the left IAS innervation during the stimulation of the left S3 PSN. This implied that the stimulation of the left S3 PSN resulted in generating an action potential at a site located away from the stimulation electrode and close to the recording site both before and after nerve incision. In this case, the site of nerve damage was also "omitted." This resulted in the inability of identifying a current intensity at which nerve damage could be identified.

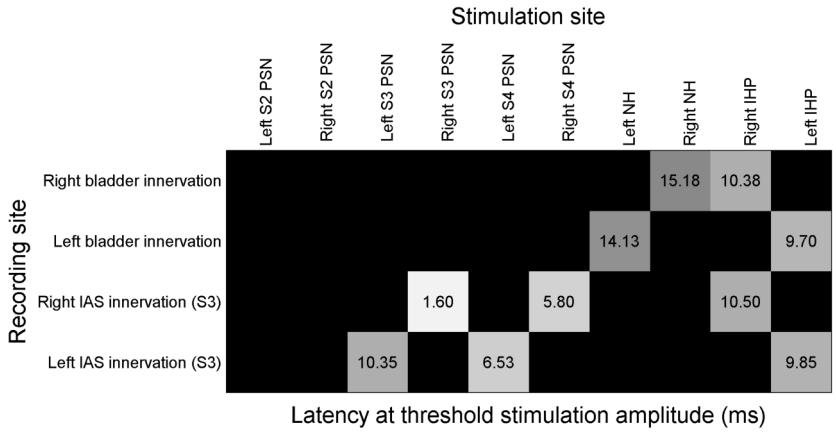

a)

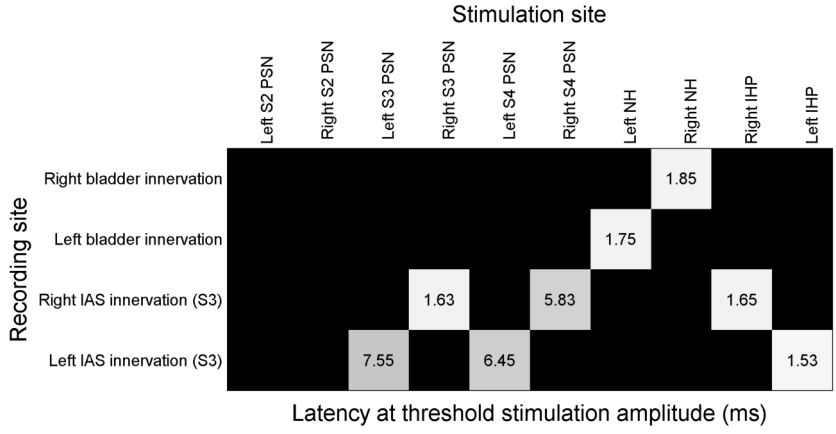

b)

Figure 5.11 Action potential latencies recorded at threshold stimulation amplitudes before (a) and after nerve incision (b). Legend: NH – hypogastric nerve, IHP – inferior hypogastric plexus, PSN – pelvic splanchnic nerve, IAS – internal anal sphincter.

5.2 Numerical simulation study of transcutaneous electrical nerve stimulation

5.2.1 Electric field generated by transcutaneous electrical nerve stimulation

Quasi-static approximation of the forward problem defined by Equation (5.1) under the conditions of TENS delivered a total of 40 solutions of the electric potential field within the modeled geometry:

$$(4 \text{ anode positions}) \times (10 \text{ cathode positions})$$

Each simulation result corresponded to 1 mA stimulation using one of the 40 electrode configurations. Each electrode configuration constituted one cathode from the ten-electrode stimulation array and one of the four anodes (see Chapter 4.2.6 on page 44).

The current density magnitude during TENS was computed from the electric potential field gradient. The examples in Figures 5.12 to 5.15 depict the obtained current density magnitudes for each anode configuration versus cathode no. 9 of the stimulation array. The figures depict three parallel planes intersecting at the cathode no. 9 that contain projections of the current density magnitude for better visualization. The maximal current density was recorded in the direct vicinity of the stimulation electrodes. The granular profile of the surface of the skin resulted in uneven distribution of current density. This is especially visible in the vicinity of the anode TENS pads.

Current lines of force were obtained from the electric potential gradient vector fields by integrating using a set of predefined seed points. Figures 5.16 to 5.19 depict the current flow for all anodes versus cathode no. 9. For clarity, the visualization focuses on the lines of force in the context of the skin surface, bone tissue and the stimulation electrodes despite being derived from the multi-tissue model as a whole. As expected, the current flow formed more complex shapes than in the case of direct nerve stimulation. This was a result of different shapes of the geometry, different positioning and bigger inter-electrode distances. Most notable was the influence of the bone tissue which acted as a barrier to the flow of current. This barrier was partial because the bone was still a conductive medium, although less conductive than the surrounding tissues.

The current density was additionally projected onto the surface of the nerve tissue (see Figure 5.20). The area with high current density is greater than the one obtained during direct nerve stimulation (see Section 5.1.2 on page 56). Placing the anode either lateral right to the

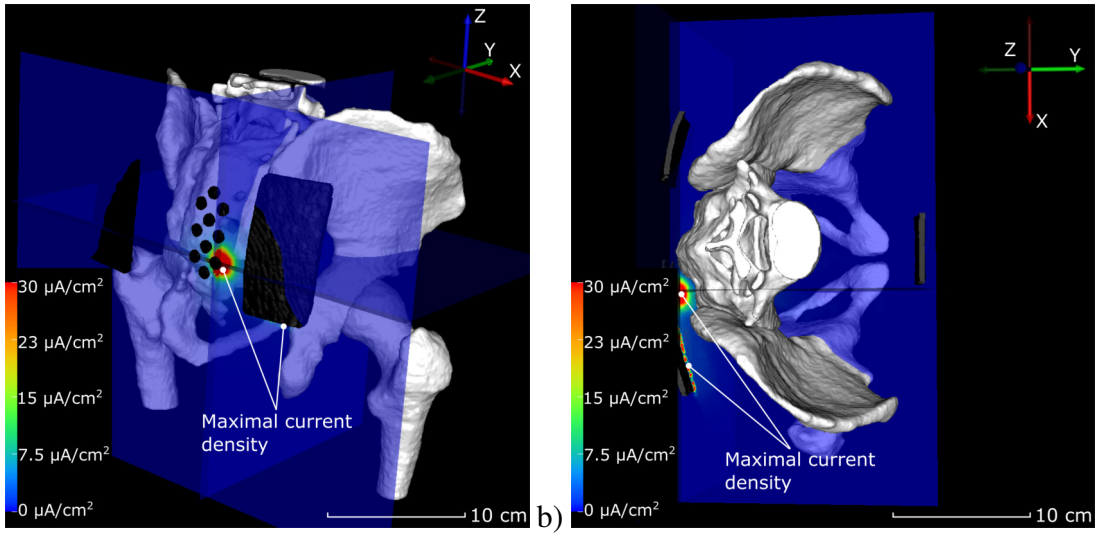

Figure 5.12 Current density distribution during transcutaneous electrical nerve stimulation at 1 mA between the right anode and the ninth cathode on the electrode array: a) arbitrary view, b) top view. Current distribution is projected onto three perpendicular planes intersecting cathode 1. The color coding corresponds to the current density magnitude.

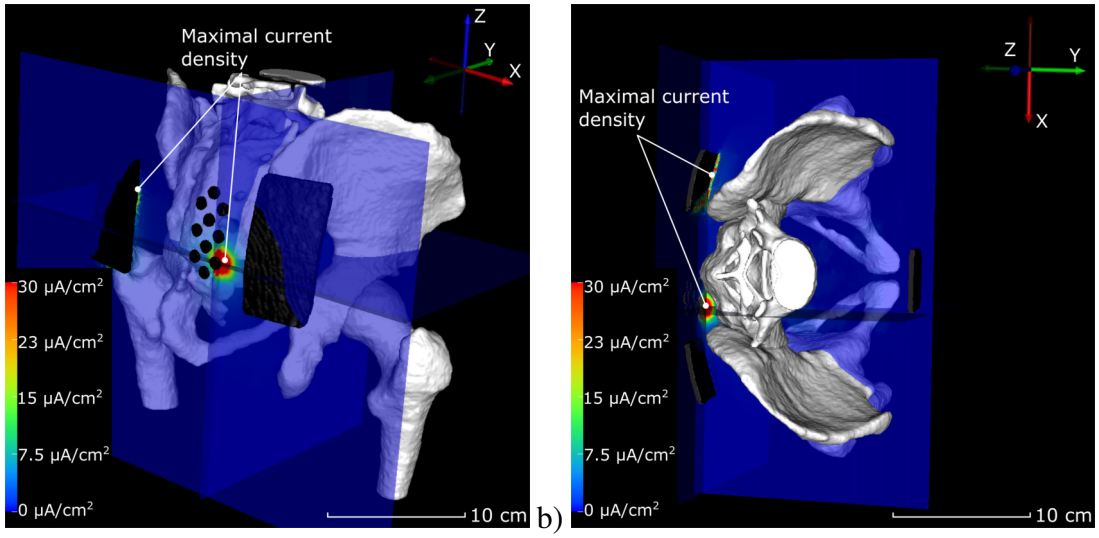

Figure 5.13 Current density distribution during transcutaneous electrical nerve stimulation at 1 mA between the left anode and the ninth cathode on the electrode array: a) arbitrary view, b) top view. Current distribution is projected onto three perpendicular planes intersecting Cathode 9. The color coding corresponds to the current density magnitude.

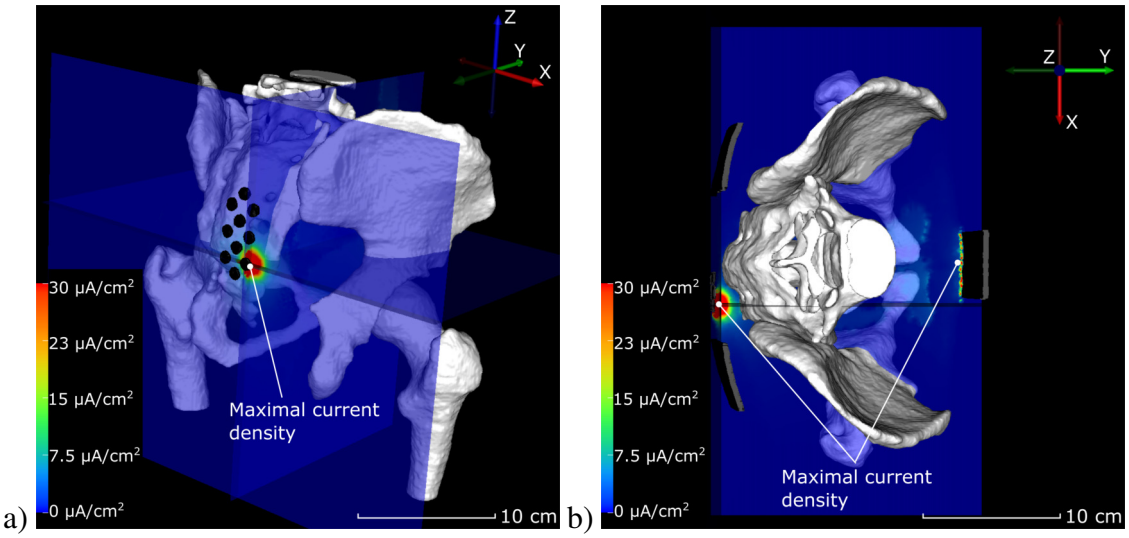

Figure 5.14 Current density distribution during transcutaneous electrical nerve stimulation at 1 mA between the anode on the abdomen and the ninth cathode on the electrode array: a) arbitrary view, b) top view. Current distribution is projected onto three perpendicular planes intersecting Cathode 9. The color coding corresponds to the current density magnitude.

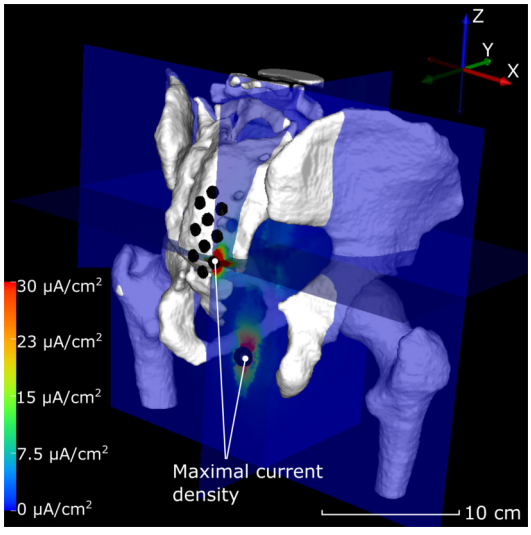

Figure 5.15 Current density distribution during transcutaneous electrical nerve stimulation at 1 mA between the anode on in the anal canal and the ninth cathode on the electrode array: arbitrary view. Current distribution is projected onto three perpendicular planes intersecting Cathode 9. The color coding corresponds to the current density magnitude.

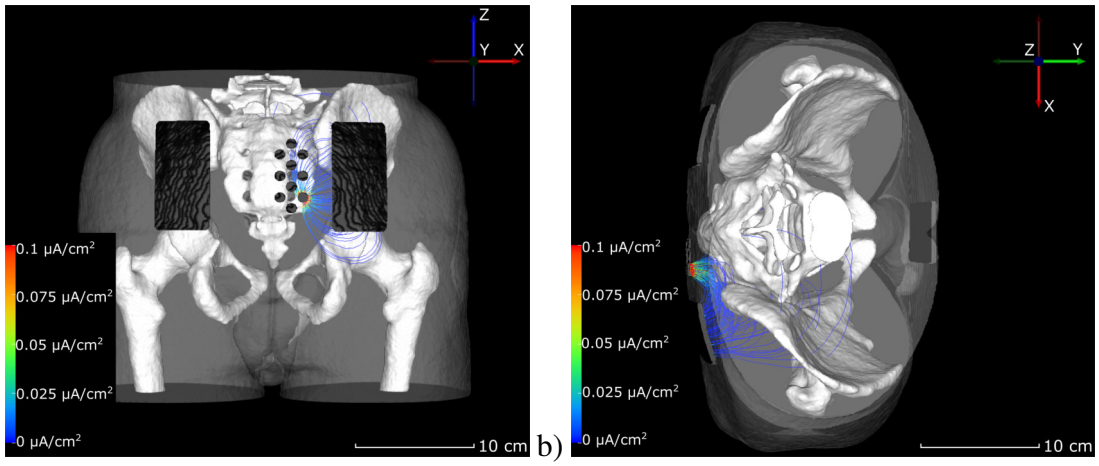

Figure 5.16 Current flow between anode located lateral left from the stimulation array and cathode no. 9: a) back view, b) top view. Current density magnitude was projected onto the lines of force.

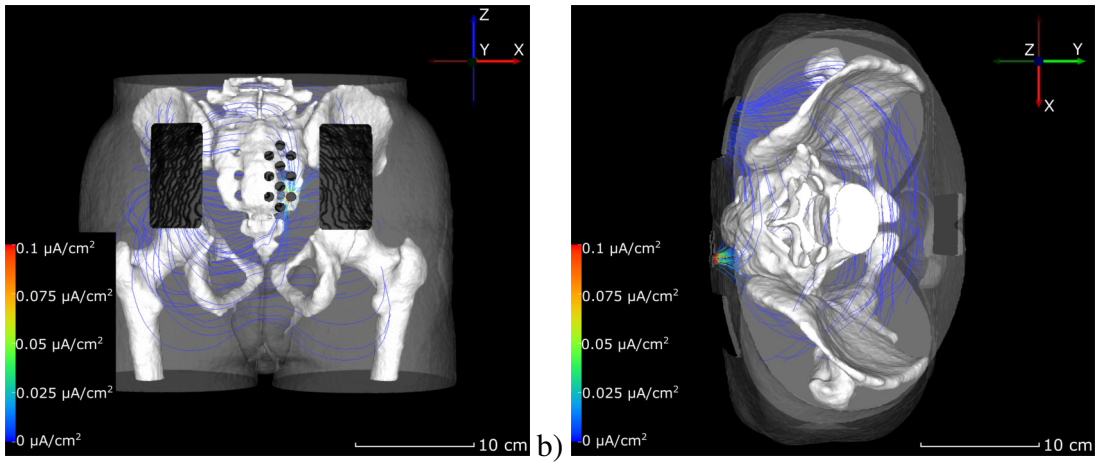

Figure 5.17 Current flow between anode located lateral right from the stimulation array and cathode no. 9: a) back view, b) top view. Current density magnitude was projected onto the lines of force.

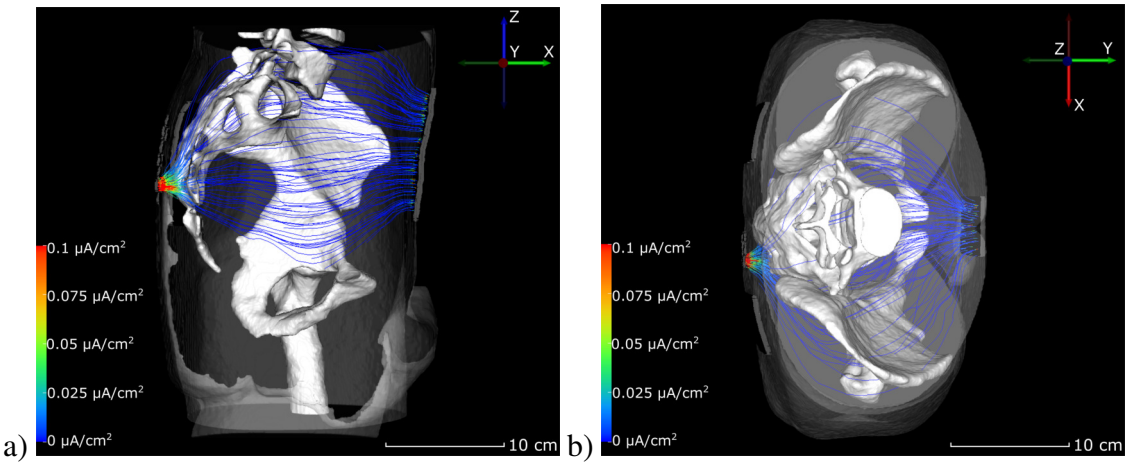

Figure 5.18 Current flow between anode located on the abdomen and cathode no. 9: a) side view, b) top view. Current density magnitude was projected onto the lines of force.

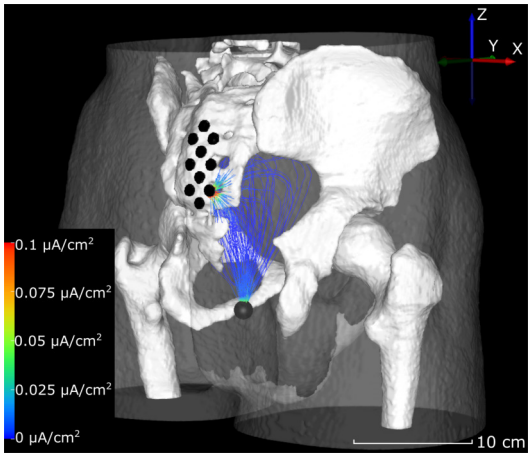

Figure 5.19 Current flow between anode located in the anal canal and cathode no. 9. Current density magnitude was projected onto the lines of force.

stimulation array or on the abdomen resulted in a current density exceeding $0.75\,\mu A/cm^2$ predominantly around the right S3/ S4 sacral nerve root as well as the first 5 cm of the right pudendal nerve. Placing the anode on the lateral left from the stimulation array resulted additionally in increased current density of approximately $0.5\,\mu A/cm^2$ in the area of the left S2-S4 sacral nerve roots up to the left hypogastric plexus and the first 5 cm of the left pudendal nerve. Placing the anode in the anal canal increased the current density around the distal parts of the left and right IAS innervation and the distal parts of both pudendal nerves.

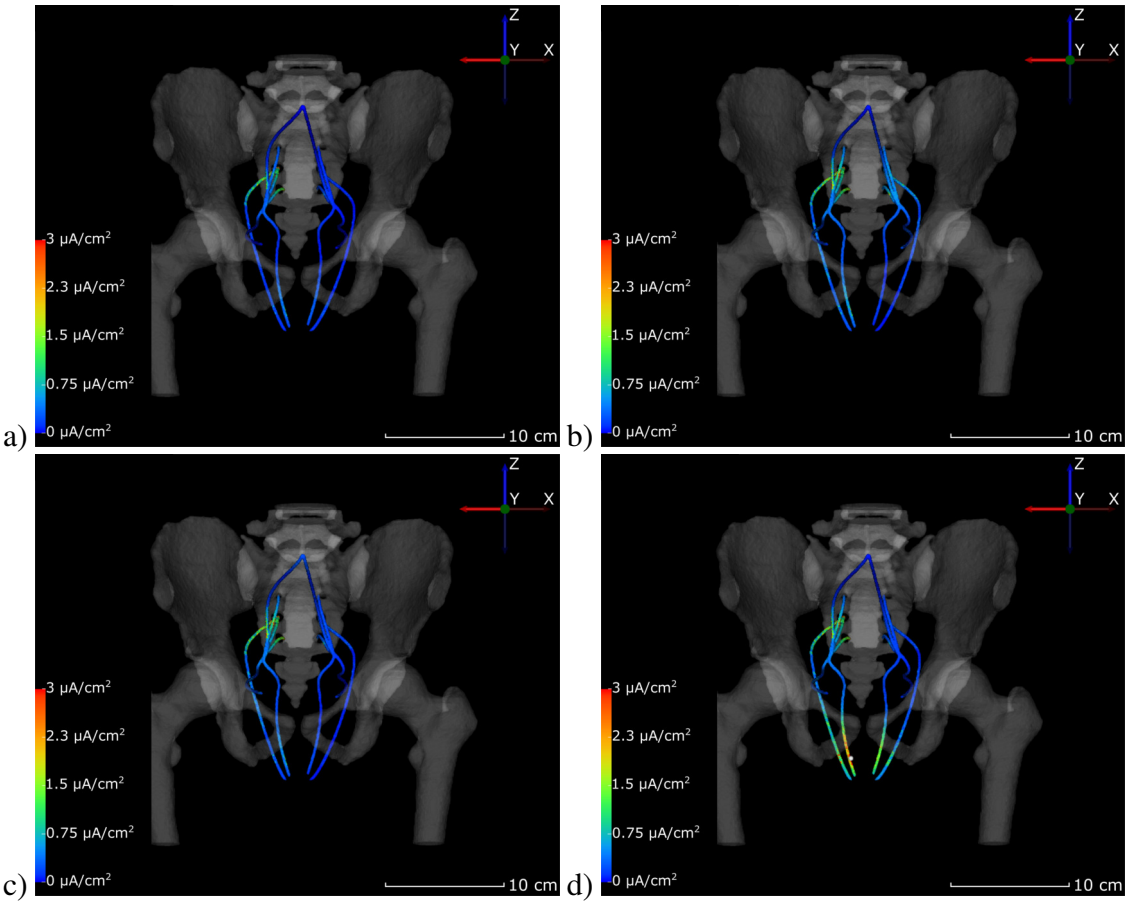

Figure 5.20 Current density magnitude projected onto the surface of the autonomous nervous tissue during transcutaneous electric nerve stimulation. The figure depicts stimulation using cathode no. 9 vs. anode placed lateral right (a), lateral left (b) from the stimulation array, on the abdomen (c), and in the anal canal (b). All four cases depict the frontal view of the nerve tissue in the context of the bone tissue. Other tissues are not depicted for the sake of visual clarity.

5.2.2 Projection of electric field onto neural tissue

The electric potential field resulting from the FEM simulations was projected onto each nerve fiber of the model of the autonomous nervous system using linear interpolation. By modulating the stimuli in time, input extracellular potentials in the form of rectangular pulses were derived for the range of stimulation amplitudes from 1 to 25 mA for all 40 electrode configurations. Figure 5.21 shows an example of the potential fields projected onto the autonomous nerves observed during transcutaneous electric stimulation using Anode 4 (inside the anal canal) vs. cathode no. 9. A more comprehensive summary of the electric potentials projected onto the nerve fibers is depicted in Appendix B.2 on page 152.

Based on the obtained results, one can immediately notice the influence of the transcutaneous stimulation on the potential along each nerve. The most negative values of the electric potential could be observed in parts of the nerve in closest proximity to the cathode. For the example depicted in 5.21a, it is the middle part of the left hypogastric nerve. In the case of the nerves stemming from the sacral nerve roots it is the initial part (see Figure 5.21b, d, e). This behavior is especially visible for high stimulation amplitudes. When parts of a nerve lay far from the stimulation electrodes, the electrical potential remained relatively constant (see Figure 5.21c). The most positive values of the electric potential could be observed for the parts of the nerve in the vicinity of the stimulation anode. This is especially visible in the example depicted in Figure 5.21b and d on the distal parts of the left pudendal nerve and left IAS innervation.

5.2.3 Simulated membrane potential before nerve incision

All projections of the electric field onto the autonomous nervous system resulting from the finite element simulations were used as input extracellular stimuli in simulations of the membrane potential. Based on input electrical field resulting from each electrode configuration, a time evolution of the membrane potential was obtained for every simulated nerve fiber and a range of stimulation amplitudes between 1 and 25 mA. This resulted in a total of 10000 simulations. Figure 5.22 shows an example of the membrane potential recorded along the left hypogastric nerve during stimulation using the anode in the anal canal versus cathode no. 9. In this particular example, an action potential resulted from electrical stimulation at 22 mA. A stimulation artifact is also visible at the moment of stimulus generation – 1 ms after the beginning of the simulation. Appendix C.3 on page 161 contains a more comprehensive summary of the obtained membrane potentials.

Figures 5.23 to 5.26 depict the stimulation amplitudes at which action potentials could be recorded from the distal parts of all nerves during stimulation using a given anode-cathode

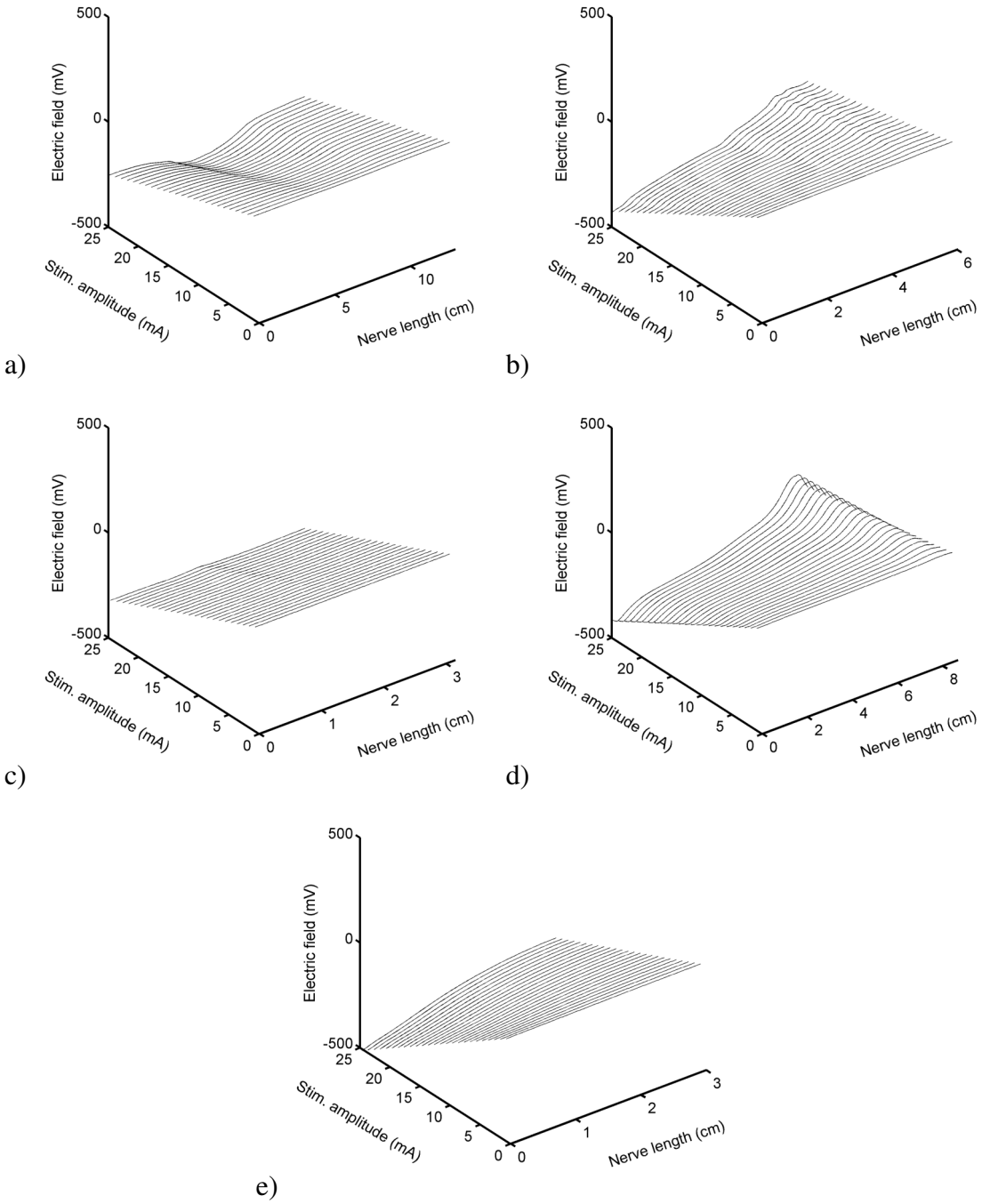

Figure 5.21 Electric field projected onto the nerve fibers during stimulation using cathode no. 9 vs. anode in the anal canal: a) left hypogastric nerve, b) left pudendal nerve, c) left S2 pelvic splanchnic nerve, d) left IAS innervation (S3), and e) left S4 pelvic splanchnic nerve. The fields are depicted for a range of stimulation amplitudes between 1 and 25 mA.

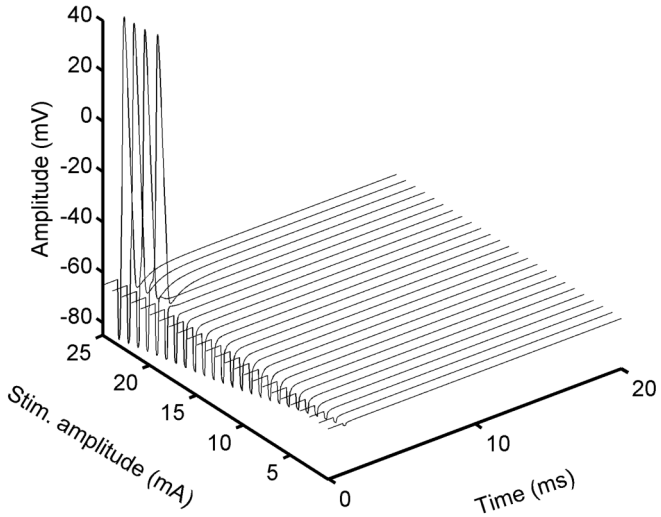

Figure 5.22 Membrane potential recorded from the distal part of the bladder innervation during transcutaneous stimulation using the anode in the anal canal versus cathode no. 9. An action potential could be recorded at 22 mA stimulation amplitude. A stimulation artifact is visible for all stimulation amplitudes 1 ms after the start of the simulation.

electrode configuration.

Anode 1: lateral right from stimulation array

Stimulation using the electrode configurations which used the anode on the lateral right side of the back delivered threshold amplitudes at which an action was first observed on the distal parts of the simulated autonomous nerve. The results are summarized in Figure 5.23.

Right and left bladder innervation barely produced an action potential: action potentials could be evoked only from the right branch at high stimulation thresholds (21 to 24 mA) and on the opposite sides of the stimulation array (C1, C2, C9, C10).

The right pudendal nerve branch required smaller stimulation amplitudes (starting at 2 mA using C5) to develop an action potential than the left branch (starting at 7 mA using C1). The left branch could be more easily activated when using the left side of the stimulation array (C1, C4, C7). A similar result could be observed in the right branch when using the middle part of the array (C1, C3, C4, C5, C6, C7, C8, C9).

The right S2 PSN could be activated at smaller amplitudes (starting at 4 mA using C2) and using a greater area of the stimulation array than the left part (C1 to C6 vs. C1, C2 and C5). The right S2 PSN reacted to stimulation using the upper (cranial) part of the stimulation

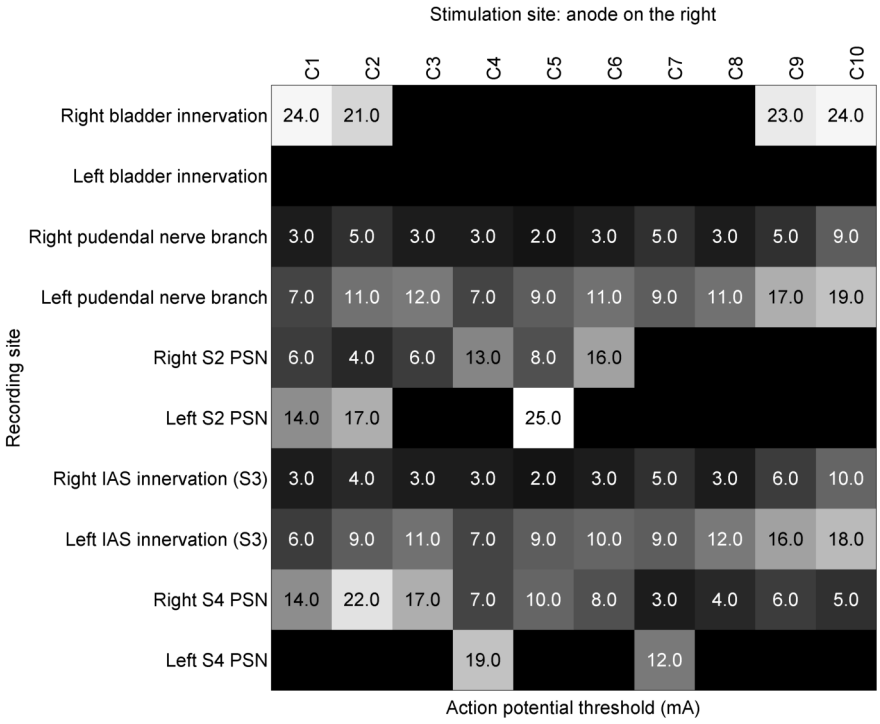

Figure 5.23 Amplitude thresholds needed to evoke neural activity during stimulation using all the contacts of the stimulation array versus the anode on the lateral right. Each value depicts the minimal stimulation amplitude in mA that resulted in evoking an action potential within the simulated model. The darker the shade of gray, the lower the stimulation threshold. Pitch black depicts situations where no action potential was evoked by stimulation in range between 1 and 25 mA.

array.

The right internal anal sphincter (IAS) innervation (S3) required a smaller amount of current to produce an action potential (min. 2 mA using C5) than the left. Producing an action potential in the right IAS innervation using the upper 2/3 of the cathode array required less current than the lower 1/3. In the case of the left IAS innervation, stimulation using the left part of the array (C1, C4, C7) required less current to produce an action potential.

A response of the left S4 PSN could only be evoked using the C4 and C7 cathodes (both constituting the left side of the stimulation array) at 19 and 12 mA, respectively. The right S4 PSN reacted already at 3 mA (C7). Stimulation using the lower part of the stimulation array (C7 to C10) required less current to evoke an action potential than the rest of the array.

Anode 2: lateral left from stimulation array

Figure 5.24 contains the threshold amplitudes evoking an action potential that could be recorded on the distal parts of the simulated innervation when stimulating using the stimulation array versus the anode placed on the lateral left side of the back.

Contrary to the stimulation using the anode on the right side of the back, the action potentials in the left and right bladder innervation could be evoked using a bigger portion of the stimulation array. Using the caudal and cranial part of the stimulation array required the lowest amplitude thresholds to activate the right and left bladder innervation, respectively. These simulated nerve structures reacted to as low as 13 mA of stimulation current.

The activation of the right pudendal nerve required less stimulation current (starting already at 2 mA) than activating the left pudendal nerve (starting at 7 mA). Stimulation using the upper 2/3 of the cathode array required less current to evoke a response than the lower 1/3. In the case of the left pudendal nerve, stimulation using the middle-to-left part of the cathode array required less current to evoke a response than the other electrode contacts.

The left and right S2 PSN reacted only when stimulating using the upper part of the stimulation array (C1 to C6): the right nerve required smaller stimulation current (starting at 5 mA) than the left (starting at 12 mA).

The right IAS innervation (S3) required less current for activation than the left. Stimulation using the upper 2/3 of the array (C1 to C6 and C8) could evoke a response of the left IAS innervation at lower amplitudes than the rest of the array. The left IAS innervation required the lowest stimulation amplitudes from the left part of the array (C1, C2, C4, and C7).

Stimulation using the lower 2/3 of the stimulation array (C4 to C10) required less current to activate the right S4 PSN than C1 to C3. The left PSN could only be activated using at C4 and C7 at 19 and 12 mA respectively.

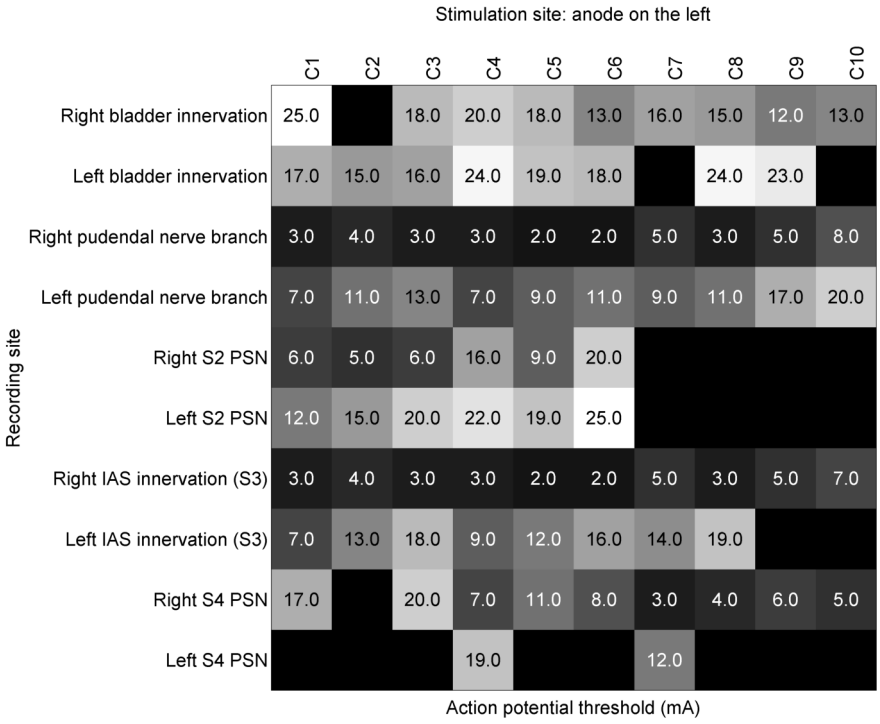

Figure 5.24 Amplitude thresholds needed to evoke neural activity during stimulation using all the contacts of the stimulation array versus anode lateral left. Each value depicts the minimal stimulation amplitude in mA that resulted in evoking an action potential within the simulated model. The darker the shade of gray, the lower the stimulation threshold. Pitch black depicts situations where no action potential was evoked by stimulation in range between 1 and 25 mA.

Anode 3: on the abdomen

Figure 5.25 depicts the threshold stimulation amplitudes at which action potentials could be recorded from the simulated autonomous innervation when using the anode placed on the abdomen.

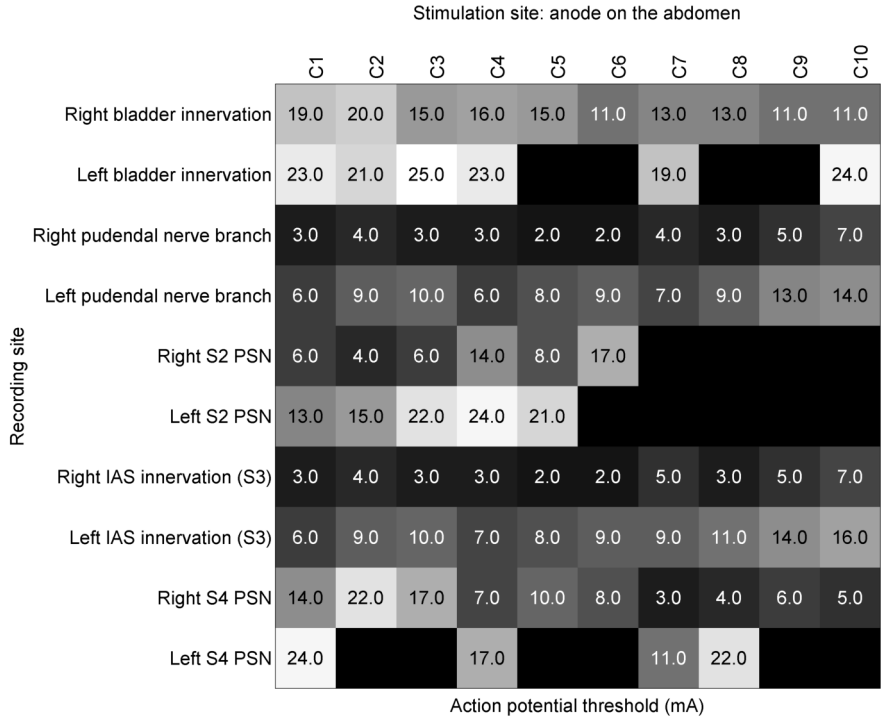

Figure 5.25 Amplitude thresholds needed to evoke neural activity during stimulation using all the contacts of the stimulation array versus anode on the abdomen. Each value depicts the minimal stimulation amplitude in mA that resulted in evoking an action potential within the simulated model. The darker the shade of gray, the lower the stimulation threshold. Pitch black depicts situations where no action potential was evoked by stimulation in range between 1 and 25 mA.

The right bladder innervation required less current to activate than the left (starting at 11 mA). The left bladder innervation could be activated using C7, C10 and the upper 1/3 of the stimulation array (C1 to C4).

The right pudendal nerve required less current to be activated (starting at 2 mA) than the left. Stimulation using the middle-right part of the array (especially C5, C6) required the least current to activate the right pudendal nerve.

The right S2 PSN required less current to activate than the left. Both of the nerves required the least amount of current when stimulating using the cranial part of the array (C1

to C4 for the right side and C1 and C2 for the left side). Stimulation using the caudal part of the array (C7 to C10) did not deliver any activation for the tested stimulation range.

The right IAS innervation (S3) required less current to be activated than the left (2 mA vs. 6 mA). Stimulation using the middle-right part of the array (especially C5 and C6) required the least current to activate the right IAS innervation. Cathodes C1, C5 and C7 required the least current to activate the left IAS innervation.

The right S4 PSN required less current to activate than the left (3 mA vs. 11 mA). The caudal part of the stimulation array (C4, C7 to C10) required the least current to activate the right S4 PSN. The left S4 PSN could only be activated using cathodes C1, C4, C7, and C8 with C7 being the electrode that required the least amount of current to activate the nerve.

Anode 4: in the anal canal

Figure 5.26 shows the threshold amplitudes at which an action potential could be recorded from the distal parts of the autonomous innervation during stimulation using electrode configurations involving the anode placed in the anal canal.

Left and right bladder innervation could be activated at similar stimulation amplitudes (14 to 15 mA). The right bladder innervation could be best activated using the middle-to-right part of the stimulation array. Stimulatin using the C4 and C7 cathodes required the highest intensity of current to evoke a response from the right bladder innervation. The upper right portion of the stimulation array (C1, C2, C3, C5, and C6) could evoke a response of the left bladder innervation at the lowest intensity of current.

The right pudendal nerve could be activated using a lower intensity of current (2 mA) than the left (5 mA). Stimulation using the upper-middle part of the stimulation array could evoke a response of the right pudendal nerve at lower current intensities. The left part of the stimulation array (C1 and C4) could activate the left pudendal nerve branch at lower intensities of current than the rest of the stimulation array.

The right S2 PSN required lower intensity of current to be activated than the left (4 mA vs. 11 mA). Both of the nerves could be activated only when using the upper part of the stimulation array (C1 to C6). Using the cathodes C1 and C2 required the least current to activate the right and left S2 PSN, respectively.

The right IAS innervation required less current to activate than the left (2 mA vs. 4 mA). The middle part of the stimulation array could evoke a response of the right IAS innervation using the lowest stimulation amplitude. The smallest activation threshold of the left IAS innervation could be achieved when stimulating using the left side of the stimulation array (C1, C4 and C7).

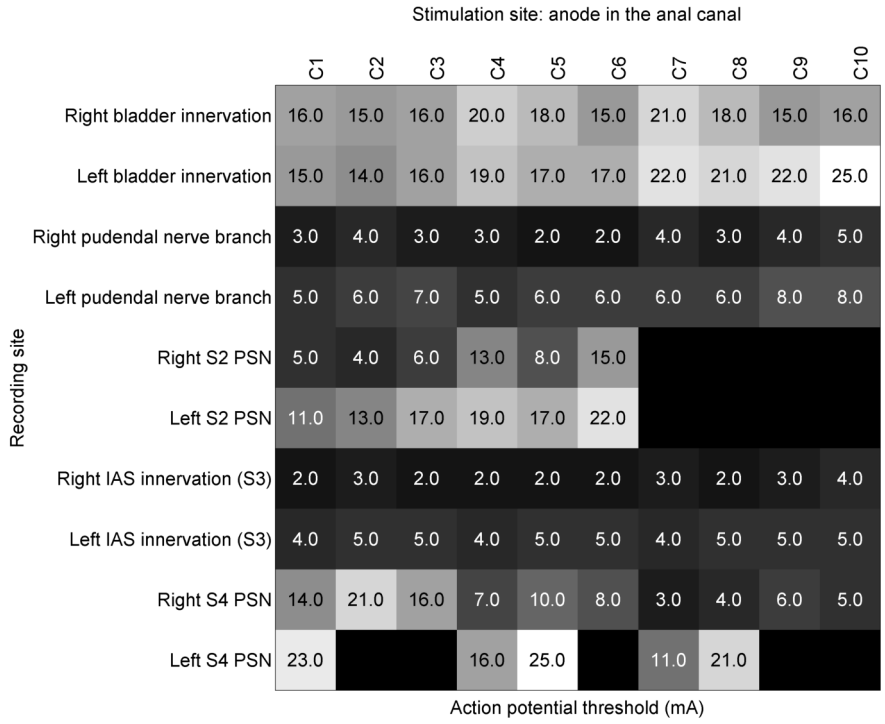

Figure 5.26 Amplitude thresholds needed to evoke neural activity during stimulation using all the contacts of the stimulation array versus anode in the anal canal. Each value depicts the minimal stimulation amplitude in mA that resulted in evoking an action potential within the simulated model. The darker the shade of gray, the lower the stimulation threshold. Pitch black depicts situations where no action potential was evoked by stimulation in range between 1 and 25 mA.

The right S4 PSN required smaller stimulation amplitudes to be activated than the left (3 mA vs. 11 mA). The lower part of the stimulation array (C4 and C6 to C10) proved to require the least stimulation current to activate the right S4 PSN. The left S4 PSN could be activated only using the left-to-middle part of the stimulation array (C1, C4, C5, C7, and C8).

5.2.4 Simulated membrane potential after nerve incision

The simulation of the membrane potential during transcutaneous electrical nerve stimulation after nerve incision (as described in Section 4.1.7 on page 36) was performed on the bladder and internal anal sphincter (IAS) innervation. The field projections derived for these nerves from the finite element simulations served as extracellular stimuli for nerve activation. Based on the input electrical field resulting from all forty electrode configurations during stimulation in the range between 1 and 25 mA, a time evolution of the membrane potential was obtained for these four nerve fibers. This resulted in a total of 4000 simulations. Figure 5.27 shows an example of the membrane potential recorded at the distal end of the right bladder innervation before and after the nerve incision for a range of 25 stimulation amplitudes. In this example, action potentials (APs) are evoked for stimulation amplitudes exceeding 16 mA only before the nerve incision. After the nerve incision, only stimulation artifacts are visible within the recorded membrane potentials. The threshold stimulation amplitudes at which an AP could be recorded at the distal ends of each simulated nerve served to help compare the data across the entire dataset of simulations (see Table 5.4).

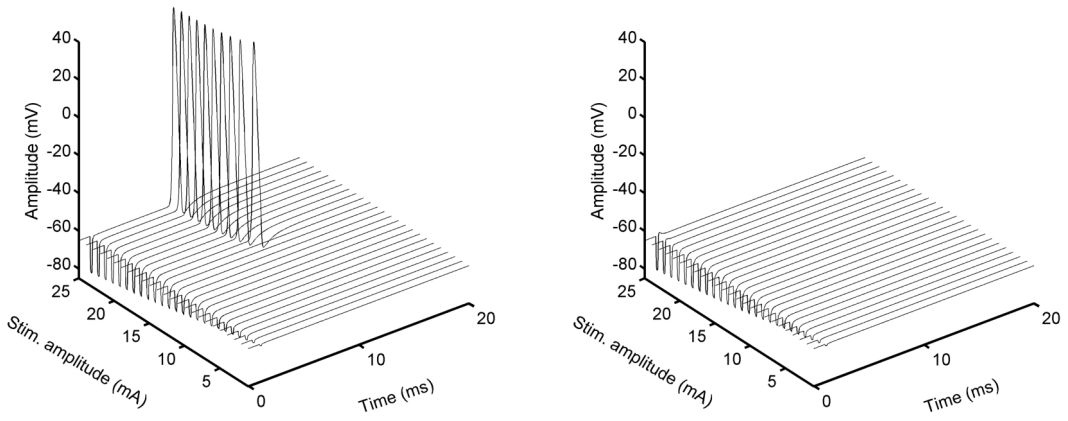

Figure 5.27 Simulated membrane potential recorded from the distal part of the right bladder innervation during transcutaneous stimulation using the anode placed on the right to the stimulation array and cathode 10 before (a) and after nerve incision (b). This simulation is a result of stimulation using 200 µs of pulse width and a range of stimulation amplitudes between 1 and 25 mA.

Table 5.4 Comparison of stimulation thresholds needed to evoke simulated neural activity during simulation using surface electrodes before and after nerve incision. Each value depicts the minimal stimulation amplitude in mA that resulted in evoking an action potential within the simulated model. The darker the shade of gray, the lower the stimulation threshold. Pitch black depicts situations where no action potential was evoked by stimulation in range between 1 and 25 mA. C1 to C10 refer to the cathodes within the stimulation array.

Stimulation threshold amplitudes (mA)

		Before nerve incision										After nerve incision									
		C1	C2	C3	C4	C5	C6	C7	C8	C9	C10	C1	C2	C3	C4	C5	C6	C7	C8	C9	C10
Anode right	Right bladder innervation	24.0	21.0							23.0	24.0		24.0								
	Left bladder innervation																				
	Right IAS innervation (S3)	3.0	4.0	3.0	3.0	2.0	3.0	5.0	3.0	6.0	10.0	3.0	4.0	3.0	3.0	2.0	3.0	5.0	3.0	6.0	10.0
	Left IAS innervation (S3)	6.0	9.0	11.0	7.0	9.0	10.0	9.0	12.0	16.0	18.0	6.0	9.0	11.0	7.0	9.0	10.0	9.0	11.0	15.0	16.0
Anode left	Right bladder innervation	25.0		18.0	20.0	18.0	13.0	16.0	15.0	12.0	13.0										
	Left bladder innervation	17.0	15.0	16.0	24.0	19.0	18.0		24.0	23.0		25.0	23.0								
	Right IAS innervation (S3)	3.0	4.0	3.0	3.0	2.0	2.0	5.0	3.0	5.0	7.0	3.0	4.0	3.0	3.0	2.0	2.0	5.0	3.0	5.0	7.0
	Left IAS innervation (S3)	7.0	13.0	18.0	9.0	12.0	16.0	14.0	19.0			7.0	14.0	19.0	9.0	12.0	17.0	14.0	20.0		
Anode abdomen	Right bladder innervation	19.0	20.0	15.0	16.0	15.0	11.0	13.0	13.0	11.0	11.0	19.0	18.0	21.0		24.0	24.0				
	Left bladder innervation	23.0	21.0	25.0	23.0			19.0			24.0	21.0	20.0	23.0		25.0	25.0				
	Right IAS innervation (S3)	3.0	4.0	3.0	3.0	2.0	2.0	5.0	3.0	5.0	7.0	3.0	4.0	3.0	3.0	2.0	2.0	5.0	3.0	5.0	7.0
	Left IAS innervation (S3)	6.0	9.0	10.0	7.0	8.0	9.0	9.0	11.0	14.0	16.0	6.0	9.0	10.0	6.0	8.0	9.0	9.0	10.0	14.0	15.0
Anode intra-anal	Right bladder innervation	16.0	15.0	16.0	20.0	18.0	15.0	21.0	18.0	15.0	16.0	14.0	13.0	15.0	19.0	17.0	17.0	21.0	21.0	23.0	
	Left bladder innervation	15.0	14.0	16.0	19.0	17.0	17.0	22.0	21.0	22.0	25.0	14.0	13.0	15.0	18.0	16.0	16.0	20.0	19.0	20.0	24.0
	Right IAS innervation (S3)	2.0	3.0	2.0	2.0	2.0	2.0	3.0	2.0	3.0	4.0	2.0	3.0	3.0	2.0	2.0	2.0	3.0	3.0	3.0	4.0
	Left IAS innervation (S3)	4.0	5.0	5.0	4.0	5.0	5.0	4.0	5.0	5.0	5.0	4.0	5.0	5.0	4.0	5.0	5.0	5.0	5.0	5.0	6.0

Additionally, to elucidate the possible differences in the recorded signals, stimulation ranges at which an AP could be identified – i.e. an AP was only present before and not after the nerve incision – were derived from the results for every electrode configuration. These were juxtaposed with the windows obtained for DNS and are depicted in Section 5.3.2 on page 88 (see Figures 5.30 to 5.33). As in the case of DNS, three distinct cases could be identified within the datasets:

1. Nerve incision **completely prohibited the conduction of APs** along the nerve fiber, which resulted in a lack of recordable AP at the distal end of a given nerve for stimulation amplitudes exceeding a threshold value.

2. Nerve incision prohibited the conduction of APs **only for a specific range of current intensities.**

3. Nerve incision **did not affect the conduction of APs** along a given nerve fiber.

Table 5.5 summarizes the effect of nerve damage on the conduction of action potentials for different stimulation electrode configurations during TENS. There was a total of 33 cases for which the nerve damage could be identified either in the left or the right bladder innervation. There were only 14 such cases for the left and right IAS innervation. Within those cases, there was no range of stimulation amplitudes that would be sensitive to nerve damage for all nerves, regardless of the electrode configuration. The ranges varied greatly depending on the electrode configuration and the considered nerve. For each anode, there were cathode configurations that exhibited sensitivity to nerve damage simultaneously for the left and right bladder innervation. These configurations exhibited nerve damage sensitivity for the same stimulation intensity ranges. In most electrode configurations, the ranges of stimulation intensity were narrow – 1 to 2 mA of width. These configurations are listed in Table 5.6. Disappointingly, the same effect could not be reproduced in the case of IAS innervation: no electrode configuration exhibited a window of stimulation amplitudes that would enable to simultaneously identify damage within both left and right IAS innervation.

5.3 Differences in stimulation selectivity and sensitivity to nerve damage depending on stimulation method

This section ponders the questions regarding the stimulation selectivity and sensitivity to nerve damage of transcutaneous and direct nerve stimulation methods.

Table 5.5 Summary of nerve damage effect on the AP conduction with regard to the used stimulation electrode configurations. Legend: IAS – internal anal sphincter, AP – action potential.

Effect on AP conduction	Anode	Cathodes	Related innervation
Complete inhibition	right	C10	right bladder innervation
	left	C4, C7, C10	right bladder innervation
		C7, C10	left bladder innervation
	on the abdomen	C3 to C10	right bladder innervation
		C4 to C6, C8, C9	left bladder innervation
	in the anal canal	C1, C9, C10	right bladder innervation
Partial inhibition	right	C1 to C6, C8, C9	right bladder innervation
		C1 to C10	left bladder innervation
		C3, C8	right IAS innervation
		C7, C10	left IAS innervation
	left	C1 to C3	left bladder innervation
		C1, C2, C3, C5, C6	right bladder innervation
		C4, C8, C10	right IAS innervation
	on the abdomen	C1, C2	left IAS innervation
		C2, C3, C7, C9	right IAS innervation
	in the anal canal	C2	right bladder innervation
		C8 to C10	left IAS innervation
No effect	right	C7	right bladder innervation
		C1, C2, C4 to C7, C9, 10	right IAS innervation
		C1 to C6, C8, C9	left IAS innervation
	left	C1	right bladder innervation
	on the abdomen	C8, C9	left bladder innervation
		all	right IAS innervation
		C1 to C3, C5 to C7, C9	left IAS innervation
	in the anal canal	C2	right bladder innervation
		C7, C10	left bladder innervation
		all	right IAS innervation
		C1, C4, C5, C7, C9, C10	left IAS innervation

Table 5.6 Electrode configurations for which stimulation amplitude windows exhibit sensitivity to nerve damage for the left and right bladder innervation simultaneously.

Anode	Cathodes	Amplitude window
right	C1	14 mA
	C2	13 mA
	C3	14 mA
	C6	16 mA
	C8	19 to 20 mA
	C9	20 to 21 mA
	C10	24 mA
left	C4	25 mA
	C7	19 to 25 mA
	C10	24 to 25 mA
on the abdomen	C3	18 to 25 mA
	C4	24 to 25 mA
	C6	18 to 25 mA
	C8	24 to 25 mA
	C9	23 to 25 mA
in the anal canal	-	-

5.3.1 Stimulation selectivity

The comparison of the stimulation selectivity is based on the fact which and how many different nerve fibers get excited during direct and transcutaneous electrical nerve stimulation. The stimulation threshold amplitudes already derived in Section 5.1.3 (page 56) and 5.2.3 (page 74) serve as the basis for the analysis. Figure 5.28 compares the threshold stimulation amplitudes at which an action potential can be evoked and recorded from the distal parts of the simulated nerve fibers. The comparison regards direct and transcutaneous electrical nerve stimulation (given the example of the electrode configurations which involved the anode placed on the left side) before nerve incision.

By comparing both of the tables one can quickly observe that direct nerve stimulation was more effective at stimulating single nerves. Within the tested stimulation range (1 to 25 mA), stimulating the PSN resulted in excitement of only single nerves. This holds true for the left and right S2 PSN and both of the hypogastric nerves. However, increasing the stimulation amplitude resulted in the excitement of additional nerve structures when stimulating the right S3 PSN, the left S4 PSN, and the right S4 PSN. For high stimulation amplitudes, the electric field spreaded to the neighboring tissues, because all the simulated tissues are modeled as closed volume conductors. Thus, the current can spread in all directions (of course taking

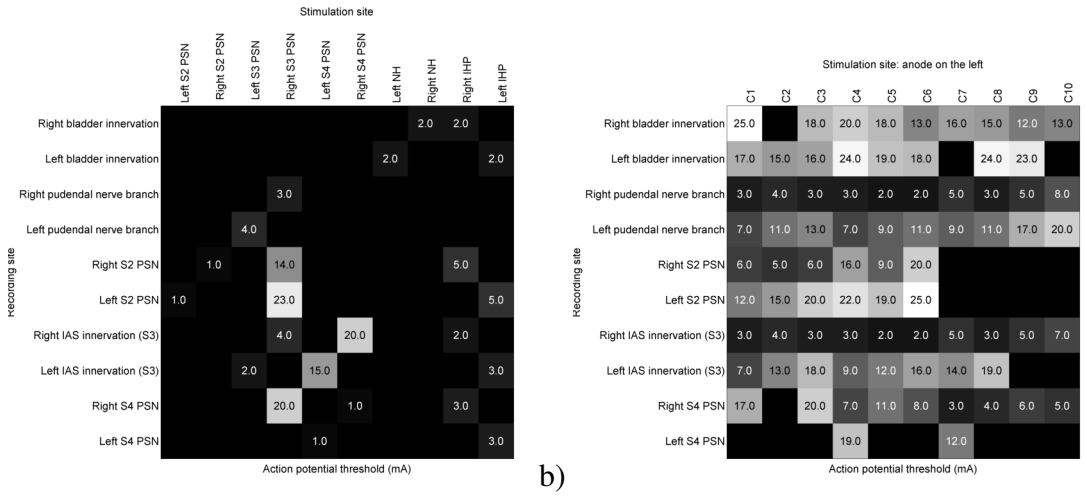

Figure 5.28 Comparison of direct (DNS) and transcutaneous nerve stimulation (TENS) in terms of stimulation selectivity: a) simulated DNS, b) simulated TENS for the anode placed lateral right to the stimulation array. Legend: NH – hypogastric nerve, IHP – inferior hypogastric plexus, PSN – pelvic splanchnic nerve.

into account the inhomogeneity of tissue conductivity). This resulted in the delivery of sufficient current to the neighboring nerves and their excitement.

Stimulation of the IHP during DNS evoked a response of all nerve structures that intersected within the plexus. The close proximity of several nerve fibers to the same stimulation site allowed for building a sufficient electrical field that resulted in the excitement of all the intersecting nerves.

With regard to transcutaneous electric stimulation, one can observe that for almost all electrode configurations, the excitement of every simulated nerve fiber is possible. The higher the stimulation amplitude, the more nerves were activated. One can observe in the dataset that the selection of electrode configuration determined which nerves were excited.

Moreover, transcutaneous stimulation exhibited side selectivity, in that the nerves on the right side (ipsilateral to the stimulation array) required a significantly smaller stimulation amplitude ($p < 0.001$) than the nerves on the left side (see Figure 5.29) regardless of the selected anode. This correlated with the side of placement of the stimulation array (right side).

5.3.2 Sensitivity to nerve damage

Sensitivity to nerve damage was analyzed based on the identified ranges of stimulation amplitudes for which an action potential could be recorded only before the simulated nerve

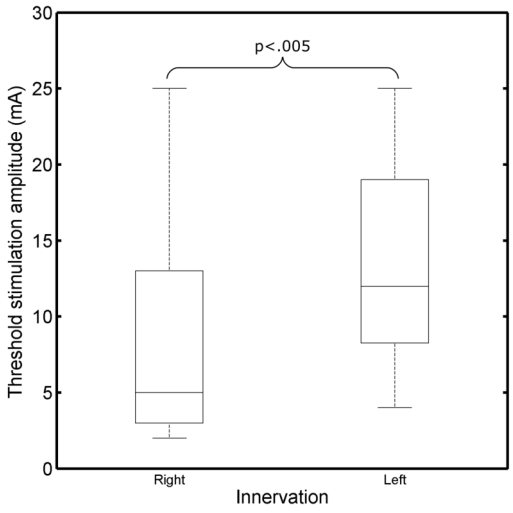

Figure 5.29 Comparison of threshold stimulation amplitudes needed to excite the nerves during transcutaneous stimulation. All the nerves were divided into two groups based on their position relative to the sagittal plane: left and right innervation. A Wilcoxon ranked sum test showed significant difference between the two groups ($p = 1.27 \times 10^{-14}$).

incision. Results for all stimulation sites simulated during DNS and all electrode configurations simulated during TENS were juxtaposed for each nerve.

Figure 5.30 shows the stimulation amplitude ranges signifying sensitivity to damage of the right bladder innervation during DNS and TENS. The stimulation threshold at which the nerve damage could be identified was lowest for the DNS of the right hypogastric nerve and the right IHP (both 2 mA) and spanned over a wide window of at least 15 mA of width. A similar result could be observed for TENS using anode on the left (2) and on the abdomen (3) for nine cathode positions. The lowest part of the stimulation array (i.e. cathodes no. 9 and 10) delivered the widest stimulation windows of nerve damage sensitivity. Although the anodes placed lateral right (1) and inside the anal canal (4) also delivered stimulation windows of nerve damage sensitivity, identifying nerve damage required more current and was possible for fewer cathode configurations.

Figure 5.31 shows the stimulation amplitude ranges signifying sensitivity to nerve damage of the left bladder innervation during DNS and TENS. DNS of the left hypogastric nerve and left IHP required the smallest current intensity (2 mA) to allow nerve damage identification: TENS required at least 13 mA. DNS also exhibited the widest windows of sensitivity to nerve damage (at least 17 mA). Electrode configurations of TENS involving the anode placed on the abdomen (3) exhibited the widest windows (as for TENS) of sensitivity to nerve damage. TENS involving the anode placed on the right (1) and on the left (2) exhibited

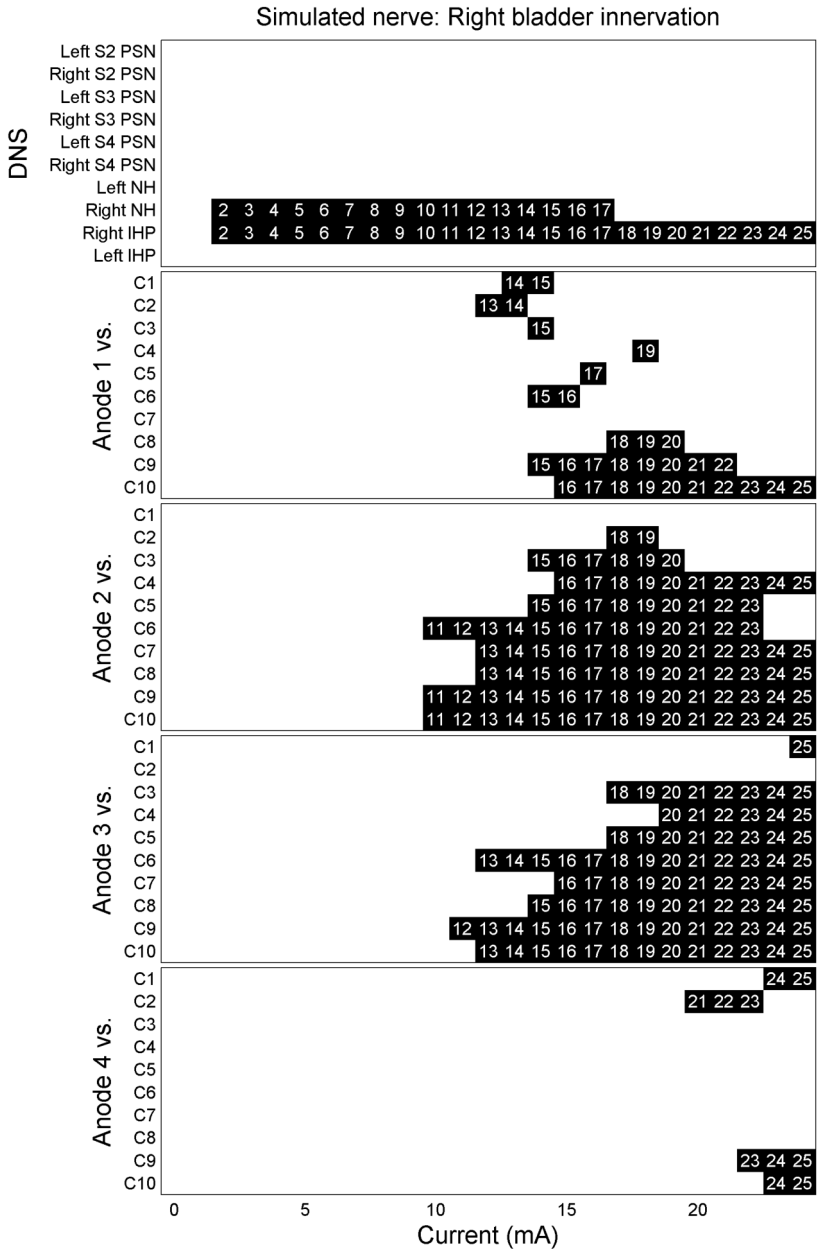

Figure 5.30 Comparison of all direct nerve stimulation sites and transcutaneous electrical nerve stimulation electrode configurations in terms of sensitivity to the damage to the right bladder innervation. Black boxes symbolize the stimulation amplitudes for which a nerve reaction resulted from stimulation only before the nerve incision. The stimulation amplitudes are additionally depicted within the black boxes as white text for more clarity. Legend: NH – hypogastric nerve, IHP – inferior hypogastric plexus, PSN – pelvic splanchnic nerve, C1-C10 – cathodes no. 1 to 10. Anode positions: right (1), left (2), abdominal (3), transanal (4).

narrower windows. The intraanal anode (4) proved insensitive to the damage of left bladder innervation.

Figure 5.32 shows the stimulation amplitude ranges signifying sensitivity to nerve damage of the right IAS innervation stemming from the S3 sacral nerve root. Sensitivity to nerve damage of this specific nerve could be identified during DNS of the right IHP and only for two electrode configuration during TENS: anode on the right (1) vs cathode no. 3 and 8. Although the stimulation threshold at which the nerve damage could be identified was identical in all three cases (2 mA), DNS of the right IHP still maintained this sensitivity over a wider range of stimulation amplitudes, whereas in the case of TENS the range was only 1 mA wide. Other electrode configurations involving the use of anode on the left (2), on the abdomen (3) and in the anal canal (4) proved insensitive to nerve damage regardless of the used cathode.

Figure 5.33 shows the stimulation amplitude ranges signifying sensitivity to nerve damage of the left IAS innervation stemming from the left S3 sacral nerve root. DNS of the left S3 PSN over a range of stimulation amplitudes between 2 and 4 mA as well as DNS of the left IHP over a range between 3 and 20 mA proved sensitive to the damage of the left IAS innervation. All twelve cases of nerve damage sensitivity during TENS exhibited very narrow stimulation windows - predominantly 1 mA and 2 mA for stimulation using the intra-anal anode (4) versus cathode no. 10.

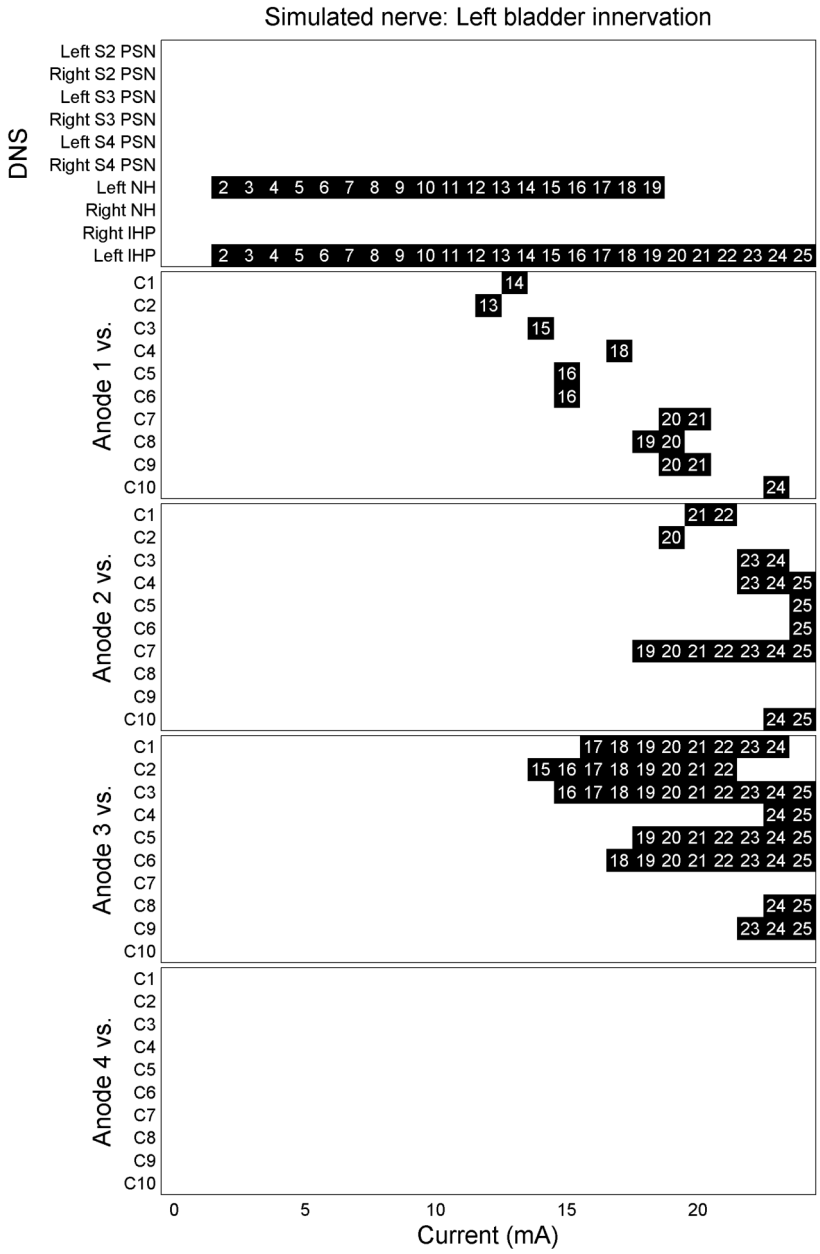

Figure 5.31 Comparison of all direct nerve stimulation sites and transcutaneous electrical nerve stimulation electrode configurations in terms of sensitivity to the damage to the left bladder innervation. Black boxes symbolize the stimulation amplitudes for which a nerve reaction could be observed only before the nerve incision. The stimulation amplitudes are additionally depicted within the black boxes as white text for more clarity. Legend: NH – hypogastric nerve, IHP – inferior hypogastric plexus, PSN – pelvic splanchnic nerve, C1-C10 – cathodes no. 1 to 10. Anode positions: right (1), left (2), abdominal (3), transanal (4).

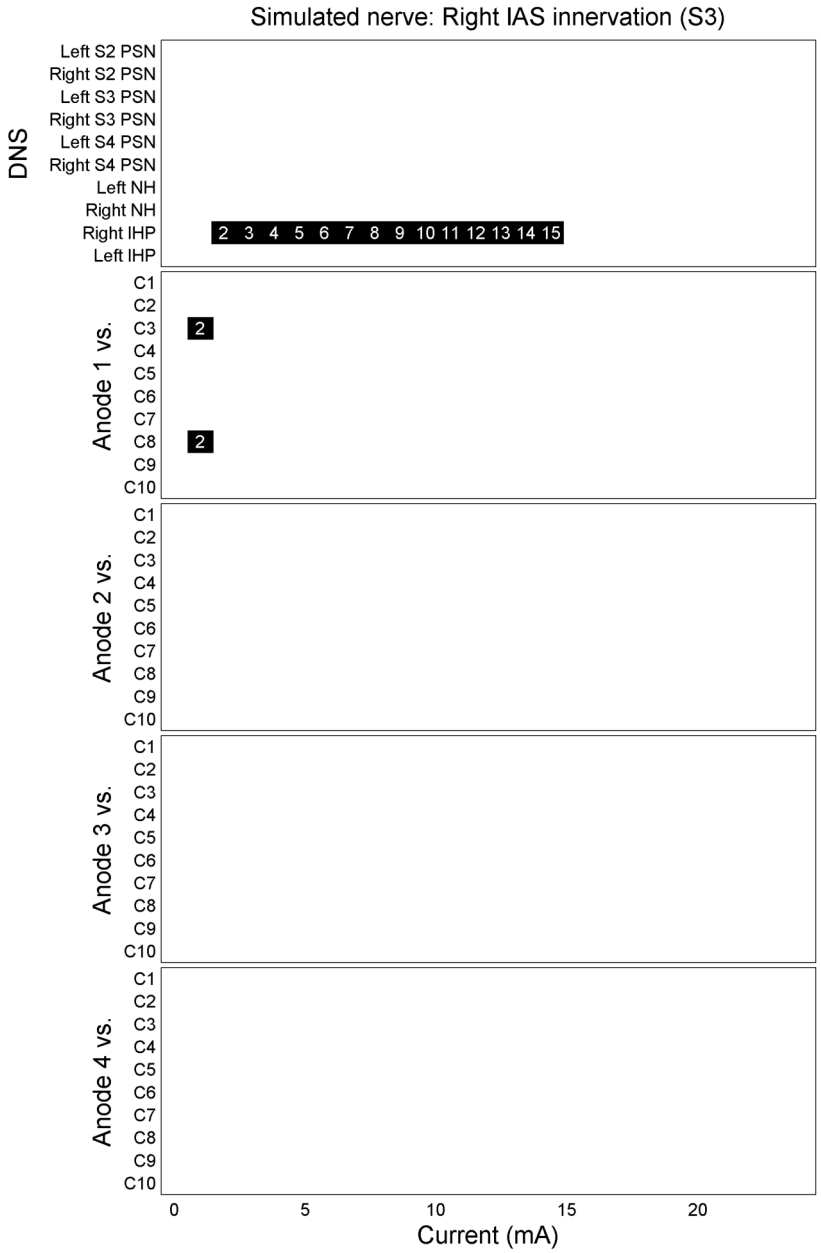

Figure 5.32 Comparison of all direct nerve stimulation sites and transcutaneous electrical nerve stimulation electrode configurations in terms of sensitivity to the damage to the right IAS innervation (S3). Black boxes symbolize the stimulation amplitudes for which a nerve reaction resulted from stimulation only before the nerve incision. The stimulation amplitudes are additionally depicted within the black boxes as white text for more clarity. Legend: NH – hypogastric nerve, IHP – inferior hypogastric plexus, PSN – pelvic splanchnic nerve, C1-C10 – cathodes no. 1 to 10. Anode positions: right (1), left (2), abdominal (3), transanal (4).

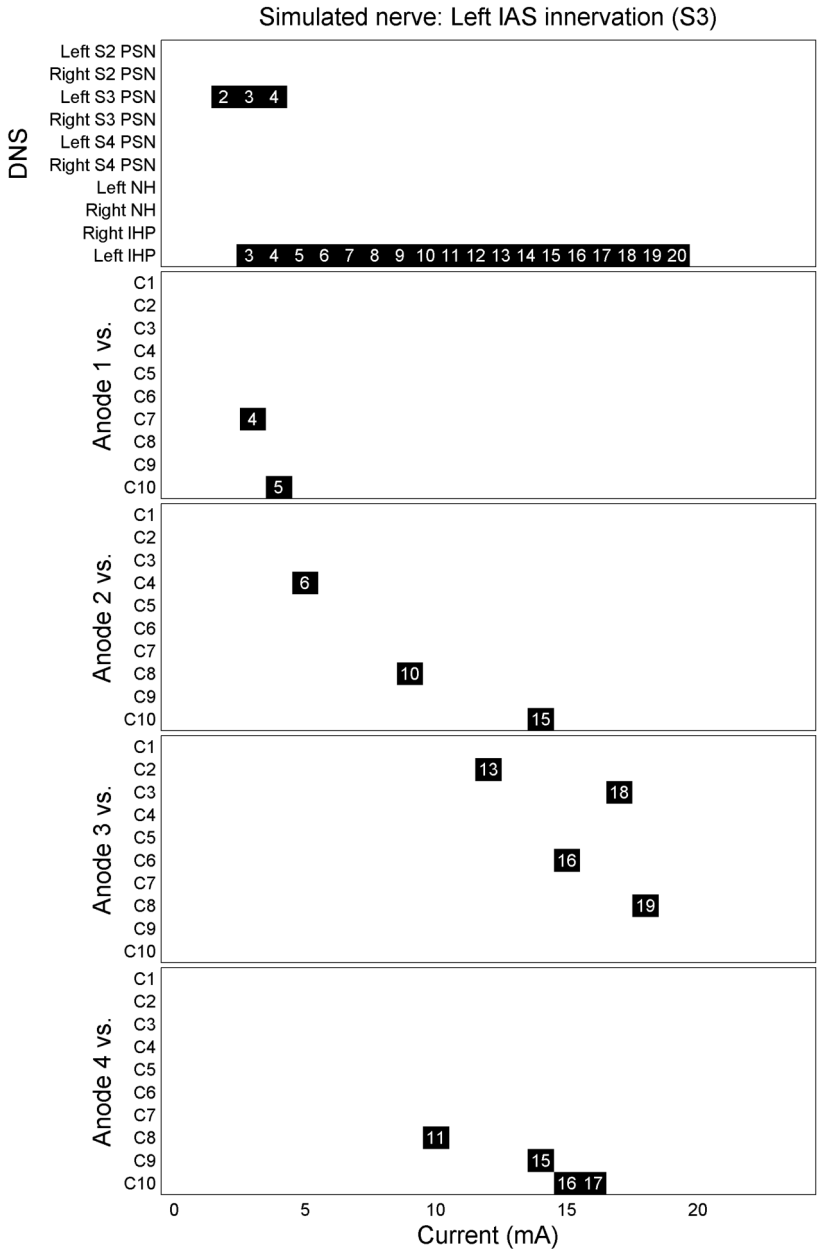

Figure 5.33 Comparison of all direct nerve stimulation sites and transcutaneous electrical nerve stimulation electrode configurations in terms of sensitivity to the damage to the left IAS innervation (S3). Black boxes symbolize the stimulation amplitudes for which a nerve reaction resulted from stimulation only before the nerve incision. The stimulation amplitudes are additionally depicted within the black boxes as white text for more clarity. Legend: NH – hypogastric nerve, IHP – inferior hypogastric plexus, PSN – pelvic splanchnic nerve, C1-C10 – cathodes no. 1 to 10. Anode positions: right (1), left (2), abdominal (3), transanal (4).

5.4 Activity of the internal anal sphincter during pelvic intraoperative neurophysiological monitoring

This section describes the results obtained from DNS and TENS of the autonomous nervous system performed during the animal experiments described in Section 4.2.

5.4.1 Analysis of processed signals during direct nerve stimulation

For every direct stimulation of the IHP, EMG signals of the IAS were recorded following lower anterior rectal resection, after a proximal incision of the IHP, and after a distal incision of the IHP. Each stimulation lasted at least 5 seconds.

Across all specimens, a stimulation-induced increase of the amplitude in the processed EMG (band-pass filtration between 5 and 25 Hz) of the IAS was present after the rectal resection and after the first incision cranial to the stimulation site (see Figure 5.34). This was qualitatively evident from intraoperative and offline analysis of the processed EMG signals. The stimulation performed after the second incision resulted in no visible amplitude increase which indicated a successful blockade of the autonomous neural pathway between the IHP and the IAS.

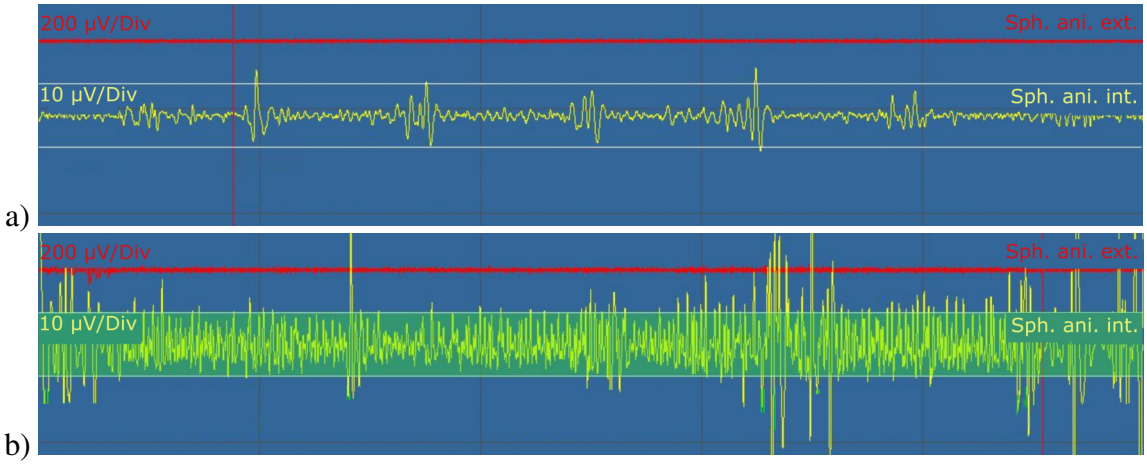

Figure 5.34 Screenshots of intraoperative measurement of the activity of the internal (green) and external anal sphincters (red) during rest (a) and during stimulation of the left inferior hypogastric plexus (b). An increase of signal amplitude is visible during stimulation. The signals were displayed online using NeuroExplorer v5.1 (inomed Medizintechnik GmbH). Time scale: 3.2 s/div.

5.4.2 Analysis of processed signals during transcutaneous electrical nerve stimulation

Signals recorded during TENS were obtained from each specimen in five experimental phases:

Phase 1: Specimens in prone position

Phase 2: Specimens in supine position

Phase 3: After rectal resection

Phase 4: After skeletal muscle relaxation

Phase 5: After bilateral nerve incision

Four needle electrode recordings of the IAS activity were acquired during each phase. Each recording contained ten 10-second periods of electrical stimulation and ten 10-second inter-stimulation rest intervals. Each stimulation was delivered by one of the ten cathodes constituting the stimulation array. This yielded a total of 1000 stimulation cases:

$$(4 \text{ anode positions}) \times (10 \text{ cathode positions}) \times (5 \text{ specimens}) \times (5 \text{ experimental phases})$$

Figure 5.35 shows an example of the signals acquired intraoperatively during TENS. A qualitative analysis of the processed EMG showed that, regardless of the used electrode configuration and experimental phase, the signals exhibited an amplitude increase during stimulation. Based on the processed EMG, no correlation between the amplitude of the signals, bilateral nerve incision, and injection of muscular relaxant could be determined.

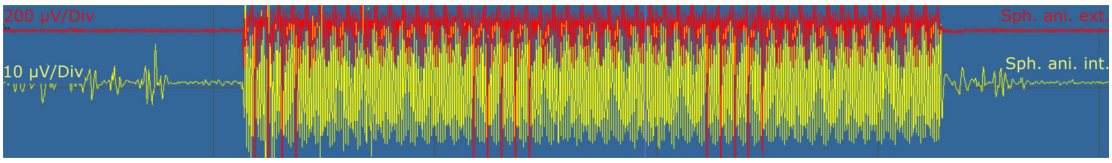

Figure 5.35 An example recording during a ten second stimulation using the surface electrodes. The red curve depicts the external anal sphincter (EAS) and the green curve depicts the internal anal sphincter electromyography. An amplitude increase can be observed for both signals. Stimulation artifacts were present within the EAS signal. The signals were displayed online using NeuroExplorer v5.1 (inomed Medizintechnik GmbH). Time scale: 3.2 s/div.

5.4.3 Analysis of raw electromyographic signals during direct nerve stimulation

In order to investigate the occurrence of stimulation artifacts, I analyzed the raw EMG signals corresponding to the filtered recordings during DNS of the IHP.

Initial qualitative analysis showed that the unfiltered signals contained the presence of stimulation artifacts in all recordings. However, the recordings obtained from the initial direct stimulation of the IHP and the stimulation after proximal nerve incision contained another type of activity as well: evoked potentials occurring at a reproducible latency. These potentials were to be found in every specimen, although their shape, amplitude and latency varied from specimen to specimen and from stimulation site to stimulation site. Figure 5.36 shows an example of unfiltered signals averaged over the stimulation window (an average of 330 recording windows, each 33 ms long). The shape and amplitude of the recorded evoked potentials depended on the phase of the experiment.

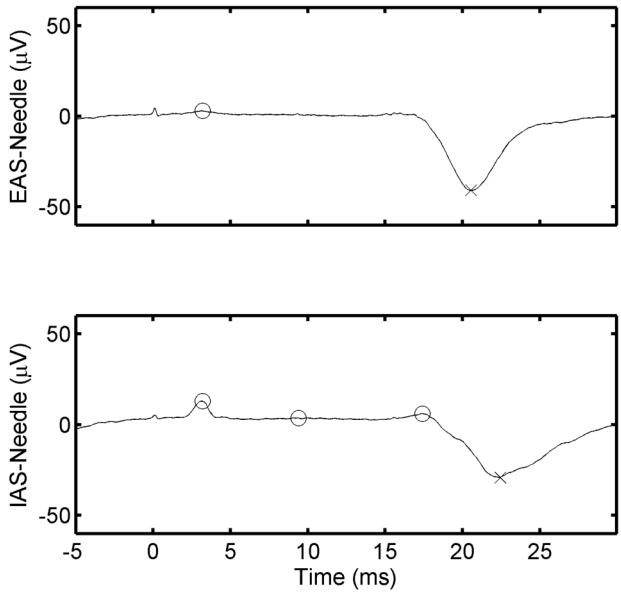

Figure 5.36 Averaged signal recorded from the external (EAS) and internal anal sphincters (IAS) during direct nerve stimulation of the left inferior hypogastric plexus. The signal is an average of 330 recording windows. Peaks with a latency of approximately 4 ms and valleys with a latency of approximately 23 ms could be identified in the signals. Legend: x — valleys, o — peaks, IAS – internal anal sphincter, EAS – external anal sphincter.

5.4.4 Sensitivity of direct nerve stimulation to detecting nerve damage

The raw signals exposed a correlation between the presence of evoked potentials and the integrity of the IHP. Figure 5.37 shows an example of the averaged signals acquired before incision, after the proximal incision, and after the distal nerve incision. In this particular example, the evoked potentials are visible only within the first two phases. Figure 5.38 shows the extracted maximal peak-to-peak amplitude for every averaged signal for all five specimens. An amplitude increase occurred after the proximal nerve incision (between the stimulation site and away from the effector muscle). After the second incision, the potentials either disappeared entirely or their amplitude dropped to approximately 5 µV. Similar recordings could be observed in both the needle placed inside the autonomously innervated IAS and the needle inside the somatically innervated EAS.

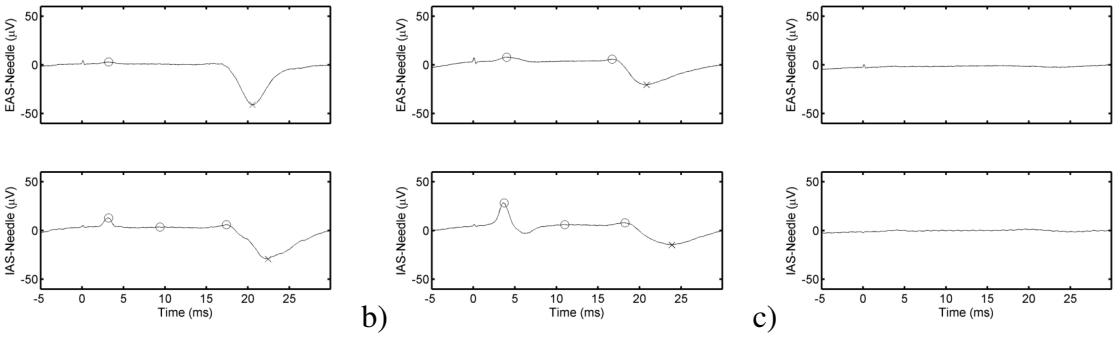

Figure 5.37 Averaged signals recorded from the external (EAS) and internal anal sphincters (IAS) during direct nerve stimulation of the left inferior hypogastric plexus. Signals were recorded during three phases: a) before nerve incision, b) after proximal nerve incision, and c) after distal nerve incision. The signals are an average of 330 recording windows. A stimulation artifact is to be seen at 0 ms for each phase. Legend: x – valleys, o – peaks.

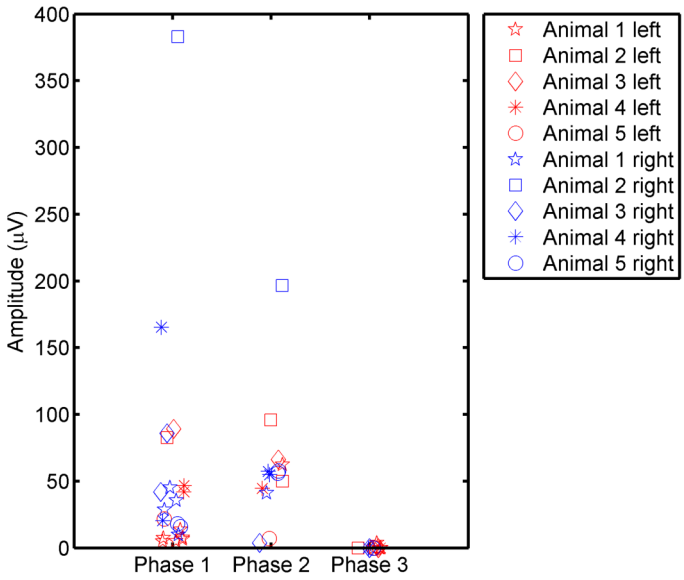

Figure 5.38 Maximal peak-to-peak amplitude recorded from the averaged signals from the internal anal sphincter during three phases of direct nerve stimulation. Phase 1: before nerve incision, Phase 2: after proximal nerve incision, and Phase 3: after distal nerve incision

5.4.5 Analysis of raw electromyographic signals during transcutaneous electrical nerve stimulation

Qualitative analysis of the raw signals acquired during TENS confirmed the presence of stimulation artifacts (see Figure 5.39).

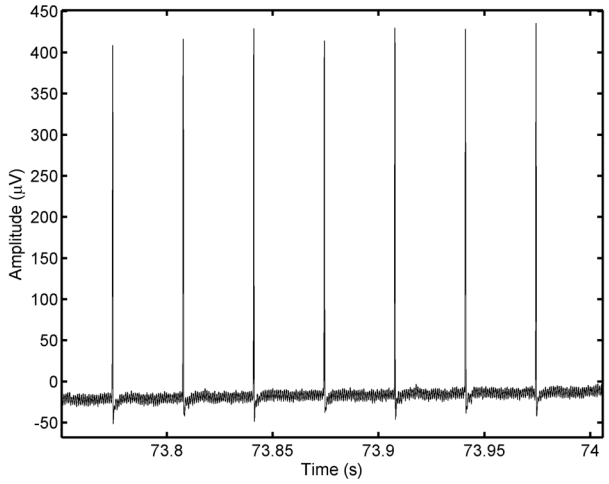

Figure 5.39 Stimulation artifacts in the unfiltered signals recorded during stimulation using the surface electrodes (cathode 5 vs. anode on the right side of the back, specimen 1).

Moreover, the recordings corresponding to specific electrode configurations contained additional activity within the signal of the IAS and EAS (see Figure 5.40) resembling the potentials evoked during DNS. The evoked potentials could be observed in 422 from a total of 1000 stimulation cases tested across five specimens in five experimental phases. A different number of local extrema could be observed across all the specimens (see Figure 5.41). Specimens 1 and 2 exhibited no significant differences in the number of local extrema across all electrode configurations and experimental phases ($p < 0.001$). No significant difference could be also observed between Specimens 4 and 5 ($p < 0.001$). The signals acquired from Specimens 4 and 5 contained significantly more local extrema than Specimens 1 and 2 ($p < 0.001$). The highest number of local extrema could be observed in Specimen 3.

Figure 5.40 a) Recordings acquired from bipolar needle electrodes inserted into the external and internal anal sphincter during transcutaneous electrical nerve stimulation using ten anode-cathode configurations. Each plot depicts a signal of 33 ms duration averaged over 330 pulses (10 seconds) with 5 ms visible prior the stimulation. Both channels show increased activity after each pulse for stimulations using cathodes 7 through 10 after the stimulation artifact. Legend: x – valleys, o – peaks. b) Stimulation electrode configuration for the recordings. b) The recordings were acquired during stimulation using cathode 1 through 10 vs. anode on the right side ofo the back in Specimen 3.

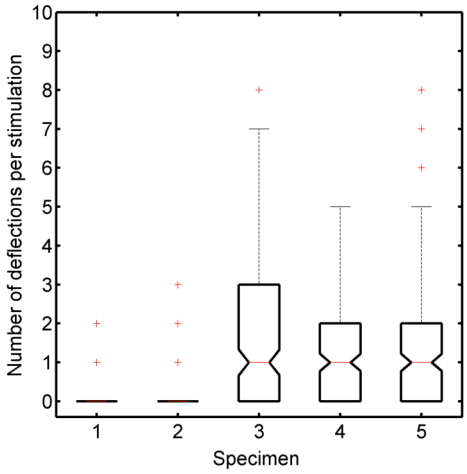

Figure 5.41 Number of local extrema extracted from each measurement during TENS for all specimens.

Figure 5.42 contains the number of local extrema identified within the signals acquired from Specimen 1 and 2 for all experimental phases, assorted according to the used anode. In this case, the anode 4 (in the anal canal) yielded the most local extrema compared to the other anodes. There was no significant difference in the number of local extrema for all cathodes, when stimulating against anode 4. For anodes 1, 2 and 3, cathode 10 yielded significantly more local extrema than all the other cathodes ($p < 0.001$, see Figure 5.43a); no significant differences were observed between the number of local extrema for the remaining cathodes and they yielded almost no local extrema ($p = 0.113$). For anode 4, no significant differences between all used cathodes could be observed ($p = 0.495$, see Figure 5.43b), however, they yielded at least one deflection.

The boxplot depicted in Figure 5.44 contains the number of local extrema identified within Specimen 4 and 5. There were no significant differences between anodes 1, 2 and 3 ($p < 0.001$); there were more local extrema for anode 4 than for the rest of the anodes. For anodes 1, 2 and 3, significant differences were identified when considering the different cathodes ($p < 0.001$, see Figure 5.45a). For anode 4, no significant differences were identified between the signals obtained for the different cathodes ($p = 0.903$, see Figure 5.45b).

The number of local extrema obtained from the signals from Specimen 3 differed significantly ($p < 0.001$), when compared across the different anodes (see Figure 5.46). Anode 1, 2 and 3 delivered comparably similar numbers of local extrema ($p = 0.006$); anode 4 delivered significantly more local extrema than all the other anodes ($p < 0.001$). For anodes 1, 2 and 3, significant differences were identified when considering the different cathodes ($p < 0.001$, see Figure 5.47a). For anode 4, no significant differences were identified between the signals

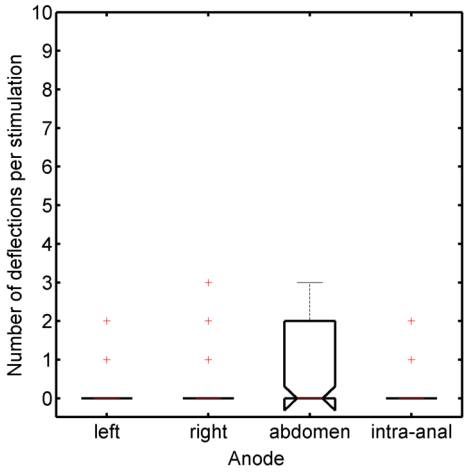

Figure 5.42 Number of local extrema extracted from each measurement during TENS for specimens 1 and 2. The results were assorted according to the used anode.

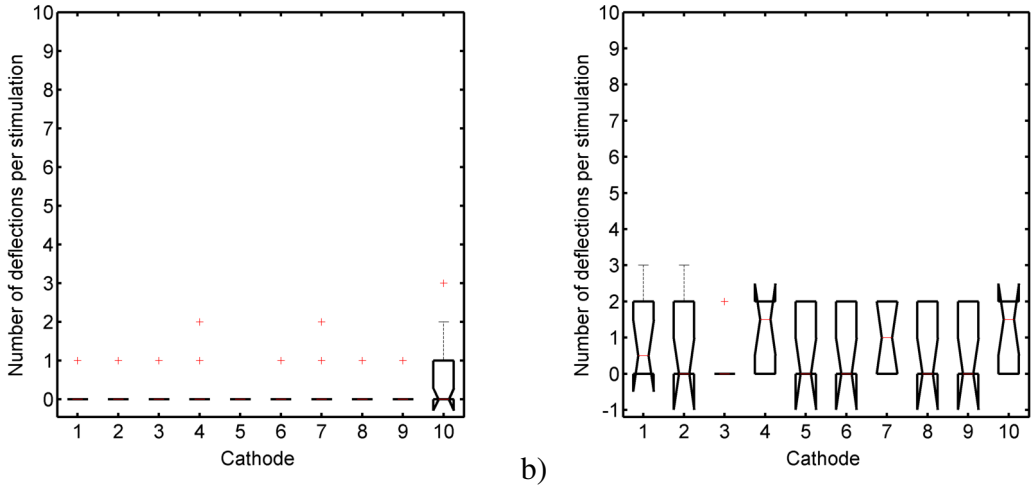

Figure 5.43 Number of local extrema extracted from each measurement during TENS for specimens 1 and 2 assorted according to the used cathode: a) local extrema extracted from anodes 1, 2 and 3, b) local extrema extracted from anode 4.

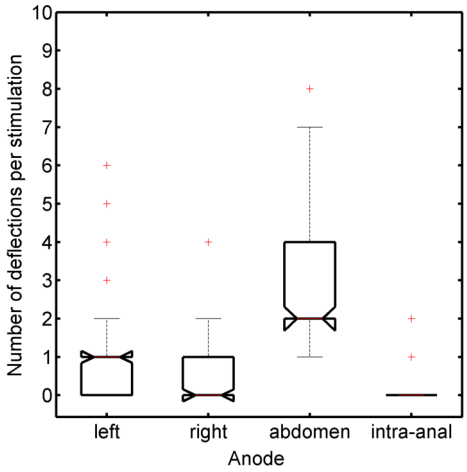

Figure 5.44 Number of local extrema extracted from each measurement during TENS for specimens 4 and 5. The results were assorted according to the used anode.

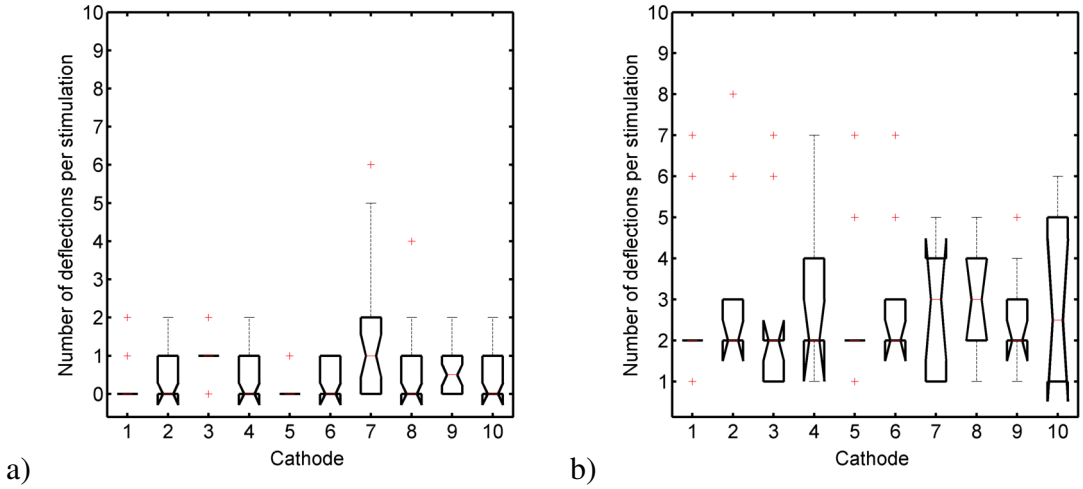

Figure 5.45 Number of local extrema extracted from each measurement during TENS for specimens 4 and 5 assorted according to the used cathode: a) local extrema extracted from anodes 1, 2 and 3, b) local extrema extracted from anode 4.

obtained for the different cathodes ($p = 0.002$, see Figure 5.47b).

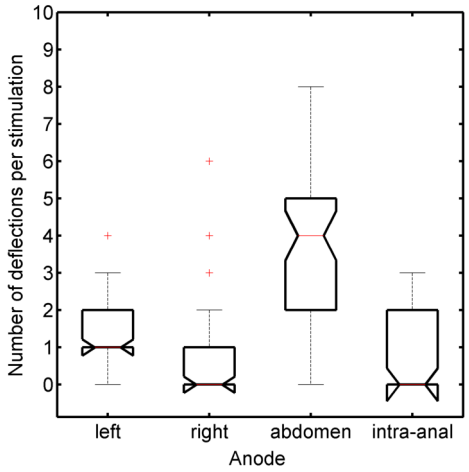

Figure 5.46 Number of local extrema extracted from each measurement during TENS for Specimens 3. The results were assorted according to the used anode.

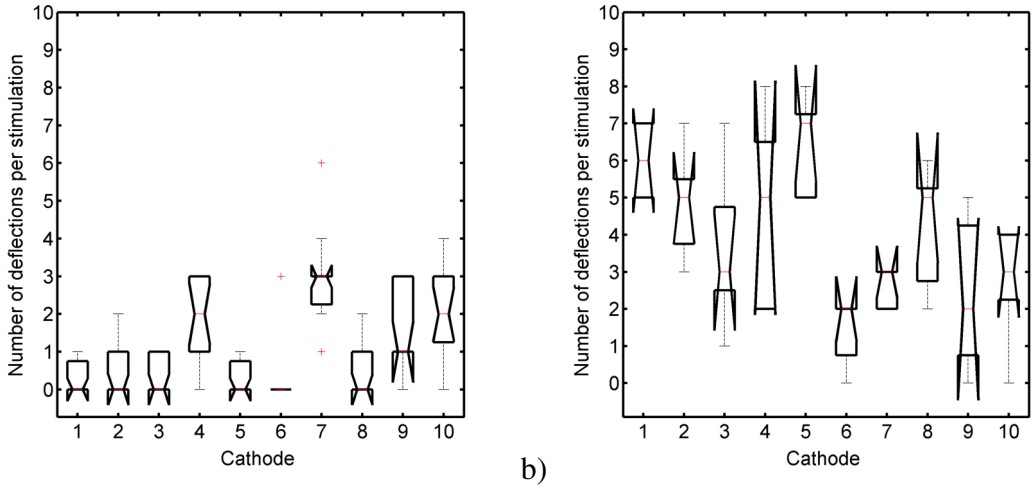

Figure 5.47 Number of local extrema extracted from each measurement during TENS for Specimen 3 assorted according to the used cathode: a) local extrema extracted from anodes 1, 2 and 3, b) local extrema extracted from anode 4.

For each measurement, peaks and valleys of the identified evoked potentials were extracted. Across the entire population of signals, the latencies formed distinct groups (see Figure 5.48). The extracted amplitudes corresponding to the peaks and valleys served to create scatter plots (as depicted in Figure 5.49) to identify any patterns and changes within the latencies and amplitudes of local extrema of the evoked potentials. Comparing the

latencies and amplitudes for the five phases of the experiment exposed varying behavior of the amplitude across the electrode configurations.

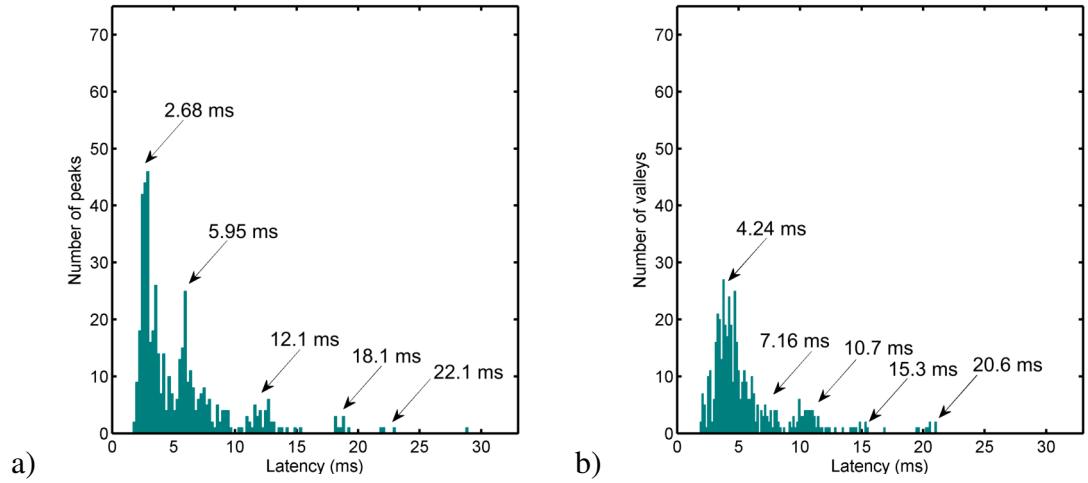

Figure 5.48 Distribution of the latency of the peaks (a) and valleys (b) extracted from the evoked potentials during transcutaneous electrical nerve stimulation. The results are an accumulation of peaks and valleys from all specimens, experimental phases and electrode configurations.

The analysis of the scatter plots revealed a correlation between the bilateral nerve damage and the presence of evoked potentials. In the entire dataset, I was able to identify peaks and valleys that either disappeared in the fifth phase after double-sided nerve incision (see Figure 5.50) or decreased their absolute amplitude between phase 4 and 5 (see Figure 5.51).

Appendix D contains a summary of the signals and their characteristics for all the electrode configurations in which I identified the absence of a given deflection of an evoked potential or a decrease of its amplitude. I selected the candidates based on the following criteria:

- The peaks (or valleys) needed to occur at least in three phases. All cases when the peaks (or valleys) first appeared as late as in Phase 3 where excluded.
- The peaks (or valleys) disappeared or decreased (increased) their amplitude in Phase 5 in comparison to all other phases.

A total of eleven electrode configurations (refer to Table 5.7) met the aforementioned criteria. Most often the expected behavior of peaks and valleys was observed in configurations in which the electrode in the anal canal served as the anode.

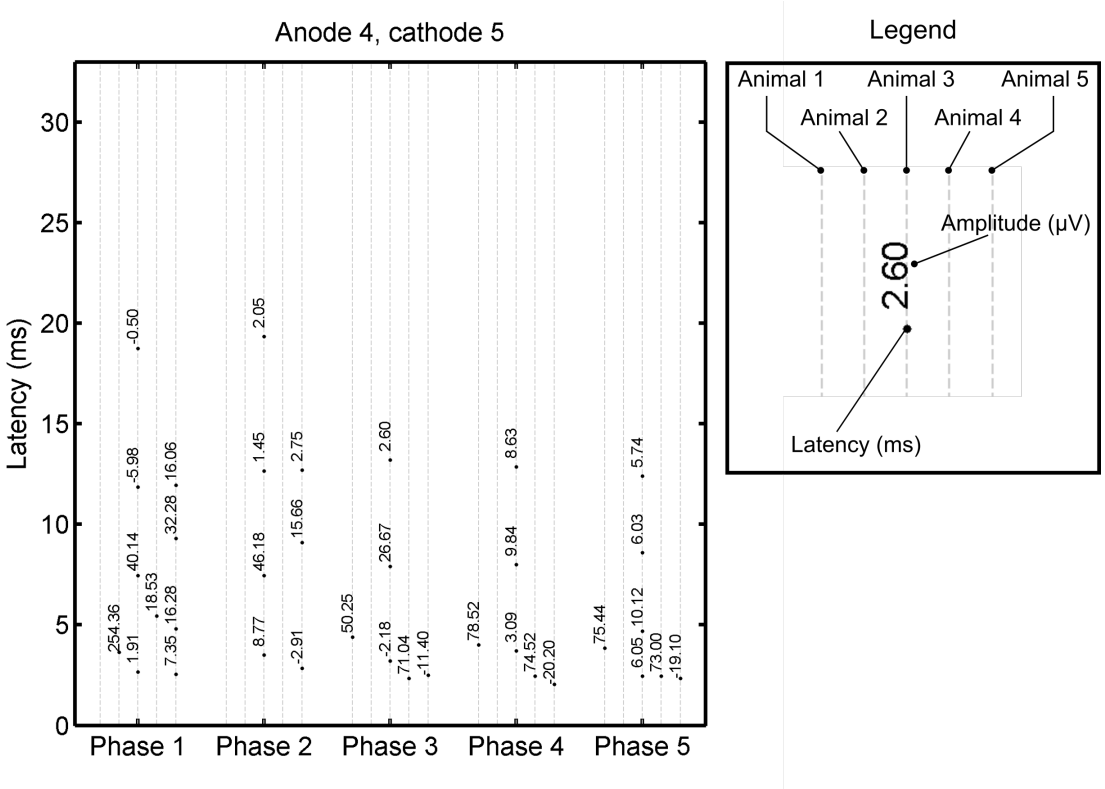

Figure 5.49 Peaks detected within the signal recorded from the internal anal sphincter during TENS. This figure shows peaks recorded during stimulation between anode 4 (placed in the anal canal) and cathode 5 of the stimulation array across all specimens and experiment phases. The vertical location (represented by a black dot) of each value corresponds to the latency at which the peak was detected.

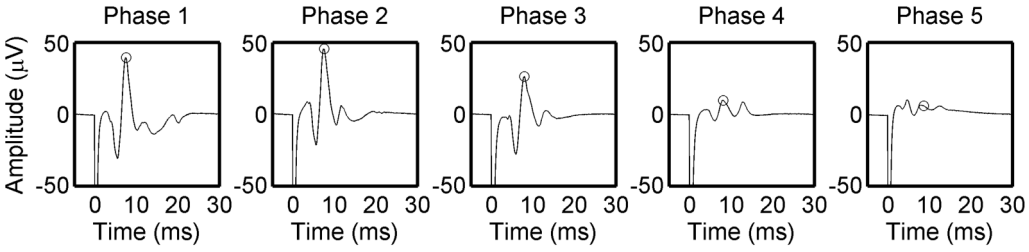

Figure 5.50 Averaged signals recorded from the internal anal sphincter TENS using anode 4 (placed in the anal canal) vs. Cathode 5 in Specimen 3. In this example a peak was detected at approximately 7.5 ms latency (circle). After the double nerve incision (Phase 5) the peak has a significantly lower amplitude than in the other phases.

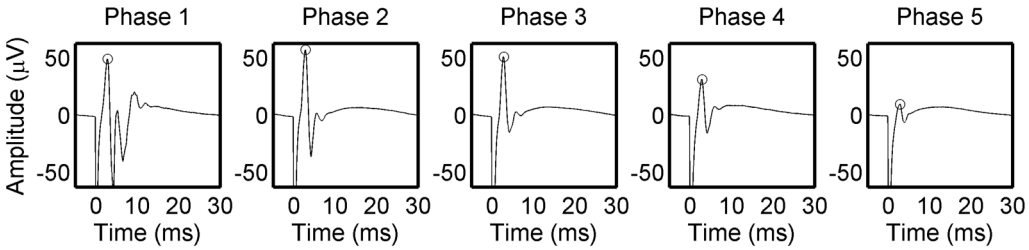

Figure 5.51 Averaged signals recorded from the internal anal sphincter during surface stimulation using anode 4 (placed in the anal canal) vs. cathode 5 in Specimen 5. A peak was detected at approximately 5.5 ms latency (circle). After the bilateral targeted nerve incision (Phase 5), the amplitude of the peak drops.

Table 5.7 Configurations of stimulation electrodes for which at least one local extremum within the averaged signals from the internal anal sphincter either decreased its absolute amplitude or disappeared completely after the bilateral nerve incision. Appendix D on page 165 contains a summary of the amplitude and latency changes within identified cases.

No.	Animal	Anode	Cathode
1	3	1	8
2	3	4	2
3	3	4	5
4	4	1	2
5	4	1	3
6	5	1	7
7	5	4	3
8	5	4	4
9	5	4	7
10	5	4	8
11	5	4	9
12	5	4	10

5.4.6 Spectral analysis of internal anal sphincter electromyography

I performed an analysis of the spectrum of the signals recorded for every identified electrode configuration that exhibited an amplitude decrease or complete disappearance of the evoked potentials. Figure 5.52 shows an example of the calculated spectra in two ranges: 0 to 25 Hz and 0 to 1000 Hz. This particular example comes from the recording from Specimen 3, anode 4 (in the anal canal), and cathode 2. Appendix D on page 165 contains a summary of the calculated spectra for all the identified cases. A significant influence of stimulation artifacts in the form of peaks at multiples of 30 Hz were observed in every single case. Several spectral ranges with increased activity were identified within the dataset: 0 to 20 Hz, 0 to 100 Hz, 100 to approximately 400 Hz, and 400 to 700 Hz. In 6 out of the 11 cases in which an amplitude drop or complete disappearance of local extrema occurred after the nerve incision also depicted changes in the signal spectra: either a drop in the range between 0 and 100 Hz or between 100 and 400 Hz. The remaining cases did not exhibit such a behavior.

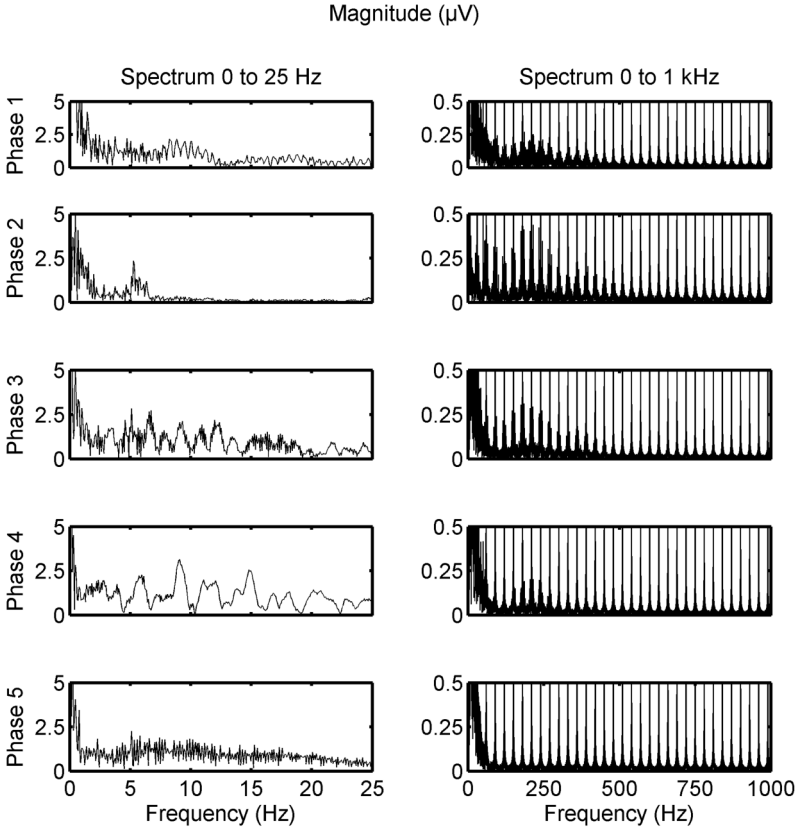

Figure 5.52 Analysis of spectrum in the range from 0 to 25 Hz and from 0 to 1 kHz of the signal in five experiment phases. Three spectral ranges of increased activity – 0 to 100 Hz, 100 to 300 Hz and 300 to 500 Hz – can be observed for phases 1 to 4. In Phase 5 only increased activity in spectrum from 0 to 100 Hz can be observed.

5.4.7 Influence of muscle relaxation on electromyographic signals

The introduction of vecuronium bromide – a non-depolarising neuromuscular blocker to prohibit the activity of the skeletal muscle tissue – had an influence on the recorded signals in Phase 4 of the experiment. The entire dataset contained 20 cases in which the peak or valley amplitudes of the evoked potentials decreased (or disappeared completely) after injecting the skeletal muscle relaxant and reappeared in Phase 5. These data came solely from Animal 1 and 3. Nine out of the 20 cases exhibited a decrease in the signal spectrum (mainly in the range between 0 to 100 Hz). Figure 5.53 shows the signals recorded in five phases of the experiment for Specimen 3, stimulation using anode 4 vs. cathode 10. In this case the evoked potential detected approximately at 2.85 ms and 6.15 ms after the stimulation pulse disappeared within the first 50 minutes after injecting the muscle relaxant. Analogous behavior was observed within all 20 cases. For a summary of the signals, the deflection amplitudes, and latencies, refer to Appendix D.2 on page 185.

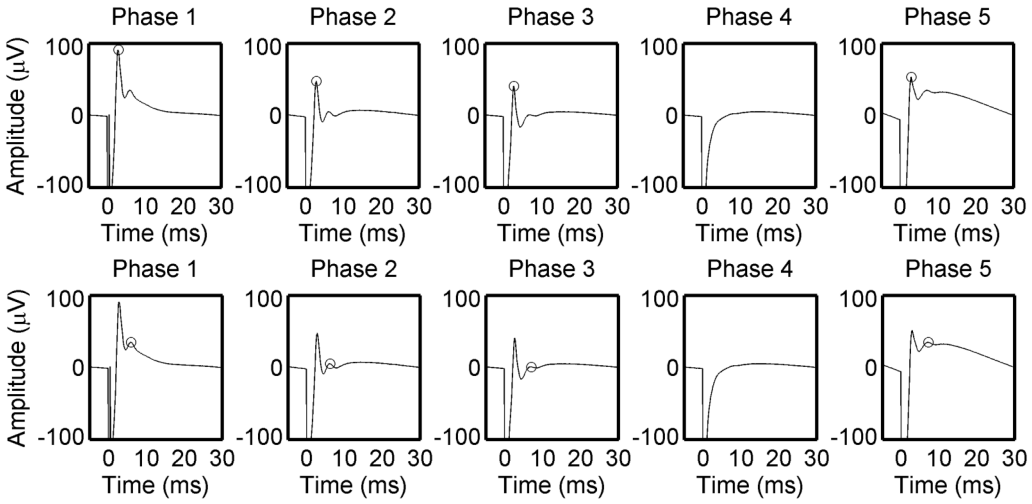

Figure 5.53 Averaged signals recorded from Specimen 3 during transcutaneous electrical nerve stimulation using the anode 4 (anal canal) vs. cathode 10. Two peaks were identified within the signals (represented by a ○ within the graphs) with the following latencies after the stimulation pulse: 2.85 ms – plot a), and 6.15 ms – plot b). These peaks are visible throughout Phases 1 to 3 and 5. Both of the peaks disappear after injecting the muscle relaxant (Phase 4). Legend: Phase 1 – specimen in prone position, Phase 2 – specimen in supine position, Phase 3 – after rectal resection, Phase 4 – after injection of muscle relaxant, Phase 5 – after bilateral targeted incision of the inferior hypogastric plexus.

Chapter 6

Discussion

The combination of the finite element method (FEM) and neuronal modeling has been widely used to investigate the neurophysiological phenomena within the human body resulting from stimulation-induced electrical field both for diagnostic and treatment purposes. From examining the technological aspects of deep brain stimulation for Parkinson patients, transcranial direct current stimulation for the treatment of a wide range of neurological disorders, stimulation of the cochlea for improving hearing aids, this modeling approach also finds application in stimulation within the spinal cord and the sacral area. Rattay et al. analyzed the neurophysiology of muscle recruitment due to epidural stimulation of the spinal cord to investigate the patterns of muscular contractions [61]. Holsheimer's simulations showed that spinal cord stimulation could be used in the context of pain relief [62]. Hirata et al. investigated feasibility of sacral nerve stimulation using implantable devices for the treatment of bladder overactivity [63]. Laakso investigated how far magnetic stimulation can be used to target specific sacral nerve roots [64]. To the author's knowledge, no similar approach was undertaken in the context of IONM.

The presented work proved that investigating the *spatial* and *electrical parameters* in a study combining *numerical modeling of the excitability of the autonomous nervous system within the pelvic floor* and *in-vivo experimentation of the electrophysiology of the internal anal sphincter* is an *effective tool to assess the suitability of TENS in pIONM*. The standard method of direct nerve stimulation (DNS) was treated as reference. This chapter provides proof for the stated thesis by discussing the suitability of TENS based on two criteria established by rectal surgeons' expectations: 1) the ability to perform intraoperative nerve mapping, and 2) the ability to assess the intraoperative nerve function in different phases of rectal cancer surgery.

6.1 Intraoperative nerve mapping

Nerve mapping aims at identifying the autonomous nervous tissue within the pelvic floor during surgery. By stimulating the exposed tissues using electrical current and concomitantly observing the activity of the autonomically innervated muscles, the surgeon develops a mental map of the autonomic nervous system in the context of the surrounding tissues within the operative field. This opens the possibility to locate the proper plane of dissection during TME and to avoid the sheath containing the autonomic nerve fibers responsible for controlling anorectal and urogenital function.

To facilitate successful nerve mapping, a stimulation method should enable selective stimulation of individual nerve structures causing neuromodulation within the ANS that results in a recordable response from the effector organs.

Can simulated DNS evoke a neural response within the ANS?

Understanding whether a stimulation method can yield a neural response within the autonomic nervous system is fundamental for exploring the possibility to perform intraoperative nerve mapping. Before a nerve structure can be identified by electrophysiological monitoring, the electric field generated by electrical stimulation needs to excite a given nerve structure and cause neuromodulation.

The numerical simulations showed that DNS could evoke a response within the autonomous nervous system. The amplitudes of stimulation current producing an action potential in the numerical model fell within the tested stimulation range from the experimental studies. Simulated electric field obtained from FEM produced action potentials that could be recorded from the distal ends of the simulated fibers for ten different stimulation sites at a range of stimulation amplitudes from 1 to 5 mA for the targeted innervation and between 14 and 23 mA for accidental activation of the neighboring neural tissue. During stimulation of the inferior hypogastric plexus, the modeled neurons reacted to amplitudes ranging from 2 to 5 mA and produced action potentials of 2 to 3 mA within the modeled IAS innervation and 2 mA for the bladder innervation.

Kneist et al. reported activating the internal anal sphincter during pIONM by applying electrical stimuli to the pelvic splanchnic nerves and the inferior hypogastric plexus with stimulation current between 5 and 20 mA [18, 23, 24, 29, 65, 66]. The authors used the same microfork stimulation probe as the one simulated within the numerical study.

The stimulation thresholds that resulted in producing action potentials within the model were lower than the values reported within the literature during DNS. The differences in neural excitability between the model and the clinical data may have resulted from variable

electrode stimulation placement and from inter-individual differences in tissue composition that may result in differences in excitability thresholds.

Is DNS a selective stimulation method?

The simulations confirmed the selectivity of DNS. The action potentials could be recorded using virtual electrodes from distal nerve endings only from the directly stimulated nerves and the stimulation of nerve plexi produced a response only within the nerves constituting the plexi.

Currently, there is no literature regarding pIONM that reports any insight regarding stimulation selectivity. However, based on practical experience of multiple surgeons, stimulation of the inferior hypogastric plexus often resulted in simultaneous response of the IAS and the bladder, stimulation of pelvic splanchnic nerves usually resulted in activation of the IAS, and stimulation of the autonomic fibers going in the direction of the bladder activated the detrusor muscle. Reaction of the mentioned musculature could be observed intraoperatively.

Although extensive cadaver-based neuroanatomical research showed that *post-mortem* visualization of the autonomous nervous system provided invaluable insight into the neuroanatomy of the ANS in the pelvic floor, intraoperative visual exposition of the autonomic nerves might be incomplete and insufficient for functional preservation. Kneist et al. showed that the combination of novel minimally invasive laparoscopic techniques and selective intraoperative nerve mapping could provide invaluable insight into the neuroanatomy of the pelvic "no man's land" [29, 26].

Does DNS pose the risk of activating skeletal muscle tissue by accidental stimulation of the pudendal nerve?

An unexpected finding arose from the numerical study. The simulations suggested that there might be an involvement of the activation of the pudendal nerve during DNS for pIONM: stimulating the S3 pelvic splanchnic nerve also produced an AP within the pudendal nerve that originated from the same sacral nerve root.

Accidental stimulation of the pudendal nerve during pIONM when applied during peritoneal laparoscopic surgery seems improbable because the remoteness of the origin of the nerve and the operative field. However, apart from percutaneous and intra-foraminal (S3) stimulation of the pudendal nerve [67, 68], the literature suggests that the pudendal nerve can also be approached from the abdominal area. Possover et al. showed that it is possible to stimulate the pudendal nerve from the retroperitoneal area for pain treatment [69].

Potentially, this could lead to neuromodulation within the entire pudendal nerve branch innervating the EAS and cause its contraction. Because of close anatomical location of the IAS and EAS, any contraction within the EAS might be recordable within the EMG activity of the IAS. Thus, the simulations suggest that stimulation of deep PSN might activate the pudendal nerve. This insight suggests that the application of muscular relaxants is even more important to avoid accidental activation of the somatic musculature within the pelvic floor. Such activation might obscure the recorded EMG signal of the IAS because of close vicinity of the EAS and provide false positive signals.

Can DNS produce a response within the processed EMG of the IAS?

The experimental study showed that DNS produced an increase of the amplitude of the processed EMG of the IAS in all experimental phases prior to targeted nerve incision. Unexpectedly, the raw signal analysis of the IAS EMG revealed the presence of evoked action potentials during all phases of the experiment prior to distal nerve incision.

Kneist et al. showed that the IAS EMG exhibits the highest signal amplitude within the spectrum between 5 and 20 Hz during electric stimulation of pelvic nerves [23]. Other literature also reported slow wave and spiking activity occuring spontaneously in other smooth muscle tissue. The slow wave activity was associated with the regulation of the electrical conduction of the smooth muscle tissue, whereas the spiking activity was associated with the contraction of the smooth muscle tissue of the gastrointestinal tract in animal specimens and humans [70, 71, 72, 73]. Studies of the colon and the lower esophageal sphincter have shown that action potentials within smooth muscle recordings could be evoked via electric stimulation of the intrinsic colon innervation and the vagal nerve [74, 75]. To the author's knowledge, there has been no literature report of evoking action potentials within the IAS due to electric stimulation of the autonomous nervous system within the pelvic floor.

The discovery of evoked potentials within the IAS EMG due to stimulation of the IHP in pig specimens complements the state-of-the-art knowledge regarding the IAS electrophysiology. Current signal processing techniques routinely employed for pIONM disregard the high-frequency information by employing filtration between 5 and 25 Hz. Reconsidering the signal processing technique to include the high-frequency content might increase the nerve identifiability and specificity of stimulation during pIONM.

Can TENS evoke a neural response within the ANS?

The simulations showed that TENS could evoke a response within the autonomous nervous system. Simulated electric field obtained from FEM produced action potentials that could

be recorded from the distal ends of the simulated fibers for forty different cathode-anode configurations.

Is TENS a selective stimulation method?

Despite using different electrode configurations, TENS did not reproduce the level of selectivity observed during DNS. Although highly dependent on the used anode-cathode combination, there were several patterns within the stimulation current threshold evoking a reaction within the ANS. The higher the intensity of the stimulation current, the higher the recruitment level of the modeled nerve fibers. On average, the nerves located on the ispilateral side of the stimulation array required a smaller current amplitude to produce an action potential. This shows the aspect of side selectivity which is determined by the location of the stimulation array. What is more, the modeled pelvic splanchnic nerves always required the least stimulation current for the electrode configuration located in the nearest vicinity of a given nerve. Conversely, the nerve fibers originating from the SHP, via the hypogastric nerves towards the bladder innervation required significantly higher current intensity to produce a response than in the case of the innervation originating from the sacral nerve roots (i.e. pelvic splanchnic nerves and the pudendal nerves).

Rattay et al. reported that the stimulation threshold is a function of electrode position and polarity [61]. During simulated epidural stimulation of the spinal cord, dorsal roots exhibited a lower activation threshold than the ventral roots, the cathodes located closest to a given dorsal root required the least stimulation threshold to activate, and stimulation along the descending course of the nerves lead to their excitation. Keller et al. described the level of electric current as the factor limiting the selective activation of muscle tissue of the forearm using TENS [76].

The findings of the presented study come to similar conclusions as the ones described in the literature. Dorsally located parts of the model (pelvic splanchnic nerves originating from the sacral nerve roots) exhibited a lower activation threshold than the ventral parts (SHP, HN, bladder innervation). Although the model of Rattay included a more precise geometry of the spinal cord, the model did not account for the tissues surrounding the spinal cord. The model used for the study presented in this dissertation regarded the pelvic autonomic nervous system in the context of the surrounding tissues within the pelvis.

Can TENS produce a response within the processed EMG of the IAS?

The standard signal processing method of DNS could not be applied to TENS because it was prone to stimulation artifacts within the IAS EMG and delivered false positive results

that might lead to signal misinterpretation during pIONM. Both the low and high-frequency content of the IAS EMG correlated with inflicting targeted nerve damage. Analyzing the signals both in the frequency domain – spectrum between 5 and 25 Hz – and time domain – the averaged raw EMG – could increase the probability of identifying the spatial configuration of stimulation electrodes whose stimulation results were sensitive to nerve damage. This sensitivity is paramount for nerve mapping during pIONM.

The qualitative analysis of the intraoperative EMG signals showed that TENS produced a response in the form of an amplitude increase within the IAS EMG processed in between 5 and 25 Hz. This was observed for every cathode-anode configuration without any identifiable differences in the processed amplitudes among the configurations. However, the raw signal analysis revealed the presence of high-amplitude stimulation artifacts for every recording during TENS. The stimulation artifacts always resulted in a biphasic peak followed by an exponential decay of the amplitude. The low-frequency harmonics of this exponential decay may have contributed to the processed IAS EMG signal and may have led to an increase of the recorded amplitude.

The raw signal analysis of the IAS EMG also revealed the presence of evoked potentials in 422 electrode configurations of a total of 1000 (200 per specimen). These evoked potentials contained local extrema at latencies that were reproducible within different phases of the experiment. Across the entire population of signals, the local maxima formed distinct groups. The form and number of the deflections varied depending on the used electrode configuration. In some cases, the presence and the amplitudes of specific local extrema varied depending on the experimental phase (see Chapter 5.4.5 on page 100 and Section 6.2 on page 118).

Kauff et al. reported a positive amplitude increase of the processed IAS EMG during extracorporeal stimulation of the S2-S3 region using self-adhesive electrode pads in a case study on a 74-year old woman [77]. Because these findings were based solely on observing intraoperative processed IAS EMG, there is a chance that stimulation artifacts produced by TENS contributed to this signal increase. The authors did not provide any information regarding the postoperative follow-up of the patient regarding the anorectal function. Thus, it is impossible to conclude that the observed response was a result of neuromodulation of the ANS and not due to stimulation artifacts.

Using the same experimental setup as the one described within the presented work, Kauff et al. [58] reported that the area under the spectrum within 5 to 25 Hz can be used to identify differences before and after bilateral targeted incision of the inferior hypogastric plexus. The electrode configurations, reported by Kauff, that yielded an AUC increase within 5 to 25 Hz were disparate with the ones reported in this study. This suggests that both the low- and high-frequency content might contain information correlating with inflicting targeted nerve

damage. Combining these two signal processing methods might increase the likelihood of using a stimulation electrode configuration that would produce results sensitive to nerve damage.

What is the involvement of skeletal muscle tissue in the EMG of the IAS during TENS?

TENS might produce direct and indirect response within the skeletal musculature (e.g. of the EAS or the levator ani muscle) of the pelvic floor. This suggested that the needle EMG received not only the signal coming from the IAS but also from the more voluminous skeletal muscle tissue in the vicinity. A combination of observations stemming from both the experimental and modeling study suggested the involvement of skeletal muscle tissue within the IAS EMG during TENS.

The numerical simulations showed that activation of the pudendal nerve via TENS could be likely. Every configuration used for TENS produced action potentials which could be recorded at the distal end of the pudendal nerve. The activation of the nerve occurred at stimulation amplitudes as low as 2 mA and 5 mA for the right and left branch, respectively. What is more, the high current density within the anal canal during intra-anal stimulation might signify that intra-anal stimulation might directly excite the muscle tissue of the pelvic floor in the vicinity.

In the experimental study, TENS produced more complex evoked potentials in comparison to DNS. This suggests a possible involvement of more muscular structures. The most complex evoked potentials – containing the highest number of local extrema – were observed during the stimulation using the intra-anal electrode. Additionally, twitches and movement of the back musculature and the porcine tail could be observed during TENS.

Introducing muscular relaxants correlated with a decreased amplitude of the evoked potentials produced by TENS. This was observed in Phase 4 within 50 minutes after injection. Spectral analysis showed that the high-frequency content of the signal also was reduced for these electrode configurations.

The use of non-depolarising neuromuscular blockers (such as the used vecuronium bromide) effectively paralyzed skeletal muscle tissue [78] and reduced the amplitude of evoked potentials [79, 80, 81, 82, 83]. The mechanical contractability of the smooth muscle tissue, however, was proved insensitive to the activity of non-depolarizing neuromuscular blockers that bind with nicotinic acetylocholine receptors [84, 43]. Considering the IAS electrophysiology based on processed EMG, the use of rocuronium bromide as the go-to muscle relaxant during total mesorectal excision seems not to influence the amplitudes of the

stimulation-induced IAS activity. The literature does not report any connection between the amplitude of evoked potentials recorded from the IAS during stimulation of the autonomic nervous system of the pelvic floor and the introduction of muscular relaxants. However, because of the lack of effect of the neuromuscular blockade on the processed IAS EMG, it may be unlikely that the amplitude of the evoked potentials were also involved. Thus, any influence of the muscular blockers on IAS EMG might indicate the involvement of additional somatic nerve structures.

6.2 Intraoperative function monitoring

Once the surgeon creates a mental model of the position of the autonomic nerves based on the results from intraoperative nerve mapping, he can re-evaluate their function and identify any changes in the reaction during critical phases of the dissection. The surgeon performs this by repeating the stimulation routine at each critical phase. TENS can be used to monitor the ANS function during total mesorectal excision. However, sensitivity to nerve damage could be confirmed only by verification through targeted nerve incision.

Did targeted nerve incision prohibit the conduction of APs due to DNS?

The numerical study showed that the targeted nerve incision prohibited the conduction of action potentials resulting from DNS of the autonomic nervous system within the small pelvis.

Targeted nerve incision of the IHP successfully blocked the conduction of action potential along the distal parts of the simulated nerve fibers: the action potentials could no longer be observed in the simulated recordings at distal parts of the bladder and sphincter innervation following the nerve incision during DNS. However, this effect occurred only in specific ranges of stimulation amplitudes. These ranges varied depending on the stimulation site. Unexpectedly, there was an upper limit to these stimulation ranges. After exceeding a threshold stimulation amplitude, action potentials reoccurred at the distal ends of the nerve models. Moreover, simulated stimulation of the right S3, left S4 and right S4 pelvic splanchnic nerve resulted in evoking an action potential within a non-targeted nerve fiber for current intensities exceeding 14 mA.

DNS allowed to precisely locate the damaged nerve: identification of nerve damage was possible only by stimulating the damaged nerve fiber. Depending on the stimulation site, action potentials reappeared in the recordings during nerve stimulation with high current intensity. However, the latencies of the recorded action potentials were lower after exceeding

the upper stimulation threshold. This might suggest that for high stimulation amplitudes the nerve is activated at a different location, distal from the nerve incision. This no longer prohibited the conduction and recording of action potentials at the distal end of a given nerve fiber. Although this finding was unexpected, the fact that the action potentials reappeared after exceeding a specific stimulation amplitude could be explained by considering the modeled geometry: the electrodes were "immersed" within the tissues in direct vicinity of the nerve structures. In a laparoscopic setting, however, the abdominal space is filled with CO_2 gas, which poses additional constraints onto the electric conductivity. Although the current could freely (limited by the simulated tissue conductivity) flow in all directions within the modeled volume conductor, in the surgical setting the gas forms an impenetrable barrier and the current travels only within the exposed tissue sheath. In the standard clinical practice, the stimulation amplitudes used for DNS range between 6 and 12 mA. Thus, in order to increase the stimulation selectivity, amplitudes in the lower part of this stimulation range are advisable.

Finite element method modeling of the electric field combined with a neuronal membrane model allowed identifying the differences between DNS in terms of sensitivity to nerve damage. To the author's knowledge, no mention of such an approach applied in the context of intraoperative neuromonitoring for the surgery of rectal cancer is present within the literature. The approach showed that computational analysis of nerve damage for the purposes of intraoperative neuromonitoring is feasible and can provide insight into the limitations of stimulation methods in terms of their sensitivity to nerve damage. This might help to assess the suitability of TENS for functional monitoring.

Can nerve damage be identified in the IAS EMG during DNS?

The experimental study showed that nerve damage can be identified in the IAS EMG both as a decrease of the amplitude of processed EMG and a decrease of the amplitude of the recorded evoked potentials.

The analysis of raw signals during DNS showed that, apart from the decreased amplitude within the processed EMG, the reduction of high-frequency content of the evoked potentials correlated with inflicting targeted damage to the IHP. Unexpectedly, inflicting nerve damage proximally to the stimulation site correlated with an increase of the amplitudes of the evoked potentials within the tested group. This might indicate that a possible inhibitory component could be effectively blocked by proximal incision resulting in an increased amplitude of the evoked response. On the other hand, targeted damage distal to the stimulation site resulted in a complete disappearance or a decrease of the amplitude of the recorded evoked potentials.

The standard method of using the processed EMG within the spectrum of 5 to 25 Hz proved effective at predicting targeted nerve damage applied to the IHP during DNS. Kauff et al. showed that targeted nerve incision of the inferior hypogastric plexus using four different surgical techniques caused a drop in the processed EMG [85]. Nerve damage could also be identified by analyzing the area under the curve calculated over the spectrum between 5 and 25 Hz within the IAS EMG [58]. To the authors knowledge, no mention of effects of targeted nerve incision on potentials evoked by stimulating the IHP was reported in the literature up to this date. Thus, the analysis of high-frequency content within the signal of the IAS might be worth considering as an additional source of information that could help monitor the autonomic nerve integrity during pIONM.

Did targeted nerve incision prohibit the conduction of action potentials during TENS?

The results of the simulations showed that the targeted nerve incision prohibited the conduction of action potentials due to TENS predominantly within the hypogastric nerves and only in a limited number of cases for other nerves. This is because TENS also produced responses within the parts of the nerve that were geometrically located between the incision site and the recording site. This might indicate that TENS is insensitive to nerve damage.

The absence of action potentials resulting from targeted nerve damage could be observed during TENS. The widest range of stimulation amplitudes for which nerve damage could be identified was observed in the modeled pathway between the hypogastric nerves and the bladder innervation. For IAS innervation, the sensitivity to nerve damage is very limited. The ranges of stimulation amplitudes for which there is a difference between the situation before and after nerve incision were narrower. As with the DNS stimulations, the latencies of the APs that reappeared after exceeding the upper limit of the identified stimulation ranges were lower. This also may suggest that the center of excitation occurred distally to the targeted nerve damage effectively allowing the conduction of action potentials into the distal ends of the modeled nerve fibers.

Simulations helped to identify the stimulation intensity ranges for which TENS was sensitive to nerve damage. The variable width of these ranges depended on the used electrode configurations and the monitored nerves. The fact that TENS proved most sensitive to the damage of hypogastric nerves and the bladder innervation suggests that it might be useful for monitoring of the functions controlled by these nerve structures: sexual function monitoring. Currently in the operating room, the proper stimulation range at this point is impossible to verify. Validation would involve inflicting targeted nerve damage only to check which

configuration yields the result sensitive to nerve damage. At this point no further preservation of nerve function would be possible. Simulations helped to identify this risk. To the author's knowledge, this dissertation is the first report of applying the combination of finite element method and neural modeling to investigate the sensitivity of TENS to nerve damage.

Can nerve damage be identified intraoperatively in the IAS EMG during TENS?

Analysis of the signal traits is crucial in identifying nerve damage intraoperatively. Nerve damage could be identified in the IAS EMG only by means of evoked potentials – not the processed EMG. Only specific electrode configurations produced the effect, signifying that the electric field needs to be controlled in order to evoke a response within the nerves proximal to the operative field. Thus, the experimental study showed that band-pass filtration between 5 and 25 Hz cannot be directly applied to TENS for pIONM.

Qualitative intraoperative analysis of the IAS EMG during TENS did not exhibit an amplitude decrease within the processed EMG of the IAS due to targeted nerve damage. However, the raw EMG signals contained evoked potentials that either disappeared or lost a portion of their amplitude after targeted nerve incision of the IHP for a limited number of electrode configurations. This happened despite lower stimulation selectivity as compared to DNS (see Section 5.3.1 on page 87). Because of the differences of stimulation selectivity, identifying electrode configurations sensitive to nerve damage was an unexpected result.

A first attempt to apply extracorporeal stimulation during pIONM has been reported by Kauff et al. [77]. The authors reported an amplitude increase within the processed EMG of the IAS due to extracorporeal stimulation. However, the analysis of the processed EMG of the IAS during the presented study exposed the influence of stimulation artifacts produced by TENS. What is more, no correlation between the amplitude of the processed EMG and the targeted nerve damage could be found during intraoperative analysis of the filtered signals during TENS. Recently, Kauff et al. [58] reported a drop in the signal spectrum between 5 to 25 Hz following distal nerve incision during TENS for several electrode configurations. The authors used the same methodological setup as in the described study. However, the electrode configurations identified by the analysis of raw signals are disparate with the ones identified by spectral analysis.

Identification of traits within the evoked potentials elicited via percutaneous stimulation has been reported during monitoring of the posterior and anterior root muscle reflex during the surgery of the hip (total hip arthroplasty and developmental dysplasia surgery) [86]. However, this technique was used for monitoring of the sciatic and femoral nerves. Both of

these nerves constitute somatic innervation and innervate skeletal muscle tissue within the leg. To the author's knowledge, the literature does not report any mention of nerve damage identification by TENS of the sacral nerve roots using traits of the evoked potentials recorded within the IAS, let alone for pIONM. These results show that the analysis of potentials evoked by TENS might be a feasible method for identification of nerve integrity during pIONM. The presented results showed that there was also a high-frequency component within the signals that is also correlated with targeted nerve damage. Thus, using both the spectral analysis of the signals and the analysis of the evoked potentials might help to identify nerve damage based on a larger number of electrode configurations and specimen variation.

6.3 Research limitations

The presented study had several limitations. This section describes the study design limitations regarding the numerical modeling and the animal model experiments.

6.3.1 Limitations of the numerical modeling

The geometry of the finite element model was derived from magnetic resonance imaging data coming from one person. Although it provided the means to explore the basic phenomena governing the propagation of electric field inside the human body, it failed to account for inter-individual differences of the anatomy of the pelvic floor. Thus, one should be cautions when trying to generalize the conclusions based on the model.

The pelvic floor was modeled as an enclosed volume and it did not account for the conditions of the laparoscopic surgery. Including a CO_2 gas compartment within the abdominal cavity could create conditions that would more accurately model the propagation of the electric field during laparoscopic surgery. However, obtaining an MRI-based model including this gas-filled abdominal cavity is impractical – additional post-processing of the obtained tissue models would be necessary to include such a gas compartment.

To reduce the computational intensity, several simplifications of the finite element model had to be made. The model explored only the quasi-static approximation of the Laplace equation. Several literature positions suggested that this is negligible, however, the transient response of a typical nerve stimulator can incorporate high-frequency signals. Capacitive behavior of tissues – not part of the presented model – could have an impact on the propagation of the electric field and on generation of the action potential [87]. However, this seems to apply above all for voltage-controlled transcutaneous stimulation [88]. In the case of current-regulated stimulation – as modeled within the presented study – the electric field

derived from the quasi-static approach deviated less than 6% in comparison to a model incorporating capacitive behavior [89].

Moreover, the model assumed inhomogeinity by combining multiple isotropic tissue groups that exhibited different conductivity. Biological tissues exhibit a high-level of anisotropy when it comes to conducting electrical current. This affects how the electric current travels inside a given tissue. Incorporating anisotropic conductivity of tissue groups might offer a more accurate image of the electrical current resulting from electrical stimulation within the pelvic floor.

Each autonomic nerve was modeled as a single nerve fiber. In practice, nerve fascicles contain many fibers and the extent of their activity depends on the recruitment of the nerve. In the case of a single fiber model, the modeled nerve damage exhibits binary behavior: either the nerve is completely damaged or not. Modeling the nerves with many nerve fibers could allow exploring partial nerve damage and its effects on the recorded signal.

The simulations exposed the selective nature of DNS, which supports its practicability in the clinical practice and in functional neuroanatomical studies. Although, based on the distribution of the electric field, one can draw conclusions regarding the ability of DNS for selective stimulation, it should be noted that the intricate interconnections within the ANS of the pelvic floor are the topic of a vivid scientific debate and they are yet to be fully understood. Thus, to the best of the author's intentions, the models geometrical accuracy is a vast simplification of the current neuroanatomical knowledge.

The simulated signal recording of the nerve action potential was based on the voltage clamp method. However, the standard application of pelvic intraoperative neurophysiological monitoring does not incorporate any direct measurement of the action potential within the intrinsic innervation of the IAS or the bladder, but the measurement of effects of the propagation of this action potential: the electromyographic (EMG) activity of the IAS and the mechanical contraction of the bladder. Normally, EMG measures compound muscle action potentials (CMAPs) – a summation of multiple action potentials generated by multiple motor units. A model incorporating generation of a CMAP within the IAS might offer more insight into the nature of the signal recorded from a typical needle measurement of the IAS EMG [90].

6.3.2 Limitations of the experimental study

There were several limitations concerning the experimental study. The studied sample was limited to five specimens of specific gender (male) and a median weight of 29 kg. Although the sample size was large enough to perform a feasibility study, generalizing any conclusions based on the study should be performed with caution. Including a sample consisting of

both sexes and more non-uniform morphometric characteristics could offer insight into the inter-individual variance in terms of muscular response of the smooth muscle tissue to electrical stimulation of the autonomic nervous system.

Using only a single needle electrode placed within the internal anal sphincter may have contributed to the limited number of the identified electrode configurations during TENS that exhibited sensitivity to bilateral nerve damage. Although there is much debate regarding the specific routing of the autonomic innervation of the pelvic floor, the current knowledge suggests that there might be a reflex path between the inferior hypogastric plexus and the spinal cord[1]. It is unknown whether evoked potentials resulting from this reflex path influenced the signals acquired from the internal anal sphincter and delivered false positive results. Analyzing the differences in the evoked potentials from bilateral signal acquisition might help identify more specific conditions under which TENS delivers a response sensitive to nerve damage.

The numerical study suggested that using TENS might be more selective in detecting damage of the nerves located on the ipsilateral side of the stimulation array. The current study investigated the sensitivity of TENS to bilateral nerve damage. Using a symmetrical setup – adding a second stimulation array on the other side of the vertebral column – might offer insight into identification of unilateral nerve damage of the inferior hypogastric plexus.

The numerical study as well as the test under muscular relaxation suggested that the activity of the internal anal sphincter might have been influenced by the signals originating from the skeletal tissue lining the pelvic floor. In order to block this interference, it is advisable that a further investigation of the sensitivity of TENS to nerve damage be performed under continual muscle relaxation.

[1] Based on a consultation with Prof. David B. Vodušek, University Medical Center Ljubljana

Chapter 7

Conclusion and perspectives

This chapter contains the conclusions coming from the conducted research, a summary of key findings of the numerical modeling and experimental studies, significance for the field of rectal cancer surgery, and perspectives for future investigation.

7.1 Conclusions drawn from the conducted research

By combining numerical modeling of the excitation of the autonomous nervous system in the lesser pelvis and an *in-vivo* investigation of the electrophysiology of the internal anal sphincter (IAS), the presented work evaluated the suitability of transcutaneous electrical nerve stimulation (TENS) for the use in pelvic intraoperative neurophysiological monitoring (pIONM) based on the ability to perform intraoperative nerve mapping and function monitoring. Direct nerve stimulation (DNS) – the stimulation method employed as a standard during pIONM – was treated as the reference. The presented work provided proof for the following thesis statement:

Investigating the electrical and spatial parameters of electrical stimulation of the autonomous nervous system within the pelvic floor by a combination of numerical and in-vivo *modeling is an effective tool to assess the feasibility of transcutaneous electrical nerve stimulation for the purposes of pelvic intraoperative neurophysiological monitoring.*

The combination of numerical modeling and an *in-vivo* study showed that TENS proved impractical for intraoperative mapping during pIONM because of limited stimulation selectivity as compared to DNS.

The study showed that for very specific conditions TENS can be used for intraoperative function monitoring. However, this required improving the signal recording method to expose

the fine differences indicative of nerve damage. Moreover, the numerical study showed that very strict conditions need to be met in order to elicit nerve damage sensitivity. This was reflected in a very small number of total electrode configurations that were associated with nerve damage.

The combination of numerical modeling and experimental study provided insight into stimulation selectivity, sensitivity to nerve damage, current distribution during TENS and DNS within the pelvic floor, practicability of the currently used signal acquisition techniques, discovery of a new type of activity within the IAS that is indicative of nerve damage, the influence of the somatic outflow from the perspective of conducting action potentials and recording of the IAS activity.

7.2 Summary of key findings

Modeling study

- The modeling study provided insight into how the current distribution within the pelvic floor influences the production of action potentials within a simplified model of the autonomic nervous system within the lesser pelvis. The current distribution resulted from two methods of electrical stimulation: DNS and TENS using surface electrodes. Based thereupon, differences in stimulation selectivity, sensitivity to targeted nerve damage, and the extent of activation of the autonomic and somatic neural outflow were identified.

- TENS proved to be less selective in targeting the autonomic nerve structures than DNS. TENS produced a reaction of multiple nerve fibers for a every single cathode-anode configuration. DNS produced a reaction of only one nerve fiber or only the fibers constituting the inferior hypogastric plexus (IHP). However, the location of the stimulation array on one side suggested side selectivity. Unexpectedly, the numerical study showed that using high stimulation amplitudes limited the selectivity of DNS.

- Simulated targeted nerve incision blocked the conduction of action potentials produced by DNS and TENS. Using DNS, one could identify nerve damage of a specific nerve. TENS proved to be most sensitive to nerve damage within the hypogastric nerve – identifying the nerve damage was possible only under strict stimulation conditions: specific spatial distribution of the electric field and stimulation intensity.

- Moreover, the numerical study exposed the possibility of evoking a response from the somatic outflow during both DNS and TENS: DNS produced a response of the

pudendal nerve during stimulation of the S3 pelvis splanchnic nerve (PSN); TENS produced a response of the pudendal nerve for all used electrode configurations.

Experimental study

- The experimental study provided insight into the practicability of the state-of-the-art signal processing during DNS and TENS, contributed to a discovery of evoked action potentials within the IAS EMG, identified the conditions under which TENS exhibited sensitivity to nerve damage, and helped identify the influence of the somatic outflow on the recorded signals.

- Although the processed EMG of the IAS[1] is the state-of-the-art method during DNS in pIONM, using processed EMG for TENS is impractical because of sensitivity to stimulation artifacts. DNS of the IHP as well as TENS using all electrode configurations produced an amplitude increase in the processed EMG within the IAS in swine specimens. The analysis of the raw EMG within the time and frequency domains confirmed the presence of stimulation artifacts.

- The raw signal analysis helped to discover the presence of evoked action potentials within the IAS as a result of both DNS and TENS. The fact that these potentials were also visible within the EMG of the somatically innervated external anal sphincter suggested the involvement of both the somatic and autonomic neural outflow during both DNS and TENS.

- TENS produced evoked action potentials within 422 out of 1000 tested electrode configurations across all specimens.

- The evoked potentials exhibited a form and number of local extrema that could be reproduced across specific electrode configurations and experimental phases.

- The sensitivity to targeted nerve damage of the IHP on the basis of the processed EMG could only be identified when performing DNS. The presence of stimulation artifacts resulting from TENS obscured the sensitivity to nerve damage based on the processed EMG. However, damage to the nerves could be identified by means of evoked action potentials within the IAS EMG both during TENS and DNS. The evoked potentials during DNS exhibited a drop in the amplitude or complete disappearance following distal nerve incision thus proving to be indicative of nerve damage in the

[1] Electromyogramm filtered within 5 to 25 Hz to highlight the activity of smooth muscle tissue

porcine specimens. Proximal nerve damage was associated with increased peak-to-peak amplitude of the evoked potentials implying possible blockage of inhibitory pathways reducing the amplitude of the evoked potentials. Specific and highly-varying conditions needed to be met in order to achieve sensitivity to nerve damage using TENS. Only 11 out of 1000 electrode configurations exhibited sensitivity to nerve damage. In six cases this nerve damage was also associated with a decrease of the signal spectrum within the range of 0 to 100 Hz or 100 to 400 Hz.

- The experimental study showed that introduction of muscle relaxants influenced the amplitude of the evoked potentials recorded from the internal anal sphincter. This might indicate a contribution of the somatic outflow in evoking the EMG activity within the IAS. The injection of muscle relaxant caused a reduction of the amplitude of potentials evoked by specific electrode configurations. This group of configurations did not intersect with the group that exhibited sensitivity to nerve damage. In several cases this was also noticeable in the frequency domain of the signals.

7.3 Significance of the conducted research

pIONM offers the surgeon a means to improve the patients quality of life. The primary goal of total mesorectal excision is to save the patient's life by removing the life-threatening tumor. The secondary goal is to preserve the urogenital and anorectal function. The success of total mesorectal excision in the latter determines the difference between social withdrawal caused by the urogenital and anorectal dysfunction and maintaining a normal quality of life. pIONM offers a means to improve the preservation of the urogenital and anorectal function.

The integration of pIONM in the OR undergoes constant refinement. Currently, the intraoperative preparation of the methodological setup requires additional operational time. In order to perform DNS, the surgeon needs to interrupt the preparation of the tumor, retract one laparoscopic surgical tool, and insert a stimulation probe into the operative field. The integrity of the nerves is monitored intermittently – only during time slots reserved for electric stimulation. pIONM is also a means to identify the nerves within the operative field. When it comes to function monitoring, pIONM may be used to inform of already inflicted nerve damage. Long intervals between stimulation phases limit the extent to which the surgical procedure can be traced back to a specific step that caused the nerve damage. A warning of impending nerve damage is also limited. Introducing continuous stimulation using fixed electrodes might help overcome these obstacles.

Fixating stimulation electrodes on the back could be more practical during the surgery: it could be faster, less cumbersome, and would not come in contact with bodily fluids.

Stimulation could run in parallel with the surgery and the surgeon would not need to be involved in the process of stimulation. The method could help inform the surgeon on the integrity of nerves throughout the entire procedure.

This study is a step forward towards achieving continuous intraoperative neuromonitoring of the autonomic nervous system within the pelvic floor for the purposes of nerve sparing during total mesorectal excision.

7.4 Recommendations for future research

The presented research involved an experimental study that investigated the feasibility of transcutaneous electrical nerve stimulation for monitoring of the autonomic nerves of the pelvic floor. All the conclusions drawn from this study relate only to the porcine animal model. Future research should focus on reproducing these insights within the human in a clinical study.

Moreover, the study has shown that functional monitoring of the nerve integrity using transcutaneous electrical nerve stimulation is possible only under very specific and varying circumstances. These circumstances could only be identified by actually inflicting targeted nerve damage of the hypogastric plexus. But how to identify which electrode configuration is sensitive to nerve damage without damaging the nerve? Are there any traits in the signal suggestive of impending nerve damage? Future research should focus on finding the answer to these questions.

References

[1] A. Klimczak et al. “Incidence of colorectal cancer in Poland in 1999-2008.” In: *Archives of medical science : AMS* 7.4 (2011), pp. 673–8.

[2] D. Schottenfeld and J. F. Fraumeni. *Cancer epidemiology and prevention*. Oxford University Press, (2006), pp. 1392.

[3] ACS. *American Cancer Society. Cancer Facts & Figures 2016*. 2016. URL: https://www.cancer.org/research/cancer-facts-statistics/all-cancer-facts-figures/cancer-facts-figures-2016.html (visited on 10/03/2016).

[4] PTO. *Obecny Stan Zwalczania Nowotworów w Polsce*. (2014). URL: http://walkazrakiem.pl/sites/default/files/library/files/obecny_stan_zwalczania_nowotworow_w_polsce_10-07-2014.pdf.

[5] B. Cagir. *Rectal Cancer: Practice Essentials, Background, Pathophysiology*. 2016. URL: https://emedicine.medscape.com/article/281237-overview (visited on 10/03/2016).

[6] M. M. Lange et al. “Urinary dysfunction after rectal cancer treatment is mainly caused by surgery”. In: *British Journal of Surgery* 95.8 (2008), pp. 1020–1028.

[7] C. Wallner et al. “Causes of fecal and urinary incontinence after total mesorectal excision for rectal cancer based on cadaveric surgery: A study from the cooperative clinical investigators of the Dutch total mesorectal excision trial”. In: *Journal of Clinical Oncology* 26.27 (2008), pp. 4466–4472.

[8] R. S. Hollabaugh et al. “Neuroanatomy of the pelvis: implications for colonic and rectal resection.” In: *Diseases of the colon and rectum* 43 (2000), pp. 1390–1397.

[9] F. Aigner et al. “The rectogenital septum: morphology, function, and clinical relevance.” In: *Diseases of the colon and rectum* 47.2 (2004), pp. 131–40.

[10] W. Kneist, A. Heintz, and T. Junginger. “Major urinary dysfunction after mesorectal excision for rectal carcinoma”. en. In: *British Journal of Surgery* 92.2 (2005), pp. 230–234.

[11] A. D. Rink et al. “Evaluation of vector manometry for characterization of functional outcome after restorative proctocolectomy”. In: *International Journal of Colorectal Disease* 23.8 (2008), pp. 807–815.

[12] A. D. Rink et al. “Differences in ano-neorectal physiology of ileoanal and coloanal reconstructions for restorative proctectomy.” In: *Colorectal disease : the official journal of the Association of Coloproctology of Great Britain and Ireland* 12.4 (2010), pp. 342–50.

[13] V. Lent and T. Junginger. “Nervenstörungen der Harnblasen- und Sexualfunktionen nach Rektumresektionen und -extirpationen”. In: *Chirurgische Allgemeine Zeitung* 12 (2011), pp. 257–261.

[14] Y. Moriya. “Nerve-sparing surgery: surgical neuroanatomy and techniques”. In: *Rectal Cancer Surgery: Optimisation, Standardisation, Documentation*. Ed. by O. Søreide and J. Norstein. 1st. Berlin, New York: Springer, (1997).

[15] Nanda Kishore Maroju. *Total Mesorectal Excision: Overview, Periprocedural Care, Technique*. 2016. URL: http://emedicine.medscape.com/article/1893507-overview (visited on 10/25/2016).

[16] J. C. Coffey and D. P. O’Leary. “The mesentery: structure, function, and role in disease”. In: *The Lancet Gastroenterology & Hepatology* 1.3 (2016), pp. 238–247.

[17] N. Runkel and H. Reiser. “Nerve-oriented mesorectal excision (NOME): autonomic nerves as landmarks for laparoscopic rectal resection”. In: *International Journal of Colorectal Disease* 28.10 (2013), pp. 1367–1375.

[18] W. Kneist and T. Junginger. “Intraoperative electrostimulation objectifies the assessment of functional nerve preservation after mesorectal excision”. en. In: *International Journal of Colorectal Disease* 22.6 (2007), pp. 675–682.

[19] B. Baader and M. Herrmann. “Topography of the pelvic autonomic nervous system and its potential impact on surgical intervention in the pelvis”. In: *Clinical Anatomy* 16.2 (2003), pp. 119–130.

[20] C. Loftus, J. Biller, and E. Baron. *Intraoperative Neuromonitoring*. 1st. McGraw-Hill Education / Medical, (2013).

[21] W. Kneist and D. W. Kauff. “Intraoperative Neuromonitoring”. en. In: *Handbook of Medical Technology*. Ed. by R. Kramme, K.-P. Hoffmann, and R. S. Pozos. Springer Berlin Heidelberg, (2011), pp. 1043–1058.

[22] F. Aigner et al. “Anatomical considerations for transanal minimal-invasive surgery: the caudal to cephalic approach”. In: *Colorectal Disease* 17.2 (2015), O47–O53.

[23] W. Kneist et al. “Intraoperative pelvic nerve stimulation performed under continuous electromyography of the internal anal sphincter”. In: *International Journal of Colorectal Disease* 25.11 (2010), pp. 1325–1331.

[24] D. W. Kauff et al. “Evaluation of two-dimensional intraoperative neuromonitoring for predicting urinary and anorectal function after rectal cancer surgery”. en. In: *International Journal of Colorectal Disease* 28.5 (2013), pp. 659–664.

[25] W. Kneist et al. “Selective pelvic autonomic nerve stimulation with simultaneous intraoperative monitoring of internal anal sphincter and bladder innervation”. en. In: *European Surgical Research* 46.3 (2011), pp. 133–138.

[26] W. Kneist et al. “Inferior rectal plexus is no longer isolated in no man’s land”. In: *coloproctology* 39.2 (2017), pp. 85–87.

[27] D. W. Kauff, H. Lang, and W. Kneist. “Risk factor analysis for newly developed urogenital dysfunction after total mesorectal excision and impact of pelvic intraoperative neuromonitoring? a prospective 2-year follow-up study”. In: *Journal of Gastrointestinal Surgery* September 2016 (2017), pp. 1–10.

[28] D. W. Kauff et al. “Continuous intraoperative monitoring of pelvic autonomic nerves during TME to prevent urogenital and anorectal dysfunction in rectal cancer patients (NEUROS): a randomized controlled trial”. In: *BMC Cancer* 16 (2016), pp. 323.

[29] W. Kneist et al. “Topography of the extrinsic internal anal sphincter nerve supply during laparoscopic-assisted TAMIS TME: Five key zones of risk from the surgeons’ view”. In: *International Journal of Colorectal Disease* 30.1 (2014), pp. 71–78.

[30] M. Grade et al. “Pelvic intraoperative neuromonitoring during robotic-assisted low anterior resection for rectal cancer”. In: *Journal of Robotic Surgery* 10 (2015), pp. 157–160.

[31] W. Kneist et al. “Surgeons’ assessment of internal anal sphincter nerve supply during TaTME - inbetween expectations and reality”. In: *Minimally Invasive Therapy & Allied Technologies* (2016), pp. 1–6.

[32] W. E. Enker et al. “Total mesorectal excision in the operative treatment of carcinoma of the rectum.” In: *Journal of the American College of Surgeons* 181.4 (1995), pp. 335–46.

[33] A. L. DeSouza et al. “Total mesorectal excision for rectal cancer: the potential advantage of robotic assistance”. In: *Diseases of the Colon & Rectum* 53.12 (2010), pp. 1611–1617.

[34] D. W. Kauff et al. “Electrophysiology-based quality assurance of nerve-sparing in laparoscopic rectal cancer surgery: Is it worth the effort?” In: *Surgical Endoscopy* 30.10 (2016), pp. 4525–4532.

[35] D. Kauff et al. “Minimal invasive pelvic neuromonitoring - technical demands and requirements”. In: *Biomedical Engineering* 58.1 (2013), pp. 24–25.

[36] J Jonas and A Boskovic. “Intraoperative neuromonitoring for recurrent laryngeal nerve protection: comparison of intermittent and continuous nerve stimulation”. In: *Surg Technol Int* 24 (2014), pp. 133–8.

[37] R. Schneider et al. “Evolution of nerve injury with unexpected EMG signal recovery in thyroid surgery using continuous intraoperative neuromonitoring”. In: *World Journal of Surgery* 37.2 (2013), pp. 364–368.

[38] R. Schneider et al. “A new anchor electrode design for continuous neuromonitoring of the recurrent laryngeal nerve by vagal nerve stimulations”. In: *Langenbeck’s Archives of Surgery* 394.5 (2009), pp. 903–910.

[39] S. Van Slycke et al. “Initial experience with S-shaped electrode for continuous vagal nerve stimulation in thyroid surgery”. In: *Langenbeck’s Archives of Surgery* 398.5 (2013), pp. 717–722.

[40] E. Phelan et al. “Continuous vagal IONM prevents recurrent laryngeal nerve paralysis by revealing initial EMG changes of impending neuropraxic injury: A prospective, multicenter study”. In: *Laryngoscope* 124.6 (2014), pp. 1498–1505.

[41] D. W. Kauff et al. “Continuous intraoperative monitoring of autonomic nerves during low anterior rectal resection: an innovative approach for observation of functional nerve integrity in pelvic surgery.” In: *Langenbeck’s archives of surgery / Deutsche Gesellschaft für Chirurgie* 397.5 (2012), pp. 787–92.

[42] T. Gross et al. “Transcutaneous electrical nerve stimulation for treating neurogenic lower urinary tract dysfunction: a systematic review”. In: *European Urology* 69 (2016), pp. 1102–1111.

[43] F Heid et al. “Impact of inhalation vs. intravenous anaesthesia on autonomic nerves and internal anal sphincter tone.” In: *Acta anaesthesiologica Scandinavica* (2015), pp. 1–7.

[44] A. Christ et al. “The Virtual Family—development of surface-based anatomical models of two adults and two children for dosimetric simulations”. en. In: *Physics in Medicine and Biology* 55.2 (2010), N23.

[45] T. Moszkowski et al. “Modeling the pelvic region for non-invasive pelvic intraoperative neuromonitoring”. In: *Current Directions in Biomedical Engineering* 2.1 (2016), pp. 185–188.

[46] J Sokołowska-Pituchowa. *Anatomia człowieka*. Wydawnictwo Lekarskie PZWL, 2006.

[47] F. Aigner. “Clinical anatomy of the pelvic floor.” In: *Acta chirurgica Iugoslavica* 53.2 (2006), pp. 11–3.

[48] M Dannhauer et al. “A pipeline for the simulation of transcranial direct current stimulation for realistic human head models using SCIRun and BioMesh3D”. In: *Proceedings of IEEE Engineering in Medicine and Biology Society* c (2012), pp. 5486–5489.

[49] K. S. Cheng et al. “Electrode models for electric current computed tomography”. In: *IEEE Transactions on Biomedical Engineering* 36.9 (1989), pp. 918–924.

[50] P. Hasgall et al. *IT’IS Database for thermal and electromagnetic parameters of biological tissues*. 2015. URL: https://www.itis.ethz.ch/virtual-population/tissue-properties/overview/.

[51] Y. Saad. “Parallel iterative methods for sparse linear systems”. In: *Studies in Computational Mathematics* 8.C (2001), pp. 423–440.

[52] M. L. Hines and N. T. Carnevale. “The NEURON simulation environment.” In: *Neural computation* 9.6 (1997), pp. 1179–1209.

[53] M. H. Brill et al. “Conduction velocity and spike configuration in myelinated fibres: computed dependence on internode distance.” In: *Journal of neurology, neurosurgery, and psychiatry* 40.8 (1977), pp. 769–74.

[54] T. Carnevale. *Point Processes and Artificial Cells — NEURON documentation*. URL: https://www.neuron.yale.edu/neuron/static/new_doc/modelspec/programmatic/mechanisms/mech.html (visited on 12/29/2016).

[55] D. W. Kauff et al. “Online signal processing of internal anal sphincter activity during pelvic autonomic nerve stimulation: A new method to improve the reliability of intraoperative neuromonitoring signals”. In: *Colorectal Disease* 13 (2011), pp. 1422–1427.

[56] M. L. Hines, N. T. Carnevale, and M. L. Hines. “The NEURON Simulation Environment”. In: (2002), pp. 1–9.

[57] D. W. Kauff et al. “Surface electromyography reliably records electrophysiologically evoked internal anal sphincter activity: a more minimally invasive approach for monitoring extrinsic innervation”. In: *European surgical research. Europaische chirurgische Forschung. Recherches chirurgicales europeennes* 57.1-2 (2016), pp. 81–88.

[58] D. W. Kauff et al. “Transcutaneous sacral nerve stimulation for intraoperative verification of internal anal sphincter innervation”. In: *Neurogastroenterology & Motility* (2017), e13140.

[59] T. Moszkowski et al. “Extracorporeal stimulation of sacral nerve roots for observation of pelvic autonomic nerve integrity: Description of a novel methodological setup”. In: *IEEE Transactions on Biomedical Engineering* (2017), pp. 1–1.

[60] T. O’Haver. *A pragmatic introduction to signal processing: Peak Finding and Measurement*. 2017. URL: https://terpconnect.umd.edu/~toh/spectrum/PeakFindingandMeasurement.htm (visited on 01/22/2017).

[61] F. Rattay, K. Minassian, and M. R. Dimitrijevic. “Epidural electrical stimulation of posterior structures of the human lumbosacral cord: 2. quantitative analysis by computer modeling.” In: *Spinal Cord* 38.8 (2000), pp. 473–89.

[62] J. Holsheimer. “Which neuronal elements are activated directly by spinal cord stimulation”. In: *Neuromodulation: Technology at the Neural Interface* 5.1 (2002), pp. 25–31.

[63] A. Hirata et al. “Computation of induced electric field for the sacral nerve activation”. en. In: *Physics in Medicine and Biology* 58.21 (2013), pp. 7745.

[64] I. Laakso et al. “Multi-scale simulations predict responses to non-invasive nerve root stimulation”. In: *Journal of Neural Engineering* 11.5 (2014), p. 056013.

[65] W. Kneist et al. “Total Mesorectal Excision with Intraoperative Assessment of Internal Anal Sphincter Innervation Provides New Insights into Neurogenic Incontinence”. In: *Journal of the American College of Surgeons* 214.3 (2012), pp. 306–312.

[66] W. Kneist et al. “Intraoperative monitoring of bladder and internal anal sphincter innervation: a predictor of erectile function following low anterior rectal resection for rectal cancer? Results of a prospective clinical study”. In: *Digestive surgery* 30.4-6 (2013), pp. 459–465.

[67] S. Bock et al. “First experiences with pudendal nerve stimulation in fecal incontinence: A technical report”. In: *Techniques in Coloproctology* 14.1 (2010), pp. 41–44.

[68] S. Engelberg et al. “Sacral neuromodulation - evolution of techniques, procedures and outlook into the future”. In: *Biomedical Engineering / Biomedizinische Technik* 59.s1 Track E (2014), pp. 352–355.

[69] M. Possover, J. Baekelandt, and V. Chiantera. “The laparoscopic implantation of neuroprothesis (LION) procedure to control intractable abdomino-pelvic neuralgia”. In: *Neuromodulation* 10.1 (2007), pp. 18–23.

[70] T. Bennett. “Nerve-mediated excitation and inhibition of the avian gizard”. In: *Journal of Physiology* 204 (1969), pp. 669–686.

[71] B. Y. M. Bouvier and J Gonella. “Nervous control of the internal anal sphincter of the cat”. In: *Journal of Physiology* 310 (1981), pp. 457–469.

[72] D Kirk. “An electrophysiological study of the smooth muscle of the human colon.” In: *Ann R Coll Surg Engl* 63.6 (1981), pp. 393–8.

[73] J. H. Waldhausen et al. “Gastrointestinal myoelectric and clinical patterns of recovery after laparotomy.” In: *Annals of surgery* 211.6 (1990), pp. 777–784.

[74] J. B. Furness. “An electrophysiological study of the innervation of the smooth muscle of the colon.” In: *The Journal of physiology* 205.3 (1969), pp. 549–62.

[75] J Gonella, J. P. Niel, and C Roman. “Vagal control of lower oesophageal sphincter motility in the cat.” In: *The Journal of physiology* 273.3 (1977), pp. 647–64.

[76] T. Keller and A. Kuhn. “Electrodes for transcutaneous (surface) electrical stimulation”. In: *Journal of Automatic Control* 18.2 (2008), pp. 35–45.

[77] D. Kauff et al. “Laparoscopic pelvic neuromonitoring permits superior nerve sparing”. In: *Biomedical engineering* 59 Suppl 1 (2014), pp. 326–84.

[78] W. C. Bowman. “Neuromuscular block”. In: *British journal of pharmacology* Suppl 1 (2006), pp. 277–86.

[79] F. Marusch et al. “Influence of muscle relaxation on neuromonitoring of the recurrent laryngeal nerve during thyroid surgery”. In: *British Journal of Anaesthesia* 94.5 (2005), pp. 596–600.

[80] K.-S. Chu et al. “Feasibility of intraoperative neuromonitoring during thyroid surgery after administration of nondepolarizing neuromuscular blocking agents”. In: *World Journal of Surgery* 33.7 (2009), pp. 1408–1413.

[81] K.-S. Chu et al. “Influence of nondepolarizing muscle relaxants on intraoperative neuromonitoring during thyroid surgery.” In: *Journal of otolaryngology - head & neck surgery = Le Journal d’oto-rhino-laryngologie et de chirurgie cervico-faciale* 39.4 (2010), pp. 397–402.

[82] I.-C. Lu et al. “A comparative study between 1 and 2 effective doses of rocuronium for intraoperative neuromonitoring during thyroid surgery”. In: *Surgery* 149.4 (2011), pp. 543–548.

[83] O. Empis de Vendin et al. “Recurrent laryngeal nerve monitoring and rocuronium: a selective sugammadex reversal protocol”. In: *World Journal of Surgery* (2017), pp. 1–6.

[84] R Bhardwaj et al. “Neuromyogenic properties of the internal anal sphincter: therapeutic rationale for anal fissures.” In: *Gut* 46.6 (2000), pp. 861–8.

[85] D. W. Kauff et al. “Impact of selective surgical pelvic autonomic nerve damage on the evoked neuromonitoring signal of the internal anal sphincter”. In: *Biomedizinische Technik. Biomedical engineering* 57.Suppl. 1 (2012), pp. 439 –442.

[86] A. Climent et al. “Multimodal intraoperative evoked potential monitoring (IOM) for hip surgery”. In: *Clinical Neurophysiology* 125.5 (2014), e16.

[87] F. Rattay et al. “Finite Element Modeling for Extracellular Stimulation”. In: *Encyclopedia of Computational Neuroscience* 0.Massaro 1975 (2013), pp. 1–6. arXiv: 1501.01854.

[88] A. Kuhn et al. “A model for transcutaneous current stimulation: simulations and experiments”. In: *Medical & Biological Engineering & Computing* 47.3 (2009), pp. 279–289.

[89] S. Miocinovic et al. “Experimental and theoretical characterization of the voltage distribution generated by deep brain stimulation”. In: *Experimental Neurology* 216.1 (2009), pp. 166–176.

[90] J. Gomez-Tames, J. Gonzalez, and W. Yu. “A simulation study: Effect of the inter-electrode distance, electrode size and shape in Transcutaneous Electrical Stimulation”. In: *34th Annual International Conference of the IEEE EMBS, San Diego, California, USA*. (2012), pp. 3576–3579.

Appendix A

Software for automated stimulation

This appendix describes the source code of the software for automated stimulation. The software allowed programming stimulation procedures using the ISIS Neurostimulator (inomed Medizintechnik GmbH, Emmendingen, Germany). Each stimulation made use of a ten-electrode stimulation array and a sequence of pre-programmed stimulation parameters. Figure A.1 depicts a simplified diagram of the state machine forming the backbone of the software. Figures A.3 to A.9 depict the code underlying each machine state.

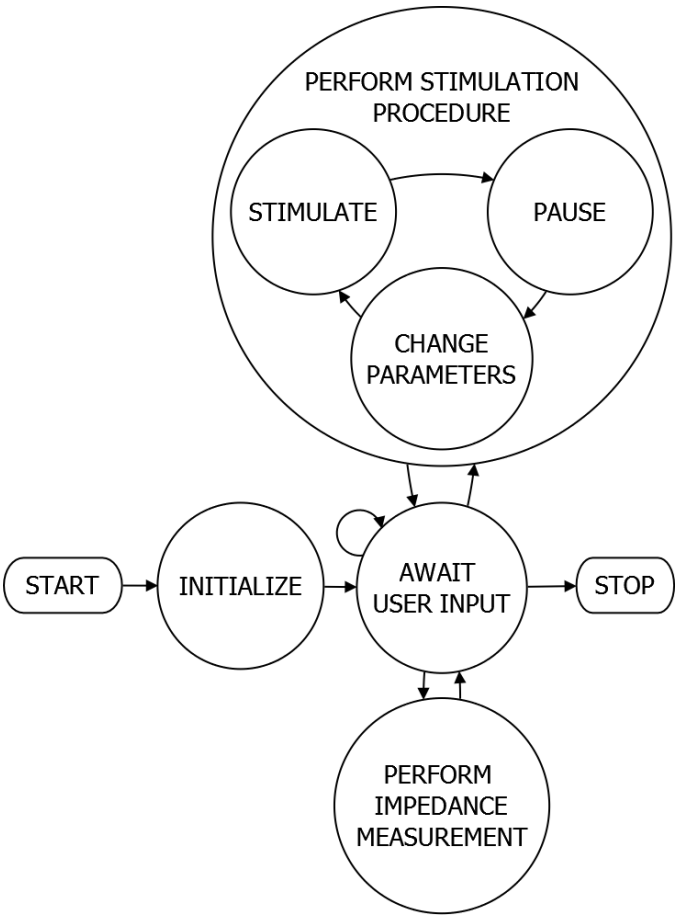

Figure A.1 Simplified state machine diagram of the software for automated stimulation. The software operates based on a state machine controlled by a software counter. The counter allows to perform timed stimulation procedures. User input determines the timing and stimulation parameters.

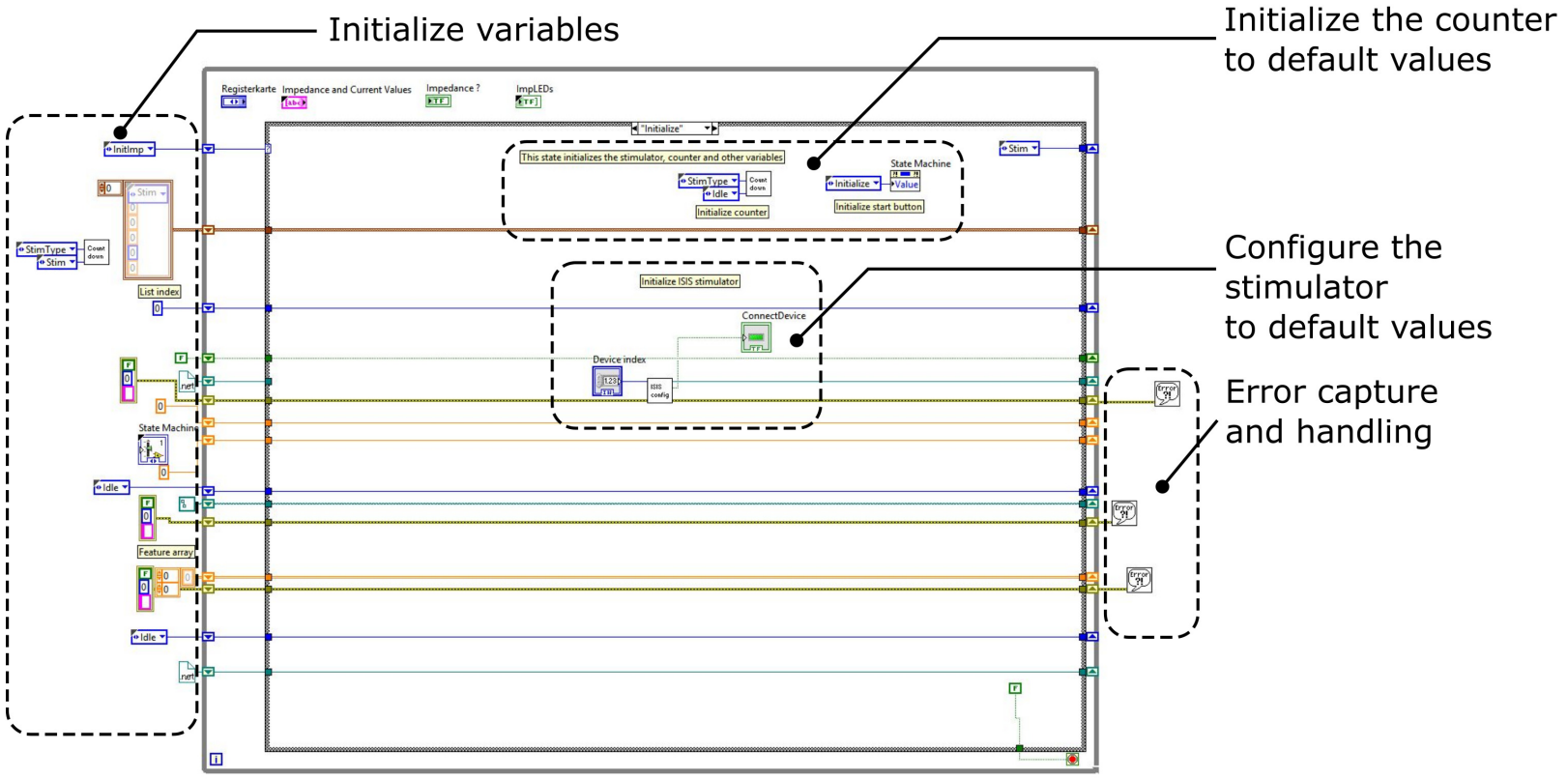

Figure A.2 Machine state: Initialize. This state sets the software variables into their default values, prepares the stimulator for operation, and prepares the software for error handling. A state machine architecture comprises the backbone of the software according to LabVIEW programing standard practice.

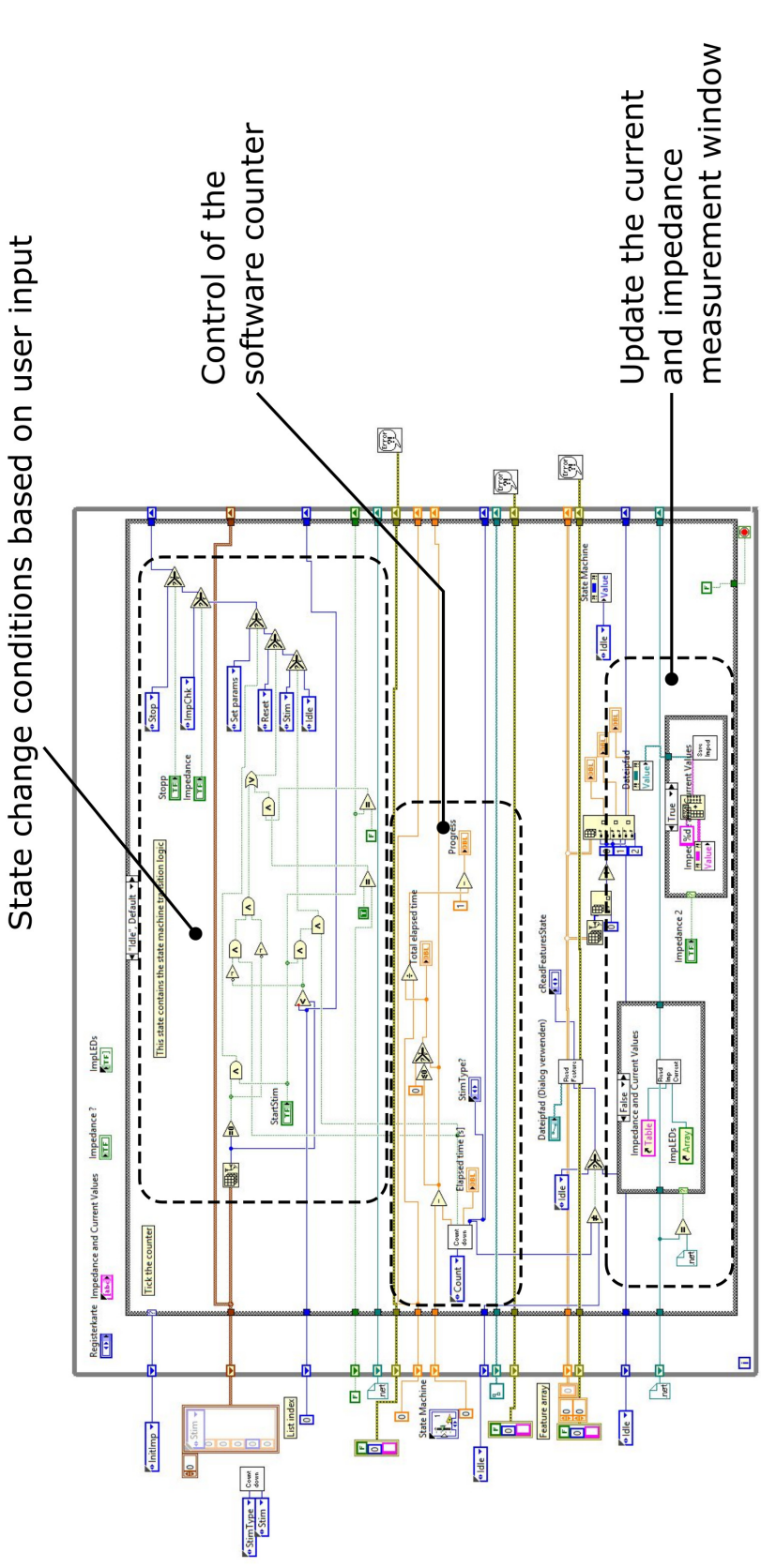

Figure A.3 Machine state: Idle. This states awaits the user's command to perform either a stimulation procedure, an impedance measurement or stopping the execution of the program. The "Idle" state contains the logic controlling the transition from state to state.

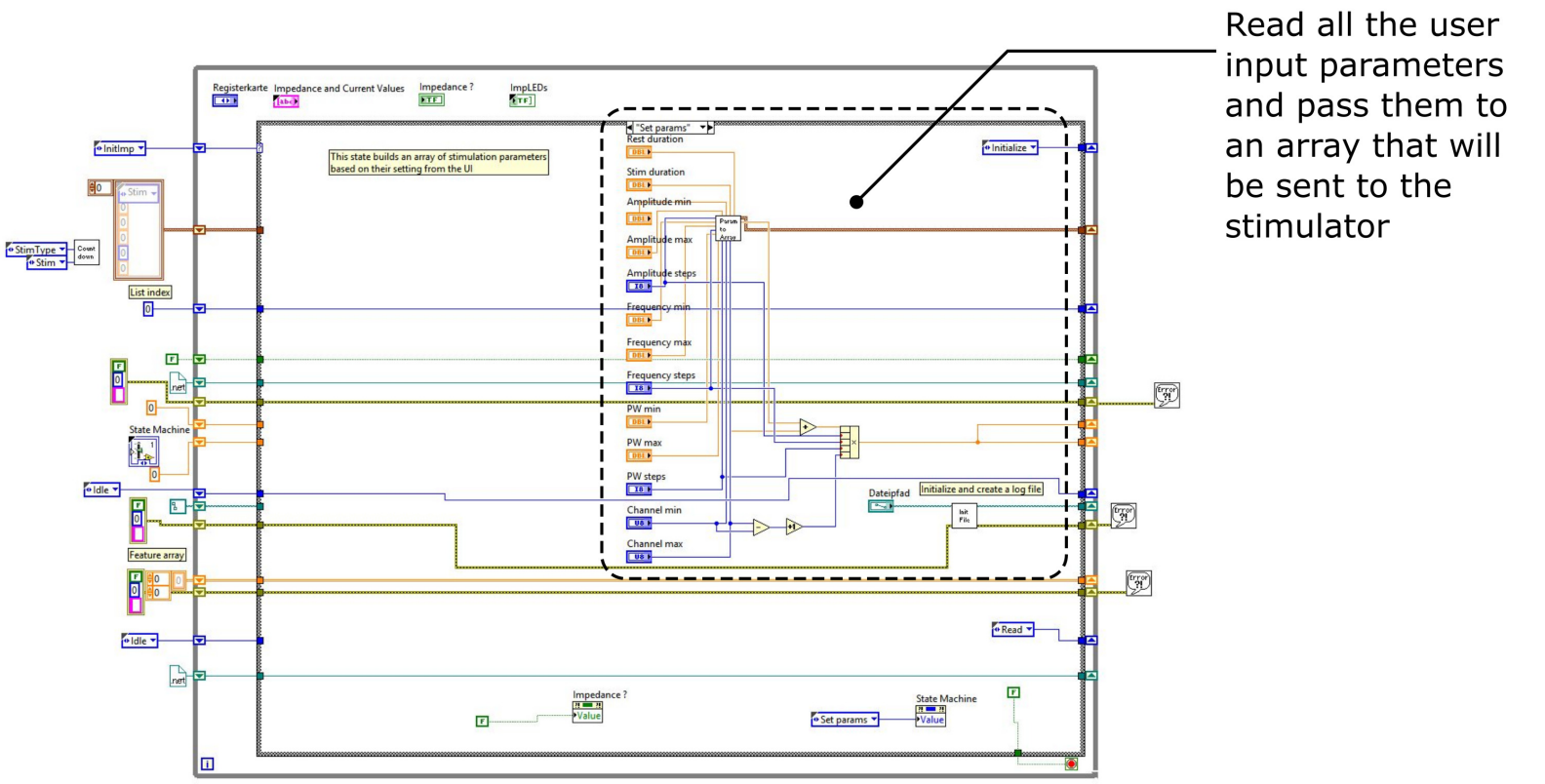

Figure A.4 Machine state: Set parameters. This state reads the stimulation parameters that the user passed to the software using the graphical user interface (GUI). The parameters are subsequently clustered and passed to the next state. This happens once the user has pressed the "Start stimulation" button on the GUI.

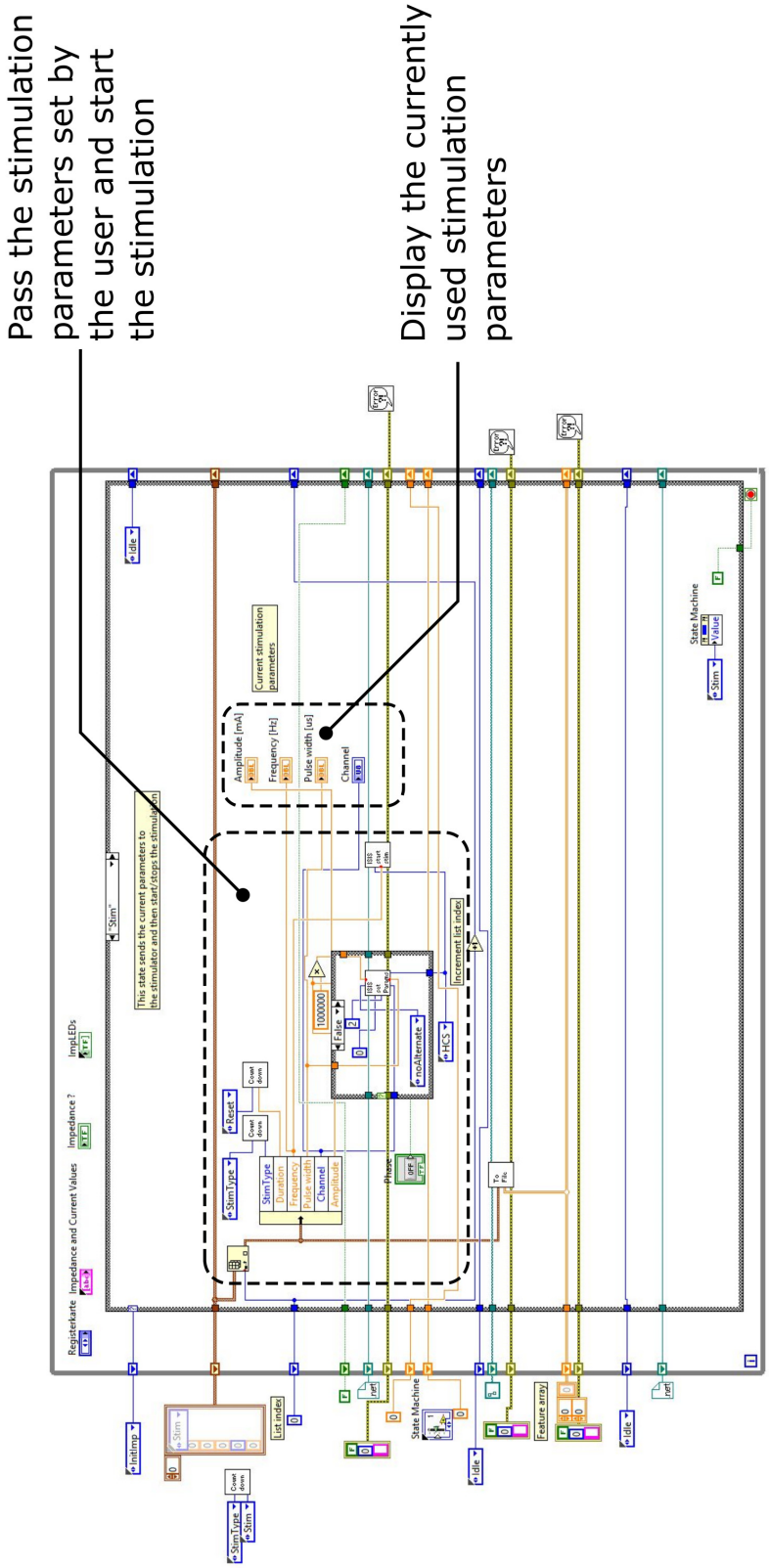

Figure A.5 Machine state: Stimulate. This state passes the set of stimulation parameters into the ISIS Neurostimulator (inomed Medizintechnik GmbH, Emmendingen, Germany) using a proprietary USB-Human Interface Device library. This library allows to pass low-level commands into the stimulator.

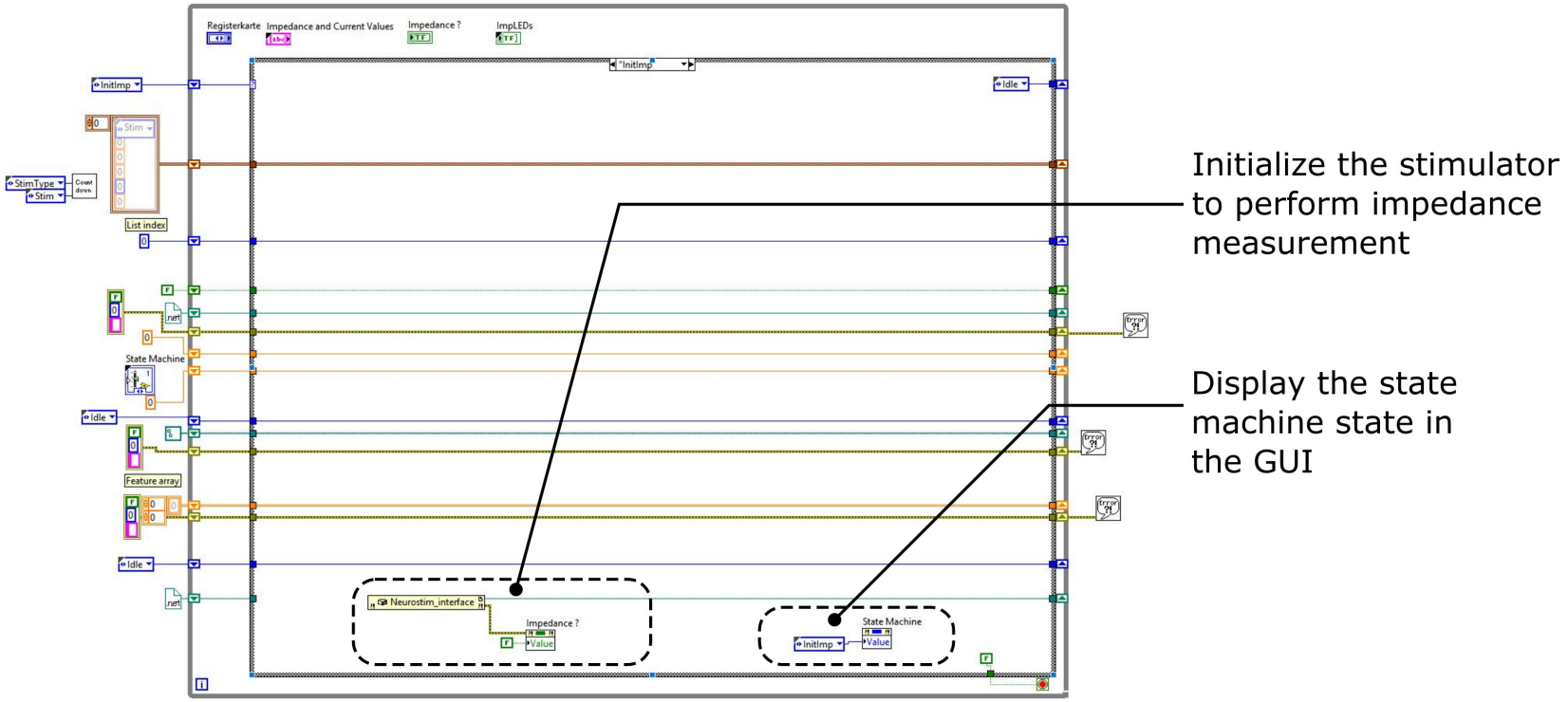

Figure A.6 Machine state: Initialize impedance measurement. This state passes a command to the stimulator to initialize the impedance measurement.

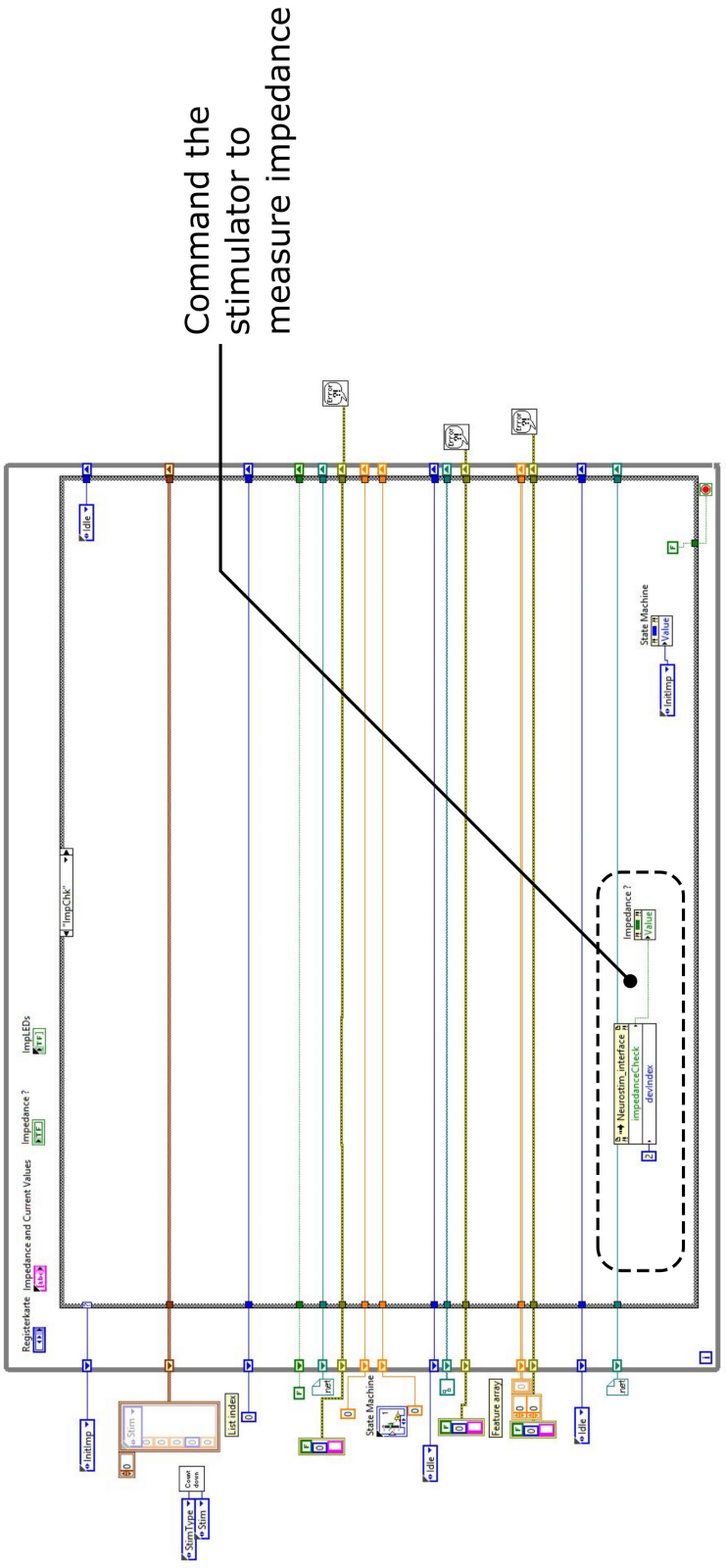

Figure A.7 Machine state: Impedance check. This state sends a command to the stimulator to commence an impedance measurement on all stimulator channels. This happens continuously unless aborted by the user.

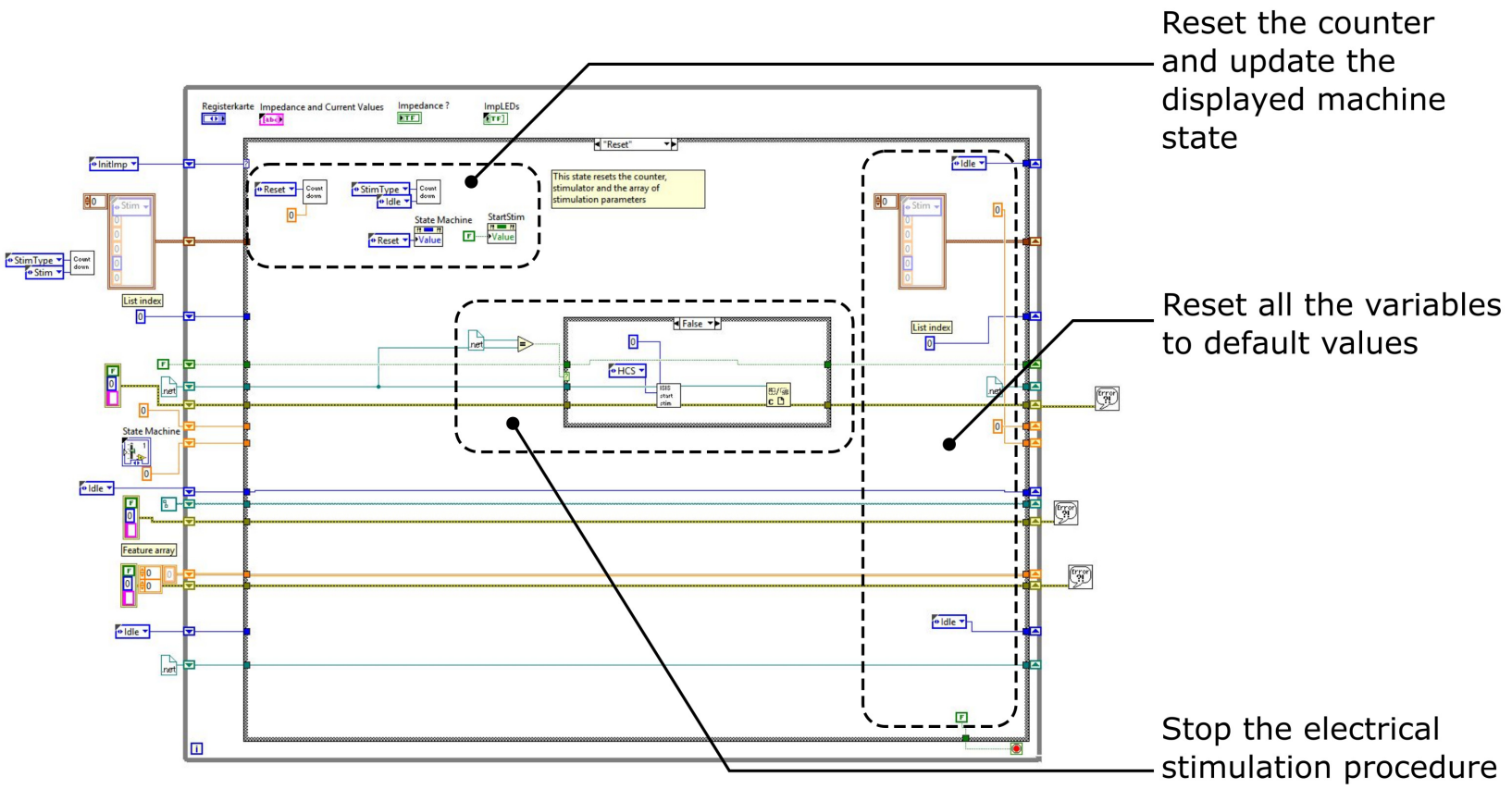

Figure A.8 Machine state: Reset. This state is used after the execution of the stimulation to reset the software counter and stimulator. This allows to stop the stimulation and get ready for a pause period.

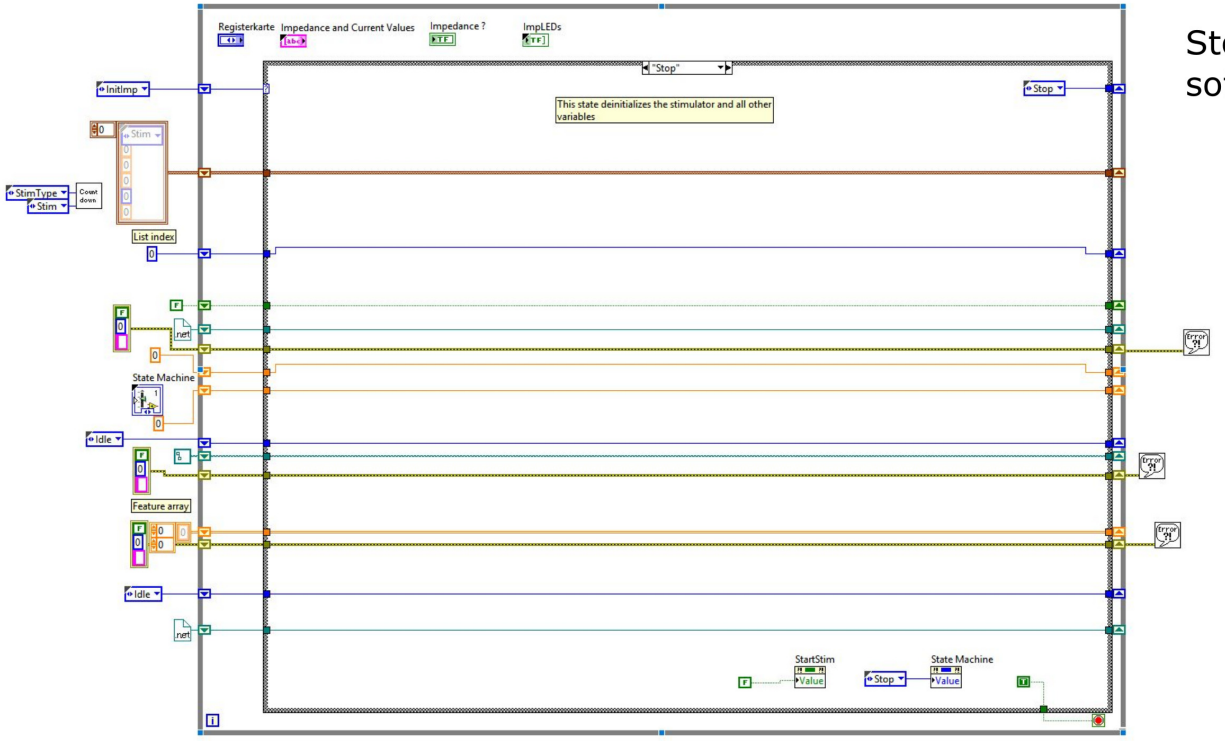

Stop the execution of the software

Figure A.9 Machine state: Stop. This machine state executes once the user has used the button "Stop." This stops the execution of the software.

Appendix B

Electrical field projected onto the nerve fiber model

This appendix summarizes the electrical field projected onto the nerve fiber model. The projected electric field is a result of the finite element simulation of the direct nerve stimulation (DNS) and transcutaneous electrical nerve stimulation (TENS).

B.1 Direct nerve stimulation

Table B.1 summarizes the scenarios of DNS when the nerve fibers were exposed to significant electric field as modeled using the finite element method. Figure B.1 shows the electric field projected as an extracellular potential along the length of the nerve fibers during direct nerve stimulation. Figure B.2 exemplifies one of multiple situations when the direct stimulation of one nerve had a negligible effect on the electric field observed along a nerve placed in a distance to the stimulation site (e.g. the electric field along the right hypogastric nerve during stimulation of the left S2 pelvic splanchnic nerve).

Table B.1 Annotation of the stimulation and recording sites corresponding to the electrical field projected onto the nerve fibers during simulated direct nerve stimulation. Legend: PSN – pelvis splanchnic nerve, NH – hypogastric nerve, IHP – inferior hypogastric plexus, IAS – internal anal sphincter

Subfigure	Scenario no.	Recording site	Stimulation site
a)	0	left S2 PSN	left S2 PSN
b)	1	right S2 PSN	right S2 PSN
c)	2	left IAS inneravtion (S3)	left S3 PSN
d)	2	left pudendal nerve	left S3 PSN
e)	3	right IAS innervation (S3)	right S3 PSN
f)	3	right pudendal nerve	right S3 PSN
g)	4	left S4 PSN	left S4 PSN
h)	5	right S4 PSN	right S4 PSN
i)	6	left bladder innervation	left NH (S2 level)
j)	7	right bladder innervation	right NH (S2 level)
k)	8	right S2 PSN	right IHP
l)	8	right IAS innervation (S3) PSN	right IHP
m)	8	right S4 PSNve	right IHP
n)	8	right NH	right IHP
o)	9	left S2 PSN	left IHP
p)	9	left IAS innervation (S3)	left IHP
q)	9	left S4 PSN	left IHP
r)	9	left bladder innervation	left IHP

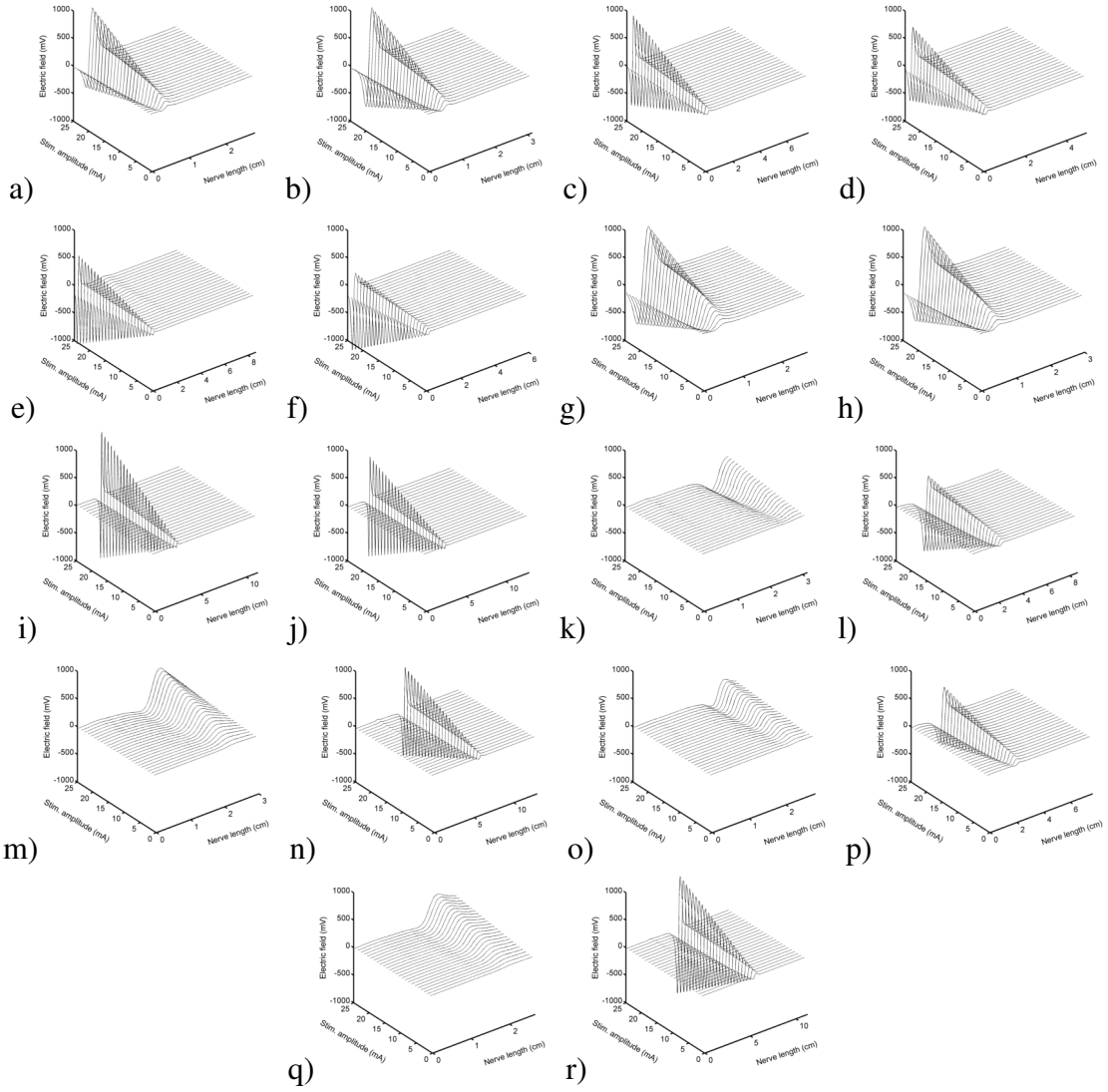

Figure B.1 Extracellular electric field projected onto the nerve fiber models during direct nerve stimulation. This figure shows only the situations where significant extracellular electric potential was observed. See Table B.1 for detailed description regarding the figure annotation

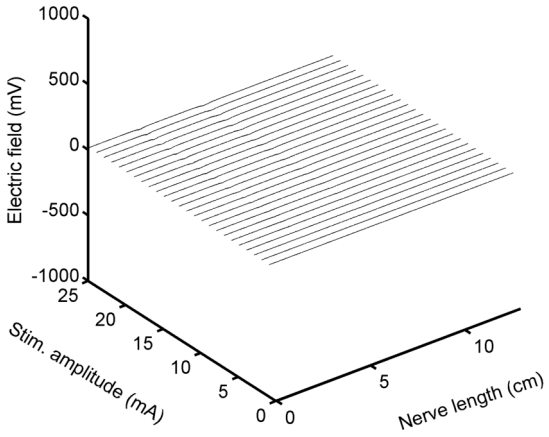

Figure B.2 An example of the projected electric field from a nerve (left hypogastric nerve model) which was not directly stimulated. Regardless of the stimulation amplitude, there is no significant increase of electric potential along the length of the nerve

B.2 Transcutaneous electrical nerve stimulation

Table B.2 summarizes the scenarios of TENS when the nerve fibers were exposed to significant electric field as modeled using the finite element method. Figure B.3 shows the electric field projected as an extracellular potential along the length of the right hypogastric nerve model for four different anode positions. Figure B.4 shows the electric field projected onto the right hypogastric nerve model for ten different cathode positions and a fixed anode position.

Table B.2 Annotation of the stimulation and recording sites corresponding to the electrical field projected onto the nerve fibers during simulated transcutaneous electrical nerve stimulation. Legend: PSN – pelvis splanchnic nerve, NH – hypogastric nerve, IHP – inferior hypogastric plexus, IAS – internal anal sphincter

Subfigure	Scenario no.	Recording site	Stimulation site
a)	0	left S2 PSN	left S2 PSN
b)	1	right S2 PSN	right S2 PSN
c)	2	left IAS inneravtion (S3)	left S3 PSN
d)	2	left pudendal nerve	left S3 PSN
e)	3	right IAS innervation (S3)	right S3 PSN
f)	3	right pudendal nerve	right S3 PSN
g)	4	left S4 PSN	left S4 PSN
h)	5	right S4 PSN	right S4 PSN
i)	6	left bladder innervation	left NH (S2 level)
j)	7	right bladder innervation	right NH (S2 level)
k)	8	right S2 PSN	right IHP
l)	8	right IAS innervation (S3) PSN	right IHP
m)	8	right S4 PSN	right IHP
n)	8	right NH	right IHP
o)	9	left S2 PSN	left IHP
p)	9	left IAS innervation (S3)	left IHP
q)	9	left S4 PSN	left IHP
r)	9	left bladder innervation	left IHP

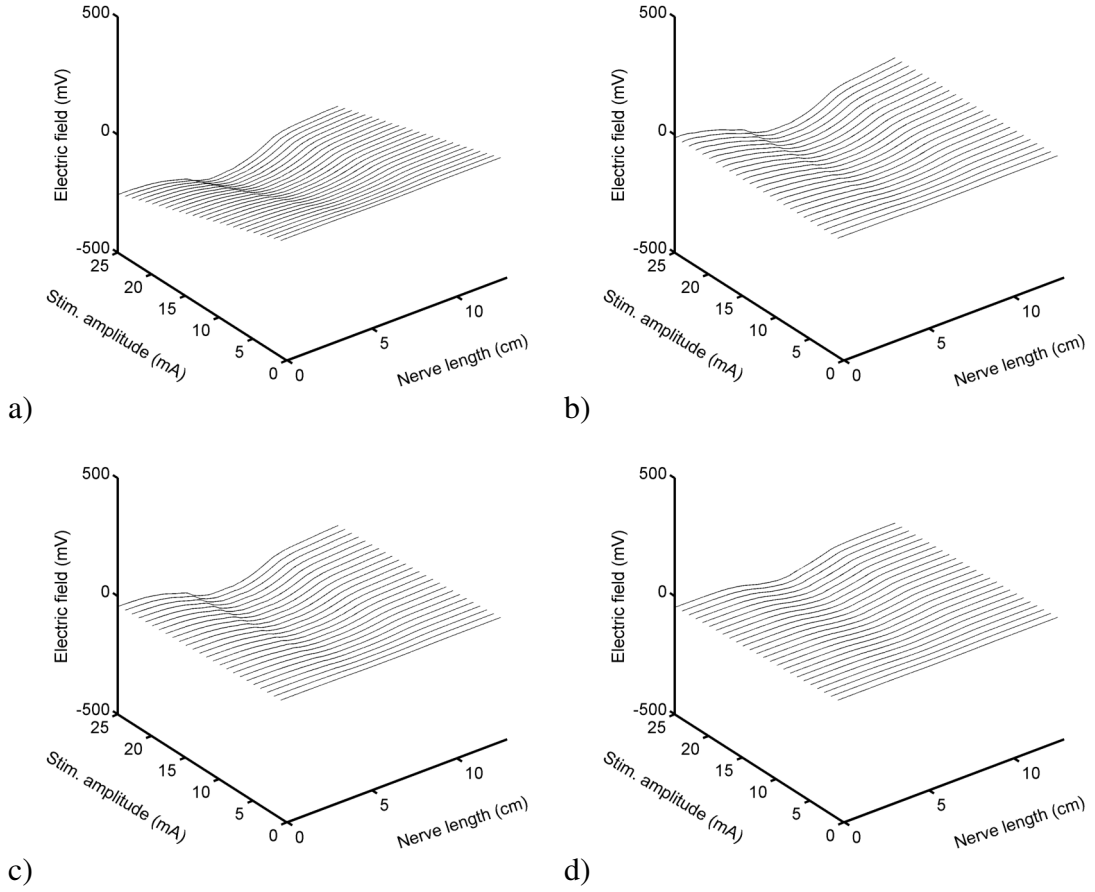

Figure B.3 Extracellular electric field projected onto the right hypogastricus nerve model for four different anode positions during transcutaneous electrical nerve stimulation. This example shows results for four electrode configurations: a) cathode 9 vs. anode in the anal canal, b) cathode 9 vs. anode on the abdomen, c) cathode 9 vs. anode left, and d) cathode 9 vs. anode right

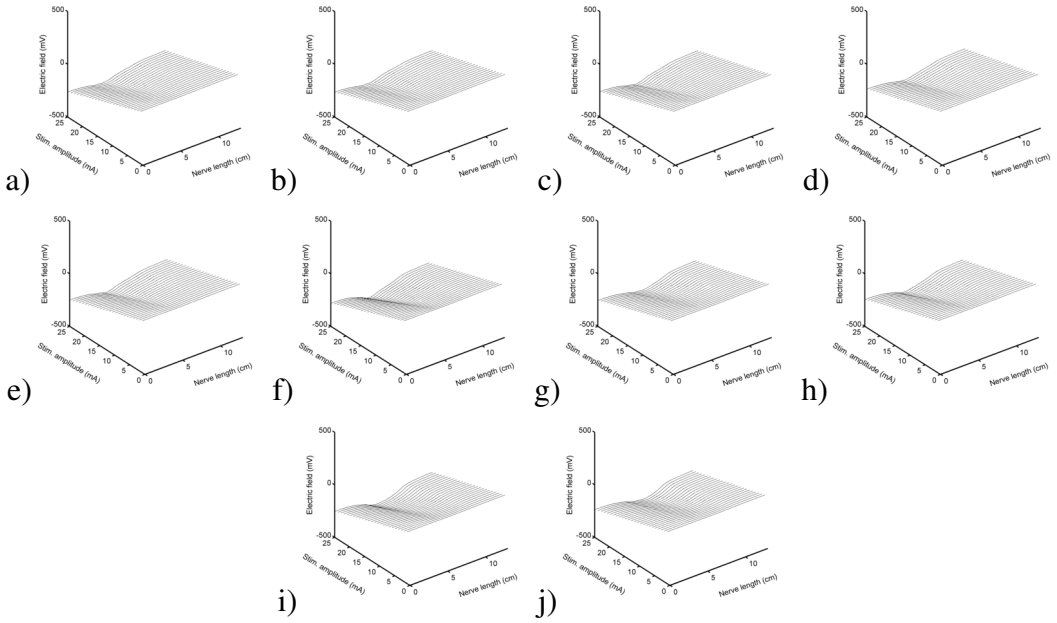

Figure B.4 Extracellular electric field projected onto the right hypogastric nerve fiber model for ten different cathode positions during transcutaneous electrical nerve stimulation. This example shows results for ten electrode configurations: a)-j) correspond the cathodes 1-10 during stimulation versus anode in the anal canal.

Appendix C

Modeled membrane potential resulting from extracellular stimuli

This appendix summarizes the time evolution of the modeled membrane potential resulting from the input extracellular stimuli generated during direct nerve stimulation (DNS) and transcutaneous electrical nerve stimulation (TENS). For a summary of the extracellular stimuli obtained from the finite element modeling, refer to Appendix B on page 149. In each case, the extracellular potential formed the basis for rectangular pulse stimulation (pulse width: 200 µs). Each simulation lasted 33 ms and the stimulation pulse was applied 1 ms after the beginning of each simulation. Each membrane potential was recorded from the distal end of each modeled nerve fiber.

C.1 Direct nerve stimulation before nerve incision

Figures C.1 and **??** summarize the membrane potentials generated during DNS before and after targeted nerve incision, respectively. Table C.1 summarizes the recording and stimulation sites for DNS. Only the bladder and IAS innervation underwent targeted nerve incision.

Table C.1 Annotation of the stimulation and recording sites corresponding to the evoked membrane potential in autonomic nerves during simulated direct nerve stimulation. Legend: PSN – pelvis splanchnic nerve, NH – hypogastric nerve, IHP – inferior hypogastric plexus, IAS – internal anal sphincter

Subfigure	Scenario no.	Recording site	Stimulation site
a)	0	left S2 PSN	left S2 PSN
b)	1	right S2 PSN	right S2 PSN
c)	2	left IAS inneravtion (S3)	left S3 PSN
d)	2	left pudendal nerve	left S3 PSN
e)	3	right IAS innervation (S3)	right S3 PSN
f)	3	right pudendal nerve	right S3 PSN
g)	4	left S4 PSN	left S4 PSN
h)	5	right S4 PSN	right S4 PSN
i)	6	left bladder innervation	left NH (S2 level)
j)	7	right bladder innervation	right NH (S2 level)
k)	8	right S2 PSN	right IHP
l)	8	right IAS innervation (S3) PSN	right IHP
m)	8	right S4 PSNve	right IHP
n)	8	right NH	right IHP
o)	9	left S2 PSN	left IHP
p)	9	left IAS innervation (S3)	left IHP
q)	9	left S4 PSN	left IHP
r)	9	left bladder innervation	left IHP

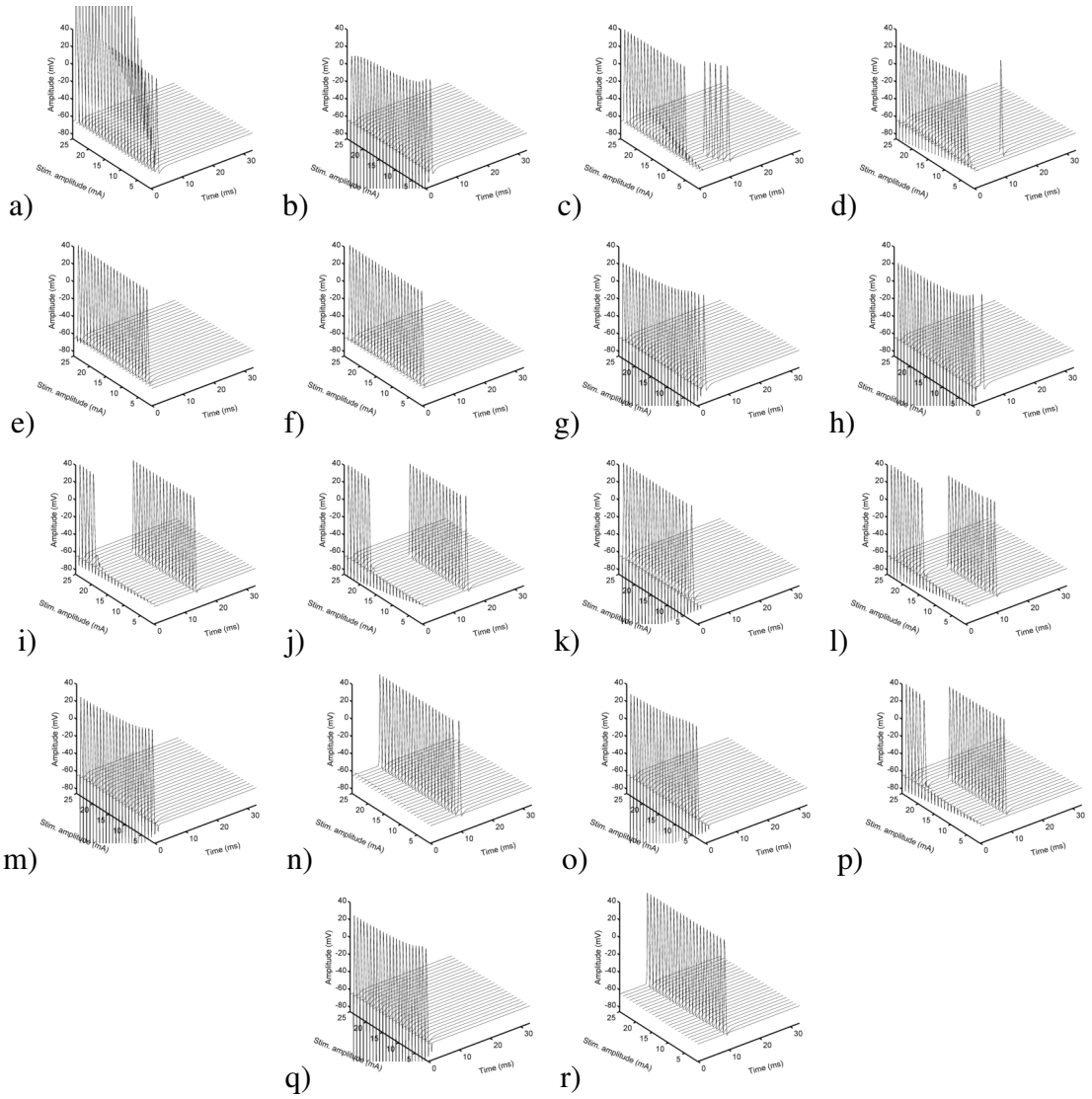

Figure C.1 Membrane potential generated by direct nerve stimulation for ten different stimulation sites before targeted nerve incision. This figure shows only the nerves where an action potential was present. See Table C.1 for detailed description regarding the figure annotation

C.2 Direct nerve stimulation after nerve incision

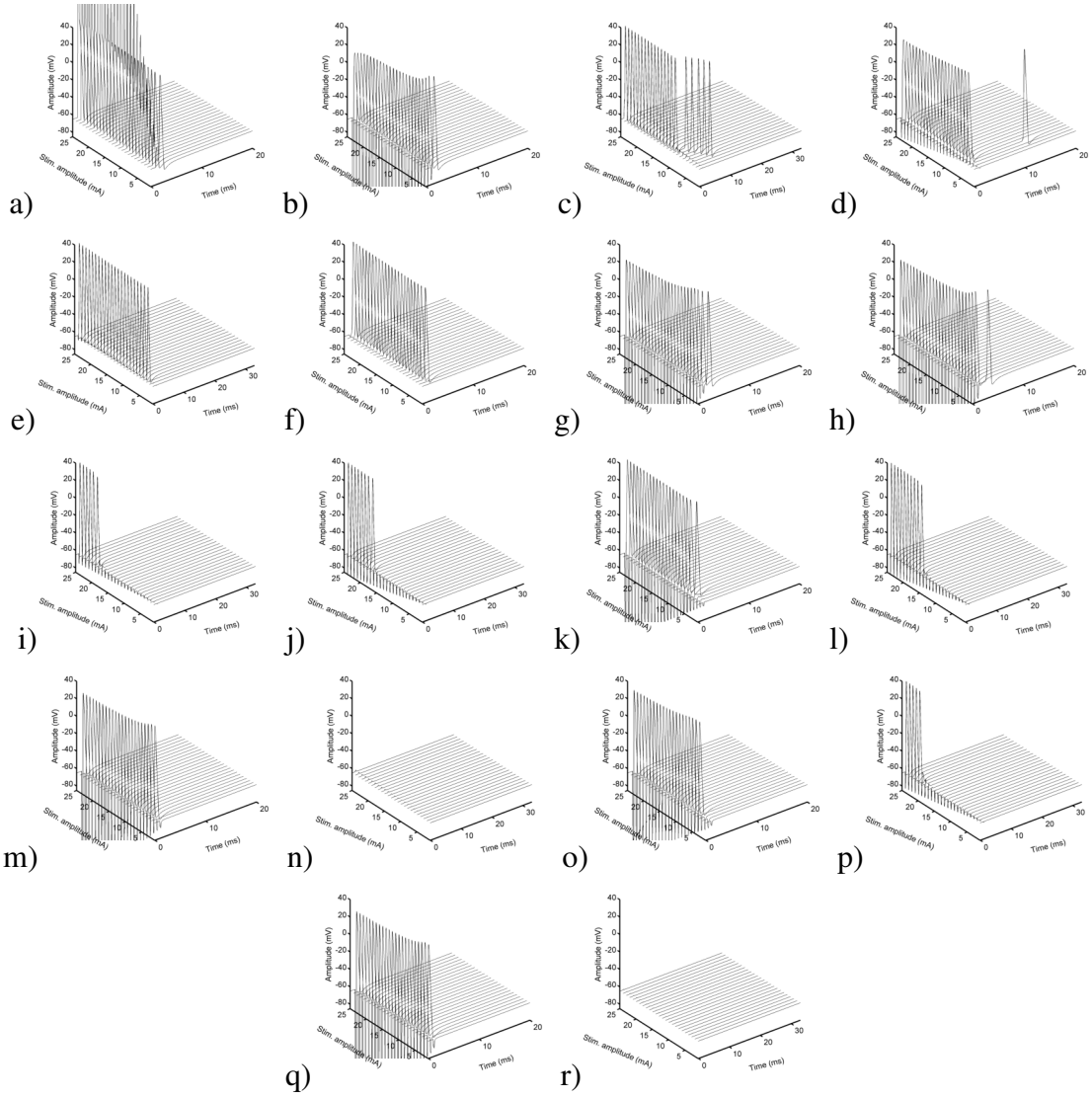

Figure C.2 Membrane potential generated by direct nerve stimulation for ten different stimulation sites after targeted nerve incision. This figure shows only the nerves where an action potential was present. See Table C.1 for detailed description regarding the figure annotation

C.3 Transcutaneous electrical nerve stimulation before nerve incision

Figures C.3 and C.5 summarize the hypogastric nerve membrane potentials generated during TENS for four different anode positions (in the anal canal, on the abdomen, left, and right side of the back) before and after targeted nerve incision, respectively. Figures C.4 and C.6 depict the membrane potentials of the hypogastric nerve for the anode located in the anal canal and cathodes 1 to 10 before and after nerve incision, respectively. Only the bladder and IAS innervation underwent targeted nerve incision.

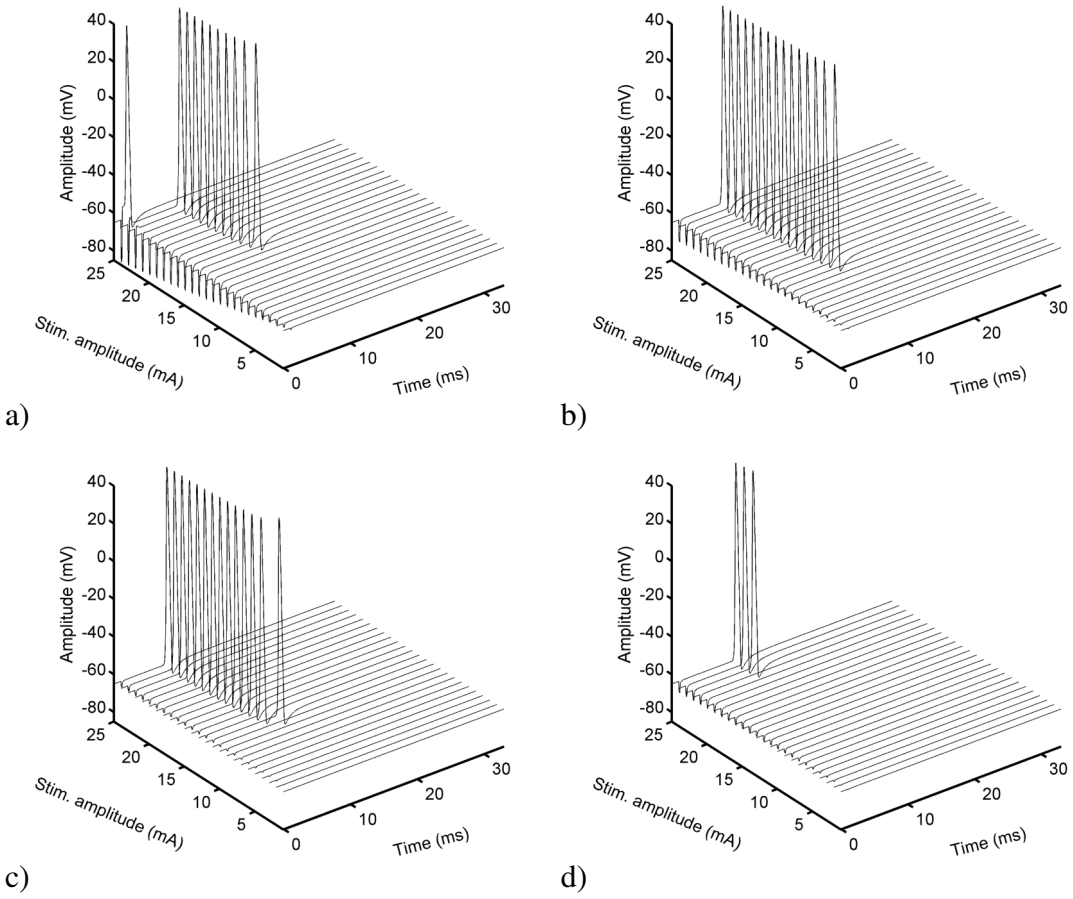

Figure C.3 Membrane potential generated by transcutaneous electrical nerve stimulation using different anodes before nerve incision. This example shows results for four electrode configurations: a) cathode 9 vs. anode in the anal canal, b) cathode 9 vs. anode on the abdomen, c) cathode 9 vs. anode left, and d) cathode 9 vs. anode right

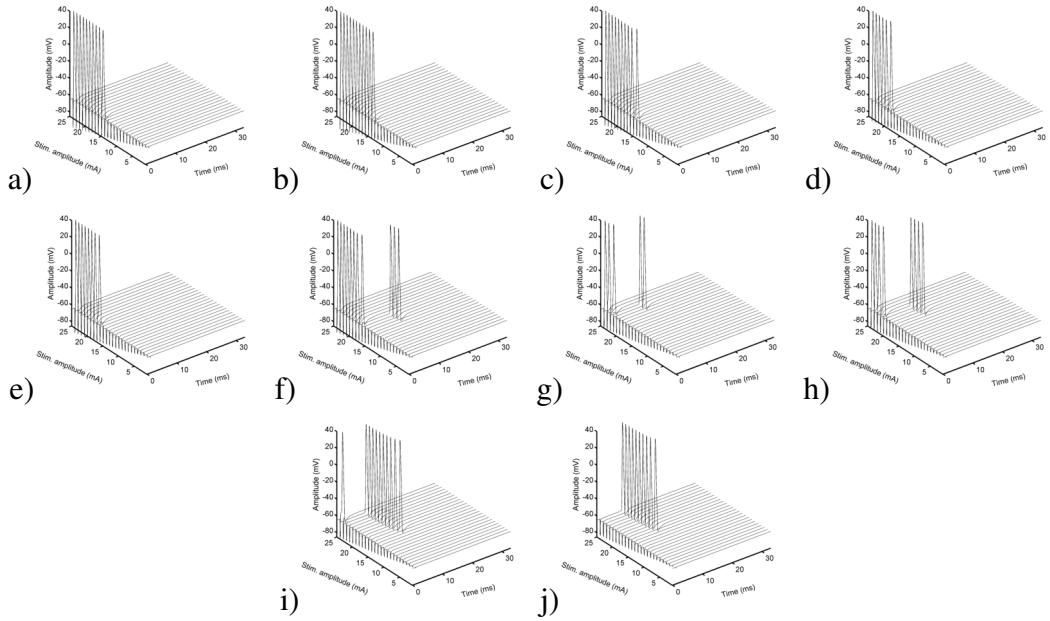

Figure C.4 Membrane potential generated by transcutaneous electrical nerve stimulation using the anode in the anal canal and different assortment of cathodes before nerve incision: a)-j) correspond the cathodes 1-10

C.4 Transcutaneous electrical nerve stimulation after nerve incision

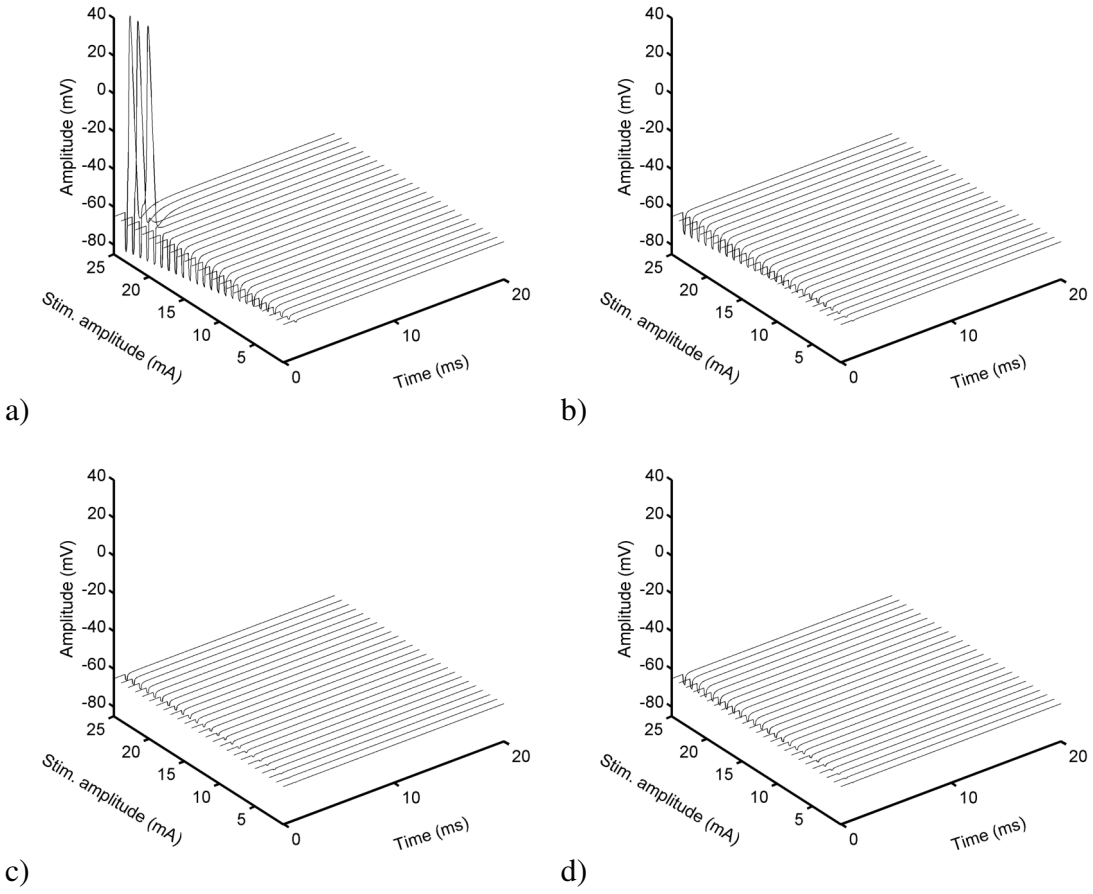

Figure C.5 Membrane potential generated by transcutaneous electrical nerve stimulation using different anodes after nerve incision. This example shows results for four electrode configurations: a) cathode 9 vs. anode in the anal canal, b) cathode 9 vs. anode on the abdomen, c) cathode 9 vs. anode left, and d) cathode 9 vs. anode right

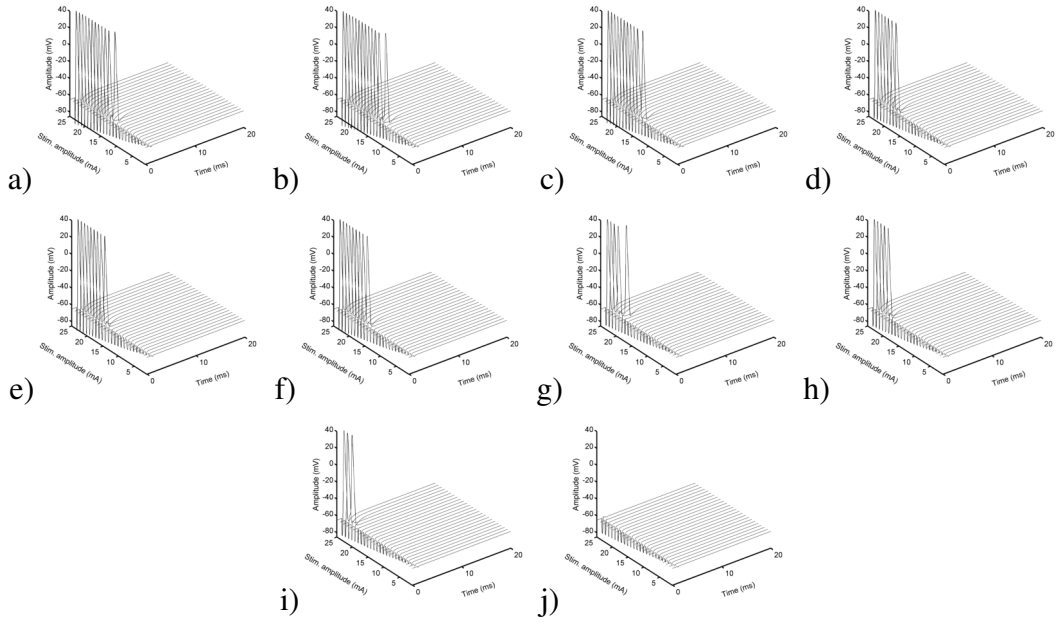

Figure C.6 Membrane potential generated by transcutaneous electrical nerve stimulation using the anode in the anal canal and different assortment of cathodes after nerve incision: a)-j) correspond the cathodes 1-10

Appendix D

Averaged signals obtained during transcutaneous electrical nerve stimulation

This appendix summarizes the averaged raw signals derived from the needle recordings of the internal anal sphincter (IAS) electromyographic (EMG) activity. The recordings were analyzed in terms of the characteristics of the identified deflections – peaks and valleys. Additionally, depiction of the frequency domain for the given electrode configurations has been added to every recording. This chapter contains the results that regard only the cases where a change in the signal amplitude correlated with targeted nerve incision of the inferior hypogastric plexus (Section D.1) or injection of the muscular relaxant (Section D.2).

D.1 Influence of nerve incision on internal anal sphincter electromyography

D.1.1 Summary of the peaks identified in the entire dataset

The latencies and amplitudes of peaks identified across five experiment phases whose presence correlated with targeted incision of the inferior hypogastric plexus are summarized in Table D.1 and D.2, respectively. The signals from which these peaks were derived are depicted in Figure D.1 to D.9.

Table D.1 Amplitudes of the identified peaks that correlated with targeted incision of the inferior hypogastric plexus during stimulation for different electrode configurations and experiment phases. The X signifies that a peak could not be detected in a given phase. The amplitude difference between Phase 4 and Phase 5 expressed per cent. The amplitude differences signified with an asterisk (*) were calculated between Phase 3 and Phase 5 because of a lacking local maximum in Phase 4.

Fig.	Animal	Anode	Cathode	Peak no.	Amplitude (μV)					Difference
					Phase 1	Phase 2	Phase 3	Phase 4	Phase 5	
D.1	3	1	8	1	56.95	12.93	13.98	X	7.63	45%*
D.2a	3	4	2	1	5.55	15.01	15.25	8.10	X	100%
D.2b				2	X	7.32	9.68	6.62	X	100%
D.3	3	4	5	1	40.1	46.18	26.67	9.84	6.03	39%
D.4	5	1	7	1	32.19	20.92	16.10	16.04	12.36	23%
D.5a	5	4	4	1	48.73	57.04	51.12	31.34	9.63	69%
D.5b				2	3.86	1.60	2.77	7.51	X	100%
D.6a	5	4	7	1	X	197.39	204.68	218.63	161.05	26%
D.6b				2	47.62	34.51	20.07	X	14.45	28%*
D.7a	5	4	8	1	67.85	75.07	68.77	49.62	33.52	32%
D.7b				2	15.42	19.99	14.11	12.51	X	100%
D.8	5	4	9	1	29.18	5.60	17.63	-4.26	-11.06	-160%
D.9a	5	4	10	1	239.69	202.44	189.98	163.83	132.77	19%
D.9b				2	36.66	74.83	49.78	46.73	34.91	25%

Table D.2 Latencies of the identified peaks that correlated with targeted incision of the inferior hypogastric plexus during stimulation for different electrode configurations and experiment phases. The X signifies that a peak could not be detected in a given phase

Fig.	Animal	Anode	Cathode	Peak no.	Latency (ms)				
					Phase 1	Phase 2	Phase 3	Phase 4	Phase 5
D.1	3	1	8	1	5.05	5.40	5.20	X	5.65
D.2a	3	4	2	1	7.40	7.15	7.75	7.90	X
D.2b				2	X	11.65	12.50	12.65	X
D.3	3	4	5	1	7.45	7.45	7.90	8.00	8.60
D.4	5	1	7	1	5.95	5.85	5.85	6.00	6.25
D.5a	5	4	4	1	2.90	2.85	2.80	2.85	2.85
D.5b				2	5.20	5.60	5.95	6.00	X
D.6a	5	4	7	1	X	2.50	2.65	2.65	2.65
D.6b				2	7.70	7.40	7.05	X	6.75
D.7a	5	4	8	1	2.65	2.85	2.85	2.65	2.70
D.7b				2	5.60	5.55	6.05	5.90	X
D.8	5	4	9	1	3.00	2.90	2.90	2.70	2.75
D.9a	5	4	10	1	2.45	2.60	2.60	2.50	2.55
D.9b				2	5.55	5.55	5.70	5.75	5.70

a)

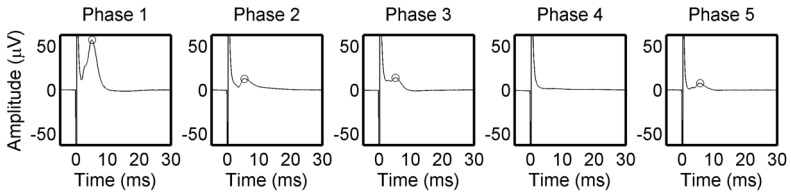

b)

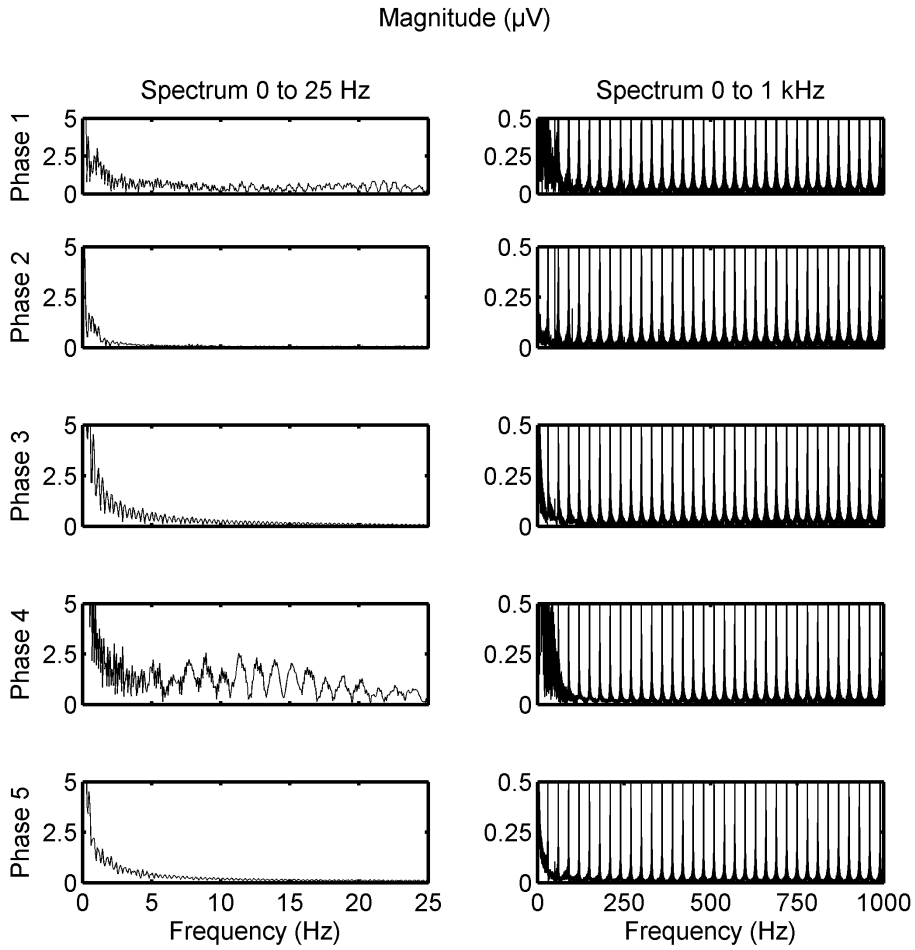

Figure D.1 Animal 3, anode right, cathode 8: a) averaged signals acquired during all five phases of the experiment: 'o' depicts the peak identified 5.05 ms after the stimulation pulse in Phase 1 - prone position, b) spectral analysis of the signals acquired during all five phases of the experiment (0 to 25 Hz and 0 to 1 kHz)

a)

b)

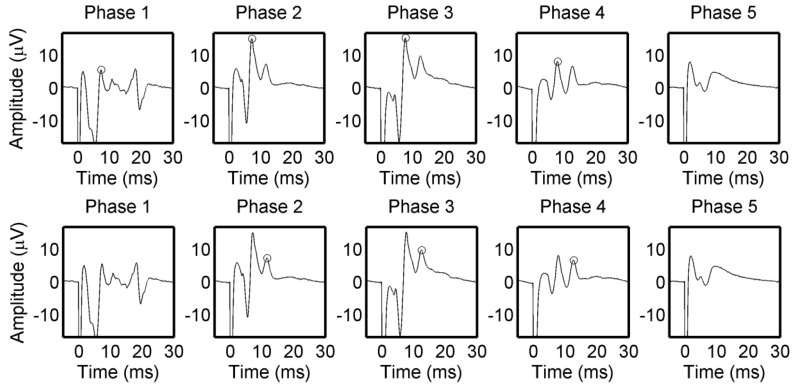

c)

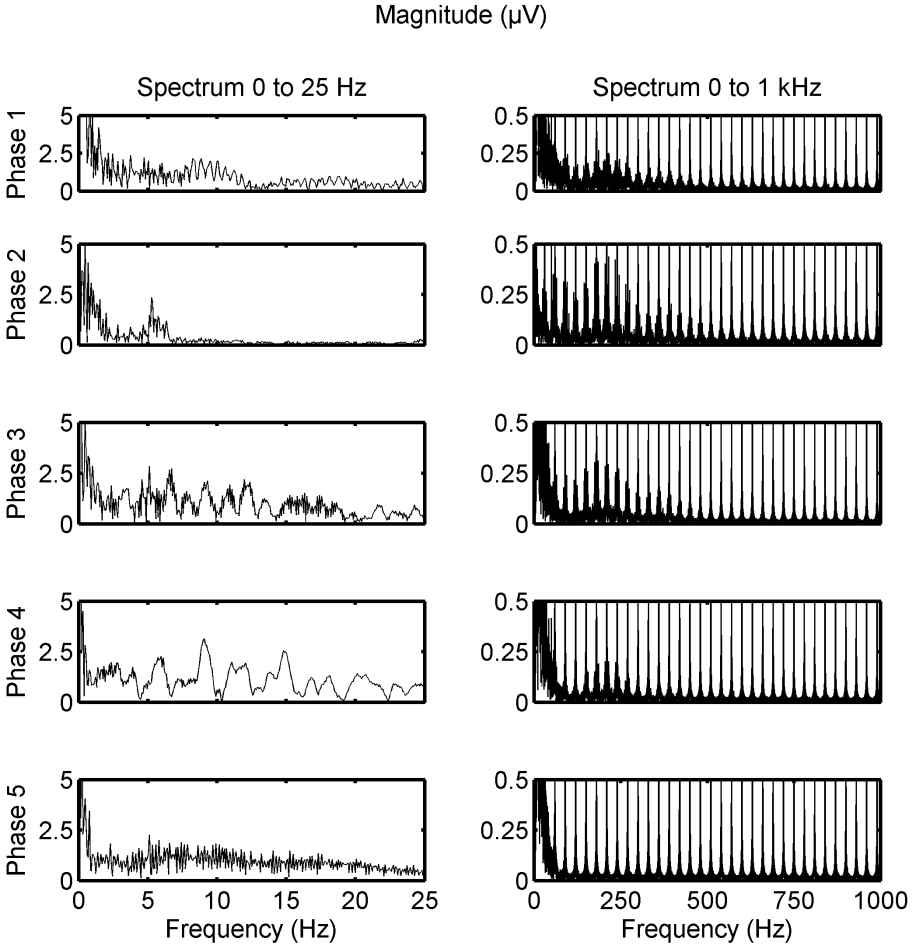

Figure D.2 Animal 3, anode in the anal canal, cathode 2: averaged signals acquired during all five phases of the experiment: 'o' depicts the peak identified 7.40 ms (a) and 11.65 ms (b) after the stimulation pulse in Phase 1 - prone position and Phase 2 - supine position, respectively. c) Spectral analysis of the signals acquired during all five phases of the experiment (0 to 25 Hz and 0 to 1 kHz)

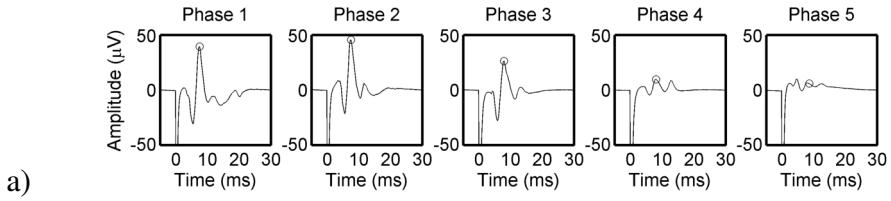

a)

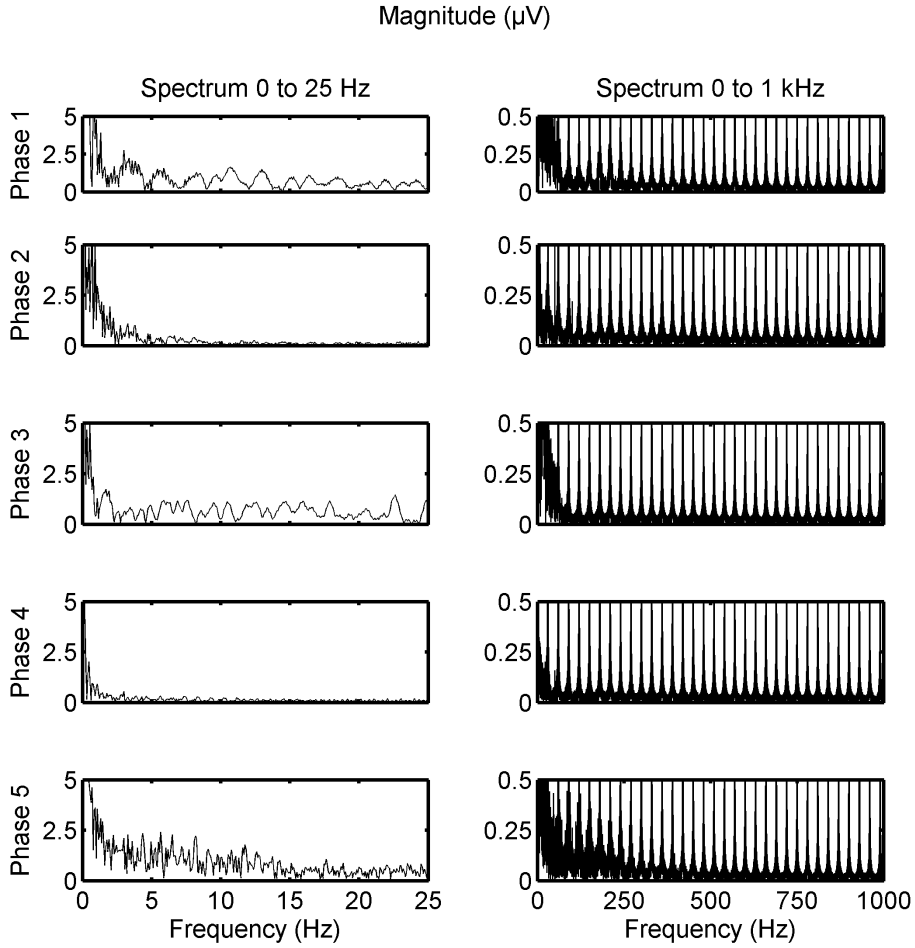

b)

Figure D.3 Animal 3, anode in the anal canal, cathode 5: a) averaged signals acquired during all five phases of the experiment: 'o' depicts the peak identified 7.45 ms after the stimulation pulse in Phase 1 - prone position, b) spectral analysis of the signals acquired during all five phases of the experiment (0 to 25 Hz and 0 to 1 kHz)

a)

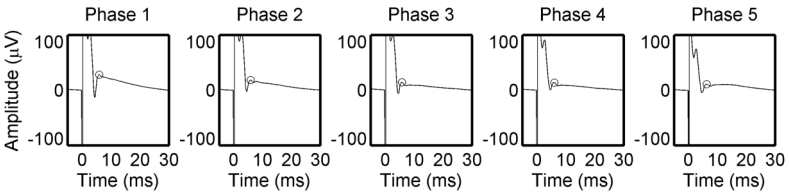

b)

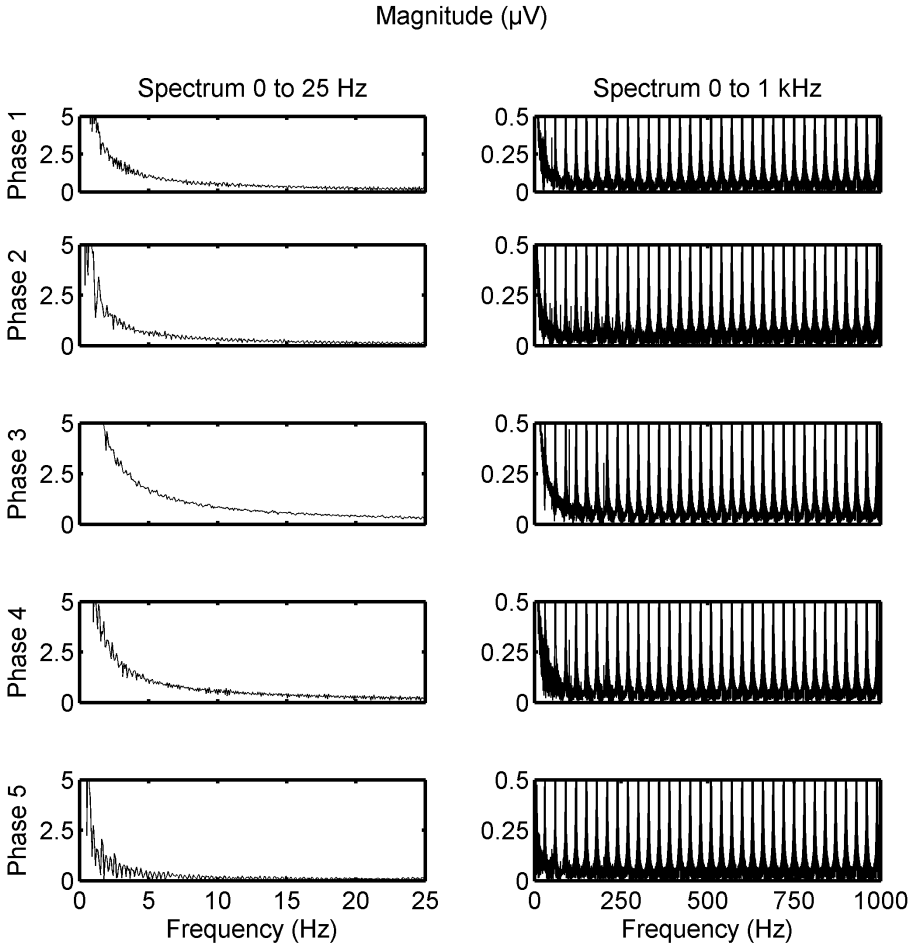

Figure D.4 Animal 5, anode right, cathode 7: a) averaged signals acquired during all five phases of the experiment: 'o' depicts the peak identified 5.95 ms after the stimulation pulse in Phase 1 - prone position, b) spectral analysis of the signals acquired during all five phases of the experiment (0 to 25 Hz and 0 to 1 kHz)

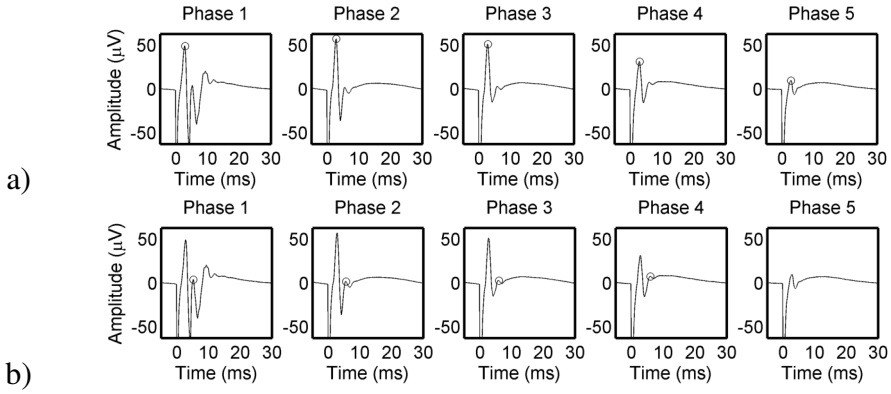

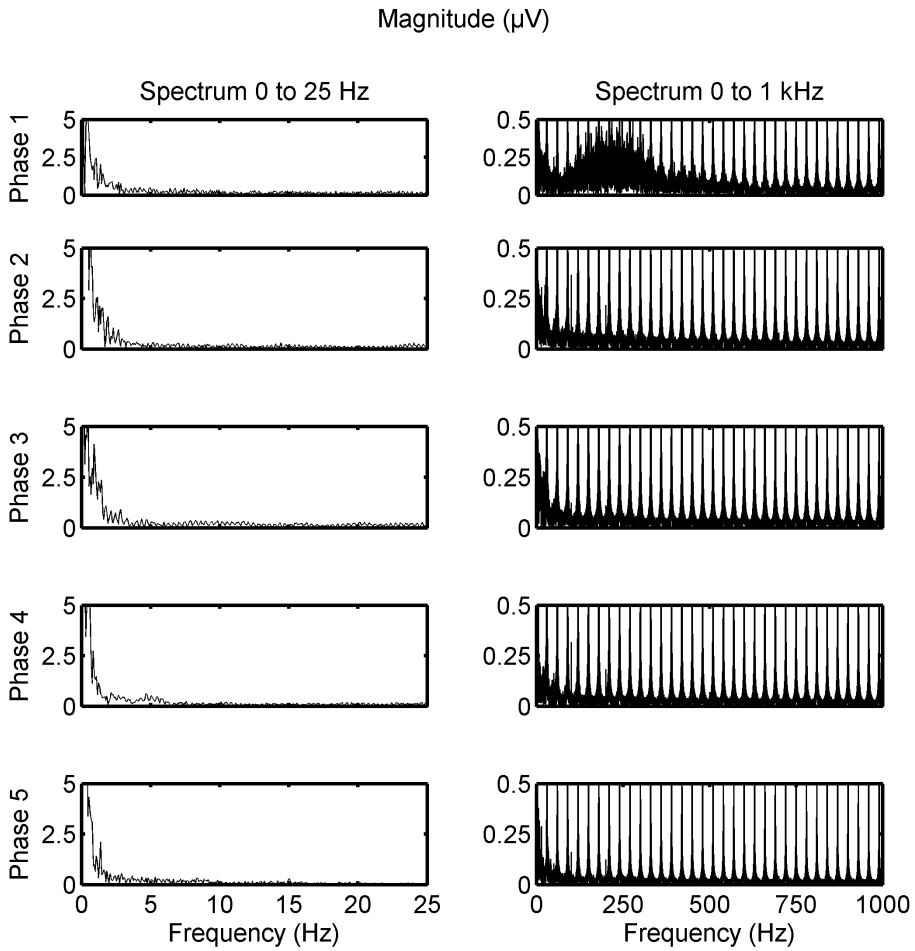

Figure D.5 Animal 5, anode in the anal canal, cathode 4: averaged signals acquired during all five phases of the experiment: 'o' depicts the peak identified 2.90 ms (a) and 5.20 ms (b) after the stimulation pulse in Phase 1 - prone position, c) spectral analysis of the signals acquired during all five phases of the experiment (0 to 25 Hz and 0 to 1 kHz)

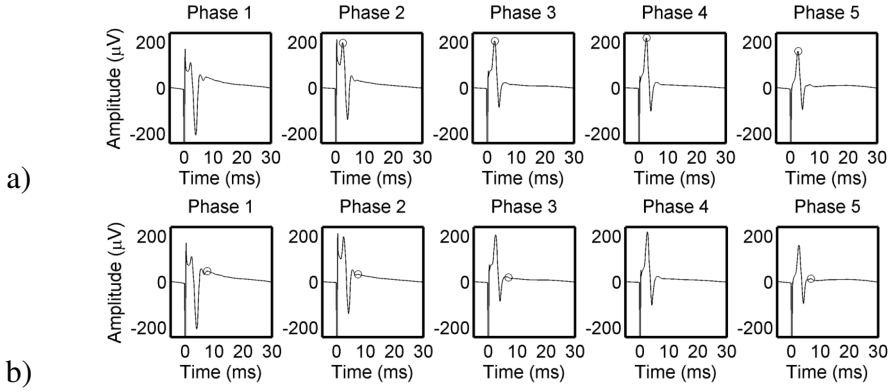

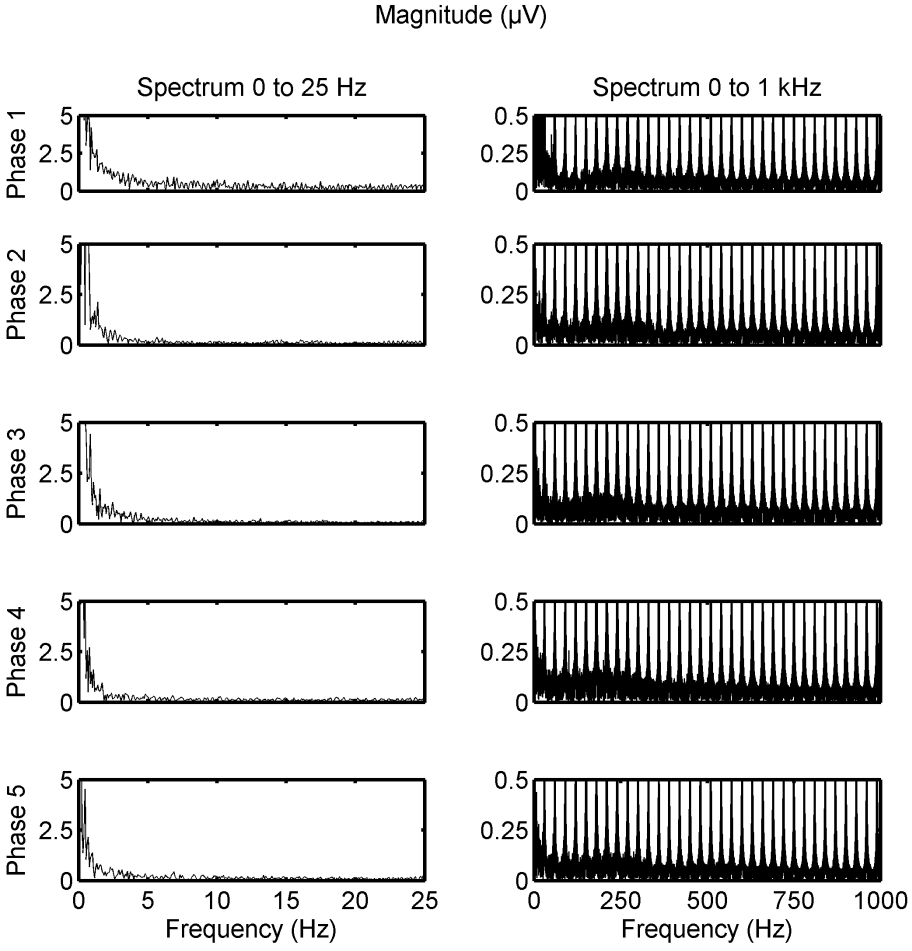

Figure D.6 Animal 5, anode in the anal canal, cathode 7: a) averaged signals acquired during all five phases of the experiment: 'o' depicts the peak identified 2.50 ms and 7.70 ms after the stimulation pulse in Phase 2 - supine position and Phase 1 - prone position, respectively. b) Spectral analysis of the signals acquired during all five phases of the experiment (0 to 25 Hz and 0 to 1 kHz)

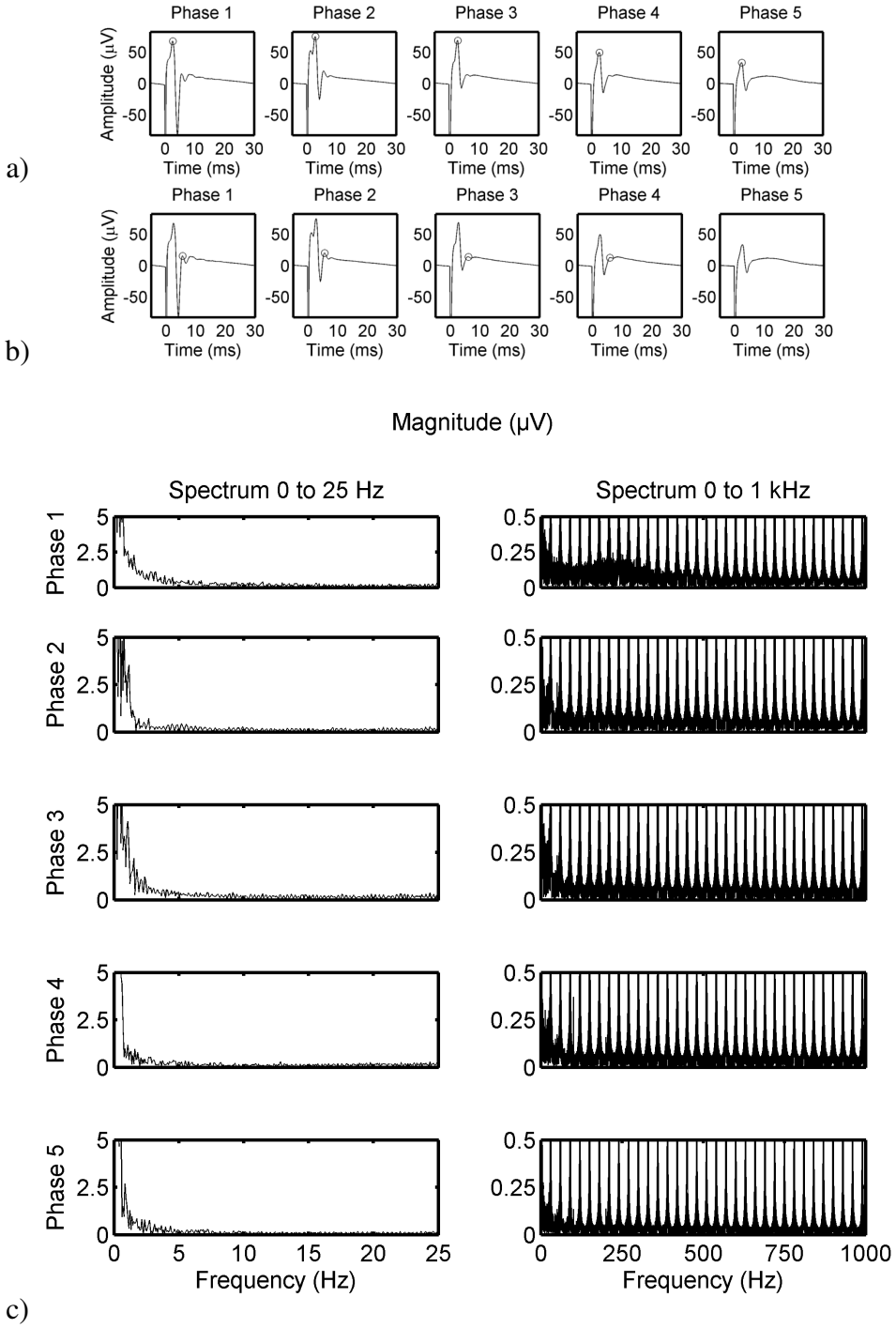

Figure D.7 Animal 5, anode in the anal canal, cathode 8: averaged signals acquired during all five phases of the experiment: 'o' depicts the peak identified 2.65 ms (a) and 5.60 ms (b) after the stimulation pulse in Phase 1 - prone position, c) spectral analysis of the signals acquired during all five phases of the experiment (0 to 25 Hz and 0 to 1 kHz)

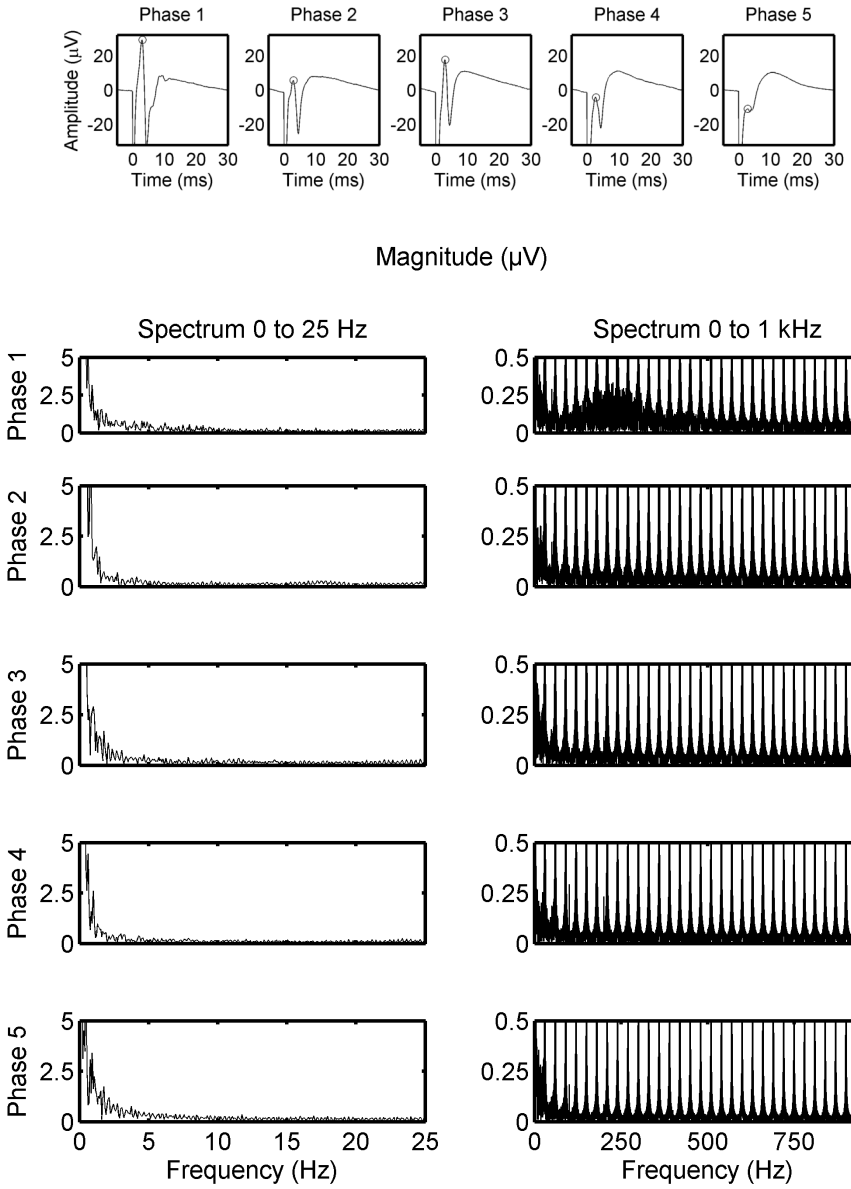

Figure D.8 Animal 5, anode in the anal canal, cathode 9: a) averaged signals acquired during all five phases of the experiment: 'o' depicts the peak identified 3.00 ms after the stimulation pulse in Phase 1 - prone position, b) spectral analysis of the signals acquired during all five phases of the experiment (0 to 25 Hz and 0 to 1 kHz)

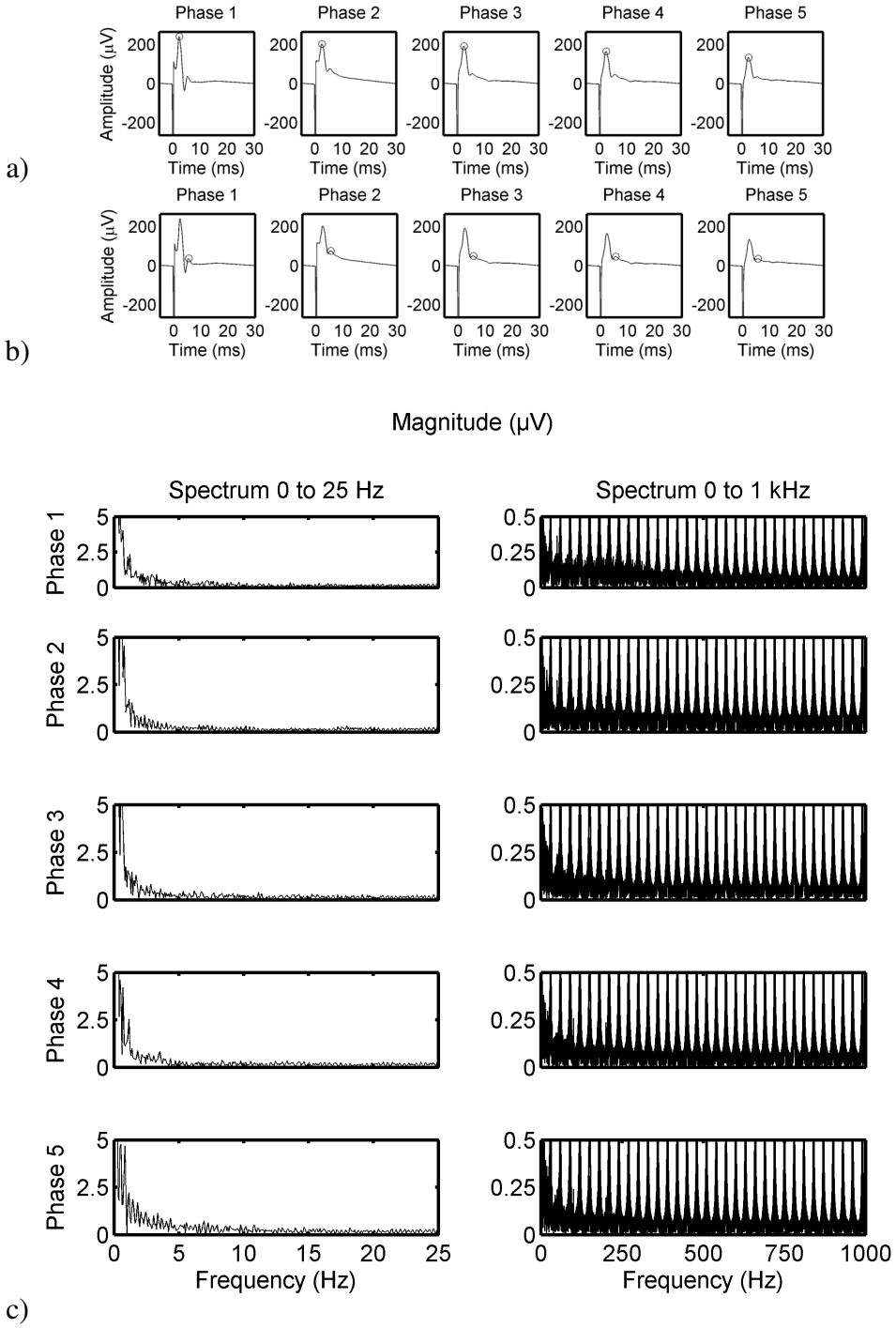

Figure D.9 Animal 5, anode in the anal canal, cathode 10: averaged signals acquired during all five phases of the experiment: 'o' depicts the peak identified 2.45 ms (a) and 5.55 ms (b) after the stimulation pulse in Phase 1 - prone position, c) spectral analysis of the signals acquired during all five phases of the experiment (0 to 25 Hz and 0 to 1 kHz)

D.1.2 Summary of the valleys identified in the entire dataset

The latencies and amplitudes of valleys identified across five experiment phases whose presence correlated with targeted incision of the inferior hypogastric plexus are summarized in Table D.3 and D.4, respectively. The signals from which these peaks were derived are depicted in Figure D.10 to D.17.

Table D.3 Amplitudes of the identified valleys during stimulation for different electrode configurations and experiment phases. The X signifies that a peak could not be detected in a given phase. The amplitude difference between Phase 4 and Phase 5 expressed per cent.

Fig.	Animal	Anode	Cathode	Peak no.	Amplitude (μV)					Difference
					Phase 1	Phase 2	Phase 3	Phase 4	Phase 5	
D.10	3	4	2	1	-18.96	-10.78	-16.39	-3.54	-1.02	71%
D.10				2	-1.00	2.48	2.85	-1.64	X	100%
D.11	3	4	5	1	-31.10	-21.61	-28.41	-4.60	-0.84	82%
D.11				2	-11.34	-7.78	-8.37	-1.48	3.07	307%
D.12	4	1	2	1	-22.83	-18.77	- 19.53	-5.30	6.26	218%
D.13	4	1	3	1	-15.15	-12.95	-12.51	-8.19	-6.40	22%
D.14	5	4	3	1	-57.15	X	-50.04	-44.36	-35.19	21%
D.15	5	4	4	1	-65.86	-35.96	-11.17	-15.70	-6.28	60%
D.15				2	-40.03	-4.78	-0.26	5.04	X	100%
D.16	5	4	8	1	3.87	10.46	11.84	11.81	X	100%
D.17	5	4	9	1	-37.73	-25.62	-20.66	-22.23	-12.57	43%

Table D.4 Latencies of the identified valleys during stimulation for different electrode configurations and experiment phases. The X signifies that a peak could not be detected in a given phase

Fig.	Animal	Anode	Cathode	Peak no.	Latency (ms)				
					Phase 1	Phase 2	Phase 3	Phase 4	Phase 5
D.10	3	4	2	1	5.45	5.50	5.75	5.95	6.50
D.10				2	9.35	9.95	10.70	10.60	X
D.11	3	4	5	1	5.55	5.65	5.90	6.25	6.30
D.11				2	10.25	10.50	11.45	10.85	10.45
D.12	4	1	2	1	3.85	4.00	3.85	4.05	4.70
D.13	4	1	3	1	4.35	4.45	4.30	4.10	4.10
D.14	5	4	3	1	3.70	X	3.30	3.10	3.10
D.15	5	4	4	1	4.20	4.15	3.95	4.15	3.95
D.15				2	6.60	6.80	6.95	7.05	X
D.16	5	4	8	1	6.85	7.15	7.10	6.85	X
D.17	5	4	9	1	4.35	4.50	4.35	4.30	3.45

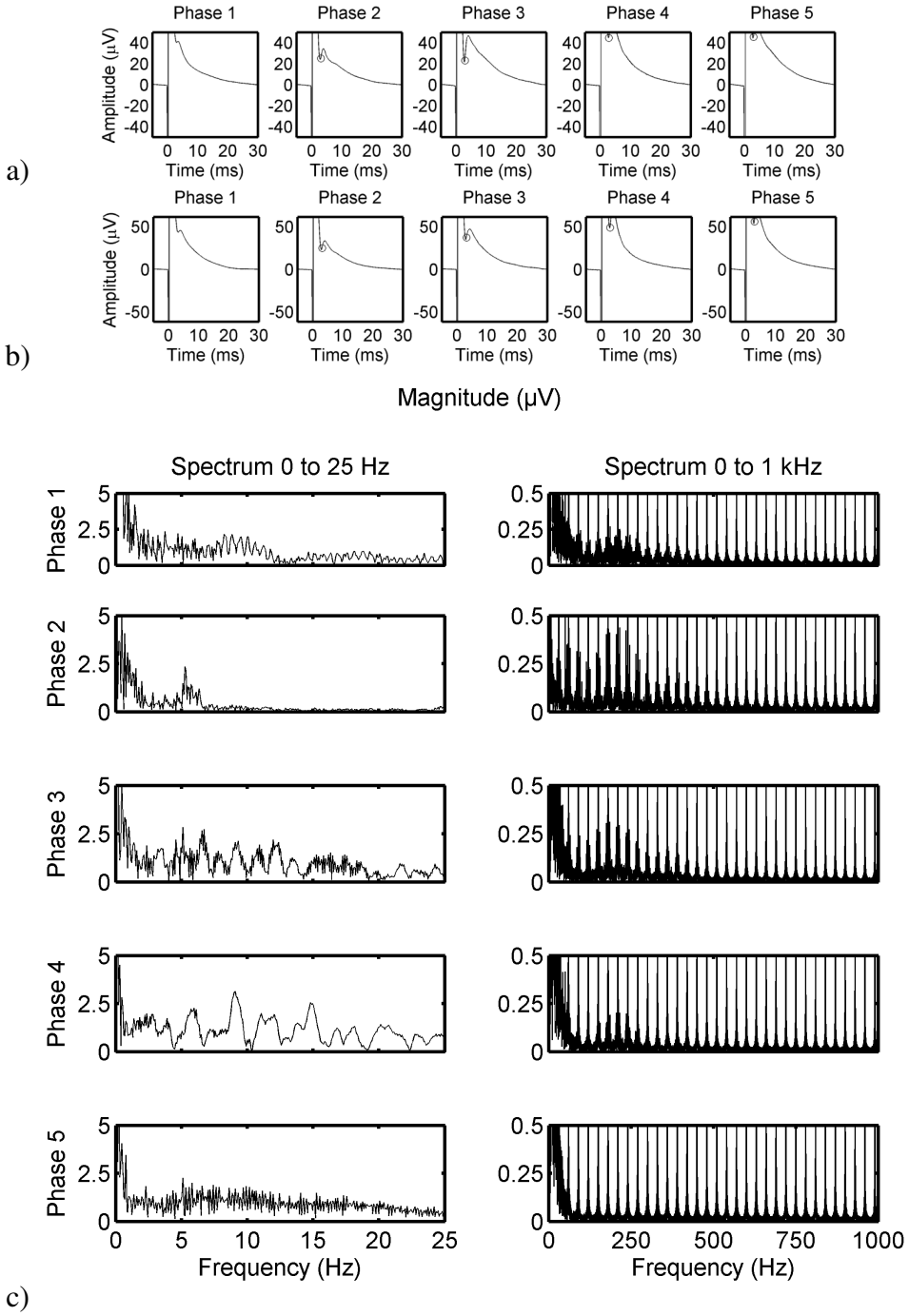

Figure D.10 Animal 3, anode in the anal canal, cathode 2: averaged signals acquired during all five phases of the experiment: 'o' depicts the valley identified 5.45 ms (a) and 9.35 ms (b) after the stimulation pulse in Phase 1 - prone position, c) spectral analysis of the signals acquired during all five phases of the experiment (0 to 25 Hz and 0 to 1 kHz)

a)

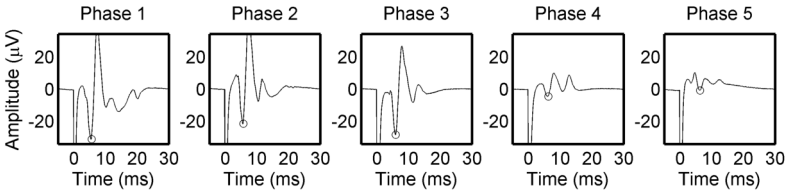

b)

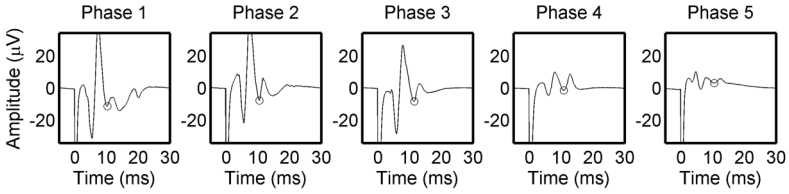

c)

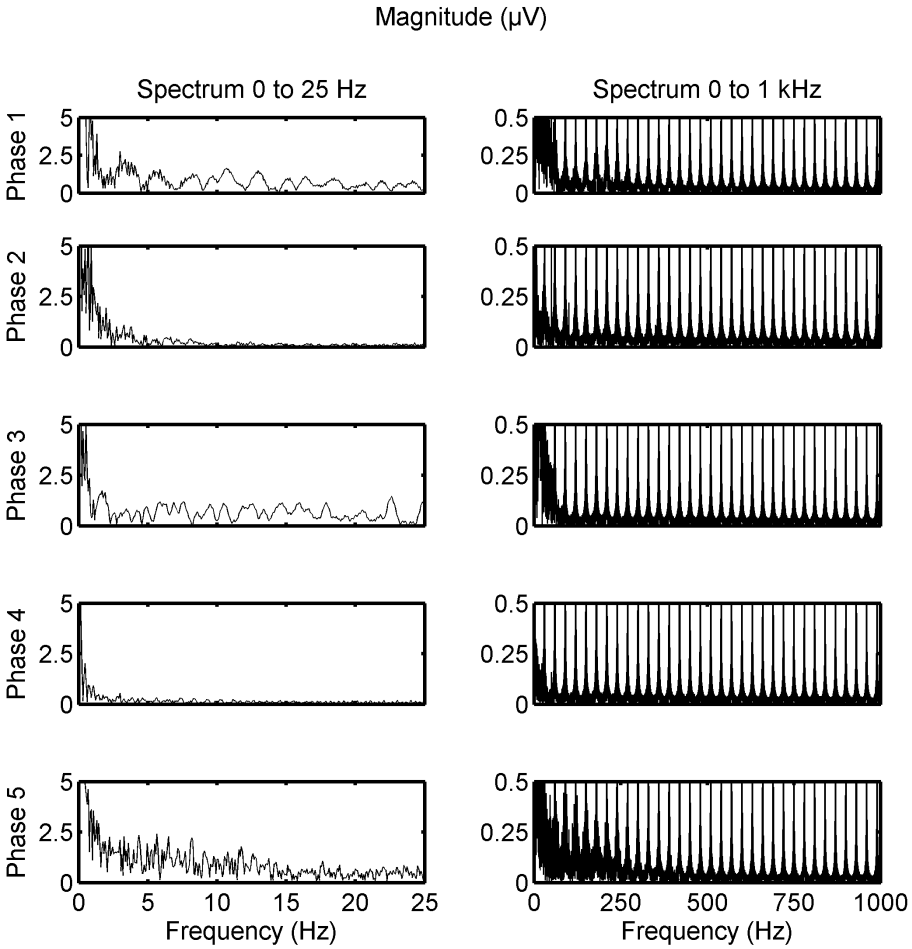

Figure D.11 Animal 3, anode in the anal canal, cathode 5: averaged signals acquired during all five phases of the experiment: 'o' depicts the valley identified 5.55 ms (a) and 10.25 ms (b) after the stimulation pulse in Phase 1 - prone position, c) spectral analysis of the signals acquired during all five phases of the experiment (0 to 25 Hz and 0 to 1 kHz)

a)

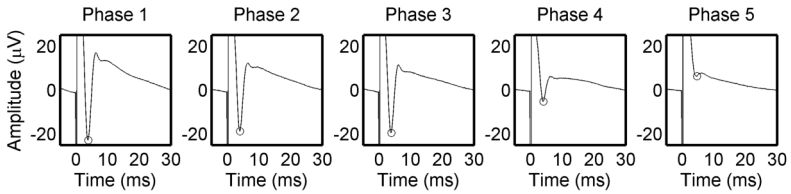

b)

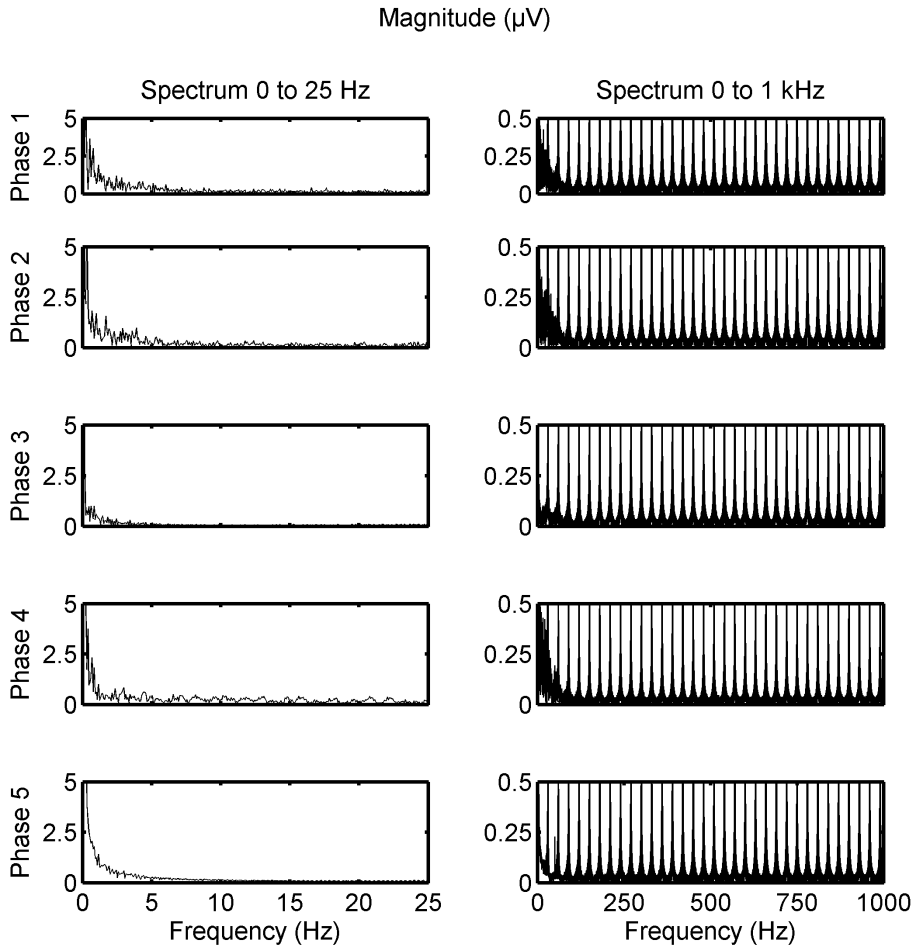

Figure D.12 Animal 4, anode right, cathode 2: a) averaged signals acquired during all five phases of the experiment: 'o' depicts the valley identified 3.85 ms after the stimulation pulse in Phase 1 - prone position, b) spectral analysis of the signals acquired during all five phases of the experiment (0 to 25 Hz and 0 to 1 kHz)

a)

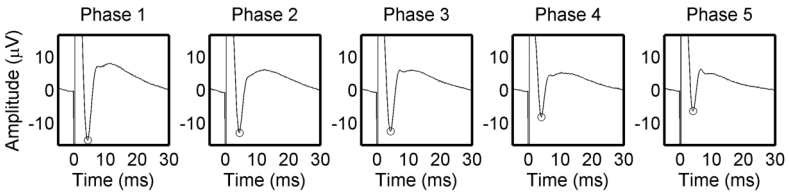

b)

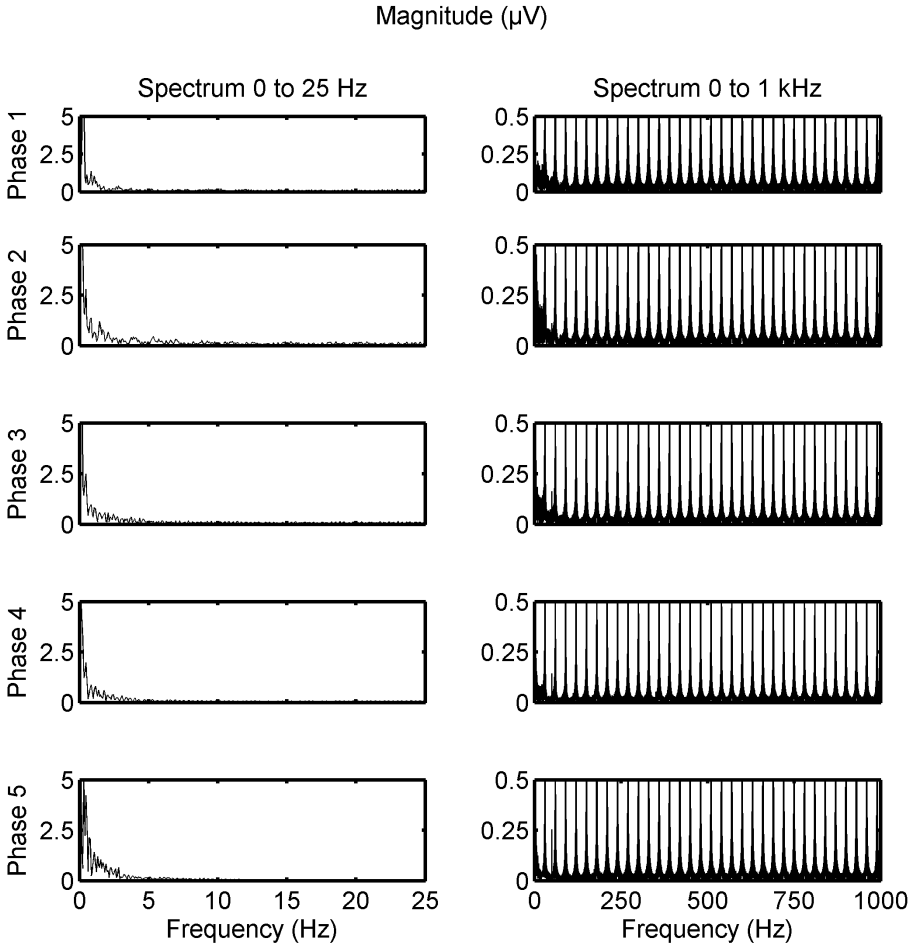

Figure D.13 Animal 4, anode right, cathode 3: a) averaged signals acquired during all five phases of the experiment: 'o' depicts the valley identified 4.35 ms after the stimulation pulse in Phase 1 - prone position, b) spectral analysis of the signals acquired during all five phases of the experiment (0 to 25 Hz and 0 to 1 kHz)

a)

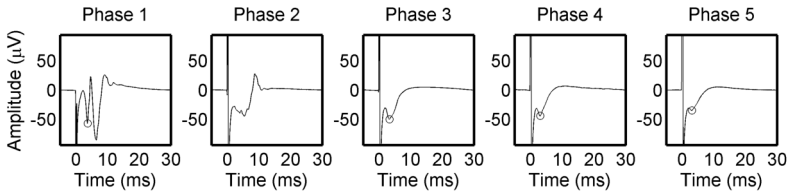

b)

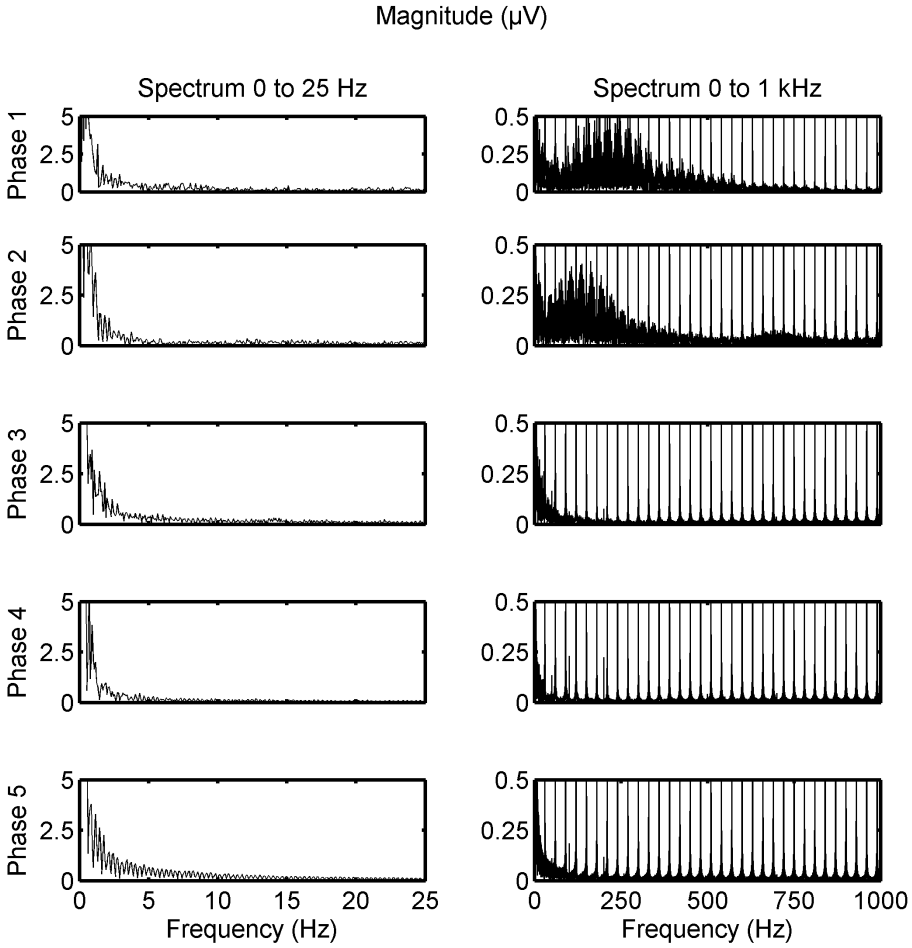

Figure D.14 Animal 5, anode in the anal canal, cathode 3: : a) averaged signals acquired during all five phases of the experiment: 'o' depicts the valley identified 3.70 ms after the stimulation pulse in Phase 1 - prone position, b) spectral analysis of the signals acquired during all five phases of the experiment (0 to 25 Hz and 0 to 1 kHz)

a)

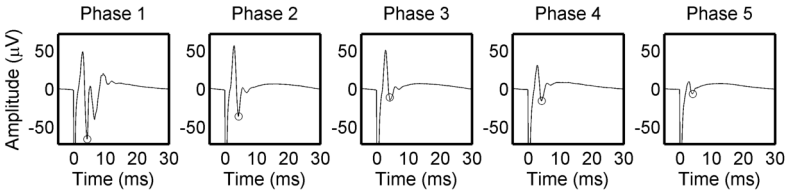

b)

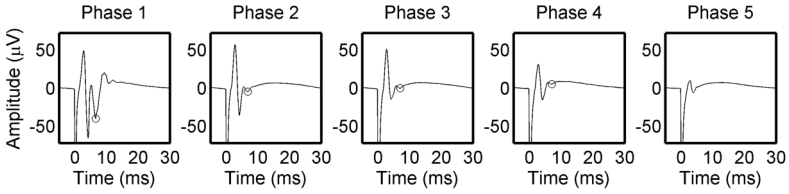

c)

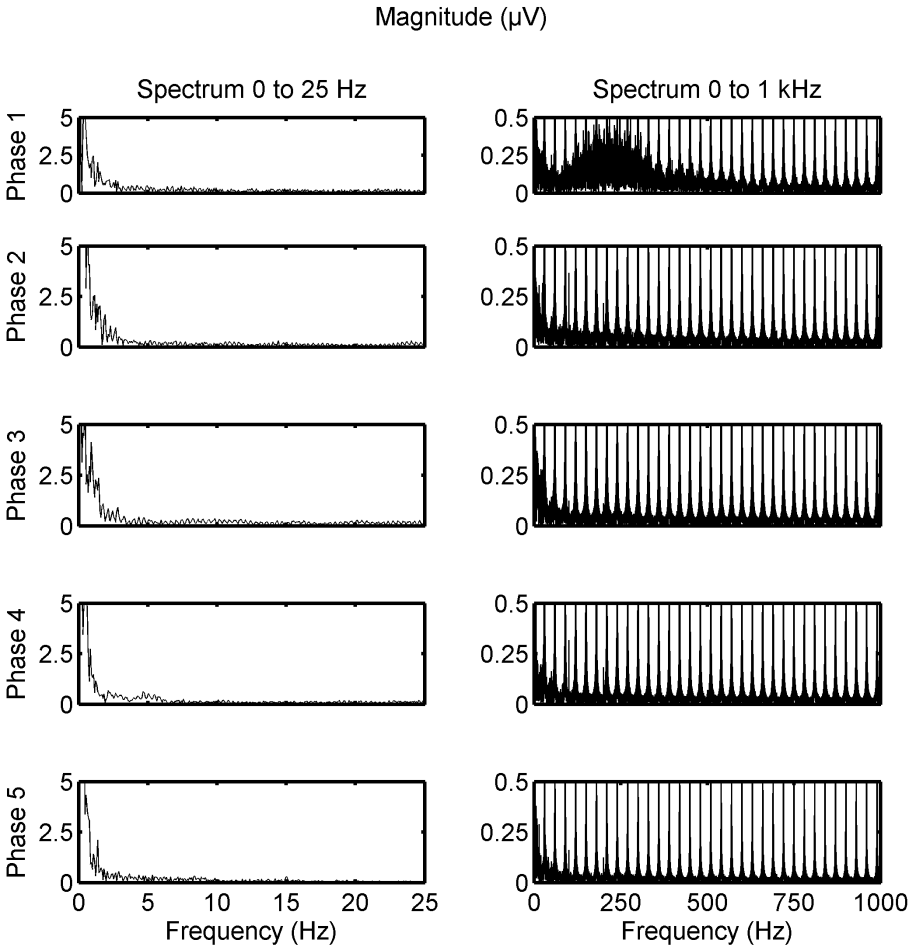

Figure D.15 Animal 5, anode in the anal canal, cathode 4: averaged signals acquired during all five phases of the experiment: 'o' depicts the valley identified 4.20 ms (a) and 6.60 ms (b) after the stimulation pulse in Phase 1 - prone position, c) spectral analysis of the signals acquired during all five phases of the experiment (0 to 25 Hz and 0 to 1 kHz)

a)

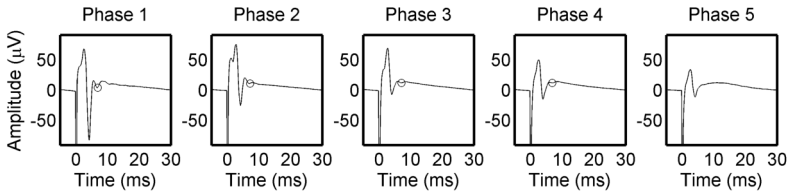

b)

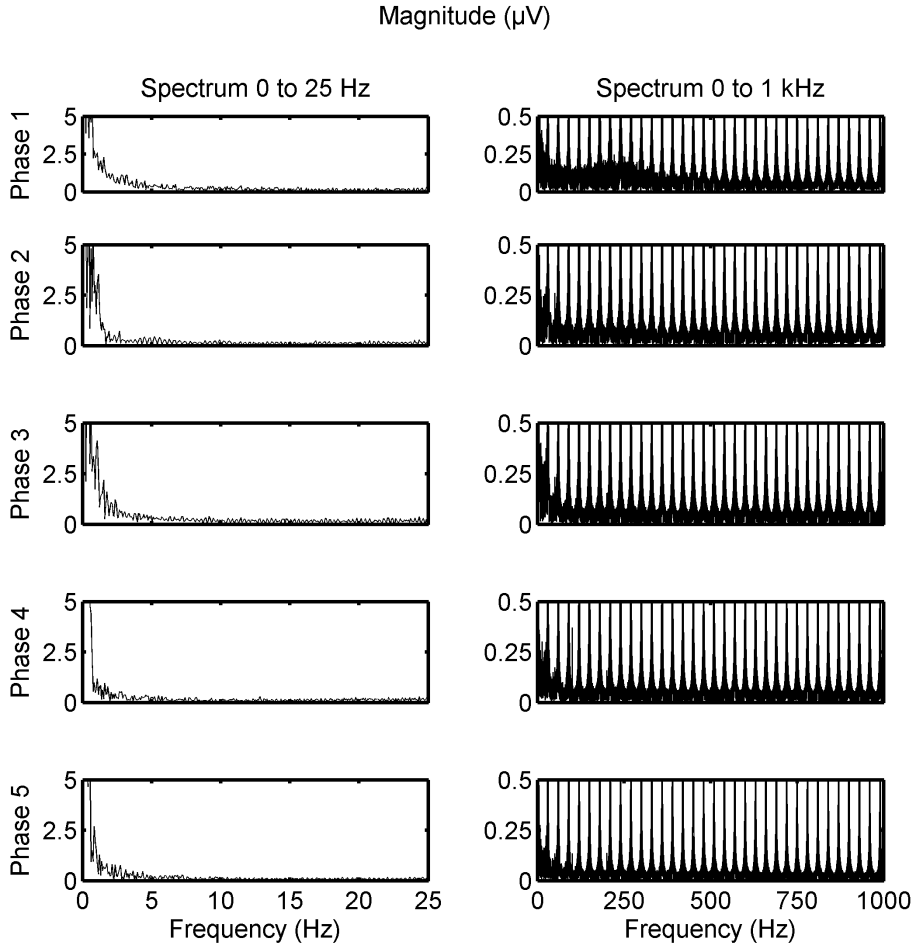

Figure D.16 Animal 5, anode in the anal canal, cathode 8: : a) averaged signals acquired during all five phases of the experiment: 'o' depicts the valley identified 6.85 ms after the stimulation pulse in Phase 1 - prone position, b) spectral analysis of the signals acquired during all five phases of the experiment (0 to 25 Hz and 0 to 1 kHz)

a)

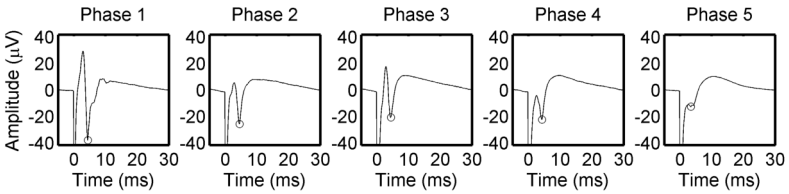

b)

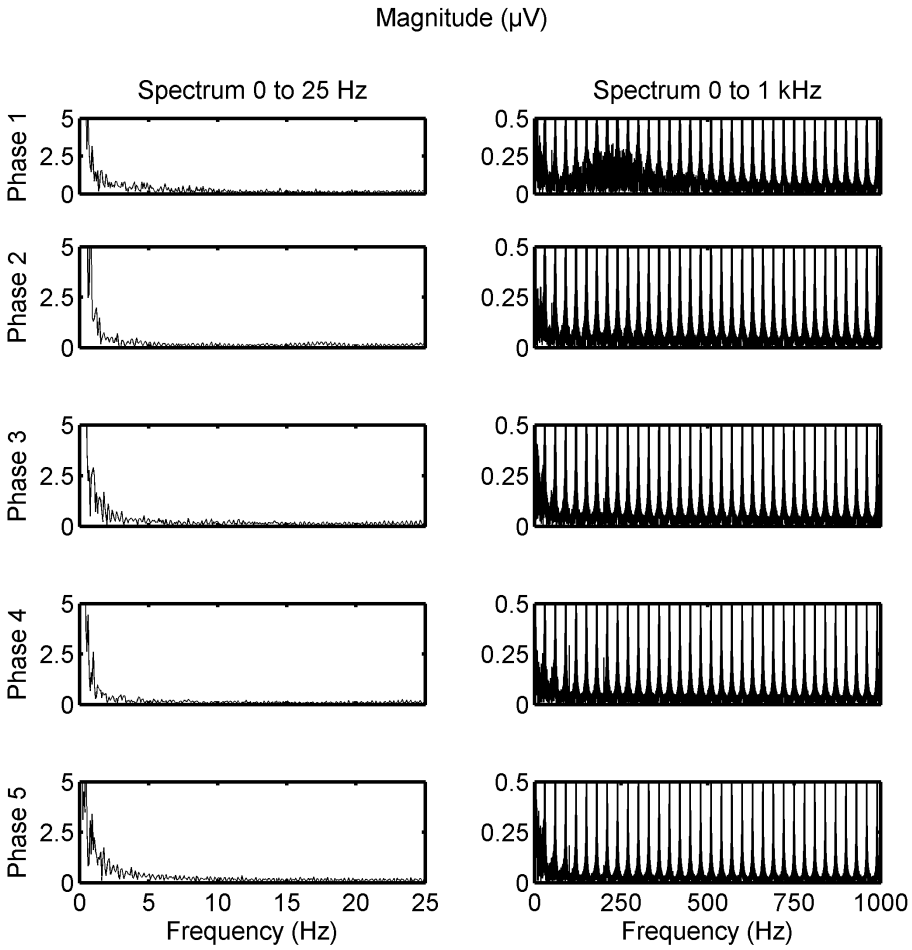

Figure D.17 Animal 5, anode in the anal canal, cathode 9: a) averaged signals acquired during all five phases of the experiment: 'o' depicts the valley identified 4.35 ms after the stimulation pulse in Phase 1 - prone position, b) spectral analysis of the signals acquired during all five phases of the experiment (0 to 25 Hz and 0 to 1 kHz)

D.2 Influence of muscle relaxation on internal anal sphincter electromyography

D.2.1 Summary of the peaks identified in the entire dataset

Table D.5 Amplitudes of the identified peaks during stimulation for different electrode configurations and experiment phases. The X signifies that a peak could not be detected in a given phase

Fig.	Animal	Anode	Cathode	Peak no.	Amplitudes (μV)				
					Phase 1	Phase 2	Phase 3	Phase 4	Phase 5
D.18	2	4	2	1	13.71	X	37.74	X	33.54
D.19	3	1	4	1	X	3.75	28.58	-21.32	2.38
D.20	3	1	7	1	97.95	112.45	114.31	X	125.50
D.20				2	40.44	30.81	21.70	17.21	32.01
D.21	3	1	8	1	56.95	12.93	13.98	X	7.63
D.22	3	1	9	1	52.90	13.98	11.98	X	11.21
D.23	3	1	10	1	80.60	13.37	26.24	X	59.04
D.24	3	3	7	1	65.73	64.94	135.14	X	175.24
D.25	3	3	9	1	43.15	7.03	7.09	X	X
D.26	3	3	10	1	82.94	20.19	35.42	X	97.20
D.26				2	34.04	-1.47	-1.93	X	44.49
D.27	3	4	1	1	64.41	66.28	33.71	9.69	33.47
D.28	3	4	4	1	56.68	49.21	X	40.60	X
D.29	3	4	6	1	-0.09	5.13	-2.66	X	10.42
D.30	3	4	9	1	89.09	36.09	35.62	X	44.43
D.31	3	4	10	1	94.94	49.64	42.67	X	43.50
D.31				2	36.31	5.30	0.84	X	36.38
D.32	3	5	9	1	39.16	13.24	9.85	X	20.82
D.32				2	28.55	13.90	10.08	X	X
D.33	3	5	10		54.88	8.94	25.12	X	102.28

Table D.6 Amplitudes of the identified peaks during stimulation for different electrode configurations and experiment phases. The X signifies that a peak could not be detected in a given phase

Fig.	Animal	Anode	Cathode	Peak no.	Amplitudes (μV)				
					Phase 1	Phase 2	Phase 3	Phase 4	Phase 5
D.18	2	4	2	1	9.10	X	8.65	X	8.65
D.19	3	1	4	1	X	3.20	3.75	3.60	3.70
D.20	3	1	7	1	2.85	3.35	3.35	X	3.85
D.20				2	5.35	5.85	7.20	6.25	6.55
D.21	3	1	8	1	5.05	5.40	5.20	X	5.65
D.22	3	1	9	1	3.00	3.45	3.50	X	3.60
D.23	3	1	10	1	2.85	3.05	2.80	X	2.95
D.24	3	3	7	1	3.15	3.30	3.55	X	3.75
D.25	3	3	9	1	6.20	6.20	6.45	X	X
D.26	3	3	10	1	2.85	2.85	2.70	X	2.80
D.26				2	5.95	6.60	6.75	X	6.30
D.27	3	4	1	1	7.15	7.20	7.70	7.80	7.95
D.28	3	4	4	1	7.40	7.25	X	6.60	X
D.29	3	4	6	1	3.60	4.15	3.95	X	4.80
D.30	3	4	9	1	3.15	3.25	2.85	X	2.85
D.31	3	4	10	1	2.85	2.85	2.70	X	2.85
D.31				2	5.95	6.15	7.00	X	7.15
D.32	3	5	9	1	3.20	3.40	3.60	X	3.55
D.32				2	5.70	5.95	6.70	X	X
D.33	3	5	10	1	2.90	3.00	2.75	X	2.85

a)

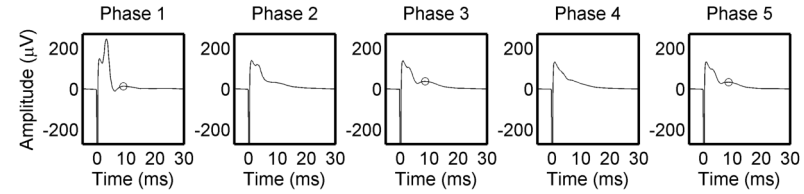

b)

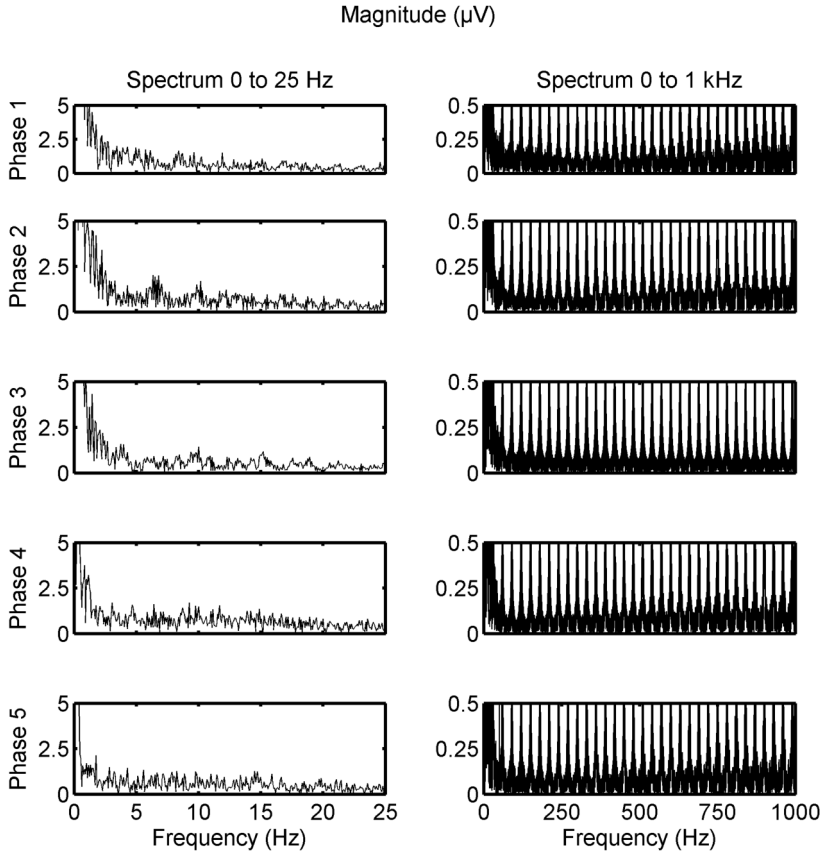

Figure D.18 Animal 2, anode in the anal canal, cathode 2: a) averaged signals acquired during all five phases of the experiment: 'o' depicts the peak identified 9.10 ms after the stimulation pulse in Phase 1 - prone position. b) Spectral analysis of the signals acquired during all five phases of the experiment (0 to 25 Hz and 0 to 1 kHz)

a)

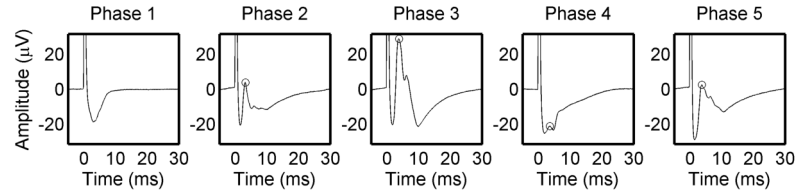

b)

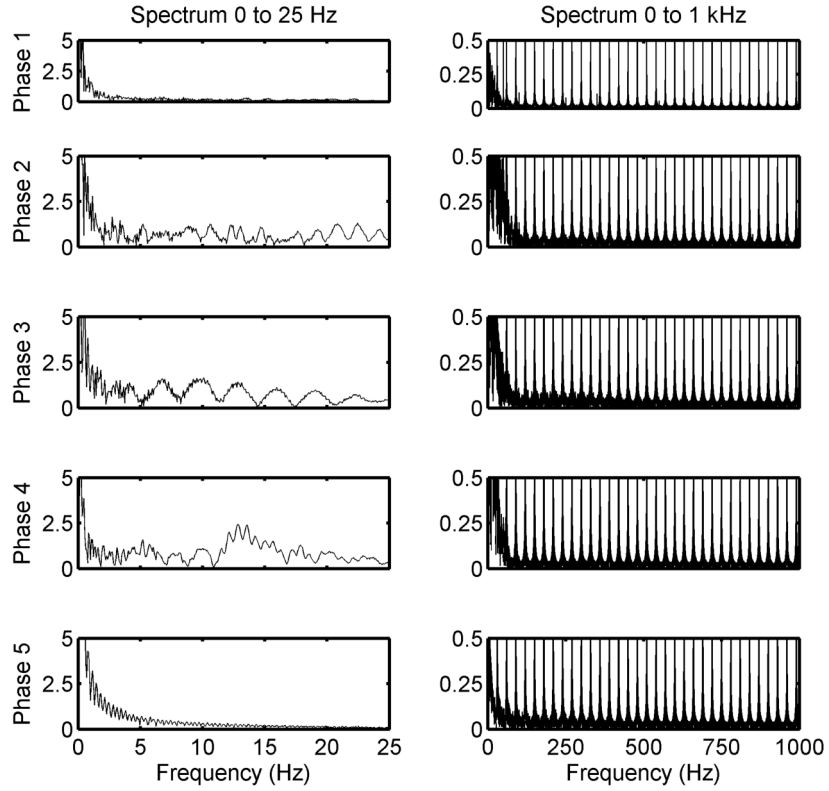

Figure D.19 Animal 3, anode right, cathode 4: a) averaged signals acquired during all five phases of the experiment: 'o' depicts the peak identified 3.20 ms after the stimulation pulse in Phase 2 - supine position. b) Spectral analysis of the signals acquired during all five phases of the experiment (0 to 25 Hz and 0 to 1 kHz)

a)

b)

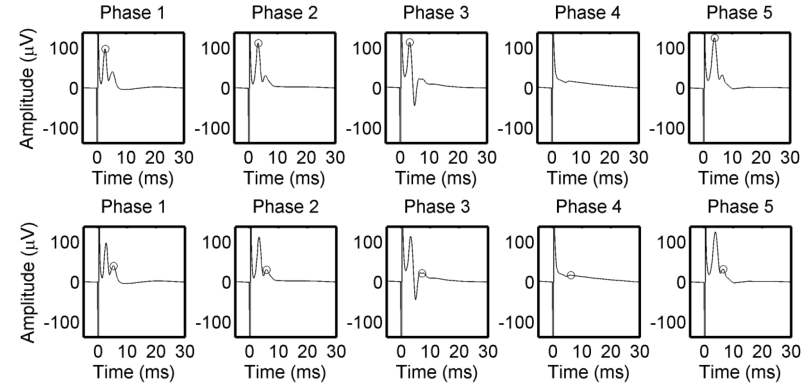

c)

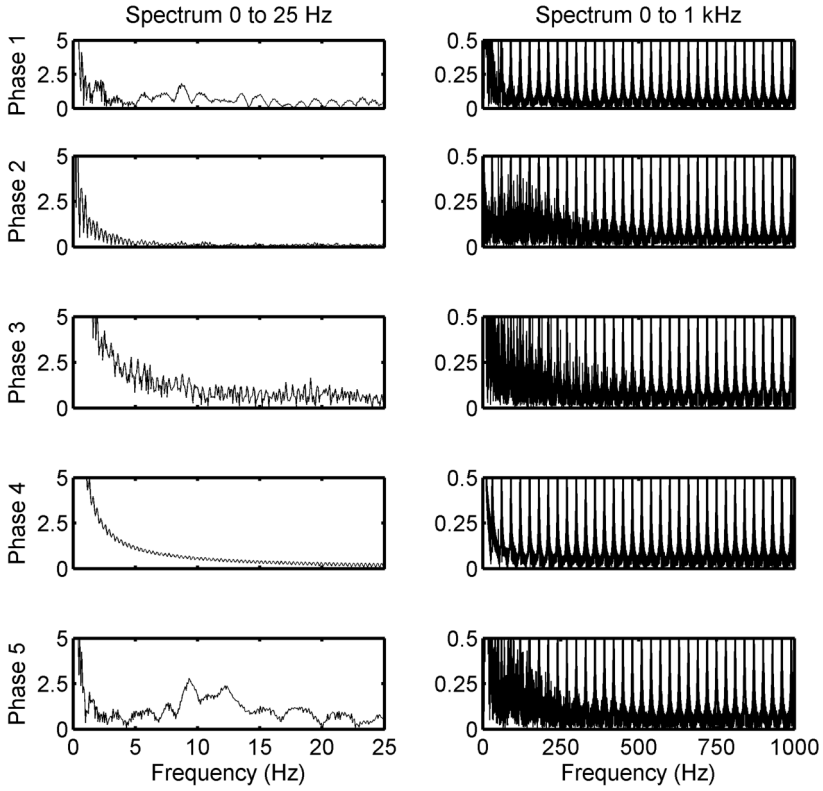

Figure D.20 Animal 3, anode right, cathode 7: averaged signals acquired during all five phases of the experiment: 'o' depicts the peak identified 3.20 ms and 5.35 ms (b) after the stimulation pulse in Phase 1 - prone position, c) spectral analysis of the signals acquired during all five phases of the experiment (0 to 25 Hz and 0 to 1 kHz)

a)

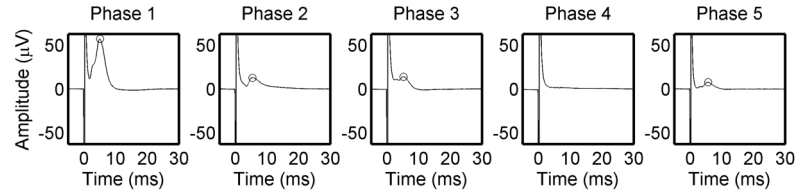

b)

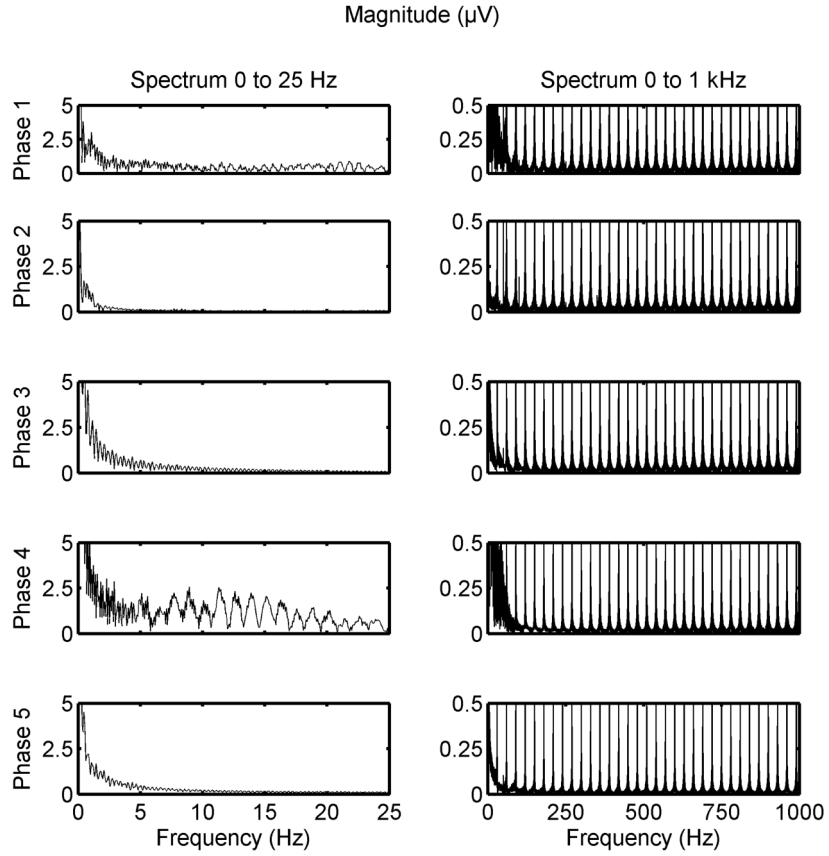

Figure D.21 Animal 3, anode right, cathode 8: a) averaged signals acquired during all five phases of the experiment: 'o' depicts the peak identified 5.05 ms after the stimulation pulse in Phase 1 - prone position, b) spectral analysis of the signals acquired during all five phases of the experiment (0 to 25 Hz and 0 to 1 kHz)

a)

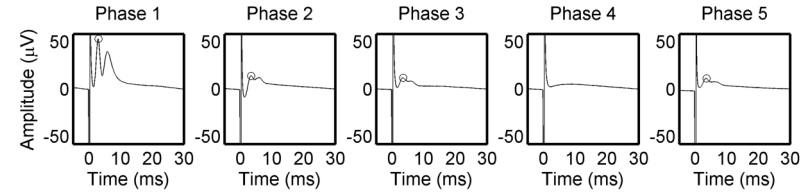

b)

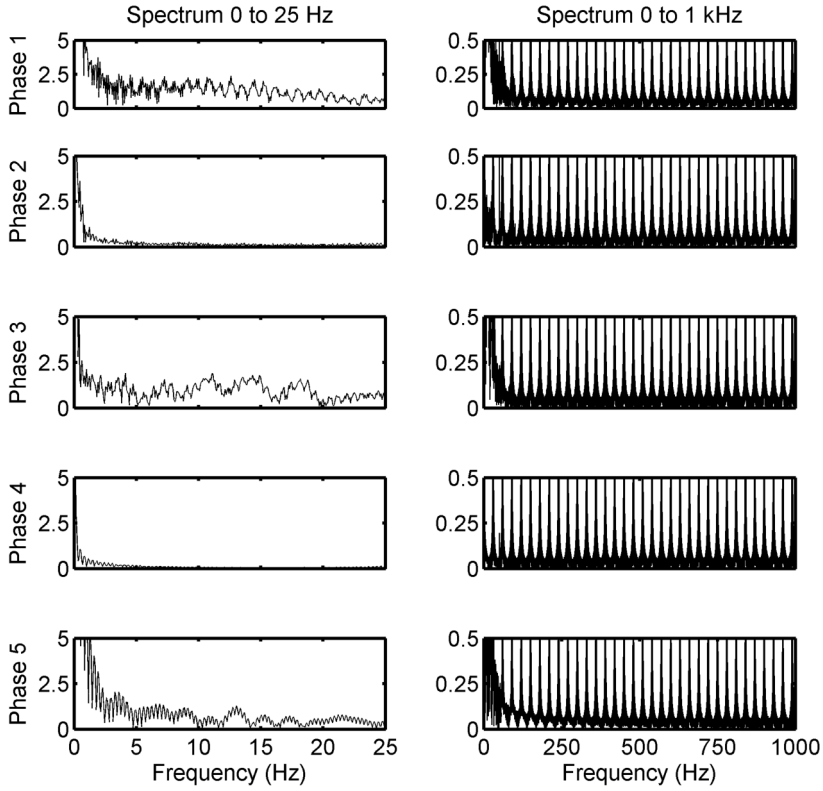

Figure D.22 Animal 3, anode right, cathode 9: a) averaged signals acquired during all five phases of the experiment: 'o' depicts the peak identified 3.00 ms after the stimulation pulse in Phase 1 - prone position, b) spectral analysis of the signals acquired during all five phases of the experiment (0 to 25 Hz and 0 to 1 kHz)

a)

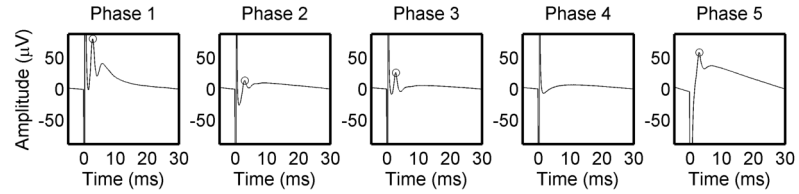

b)

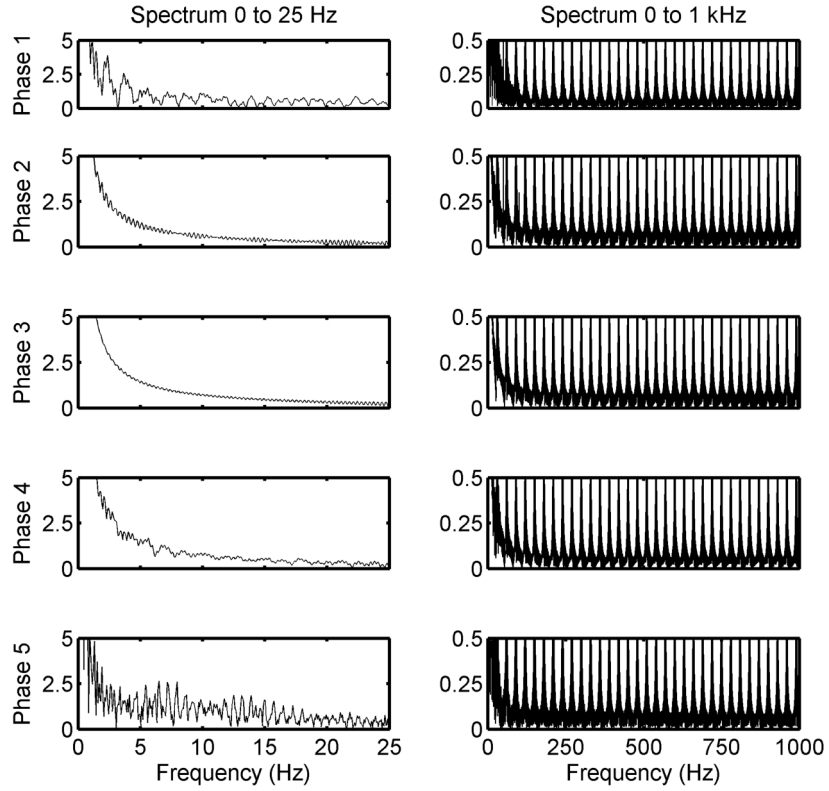

Figure D.23 Animal 3, anode right, cathode 10: a) averaged signals acquired during all five phases of the experiment: 'o' depicts the peak identified 2.85 ms after the stimulation pulse in Phase 1 - prone position, b) spectral analysis of the signals acquired during all five phases of the experiment (0 to 25 Hz and 0 to 1 kHz)

a)

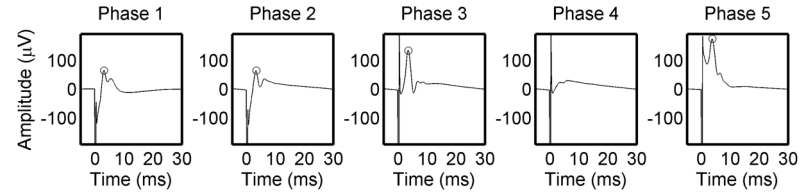

b)

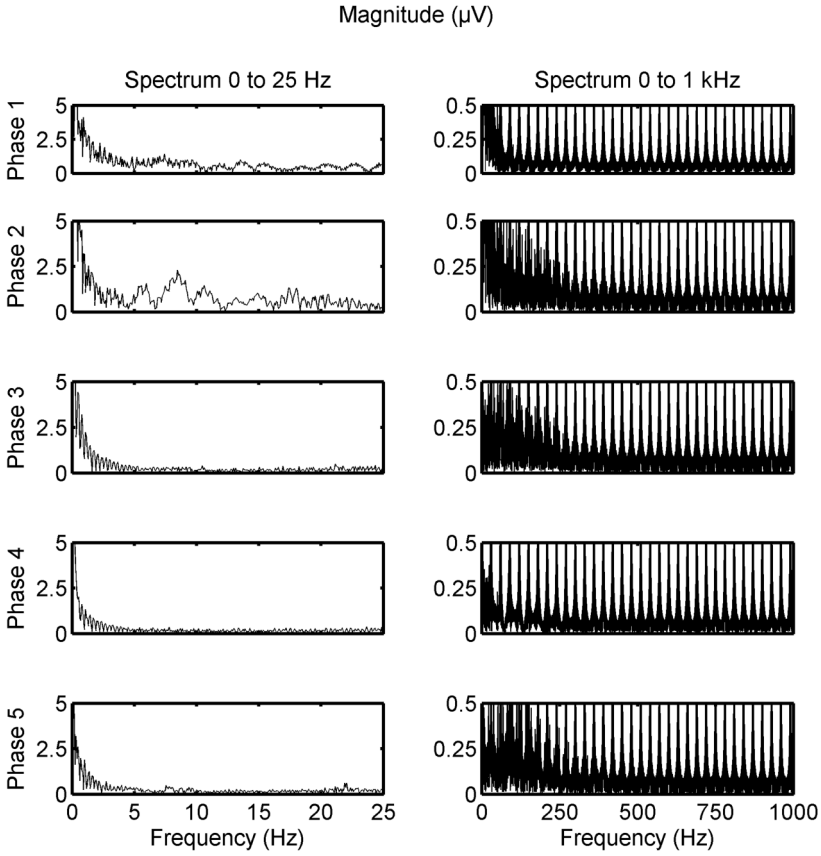

Figure D.24 Animal 3, anode left, cathode 7: a) averaged signals acquired during all five phases of the experiment: 'o' depicts the peak identified 3.15 ms after the stimulation pulse in Phase 1 - prone position, b) spectral analysis of the signals acquired during all five phases of the experiment (0 to 25 Hz and 0 to 1 kHz)

a)

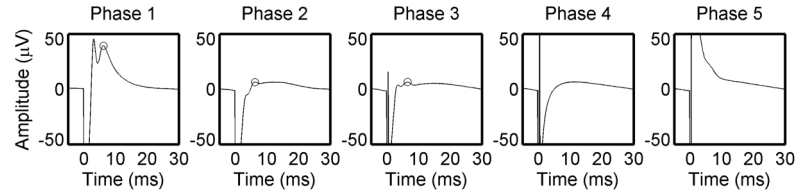

b)

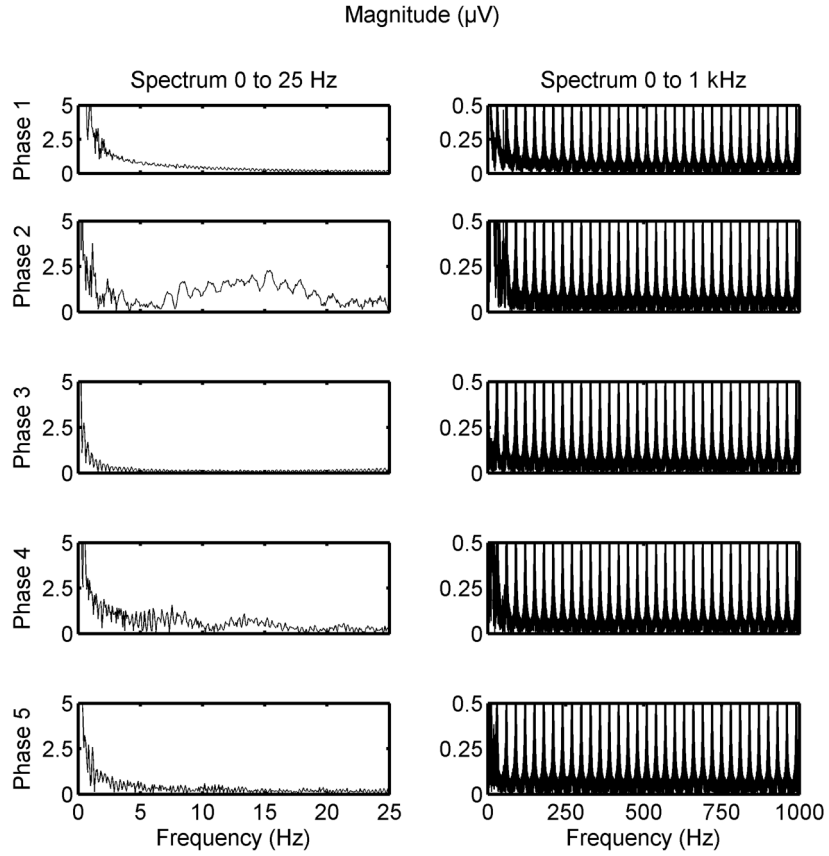

Figure D.25 Animal 3, anode left, cathode 9: a) averaged signals acquired during all five phases of the experiment: 'o' depicts the peak identified 6.20 ms after the stimulation pulse in Phase 1 - prone position, b) spectral analysis of the signals acquired during all five phases of the experiment (0 to 25 Hz and 0 to 1 kHz)

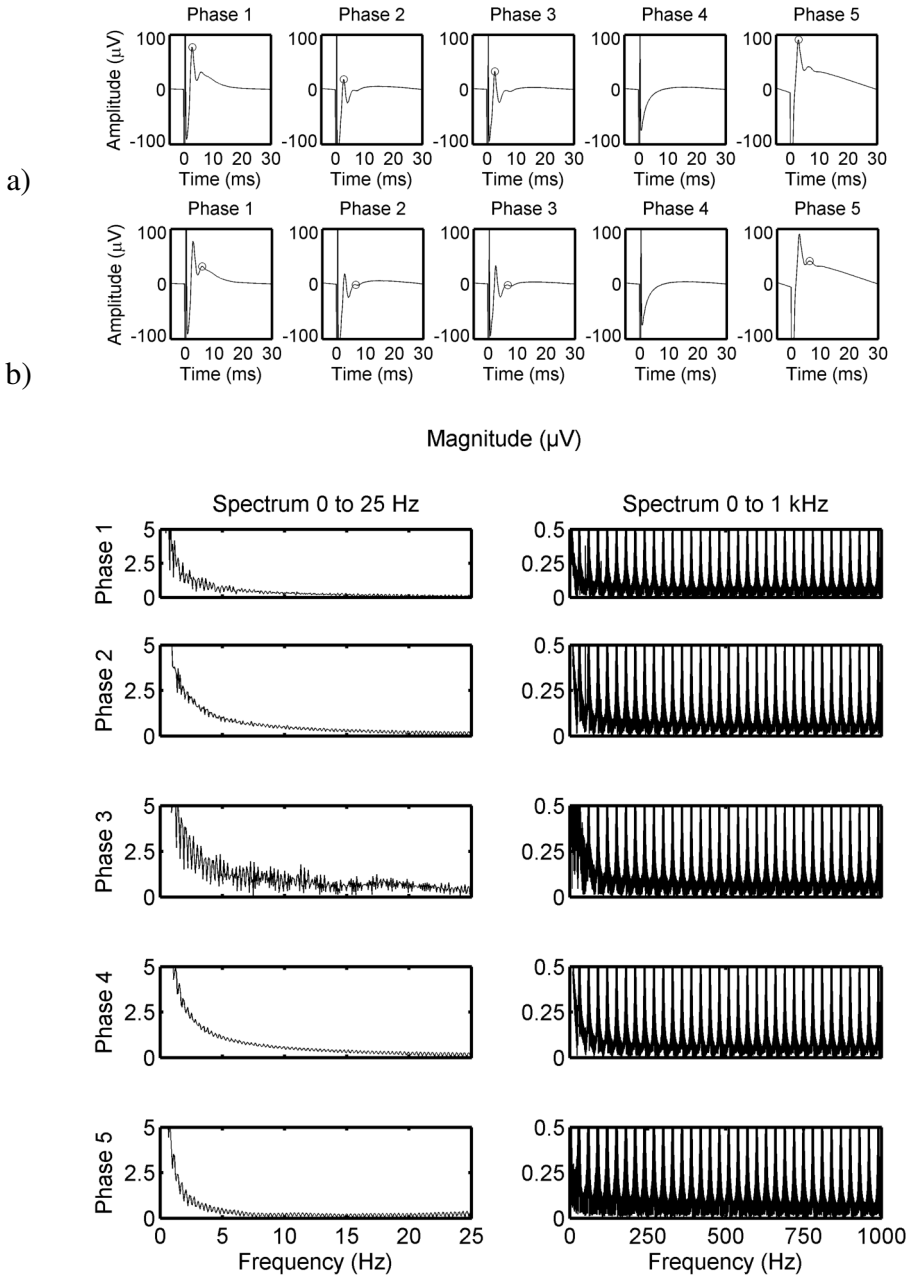

Figure D.26 Animal 3, anode left, cathode 10: averaged signals acquired during all five phases of the experiment: a) 'o' depicts the peak identified 2.85 ms after the stimulation pulse in Phase 1 - prone position, b) 'o' depicts the peak identified 5.95 ms after the stimulation pulse in Phase 1. c) Spectral analysis of the signals acquired during all five phases of the experiment (0 to 25 Hz and 0 to 1 kHz)

a)

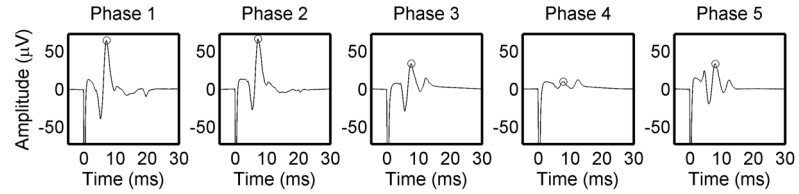

b)

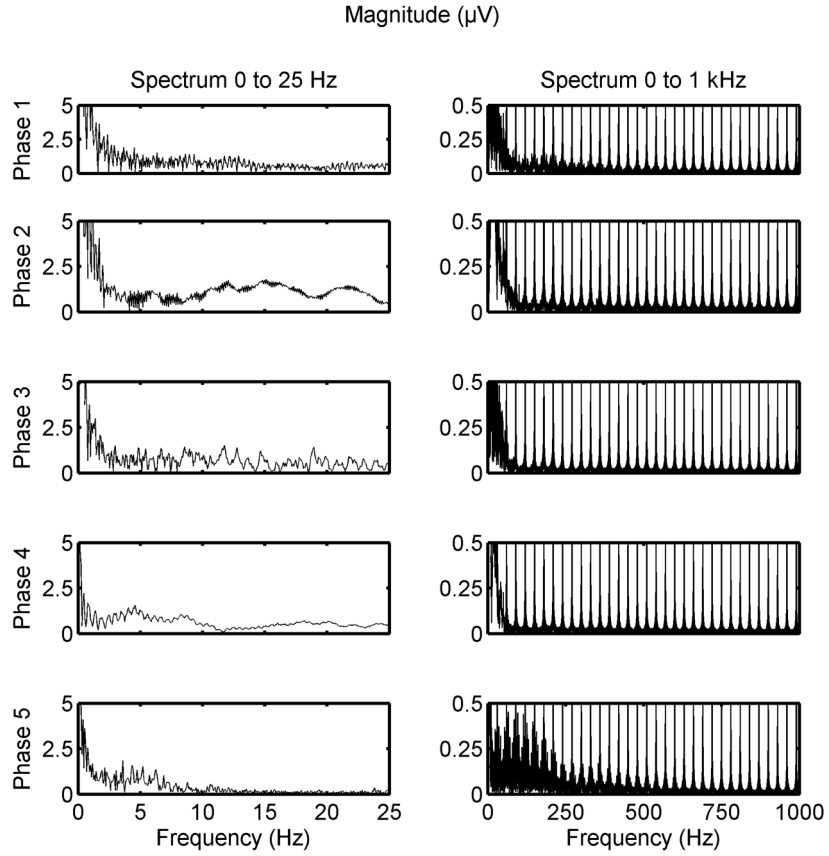

Figure D.27 Animal 3, anode in the anal canal, cathode 1: averaged signals acquired during all five phases of the experiment: a) 'o' depicts the peak identified 7.15 ms after the stimulation pulse in Phase 1 - prone position, b) Spectral analysis of the signals acquired during all five phases of the experiment (0 to 25 Hz and 0 to 1 kHz)

a)

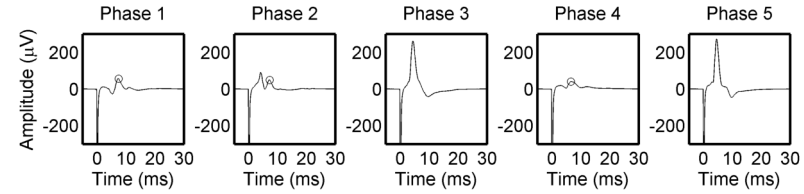

b)

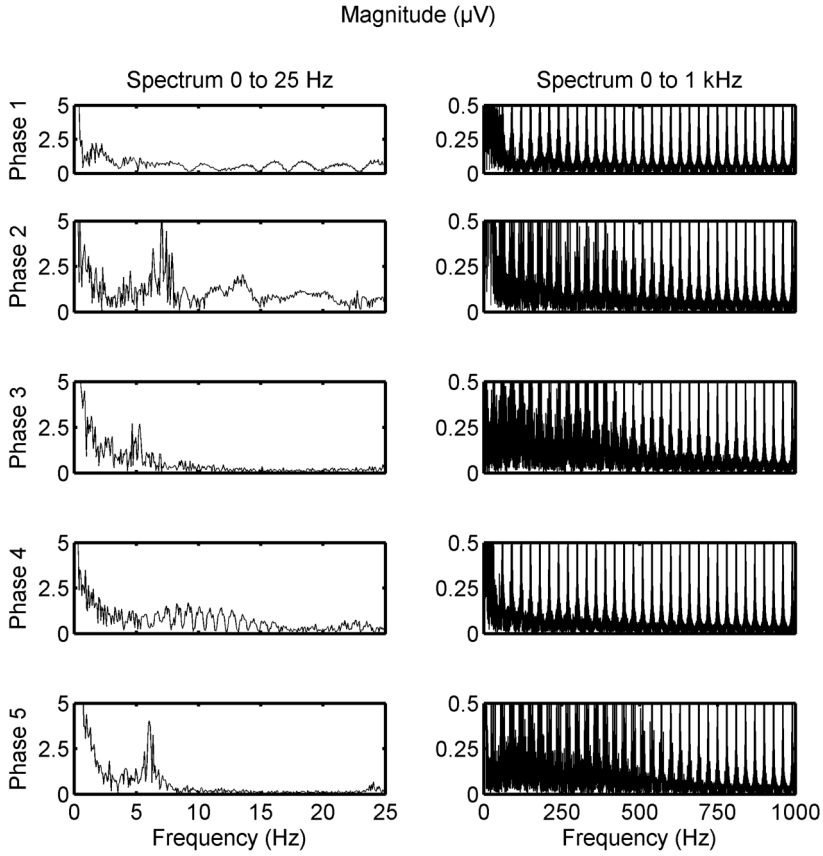

Figure D.28 Animal 3, anode in the anal canal, cathode 4: averaged signals acquired during all five phases of the experiment: a) 'o' depicts the peak identified 7.45 ms after the stimulation pulse in Phase 1 - prone position, b) Spectral analysis of the signals acquired during all five phases of the experiment (0 to 25 Hz and 0 to 1 kHz)

a)

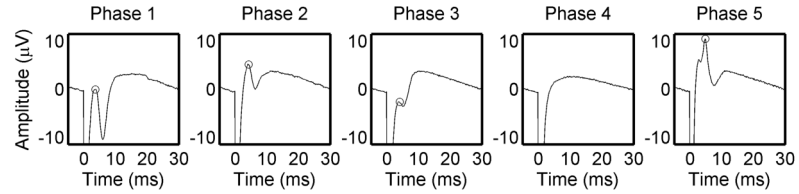

b)

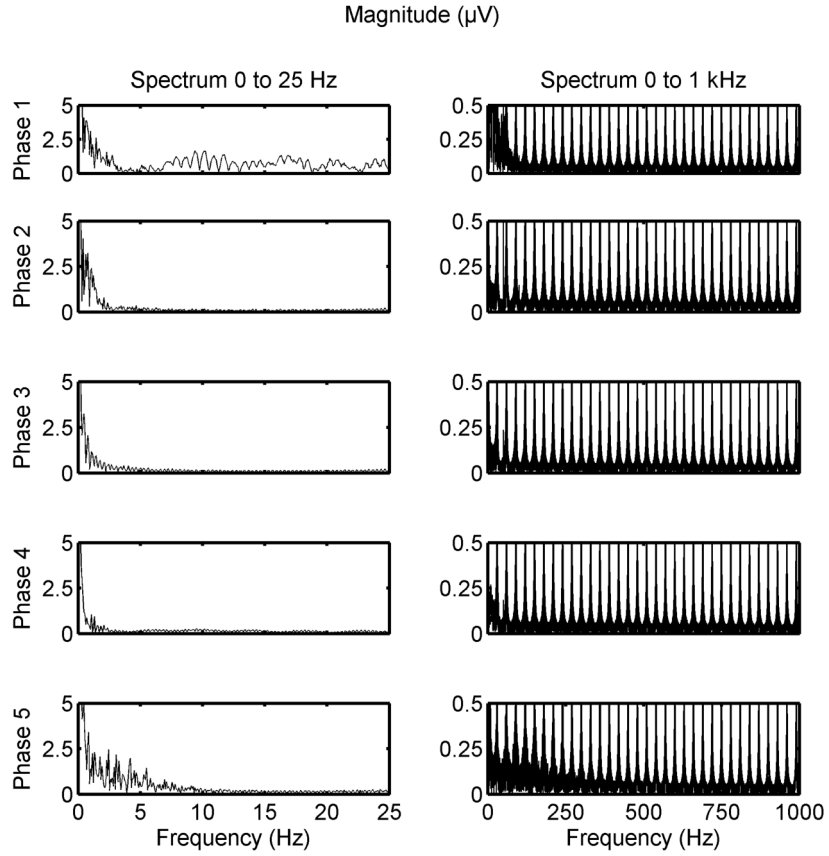

Figure D.29 Animal 3, anode in the anal canal, cathode 6: averaged signals acquired during all five phases of the experiment: a) 'o' depicts the peak identified 3.60 ms after the stimulation pulse in Phase 1 - prone position, b) Spectral analysis of the signals acquired during all five phases of the experiment (0 to 25 Hz and 0 to 1 kHz)

a)

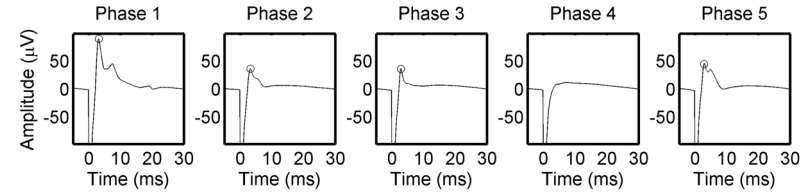

b)

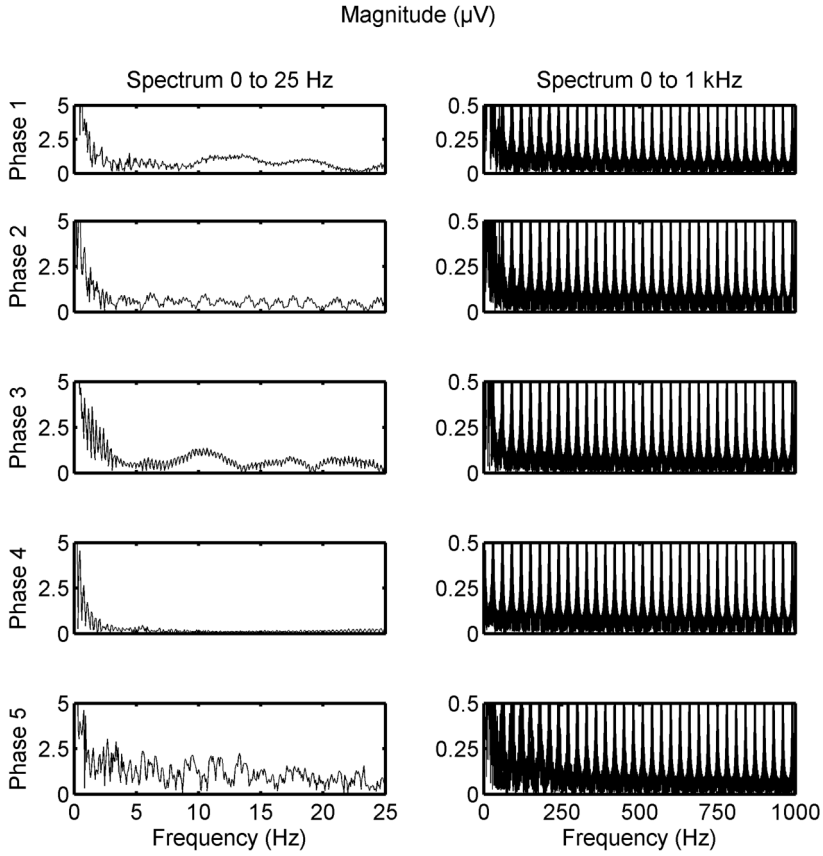

Figure D.30 Animal 3, anode in the anal canal, cathode 9: averaged signals acquired during all five phases of the experiment: a) 'o' depicts the peak identified 3.15 ms after the stimulation pulse in Phase 1 - prone position, b) Spectral analysis of the signals acquired during all five phases of the experiment (0 to 25 Hz and 0 to 1 kHz)

a)

b)

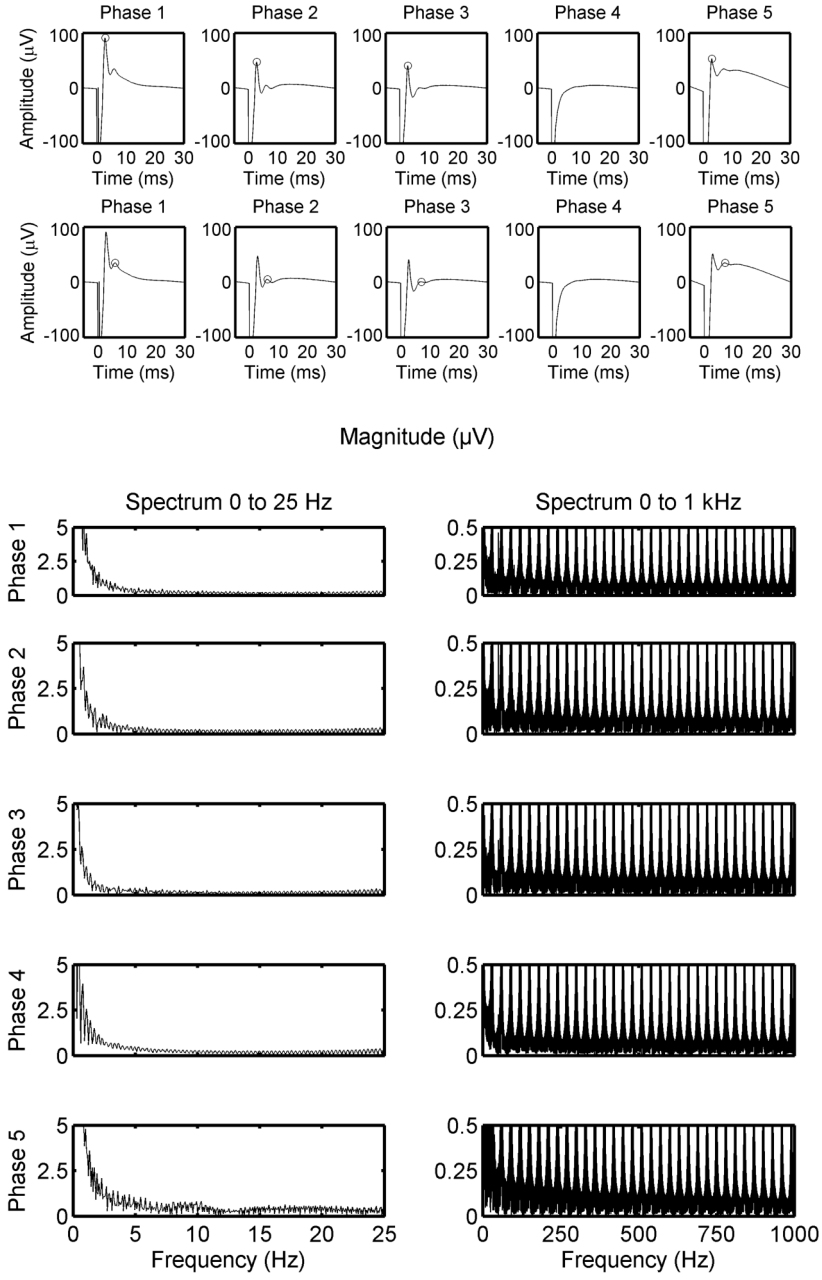

c)

Figure D.31 Animal 3, anode in the anal canal, cathode 10: averaged signals acquired during all five phases of the experiment: 'o' depicts the peak identified 2.85 ms (a) and 5.95 ms (b) after the stimulation pulse in Phase 1 - prone position, c) Spectral analysis of the signals acquired during all five phases of the experiment (0 to 25 Hz and 0 to 1 kHz)

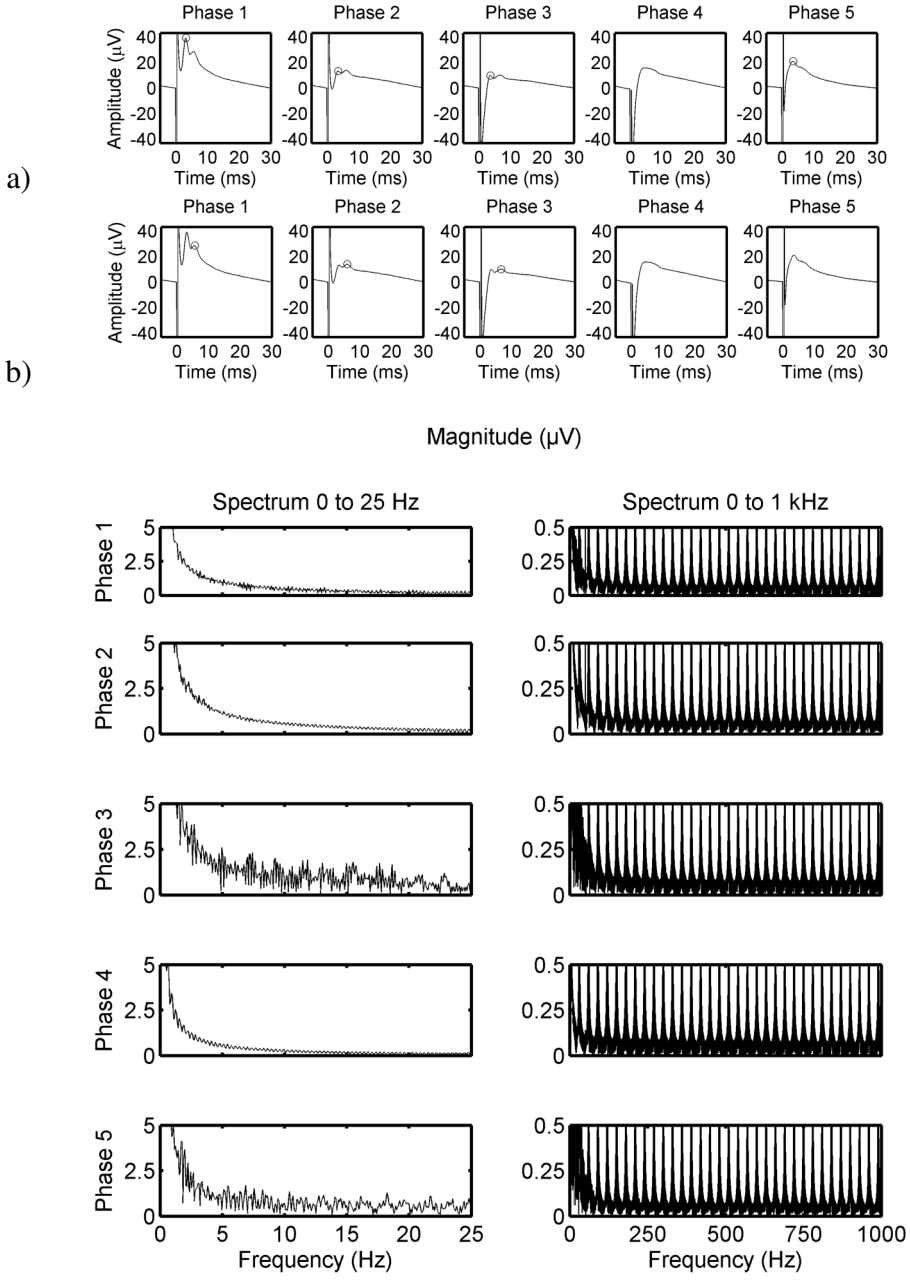

Figure D.32 Animal 3, anode on the abdomen, cathode 9: averaged signals acquired during all five phases of the experiment: 'o' depicts the peak identified 3.20 ms (a) and 5.70 ms (b) after the stimulation pulse in Phase 1 - prone position, c) Spectral analysis of the signals acquired during all five phases of the experiment (0 to 25 Hz and 0 to 1 kHz)

a)

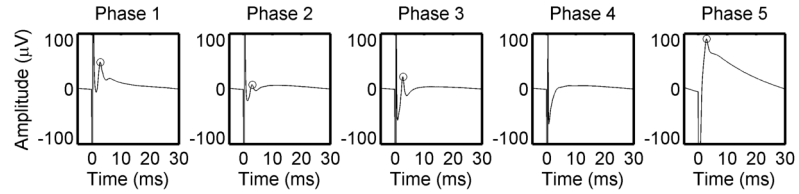

b)

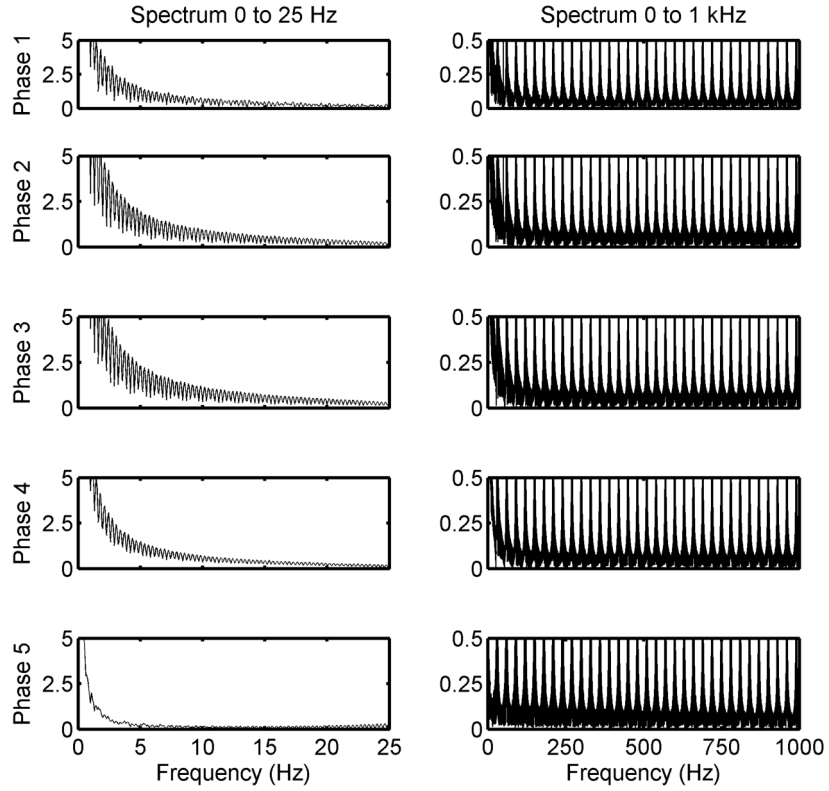

Figure D.33 Animal 3, anode on the abdomen, cathode 10: averaged signals acquired during all five phases of the experiment: a) 'o' depicts the peak identified 2.90 ms after the stimulation pulse in Phase 1 - prone position, b) Spectral analysis of the signals acquired during all five phases of the experiment (0 to 25 Hz and 0 to 1 kHz)

D.2.2 Summary of the valleys identified in the entire dataset

Table D.7 Amplitudes of the identified peaks during stimulation for different electrode configurations and experiment phases. The X signifies that a peak could not be detected in a given phase

Fig.	Animal	Anode	Cathode	Peak no.	Amplitudes (µV)				
					Phase 1	Phase 2	Phase 3	Phase 4	Phase 5
D.34	1	1	7	1	-27.29	X	-64.44	X	-42.83
D.35	1	1	8	1	-19.47	-44.41	-57.44	X	-36.22
D.36	1	1	10	1	-26.16	X	-64.90	X	-50.55
D.37	2	3	10	1	X	5.99	3.17	X	5.29
D.38	3	1	8	1	X	3.37	10.02	X	1.29
D.39	3	1	10	1	21.29	1.61	-4.27	X	32.72
D.40	3	3	10	1	17.31	-26.23	-25.01	X	37.52
D.41	3	4	2	1	-1.00	2.48	2.85	-1.64	X
D.42	3	4	6	1	-10.38	-0.02	-3.57	X	X
D.43	3	4	10	1	25.63	-9.47	-16.91	X	22.98

Table D.8 Amplitudes of the identified peaks during stimulation for different electrode configurations and experiment phases. The X signifies that a peak could not be detected in a given phase

Fig.	Animal	Anode	Cathode	Peak no.	Amplitudes (µV)				
					Phase 1	Phase 2	Phase 3	Phase 4	Phase 5
D.34	1	1	7	1	2.65	X	2.55	X	2.55
D.35	1	1	8	1	2.75	2.55	2.55	X	2.50
D.36	1	1	10	1	2.85	X	2.75	X	2.75
D.37	2	3	10	1	X	4.85	4.80	X	4.85
D.38	3	1	8	1	X	3.50	3.70	X	2.50
D.39	3	1	10	1	4.35	4.40	4.35	X	4.65
D.40	3	3	10	1	4.55	4.15	4.30	X	4.95
D.41	3	4	2	1	9.35	9.95	10.70	10.60	X
D.42	3	4	6	1	6.05	6.35	5.05	X	X
D.43	3	4	10	1	4.70	4.55	4.45	X	4.80

a)

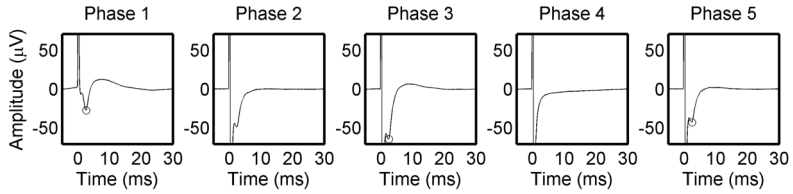

b)

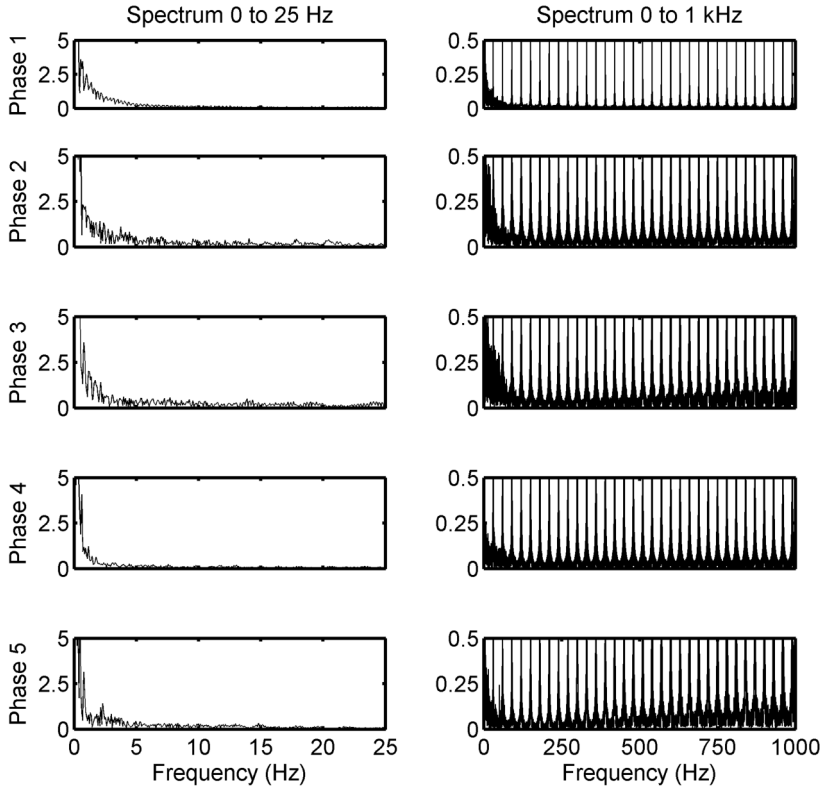

Figure D.34 Animal 1, anode right, cathode 7: averaged signals acquired during all five phases of the experiment: a) 'o' depicts the valley identified 2.65 ms after the stimulation pulse in Phase 1 - prone position, b) Spectral analysis of the signals acquired during all five phases of the experiment (0 to 25 Hz and 0 to 1 kHz)

a)

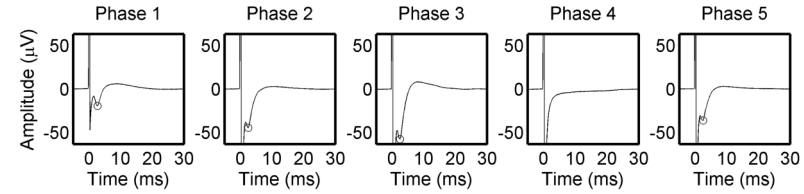

b)

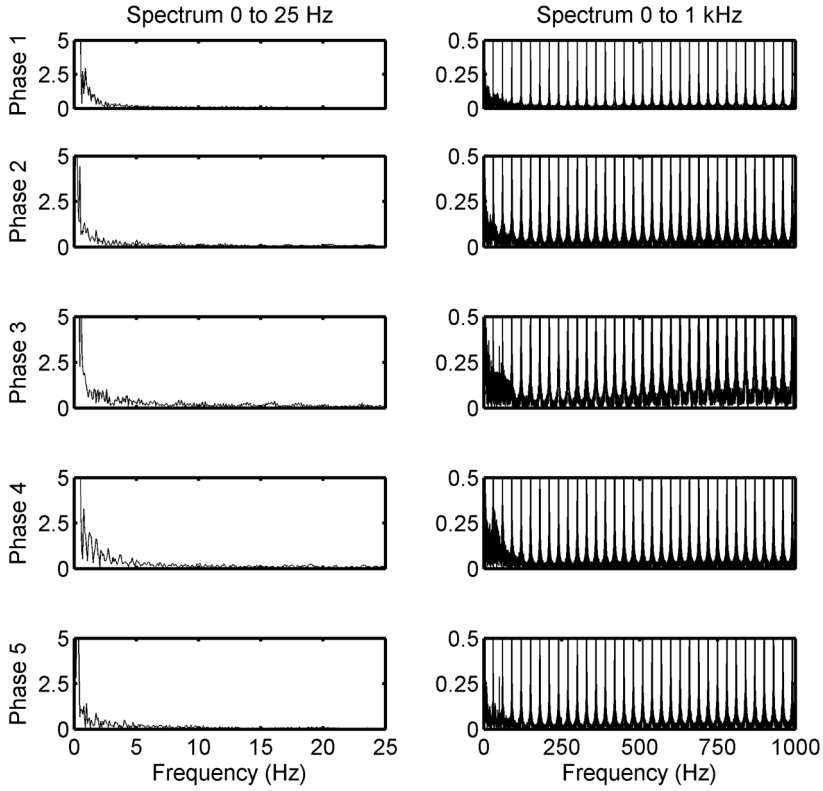

Figure D.35 Animal 1, anode right, cathode 8: averaged signals acquired during all five phases of the experiment: a) 'o' depicts the valley identified 2.75 ms after the stimulation pulse in Phase 1 - prone position, b) Spectral analysis of the signals acquired during all five phases of the experiment (0 to 25 Hz and 0 to 1 kHz)

a)

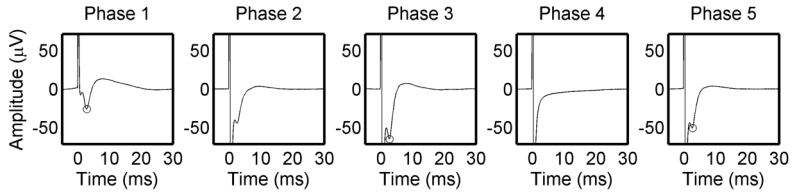

b)

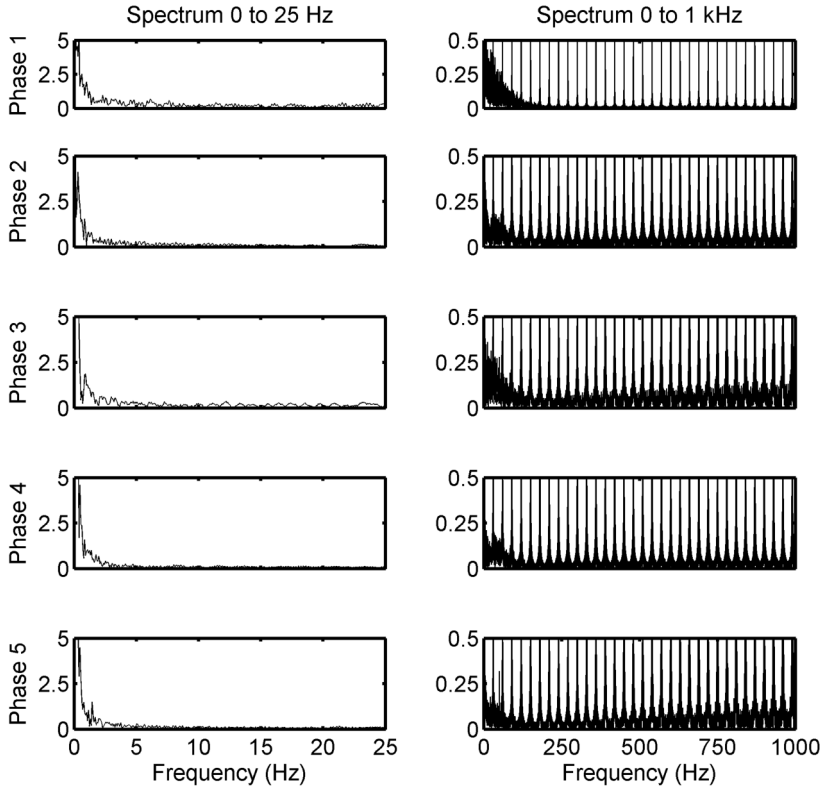

Figure D.36 Animal 1, anode right, cathode 10: averaged signals acquired during all five phases of the experiment: a) 'o' depicts the valley identified 2.85 ms after the stimulation pulse in Phase 1 - prone position, b) Spectral analysis of the signals acquired during all five phases of the experiment (0 to 25 Hz and 0 to 1 kHz)

a)

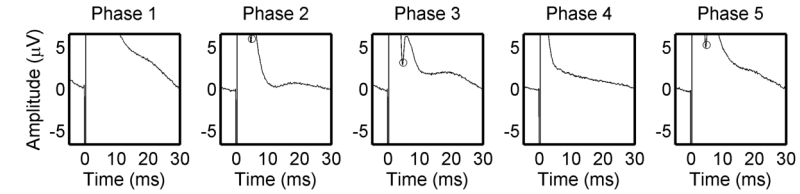

b)

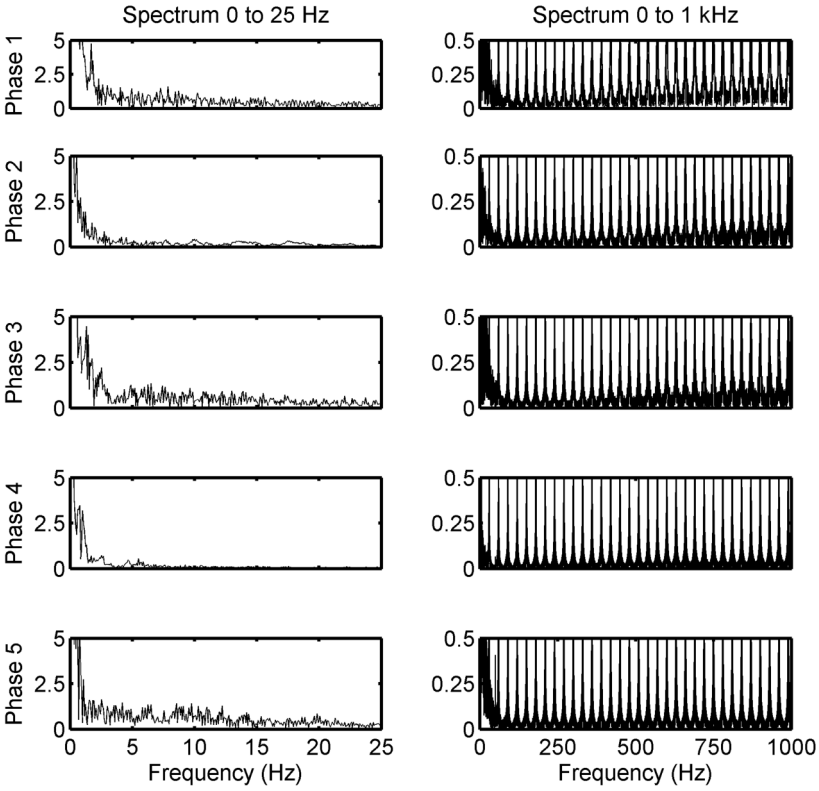

Figure D.37 Animal 2, anode left, cathode 10: averaged signals acquired during all five phases of the experiment: a) 'o' depicts the valley identified 4.85 ms after the stimulation pulse in Phase 2 - supine position, b) Spectral analysis of the signals acquired during all five phases of the experiment (0 to 25 Hz and 0 to 1 kHz)

a)

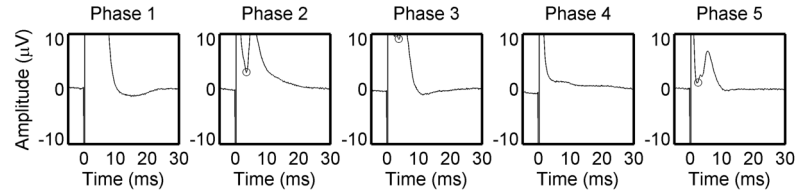

b)

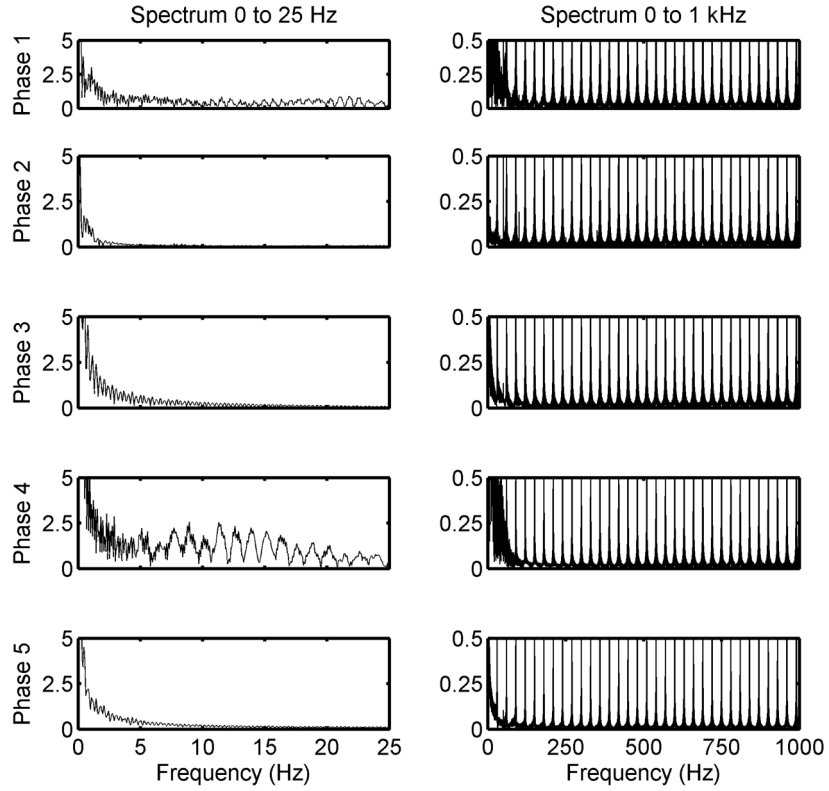

Figure D.38 Animal 3, anode right, cathode 8: averaged signals acquired during all five phases of the experiment: a) 'o' depicts the valley identified 3.50 ms after the stimulation pulse in Phase 2 - supine position, b) Spectral analysis of the signals acquired during all five phases of the experiment (0 to 25 Hz and 0 to 1 kHz)

a)

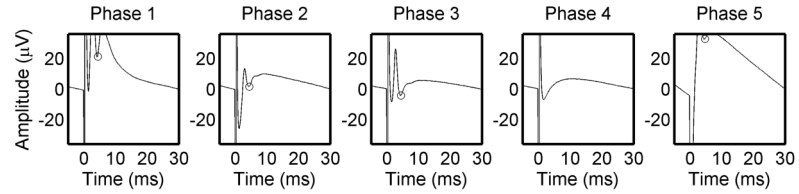

b)

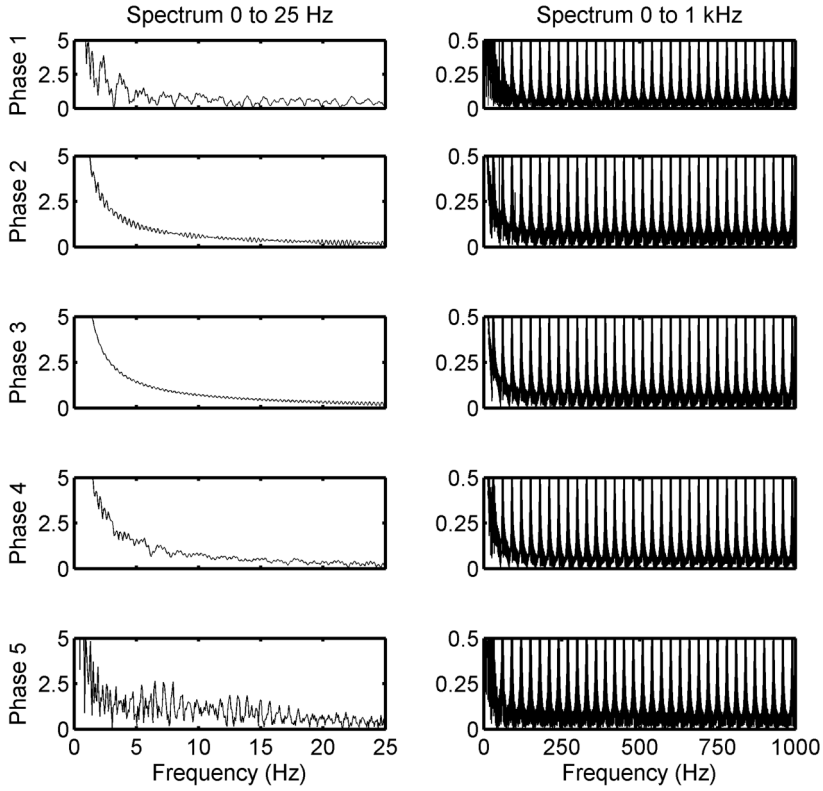

Figure D.39 Animal 3, anode right, cathode 10: averaged signals acquired during all five phases of the experiment: a) 'o' depicts the valley identified 4.35 ms after the stimulation pulse in Phase 1 - prone position, b) Spectral analysis of the signals acquired during all five phases of the experiment (0 to 25 Hz and 0 to 1 kHz)

a)

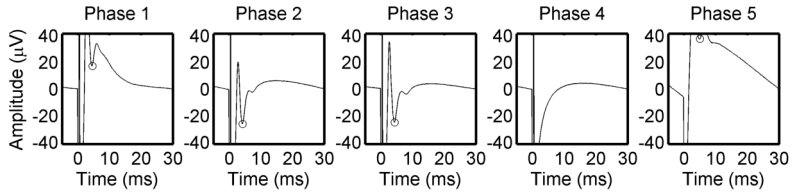

b)

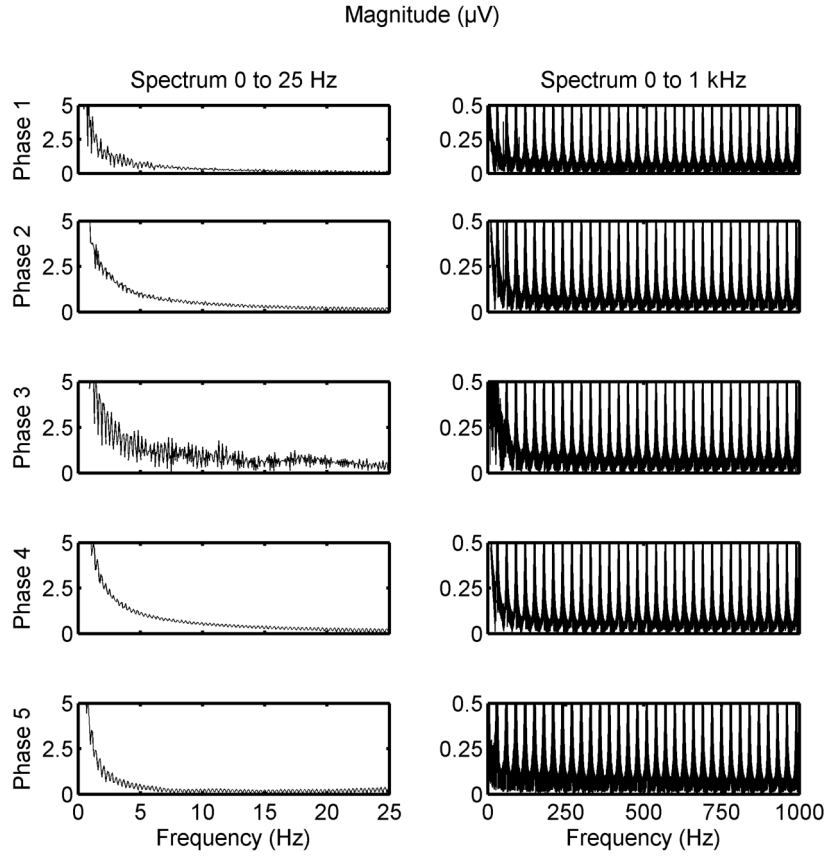

Figure D.40 Animal 3, anode left, cathode 10: averaged signals acquired during all five phases of the experiment: a) 'o' depicts the valley identified 4.55 ms after the stimulation pulse in Phase 1 - prone position, b) Spectral analysis of the signals acquired during all five phases of the experiment (0 to 25 Hz and 0 to 1 kHz)

a)

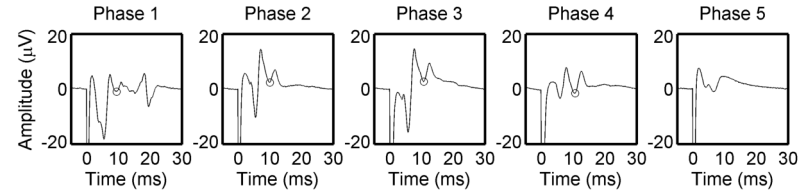

b)

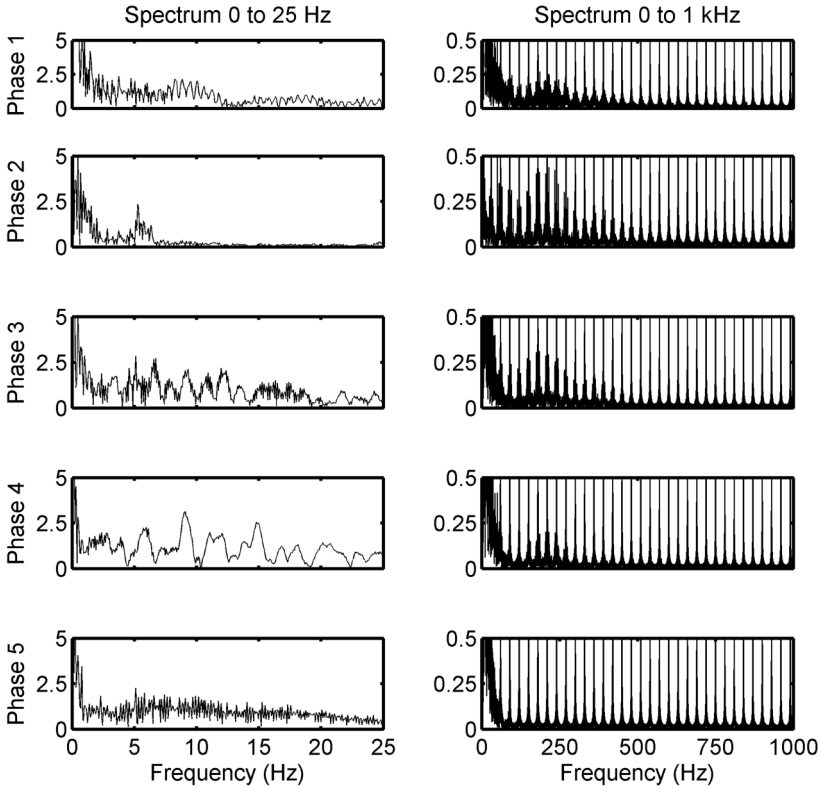

Figure D.41 Animal 3, anode in the anal canal, cathode 2: averaged signals acquired during all five phases of the experiment: a) 'o' depicts the valley identified 9.35 ms after the stimulation pulse in Phase 1 - prone position, b) Spectral analysis of the signals acquired during all five phases of the experiment (0 to 25 Hz and 0 to 1 kHz)

a)

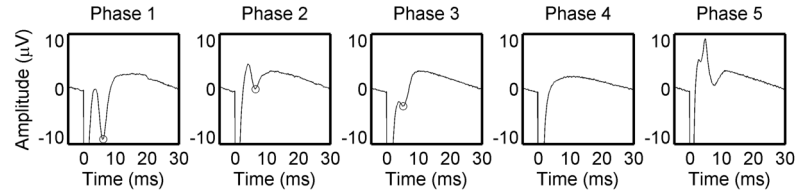

b)

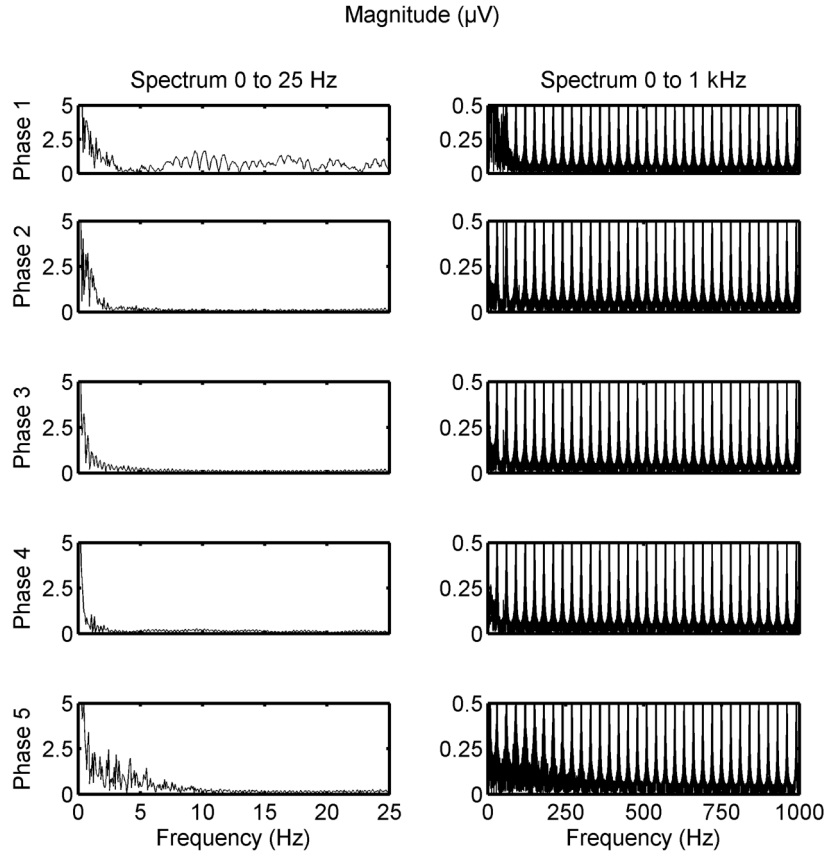

Figure D.42 Animal 3, anode in the anal canal, cathode 6: averaged signals acquired during all five phases of the experiment: a) 'o' depicts the valley identified 6.05 ms after the stimulation pulse in Phase 1 - prone position, b) Spectral analysis of the signals acquired during all five phases of the experiment (0 to 25 Hz and 0 to 1 kHz)

a)

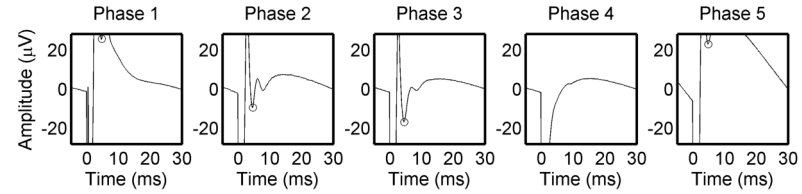

b)

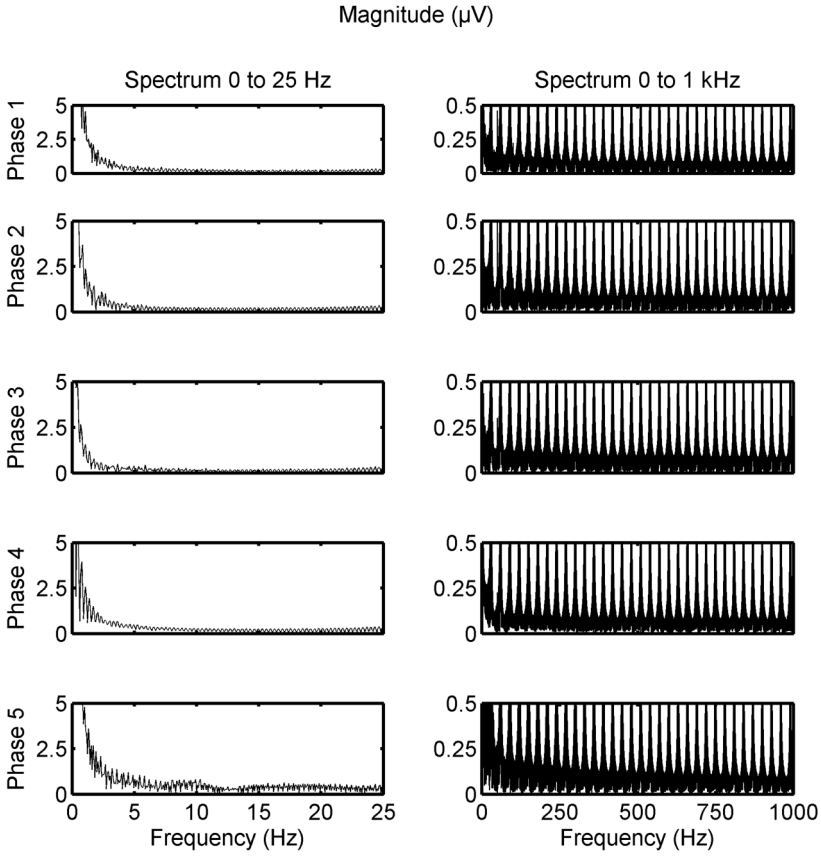

Figure D.43 Animal 3, anode in the anal canal, cathode 10: averaged signals acquired during all five phases of the experiment: a) 'o' depicts the valley identified 4.70 ms after the stimulation pulse in Phase 1 - prone position, b) Spectral analysis of the signals acquired during all five phases of the experiment (0 to 25 Hz and 0 to 1 kHz)